DYNAMICS AND CONSEQUENCES OF DEBRIS FROM THE IRREGULAR SATELLITES OF THE GIANT PLANETS

A Dissertation

Presented to the Faculty of the Graduate School

of Cornell University

in Partial Fulfillment of the Requirements for the Degree of

Doctor of Philosophy

by

Daniel Tamayo

January 2015

DYNAMICS AND CONSEQUENCES OF DEBRIS FROM THE IRREGULAR SATELLITES OF THE GIANT PLANETS

Daniel Tamayo, Ph.D.

Cornell University 2015

Each of the solar system's giant planets host a large population of irregular satellites, small moons on distant orbits that were gravitationally captured early in the solar system's history. Because of the frequent collisions between these objects, most of the original population's mass should have ground to dust in a few hundred Myr (Bottke et al. 2010). This dissertation investigates the fate of this debris, and in particular the contamination by this dust of the larger moons that orbit close to the planet. We argue that the ten-fold darkening of the Saturnian satellite Iapetus' leading hemisphere was triggered by this dark infalling material. We also present the first observations in scattered visible light of the Phoebe ring, a vast dust ring sourced by Saturn's largest irregular satellite Phoebe. Additionally, we argue that this process of mass transfer from the irregular satellites may explain the hemispherical color asymmetries observed on the largest Uranian moons (Buratti and Mosher 1991). The dynamics of this process are complicated by Uranus' extreme obliquity, which creates a range of semimajor axes in which particle orbits undergo large-amplitude, chaotic eccentricity oscillations. This phenomenon was first explained by Tremaine et al. (2009); we generalize their results by incorporating the effects of radiation pressure, which are important for small dust grains. Finally, as part of a separate project, we provide constraints on the properties of the putative planet Fomalhaut b, in light of its newly revised, extremely eccentric orbit (Kalas et al. 2013).

BIOGRAPHICAL SKETCH

Daniel Tamayo was born in Spain, and moved to the U.S. when he was twelve years old. He attended the University of Michigan, where he obtained B.S. degrees in physics, philosophy, and mathematical physics. In 2005, he joined the U.S. Peace Corps, and taught mathematics and physical science to students in 8^{th}-10^{th} grade in Otjimbingwe, a small village in Namibia. Upon completion of his service, Daniel moved to Ithaca, NY to pursue the doctoral work presented here.

To Carrie, whose love and support have allowed me to pursue my passions.

And to my parents, who gave me a world full of possibilities.

ACKNOWLEDGEMENTS

I would first like to thank my advisor, Joe Burns. I am extremely grateful for the many opportunities he has given me to attend professional conferences, and for his introducing me to several potential collaborators. Joe has also consistently made time for me, despite his jam-packed schedule, and I have benefited greatly from his insightful professional and scientific advice and comments. His careful readings of my manuscripts have also made me a *much* better scientific writer! I would also like to thank Phil Nicholson, who seems to have answers for questions on any topic imaginable, and helped me to understand several concepts I found challenging.

I am most indebted for the technical aspects of this dissertation to Matt Hedman. Matt has been extremely generous with his time, and I have learned an incredible amount from him. I feel very lucky to have been able to work with him. I would also like to thank Matt Tiscareno and Mike Evans, who have helped me navigate Cassini-related software. Additionally, they, as well as former graduate students Rebecca Harbison, Anthony Milano, and Manish Agarwal, have also given me very valuable suggestions during our weekly group meetings.

I owe a huge debt of gratitude to Rob Douglas, a great friend and programming wizard, for his repeated help and patience with my various coding dilemmas over the last six years. In two days, he also created software for me to visualize the output from my dynamical simulations, which I have subsequently tried to develop, but have mostly broken.

I also feel very fortunate to have had the opportunity to work with two fantastic undergraduate students during my time at Cornell. Heming Ge, a student in computer science, helped make important developments to Rob's initial code for the visualization of dynamical simulations. For the past year, I have also

worked with Steve Markham, a physics student, on the latest data from the Phoebe ring. He is responsible for many of the results in Chap. 4. His motivation and insight have led to the creation of several new important tools for studying this faint ring, and I look forward to seeing what they yield with the new data.

I would like to thank Manolis Papastergis, who, despite working in a completely separate field, helped me work through several hurdles in my research. I would also like to thank all the other graduate students for, among other things, the shared late-night homework sets, the board game nights, and the laughter along the way.

Last, but certainly not least, I would like to thank my family. First my grandparents, for their unwavering enthusiasm and support, despite not being quite sure what I do. Also my in-laws, for swooping in during times of crisis to take care of Nico, and for always finding astronomy news that I hadn't heard of. My wife, Carrie, has been incredibly supportive, all while working a full-time job and caring for our son more than her fair share. I am inexplicably lucky to have such a smart, beautiful, caring, and fun partner. I also want to thank our son Nico, who, despite certainly presenting the single largest obstacle to the completion of this dissertation, fills every day with joy and laughter. Finally, I would like to thank my parents. While I did not realize it until I was an adult, I see now the impact of the invaluable educational and life opportunities they provided me. I hope I can provide Nico with the same love and nurturing you gave me.

TABLE OF CONTENTS

LIST OF FIGURES

CHAPTER 1

INTRODUCTION

From the time Galileo discovered the first moons around the giant planets in 1610 until the turn of the 20th century, giant planet satellites followed an easily discernible pattern. They were large (hundreds to thousands of km in radius), and moved on nearly circular, prograde orbits (counterclockwise when looking down on the planet's North pole) that lay close to their respective planets' equatorial plane.[1] There was no need to classify this type of satellite at the time, but today these moons are known as the regular satellites.

With the advent of photographic plates, William Pickering discovered the first irregular satellite 1898. Saturn's moon Phoebe had eluded detection until this time through its small size (about 200 km across) and dark surface (albedo ≈ 0.1 at visible wavelengths, Simonelli et al. 1999). But the moon's most striking feature was its peculiar orbit. Not only was Phoebe over three times further out than the rest of the Saturnian moons, it moved on a *retrograde* orbit (clockwise when looking down on the planet's North pole) that was inclined by over 20° from Saturn's equatorial plane and was significantly eccentric ($e \approx 0.16$). Over the following century, a few other moons were discovered around the giant planets in similarly distant, inclined and eccentric orbits. But it was an effort begun by Brett Gladman using modern charge coupled device (CCD) detectors at the turn of the 21st century that led to the discovery of the vast majority of the irregular satellites. This rapid discovery of over a hundred new objects sparked renewed interest in this remarkable population.

[1]The notable exceptions are Neptune's Triton, which moves on a retrograde orbit (and some therefore think it should be classified as an irregular satellite), and Saturn's Iapetus, which, while prograde, is inclined to the planet's equator as described at length in Chapters 2-4.

The irregular satellites tend to be small (sim 10 km across); however, this is not particularly distinctive, as the Voyager spacecraft discovered several similarly sized small bodies nestled close to each of the giant planets. The irregular satellites are instead most naturally classified through their dynamics. In contrast to the small, concentric equatorial orbits of their regular satellite counterparts, the irregulars form a swarm of mutually inclined and eccentric orbits at the outer limits of stability in their parent planets' spheres of gravitational influence (i.e., at a few tenths of the central body's Hill radius, r_H, Hamilton and Burns 1991). The distribution of their orbits is shown in Fig. 1.1 (Jewitt and Haghighipour 2007).

Figure 1.1 highlights several features of the irregular satellite population, all of which point to an alternate formation mechanism than the canonical model of accretion out of a circumplanetary disk (e.g., Canup and Ward 2002; Mosqueira and Estrada 2003). While a dissipative disk would generate low eccentricities and inclinations, capture of planetesimals from circumstellar space would generate a roughly isotropic distribution of eccentric orbits. This is consistent with the observed distribution, as the near-polar orbits missing in Fig. 1.1 would have been subsequently removed through the Kozai effect induced by the Sun's gravity (Carruba et al. 2002, , and see Chap. 5 for a detailed description of the Kozai effect). Such capture from interplanetary space requires that the incoming object lose enough energy to become gravitationally bound. The leading mechanisms for this energy exchange are gas drag in the circumplanetary nebula (Pollack et al. 1979; Ćuk and Burns 2004), and three-body interactions during close encounters between the giant planets during an early reshuffling of the planets in the Nice model (Nesvorný et al. 2007).

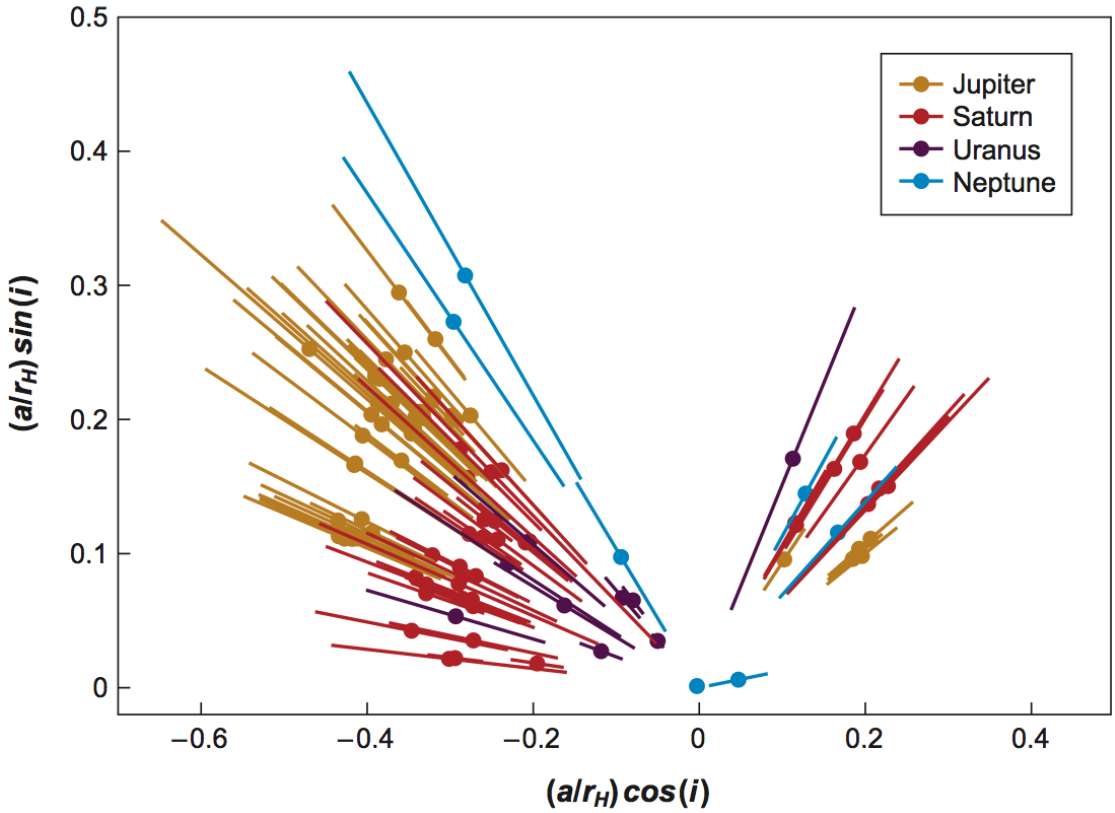

Figure 1.1: Polar plot displaying irregular satellite orbits, where the angle from the positive x axis represents the orbit's inclination i to Saturn's orbital plane. The radial coordinate at the plotted circular points gives the semimajor axis a expressed as a fraction of the radius of the planet's Hill sphere r_H. The lines on each point represent the radial excursions due to the orbit's eccentricity. The plot is taken from Jewitt and Haghighipour (2007).

But the most important feature of Fig. 1.1 for this thesis is the fact that the large eccentricities cause the orbits of the irregular satellites to overlap radially, allowing for collisions. The additional fact that the irregular satellites are confined to Hill spheres that are small on solar system scales ($\sim 0.35 - 0.7$ AU in radius) suggests that this could be a substantially collisionally evolved small-body population. Indeed, the size frequency distribution (SFD) of the irregular satellites is similar across the giant planets (Jewitt and Haghighipour 2007), and

anomalously shallow compared to other small-body populations that should have come from similar source regions in the solar system. Figure 1.2 (Figure 2 from Bottke et al. 2010) compares the SFDs for Jupiter's prograde and retrograde irregular satellites to that of Jupiter's Trojans (at the L_4 and L_5 Jupiter-Sun equilibrium Lagrangian points). All three populations are thought to have been created from a similar pool of planetesimals; however, at large sizes, the irregular satellites' SFDs are much shallower than the Trojan SFD. In fact, Bottke et al. (2010) argue that for diameters > 8 km, the irregular satellites may have the shallowest SFD in the solar system.

One can understand how such a SFD may have developed by considering an initial size distribution of bodies (that stops being replenished after the circumplanetary disk dissipates or planet migration ceases). For a given particle size, only collisions with bodies of a minimum diameter and larger result in disruption. Additionally, we can assume that, like in any typical collisional cascade, particle numbers increase with decreasing diameter (Dohnanyi 1969). Bodies are therefore most likely to be disrupted by particles near the minimum size capable of doing so. But because smaller bodies collisionally evolve faster than larger ones (since there are more particles available to collide with smaller bodies), it can happen that all of the particles capable of breaking apart the largest object are themselves disrupted before doing so—the largest body would then be "stranded" (Kennedy and Wyatt 2011). Over time, progressively smaller objects become stranded, i.e., only extremely rare collisions between a body and one larger than it lead to breakup. The lack of potential disruptors for large bodies thus inflates the representation of objects with large diameters in the SFD, generating a shallow slope.

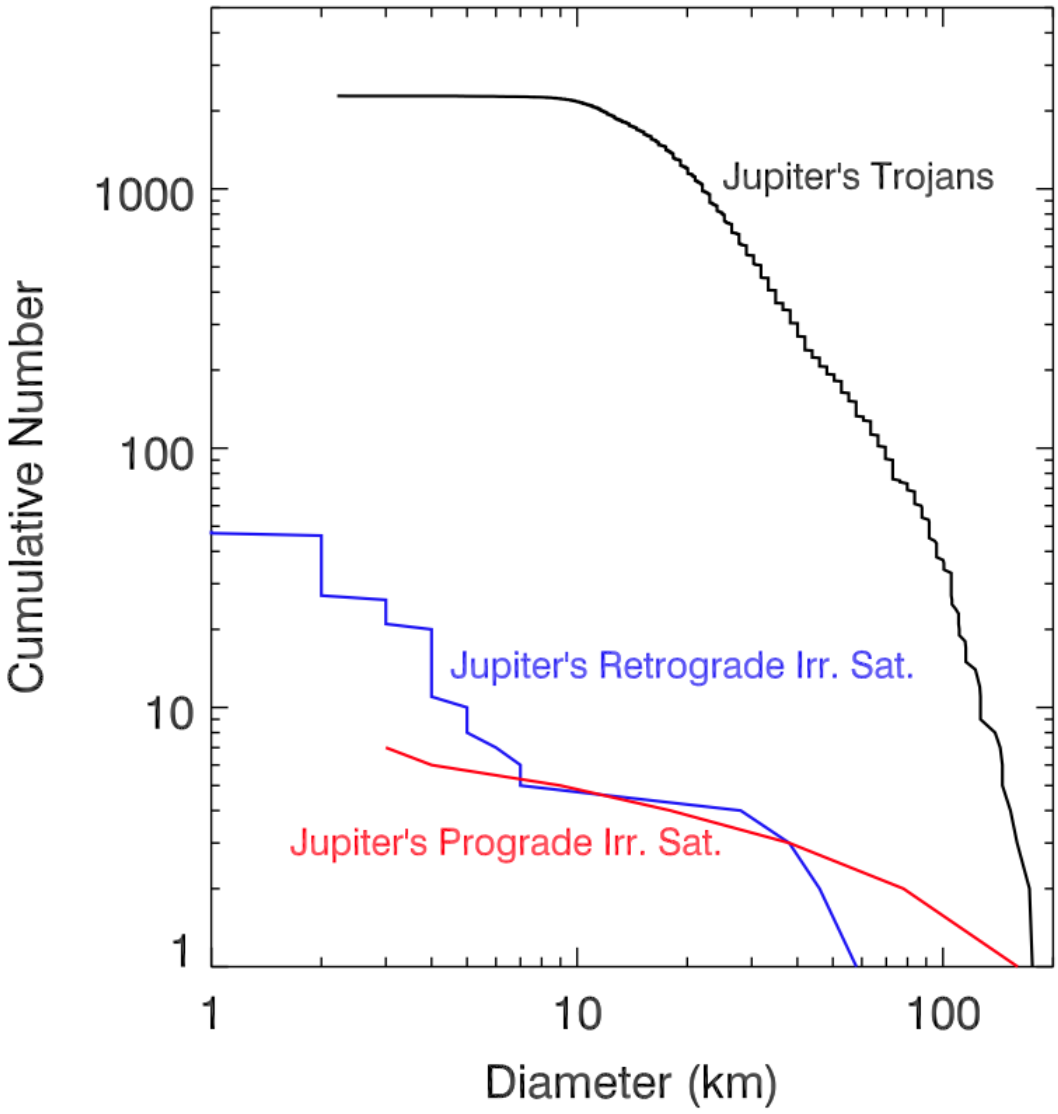

Figure 1.2: Cumulative SFD of Jupiter's Trojan asteroids, and the Jovian irregular satellites. Figure taken from Bottke et al. (2010).

This process has been investigated numerically (Bottke et al. 2010) and semi-analytically (Kennedy and Wyatt 2011) and can explain the observed irregular satellite populations. The above studies find that most of the mass in the initial irregular satellite population is ground to dust in the first few hundred million years of capture. Unfortunately, because the current SFD is roughly the asymptotic endpoint of such a process, one cannot use today's distribution to accurately infer the initial population. However, investigations of irregular satellite capture during a Nice-model reshuffling of the giant planets (Nesvorný et al. 2007) suggest that as much as 10^{20} kg of mass ($\sim$ 10 times the mass currently in the irregular satellites) would have been ground to dust around each of the giant planets early in the solar system's history.

This thesis addresses the fate of this large reservoir of debris. Poynting-Robertson drag will cause dust particle orbits to slowly spiral in toward the planet (Burns et al. 1979), where fine dust can be swept up by satellites further in. The fraction of the debris accumulated by the regular satellites is then determined by the competition between the timescale on which orbits decay past their targets and the collision timescale between the dust grains and these moons. This idea was first proposed by Soter (1974) in trying to explain the striking hemispherical albedo dichotomy on Saturn's moon Iapetus (see Fig. 1.3), but was never published in depth by the original author.

There have been many proposals to explain Iapetus' enigmatic surface. Endogenous models where dark material is extruded from Iapetus itself (Smith et al. 1982) have difficulty explaining the fact that the dark material is centered precisely on the apex of Iapetus' motion (Denk et al. 2010). Most models have thus focused on the asymmetry introduced by Iapetus' orbital velocity. Given

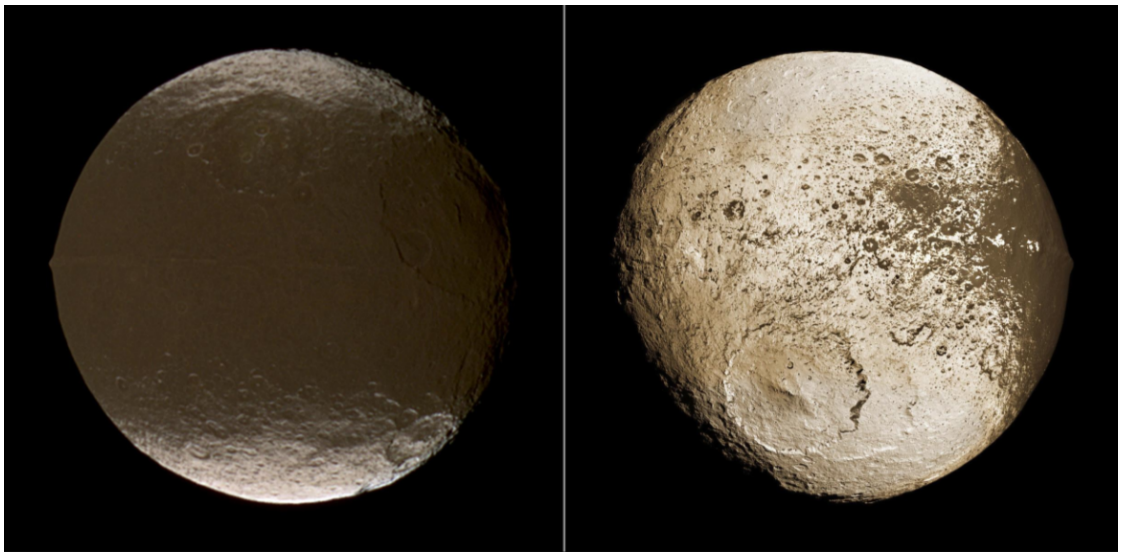

Figure 1.3: Saturn's two-faced moon Iapetus. The left panel shows the leading side of the satellite (Cassini Regio), which is ten times darker than the trailing side. The right panel shows most of the trailing hemisphere, including the mottled transition region between bright and dark terrains. Figure is taken from solarystem.nasa.gov.

an influx of material, like a car driving through the rain, more dust will strike the leading than the trailing side.

Many have investigated the effect of interplanetary impactors, but disagree on the nature of the dark material. Cook and Franklin (1970) argued that cometary debris has eroded away a thin ice veneer, exposing dark silicates underneath. Cruikshank et al. (1983) instead proposed that Iapetus' surface consists of a mix of icy and dark material, and that vaporization of ice by interplanetary impactors builds up a lag deposit of indigenous organic material on the leading side. Finally, Squyres and Sagan (1983) argued that ultraviolet radiation synthesizes dark surface organics that are then redistributed asymmetrically across the moon through interplanetary impacts.

Alternatively, material from within the Saturn system could be striking Iapetus. The two sources that have been proposed are Phoebe, the only known irregular satellite at the time (Soter 1974), and Hyperion, the small satellite orbiting interior to Iapetus (Matthews 1992).

Each of the above mechanisms was plagued with difficulties. All the exogenous models would predict that dark material should wrap over the poles (Burns et al. 1996), yet Iapetus has bright polar caps. Additionally, the putative Saturnian sources (Phoebe and Hyperion) have spectra that do not match Iapetus' dark Cassini Regio well (e.g., Tosi et al. 2010). However, several recent developments motivated a deeper look into the connection between Iapetus and the irregular satellites: a) the discovery of over one hundred new irregular satellites across the giant planets (Nicholson et al. 2008), and the subsequent modeling of their collisional evolution (Bottke et al. 2010; Kennedy and Wyatt 2011) rendered the irregular satellites a much more potent source of plausible impacting material than was previously realized; b) the three dozen new Saturnian irregular moons (additional sources of material) removes the need for Phoebe's and Iapetus' spectra to precisely match; c) Spencer and Denk (2010) proposed a model of runaway thermal sublimation of water ice to explain Iapetus' striking dichotomy, whereby any surface patch initially darkened by exogenous material would heat up (due to its reduced albedo), sublimate more ice and further darken the patch, creating a dark lag deposit. This solves the problem mentioned above of the bright poles, as continuous ballistic transport of sublimated ice particles would eventually cause them to settle on the coldest areas of the planet, i.e., the poles, and the bright trailing side; d) The Cassini spacecraft's arrival at Saturn allowed for observations of Iapetus' and Phoebe's surfacea with $\gtrsim 10$ times the resolution of previous attempts.

Chapter 2, largely reproduced from Tamayo et al. (2011), details our investigation into the connection between Iapetus and the irregular satellites. It builds off the initial study by Burns et al. (1996) by incorporating all the relevant perturbations on infalling dust grains and quantitatively evaluating collision probabilities with Iapetus and the other Saturnian satellites.

At the same time this work was being carried out, Verbiscer et al. (2009) announced the discovery of a colossal dust ring around Saturn, sourced by Phoebe. Not only did this provide a snapshot of the transfer of material from the irregular to the regular satellites, the Phoebe ring furnishes an invaluable opportunity to study the collisional processes active on the irregular satellites. The disk was only definitively detected with the Spitzer Space Telescope at 24μm over a limited radial range from the planet, leaving many questions unanswered. Does Iapetus carve out an inner edge to the disk? What is the ring's radial structure? Is the Phoebe ring sourced by continual micrometeoroid bombardment of Phoebe, or was it created in a single large event? Are the albedos of particles comparable to Phoebe? To answer these questions, one requires greater radial coverage, and, particularly for the last one, multi-wavelength observations.

To push toward longer wavelengths, we wrote a successful proposal to target the Phoebe ring with the Herschel Space Observatory, using the Photoconductor Array Camera and Spectrometer (PACS) to gather photometry at 70 and 130 μm. Unfortunately, the Phoebe ring is so faint that scattered light from Saturn (half a degree from the field of view) swamped any ring signal. Despite significant effort, we only managed to set upper limits that were unable to significantly constrain the Phoebe ring's spectral energy distribution (Tamayo et al. 2012b)

Chapter 3, reproduced from Tamayo et al. (2014), presents our efforts on the other end of the spectrum. There we detail our observations of the Phoebe ring at optical wavelengths using the Cassini spacecraft. This was particularly challenging given that the dark particles' reradiate most of their incident energy in the infrared, leaving little scattered optical light. Additionally, from Cassini's vantage point, the Phoebe ring subtends tens of degrees. The scattered light from the ring thus appears as a constant background in Cassini images that cannot be directly measured. To circumvent these issues, we developed a novel technique to indirectly measure the amount of material in the ring by observing the shadow cast by Saturn as it pierced the Phoebe ring, and looking for a dip in brightness in the region where shadowed particles had no light to scatter.

After demonstrating the viability of our method in Tamayo et al. (2014), we obtained several new observations with Cassini that we optimized to maximize both our signal and radial coverage. Chapter 4 details our analysis to date from these latest data.

Given the apparent importance of this process in the Saturnian system, one might wonder if there are signatures around the other giant planets. At Jupiter, Bottke et al. (2013) argue that irregular-satellite debris explains the dark lag deposits found on the most ancient terrains of the Galilean satellites Ganymede and Callisto, and that it could be an important source of organic compounds for Europa. I instead focused further out at Uranus (Chaps 5 and 6). While Uranus does not host a satellite with a surface dichotomy as extreme as Iapetus, Buratti and Mosher (1991) found that all five of the primary Uranian satellites, excluding the innermost Miranda, exhibit systematic hemispheric leading-trailing *color* asymmetries of roughly 2-23%. Other inner satellites in the solar system also ex-

hibit such leading-trailing color dichotomies due to their motion through a sea of charged particles in their host planets' respective magnetospheres; however, Buratti and Mosher (1991) argued against such an explanation for these largest four Uranian satellites, and instead favored an infalling-dust explanation by analogy to the Saturnian system. Nevertheless, many questions remained.

An answer to why the same process would transform the surfaces of the Uranian satellites and Iapetus so differently seems to be provided by Spencer and Denk (2010). They argued that as the most distant, tidally locked satellite in the solar system, Iapetus has an unusually slow rotation period that allows the runaway thermal sublimation process to occur (the slow rotation results in longer day-night cycles that give the satellite surface time to fully warm and sublimate efficiently). It is therefore plausible that other satellites could be contaminated by dust from their respective irregular satellites without presenting as stark a surface as Iapetus. In fact, from observations with the Cassini spacecraft, Denk et al. (2010) found that in addition to the albedo dichotomy, Iapetus also has a hemispherical color asymmetry, similar to what was observed by Buratti and Mosher (1991) on the Uranian satellites. It may therefore be that dust deposition changes the surface color, but only drives a runaway sublimation process if the conditions are right.

However, two difficulties remain for the Uranian moons. First is the fact that all four of the outermost large Uranian satellites show evidence of alteration. As in the Saturnian case (see Chap. 2), the collision timescale is much shorter than the Poynting-Robertson decay timescale on which dust grains drift by. This means that the outermost regular satellite should sweep up the majority of the material, with little, if any, getting through to the satellites further in. The

second question is whether dust infall would generate the observed coloration on the leading sides of the Uranian satellites given Uranus' extreme obliquity of 98°. Because the irregular satellites lie close to a planet's orbital plane (see Chap. 5), the material begins in a plane roughly perpendicular to Uranus' equatorial plane where the regular satellites orbit.

The paths that circum-*uranian* orbits take as they decay inward from the planet's orbital plane to its equatorial plane are surprisingly complex. Such migration under the combined perturbations from the Sun's gravity and the planet's oblateness was studied by Tremaine et al. (2009). They found that around planets with obliquities $\gtrsim 70^\circ$, there is a range of semimajor axes where particle orbits undergo chaotic, large-amplitude oscillations in both eccentricity and inclination. This suggested a resolution to the first problem mentioned above. If instead of a smooth, sequential migration past each of the satellites, particle orbits reach this unstable distance from Uranus and have their pericenters suddenly dropped inside the orbits of the four largest Uranian satellites, then material can be more equitably distributed among the four moons.

Unfortunately, the results of Tremaine et al. (2009) could not be applied directly to the problem of irregular satellite debris around Uranus. This is because grains that are small enough to decay inward through Poynting-Robertson drag will be strongly perturbed by the additional effects of radiation pressure. Chapter 5 recasts the work of Tremaine et al. (2009) in terms of orbital elements, and incorporates the effects of radiation pressure. It reproduces Tamayo et al. (2013a). Building on this theoretical framework, Chap. 6 then numerically investigates the specific case of circum-uranian particles, and the impact probabilities with the regular satellites. This work appeared as Tamayo et al. (2013b),

and we were able to both reproduce leading-trailing color asymmetries, as well as the increasing trend with distance from the planet.

The final chapter reaches beyond the solar system. Given that all the solar system's giant planets have large populations of irregular satellites, one might expect this to also be a common feature for giant exoplanets. If this is the case, then the extreme dust production around young exoplanets upon capturing these moons may raise the light levels scattered by these giant planet systems by orders of magnitude. This was proposed for the exoplanet Fomalhaut b by Kennedy and Wyatt (2011). Fomalhaut b is putatively among the handful of exoplanets that have so far been directly imaged. The problem is that the observed flux is too high. In the optical Hubble Space Telescope (HST) images, one is observing starlight that has been scattered into the detector, and the area of Fomalhaut b is equivalent to a planet with an optically thick circumplanetary disk ~ 30 Jupiter radii in radius. This seems implausible; however, an optically thin disk of irregular satellite dust spread over most of the planet's Hill sphere (with a radius of $\sim 10^4$ Jupiter radii), one can plausibly account for the observed amount of scattered light (Kennedy and Wyatt 2011).

There may thus be an important connection between Fomalhaut b and the solar system's irregular satellites, but I became interested in the system when Kalas et al. (2013) found from follow-up HST observations that the putative planet is on an extremely eccentric orbit ($e \approx 0.8$). This seems at odds with the fact that the system also contains a dynamically cold *circumstellar* debris disk (with Fomalhaut b's orbit crossing it in projection), and therefore sets important constraints. Chapter 7 finds limits on the possible mass of Fomalhaut b and the time it can have spent in its current orbit without having already disrupted the

observed debris disk. It is reproduced from Tamayo (2014).

Finally, in Chap. 8, I summarize the main results from this thesis, and point to promising directions for future work.

CHAPTER 2

FINDING THE TRIGGER TO IAPETUS' ODD GLOBAL ALBEDO PATTERN: DYNAMICS OF DUST FROM SATURN'S IRREGULAR SATELLITES

2.1 Introduction

Over three dozen dark irregular satellites have been discovered around Saturn using ground-based telescopes (Gladman et al. 2001; Sheppard et al. 2003; Jewitt et al. 2005; Sheppard et al. 2006). Numerical simulations show that these irregular satellites must have undergone intense collisional evolution that would have generated large quantities of dark dust over the age of the solar system(Nesvorný et al. 2003; Turrini et al. 2009). Indeed, Bottke et al. (2010) estimate that on the order of 10^{20} kg of dust ($\sim$ a thousandth the mass of the Earth's moon) has been generated in the outer Saturnian system through collisional grinding of these satellites. Furthermore, the recent discovery (Verbiscer et al. 2009) of a vast dust ring originating from the largest of the irregulars (Phoebe) shows that these dust-producing collisional processes are ongoing even today.

Small dust particles are strongly affected by radiation forces (Burns et al. 1979); in particular, Poynting-Robertson drag will cause particles to lose energy and slowly migrate toward their parent planet. One should therefore expect mass transfer from the dark outer irregular satellites to the generally brighter inner regular satellites (see Fig. 2.1). Iapetus is the outermost of the regular satellites and, importantly, is observed to be tidally locked (McCord et al. 1971). As such, one hemisphere permanently faces the direction of motion and would plow through the cloud of dark dust as the cloud evolves inward. Since Phoebe

(and most of the other irregulars) orbits retrograde and would generate dust particles on retrograde paths, collisions with the prograde Iapetus would occur at high relative velocities ($\sim$ 7 km/s) and the dust would mostly coat Iapetus only on its leading side. This model for the exogenous origin of the dark material on Iapetus was first proposed by Soter (1974) and seems plausible; when one looks at the observed albedo map of Iapetus, one finds that the dark region, Cassini Regio, is centered precisely around the apex of motion—a difficult fact to explain for endogenous mechanisms (Denk et al. 2010).

As Denk et al. (2010) point out, however, the extremely sharp boundaries between bright and dark material cannot be the result of simple dust deposition, which would yield more gradual transitions. To explain the striking boundaries, as well as the bright poles, Spencer and Denk (2010) propose a model of runaway ice sublimation in which areas initially darkened by dust become completely blackened. The sublimed ice then settles on the poles and on the brighter (and therefore colder) trailing side. These two processes together, exogenous dust deposition coupled with thermal ice migration, seem the most promising mechanism to forming Iapetus' striking global albedo dichotomy.

The recently discovered "Phoebe Ring" (Verbiscer et al. 2009) represents a snapshot in time of the inexorable process of mass transfer from the dark outer irregulars onto the inner icy satellites. The ring thickness implicates Phoebe as the source, showing that Soter's mechanism of coating Iapetus is ongoing. We will show below that almost all particles in the Phoebe ring of size $\gtrsim 10\mu$m will strike Iapetus; however, particles smaller than $\sim 5\mu$m will strike Saturn, its main rings, or escape the system within a half-Saturn orbit($\sim$ 15 yrs) due to radiation pressure (Verbiscer et al. 2009).

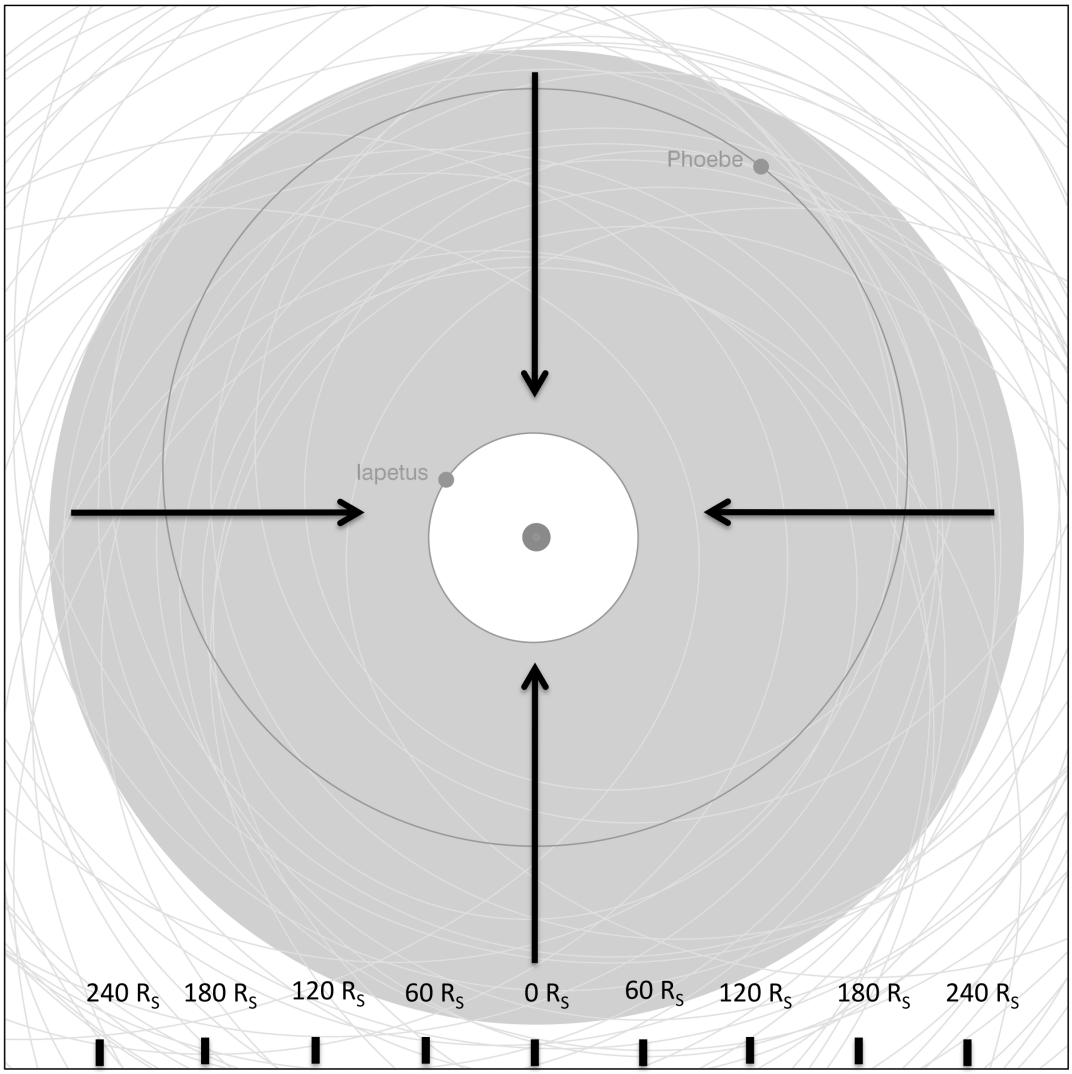

Figure 2.1: This schematic diagram depicts the expected extent of the Phoebe ring (solid gray), as well as the orbits of both Phoebe (black) and the rest of the irregular satellites (light gray). The circle at the center represents the main rings, with the E ring surrounding them. Approximate scale is provided in Saturn radii (Rs). According to the model of Soter (1974), as the ring of retrograde dust drifts inward from Phoebe's semimajor axis (arrows), Iapetus' leading side sweeps up this material, darkening its leading side. Figure provided by Matthew S. Tiscareno.

Our presentation improves on two previously published works. Burns et al. (1996) published a short analysis of the dynamics of dust particles from Phoebe and Tosi et al. (2010) included in their paper a simplified analysis that included Poynting-Robertson drag but neglected the important effects of the dominant component of solar radiation pressure (radial from the Sun), which affects particles' eccentricities and can quickly drive small grains out of the system.

This paper performs a more in-depth analysis, considering all the important radiation and tidal perturbations from the Sun and calculating the expected coverage on the Iapetus surface. We also include the precession of Iapetus' orbital axis, which extends coverage over the poles.

The paper is organized as follows. Sec.2 discusses the determination of probabilities for dust striking Iapetus from numerically integrated dust orbits. In Sec.3 we present calculated distributions of dust on the Iapetus surface, comparing them to the observed distribution and using them to obtain estimates for polar deposition rates. Sec.4 addresses the same process for the dozens of irregular satellites other than Phoebe, and Sec.5 tracks the fate of dust grains that do not strike Iapetus and that instead collide with Hyperion and Titan.

2.2 Collision Probabilities

2.2.1 Orbital Integrations for Dust Particles

In order to estimate dust particles' likelihoods of striking Iapetus, we first consider the important effects of the perturbations affecting dust particle dynam-

ics. Most dust particles spend their lifetimes in a radial range (between the orbits of Phoebe and Iapetus) where the dominant perturbations are solar. The important modifications to these particle orbits therefore result from radiation pressure and solar gravity. Nevertheless, since small particles' eccentricities can bring them closer to Saturn, we also included the perturbation from Saturn's second-order zonal harmonic in our numerical integrations.

As mentioned in the introduction, particles smaller than $\sim 5\mu$m are so affected by solar radiation pressure that they are quickly removed from the system; in this size regime, electromagnetic forces from the planet's magnetosphere are negligible relative to the other perturbations (Burns et al. 2001). Note that the smallest particles might not be blown out by radiation pressure; once the particle size becomes small relative to the incident light's wavelength, the dust particles will no longer be able to effectively couple to the radiation field. Such particles presumably account for a small fraction of the total mass, and their orbits would decay too slowly to reach Iapetus—we therefore ignore them.

The equation of motion can be written as

$$\ddot{\mathbf{r}} = -\frac{GM_S}{r^3}\hat{\mathbf{r}} + \frac{SAQ_{pr}}{mc}\hat{\mathbf{S}} - \frac{SA}{mc^2}Q_{pr}[(\dot{\mathbf{r}}\cdot\hat{\mathbf{S}})\hat{\mathbf{S}} + \dot{\mathbf{r}}] - \frac{GM_{Sun}}{a^3}\nabla\left(r^2 P_2(\hat{\mathbf{a}}\cdot\hat{\mathbf{r}})\right) + GM_S {R_S}^2 J2\nabla\left(\frac{P_2(\hat{\mathbf{s}}\cdot\hat{\mathbf{r}})}{r^3}\right), \tag{2.1}$$

where the terms, in sequence, are due to the dominant Saturnian gravity, solar radiation pressure, Poynting-Robertson drag, the Sun's tidal gravity, and Saturn's J2. G is the gravitational constant, M_S Saturn's mass, r the dust particle's distance from Saturn, S the solar flux at the particle's position, A the particle's cross-sectional area, Q_{pr} the grain's pressure efficiency, m the particle mass, c the speed of light, a the semi-major axis of Saturn (assumed to be on a circular orbit about the Sun), R_S the radius of Saturn, $J2$ Saturn's second-order zonal

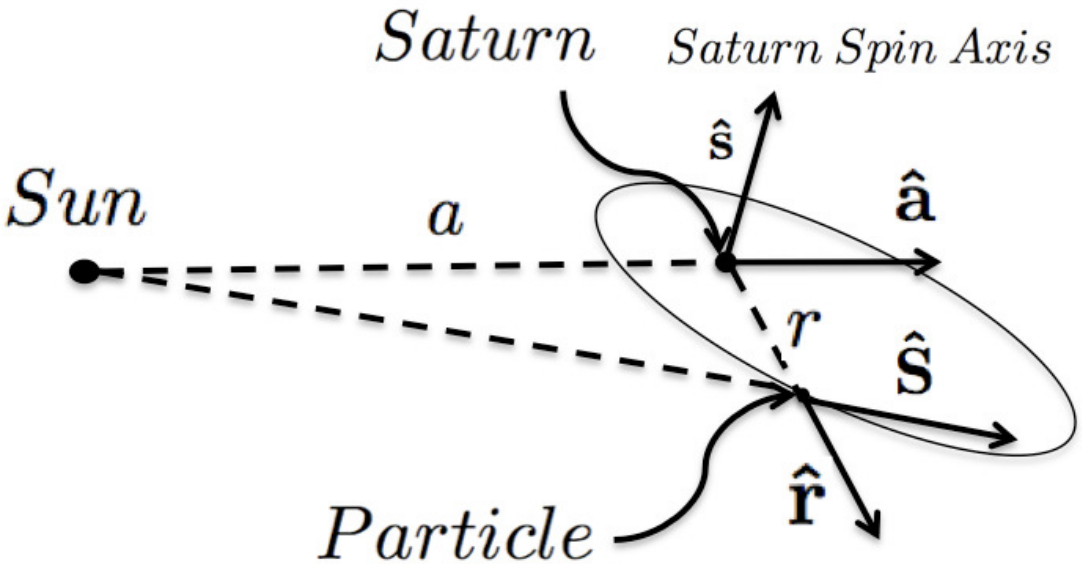

Figure 2.2: Schematic diagram showing the geometry of the important perturbations acting on dust grains in orbit around Saturn. Vectors are described in the text above.

harmonic, and P_2 the second Legendre polynomial. The vector $\mathbf{v}$ is the particle's velocity, and the other vectors can be seen in Fig. 2.2; $\hat{\mathbf{r}}$ is the direction from Saturn to the particle's position, $\hat{\mathbf{S}}$ is the direction from the Sun to the particle position, $\hat{\mathbf{a}}$ is the direction from the Sun to Saturn, and $\hat{\mathbf{s}}$ is the direction along Saturn's spin axis (perpendicular to the equatorial plane).

While commonly considered in a heliocentric context, Poynting-Robertson drag also causes particles' orbits around a host planet to decay into the planet on a timescale given by (Burns et al. 1979):

$$\tau_{PR} = 530\, years \times \frac{a_{Sat}^2}{\beta_{R/G}}, \tag{2.2}$$

where a_{Sat} is Saturn's semimajor axis in AU (≈ 9.5) and $\beta_{R/G}$ is the dimensionless

ratio of the radiation force to the *Sun's* gravitational force (in this case approximately $0.36/r$, where r is the particle size in μm). τ_{PR} therefore scales linearly with particle size.

Superimposed on this slow orbital decay (timescale $\sim 10^6$ years for spherical 10 μm particles) is a fast oscillation in the eccentricity (P $\sim$ 1 Saturn yr $\simeq$ 30 yrs) due to both solar radiation pressure and the Sun's tidal gravity (Burns et al. 1979; Hamilton and Krivov 1996). Eventually, dust-particle orbits will cross that of Iapetus as Poynting-Robertson drag reduces the orbit size and radiation pressure periodically induces large eccentricities. Over time, therefore, the dark particles will impact Iapetus' leading side.

As opposed to gravitational accelerations, accelerations due to radiation forces are mass—and therefore size—dependent. As a result, we numerically integrate orbits for different-sized particles using the well-established dust integrator "dI" (see Hamilton 1993; Hamilton and Krivov 1996; Hamilton and Krüger 2008). This provides a particle's orbital elements as a function of time for each particle size.

In any particular history, we choose particles of a given size and assign them a density (we assume that dust particles would share Phoebe's density of 1.6 g/cm^3). As discussed in further detail below, they are then started at various positions along Phoebe's orbit and initially move with Phoebe's velocity. We determine that for our assumed density, particles smaller than 4 μm are so affected by radiation pressure that within the first half-Saturn year their eccentricities reach a value of unity and the grains either collide with Saturn or its rings, or escape the Saturn system entirely. This corresponds to $\sim$ 10 particle orbits and a negligible probability of collision with Iapetus. One should therefore expect

only a significant contribution to Iapetus from particles $\gtrsim 4$ μm in size. Since dust particles are not actually spherical and will contain some void space, our assumed density is probably high and our 4 μm likely represents a lower limit.

On the other extreme, the orbital eccentricities of particles larger than 500 μm (Poynting-Robertson decay timescale $\gtrsim$ 50 million years) are almost completely unaffected by radiation forces and are dominantly affected by the Sun's tidal gravitational force, which is independent of particle size. We therefore run integrations for particle sizes of 5, 10, 25, 50, 100, and 500 μm. A 25 μm particle's orbital element evolution is shown in Fig. 2.3 with its slow semimajor axis decay and rapid eccentricity oscillations($P \sim 30$ yrs). The bottom panel shows the pericenter distance q. When q crosses a satellite's semimajor axis, collisions with that moon become possible.

A few considerations supply the appropriate initial conditions for the integrations. All particles leaving Phoebe must have initial speeds $\gtrsim$ Phoebe's escape speed v_{esc}. Since dust-producing impact events produce a distribution of ejecta velocities with a decaying tail toward higher speeds, one should expect most particles that escape Phoebe to have launch speeds near v_{esc} (Farinella et al. 1993). Therefore, since Phoebe's escape velocity is much smaller than its orbital velocity ($\sim$ 0.1 km/s vs. $\sim$ 1.7 km/s), we expect most dust particles generated in an impact with Phoebe to approximately share that moon's orbital elements. This sets the initial conditions for the semimajor axis, eccentricity and inclination ($a = 1.296 \times 10^7$ km, $e = 0.156$, $i = 175.2^\circ$ with respect to Saturn's orbital plane about the Sun).

The last three initial conditions—the three angles that determine the orientation of the orbit (see Fig. 2.4)— depend on the time of impact itself. Specifically,

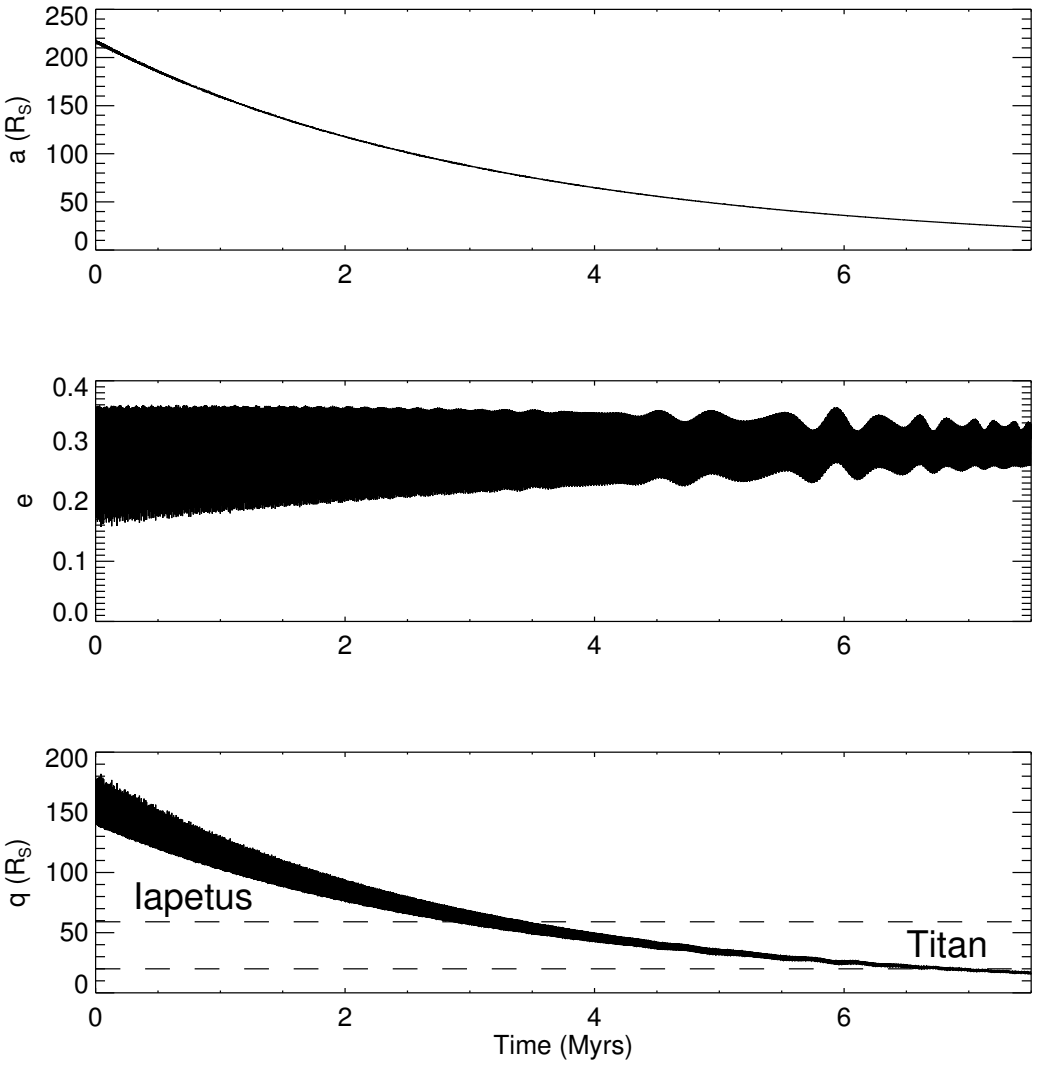

Figure 2.3: Evolution of a 25μm particle under the effects of solar perturbations. Top panel shows the particle's semimajor axis, which starts at Phoebe (a $\approx 215R_S$) and decays on a timescale $\sim$ 2.5 Myrs. Superimposed on this slow evolution of the semimajor axis is a rapid oscillation in the eccentricity (middle panel) on a timescale $\approx$ 1 Saturn year $\approx$ 30 yrs. The bottom panel shows the particle orbit's pericenter q, along with the semimajor axis of Iapetus and Titan.

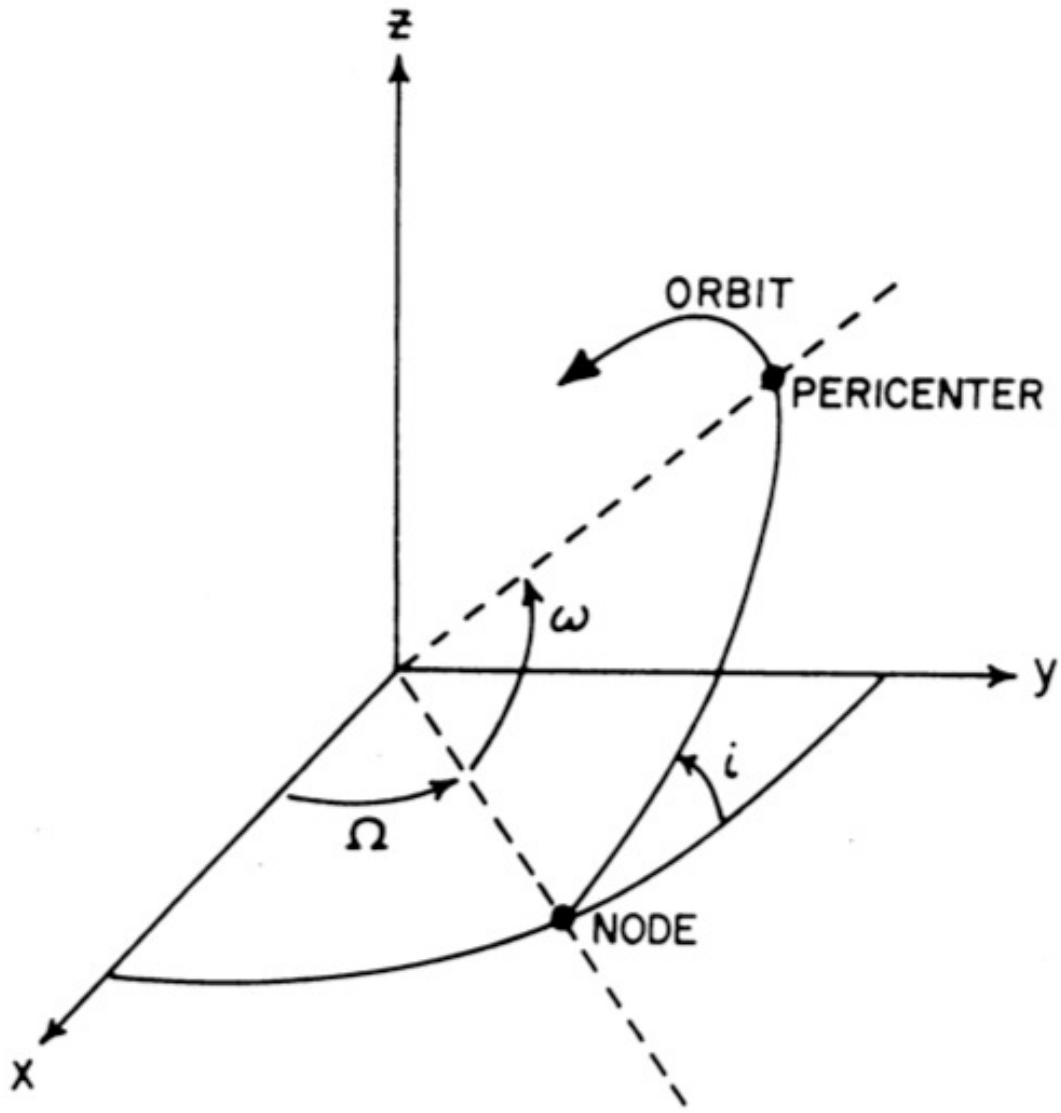

Figure 2.4: The three Euler angles that define an orbit's orientation: i, Ω and ω. (Figure from Greenberg 1982).

they are set by the orientation of Phoebe's orbit (Ω and ω), and Phoebe's position within its orbit (f, the true anomaly) at the time of impact. This would represent a formidable phase space to cover for long integrations, but fortunately several considerations limit the phase space considerably.

The shortest timescale for the perturbations involved is the $\sim$ 30-yr period of the Sun's apparent motion about Saturn. Since the dust particles' orbital periods around Saturn are much shorter than this ($\approx$ 1.5 years), the exact position of Phoebe (*f*) in its orbit at the time of impact does little to influence the subsequent evolution of the orbit's shape or orientation; thus it can be chosen arbitrarily.

Phoebe's orbit orientation at the time of impact, however, *is* important because it precesses more slowly. Nevertheless, one can still limit the phase space by inspecting the geometry. Since the dominant perturbations in this problem are all of solar origin, the logical plane from which to reference inclinations is Saturn's orbital plane (i.e., the plane in which the Sun appears to move in a Saturnocentric frame). Phoebe's inclination relative to Saturn's orbital plane of 175° means its own orbital plane is almost coplanar, albeit in a retrograde sense, with this reference plane.

In the limit of coplanarity, only one angle (rather than both Ω and ω) is required to specify the orientation of the orbit given the inclination, i.e., the angle between an arbitrary reference direction and the orbit's pericenter. In this case, the physically meaningful reference direction is the one toward the source of perturbations, the Sun. The orbital evolution of the dust particle therefore does not depend strongly on Ω and ω independently, but rather on the combination Ω - ω, which specifies the angle from the Sun's direction to pericenter. Note that for a prograde orbit, the angle from the Sun's direction to pericenter would be $\varpi \approx \Omega + \omega$, but since ω is measured in the direction of orbital motion, the appropriate combination for *retrograde* orbits is Ω - ω.

The approximations discussed above transform an intractable multidimensional space of initial conditions into a simple one-dimensional space. The ele-

ments a, e, and i are those of Phoebe's orbit, and the only other initial condition left to supply is the quantity $\Omega - \omega$, with Ω measured relative to the Sun's direction at the time of impact. Since impacts could happen at any point in the precession cycle, we chose to perform integrations for eight equally-spaced values of $\Omega - \omega$.

We therefore generate, for each particle size, eight sets of *a(t)*, *e(t)*, and *i(t)* corresponding to eight equally-spaced initial values of $\Omega - \omega$. Taking the initial values of $\Omega - \omega$ as equally likely, we average over the eight sets of outputs, yielding, for each particle size, a single set of functions *a(t)*, *e(t)*, and *i(t)*. These provide the inputs for the collision probability calculations. While we exploit Phoebe's orbit's near-alignment with Saturn's orbital plane to combine Ω and ω for our initial conditions, the numerical integrations are carried out fully in three dimensions. This allows us to track the orbital inclination, a crucial input to a 3-D collision probability calculation.

2.2.2 Collision Probabilities

In order to estimate collision probabilities, we used the formalism developed by Greenberg (1982), as improved by Bottke and Greenberg (1993). In this formalism, the dust particle's and Iapetus' semimajor axes, eccentricities and inclinations (a, e, i) are taken as known while the precession angles that determine the orientation of the orbits (Ω and ω) are treated as uniformly distributed. Barring resonances between the orbital periods of the dust particles with Iapetus, this should be a good assumption over collision timescales ($\gtrsim 10^6$ years), which are long compared to the longest precession timescale (Iapetus' orbit pole, $\tau \sim 10^3$

years). This assumption was found to agree with the angular distributions from the numerical integrations.

An alternative strategy could have been to numerically integrate many dust particle orbits and to directly see when and where on Iapetus they strike. One drawback of such a method is that Iapetus' small size relative to the dust orbits would dictate using extremely small step sizes in the integration. Our approach allowed us to perform fewer computationally expensive orbit integrations per particle size in exchange for computationally cheaper collision probability integrals.

The calculations of Greenberg (1982) are too complicated to reproduce here. The calculation is performed by first calculating the values of $(\Omega_p, \Omega_I, \omega_p, \omega_I)$ that would lead to the two orbits crossing ('p' subscripts refer to the particle and 'I' subscripts to Iapetus). Then the objects' finite size is taken into account by Taylor-expanding around these crossing solutions to find the volume in $(\Omega_p, \Omega_I, \omega_p, \omega_I)$ space over which collisions are possible. Finally one calculates from Keplerian theory the probability that both objects will simultaneously be close enough to the point of closest approach for a collision to occur within one object's orbit. The ratio of this probability to the orbital period provides a collision frequency. We compared our code to the test cases presented in Bottke and Greenberg (1993) and found it reproduced their results.

Due to the wide disparity between orbital period ($\sim$ 1 year) and the collision timescale ($\sim$ 10^6 years), it is impractical to calculate collision probabilities for every orbit. One can see in Fig. 2.3, however, that while the eccentricity is oscillating rapidly, the envelope that bounds the oscillation changes slowly, on roughly the Poynting-Robertson timescale ($\tau_{PR} \gtrsim 1$ million years). In particular,

the figure uses only 10^4 equally-spaced points in time and is still able to capture the full behavior. As a result, rather than calculating probabilities every orbit, we did so for 10^4 timesteps.

Given a, e, i for both Iapetus and dust particle, Greenberg's formalism (1982) provides a collision frequency,

$$Frequency = \frac{Probability\ of\ collision\ within\ one\ orbit}{Period\ of\ orbit}. \tag{2.3}$$

For timesteps $\Delta t \ll 1\ /\ Frequency$, one can then straightforwardly express the collision probability within Δt as

$$P = Frequency \times \Delta t. \tag{2.4}$$

One can then recursively generate a cumulative probability of collision C, i.e., the probability at time t that the particle has already struck Iapetus. Starting with $C(0) = 0$,

$$C(t_i) = C(t_{i-1}) + (1 - C(t_{i-1})) * P(t_i). \tag{2.5}$$

The probability of two collisions within a single Δt is negligible and was ignored. $P(t_i)$ depends on the orbital elements for Iapetus and the dust particle at t_i. For the dust particle we used $a(t_i)$, $e(t_i)$, and $i(t_i)$, generated as described above. For Iapetus, we used the present values of $a = 3.561 \times 10^6$ km and $e = 0.03$. Iapetus' inclination with respect to Saturn's orbital plane, however, changes significantly over time and must be considered more carefully.

To first approximation, the orbit normal precesses uniformly and at a constant inclination to a vector determined by the perturbations causing the precession. This causes the orbit normal to sweep out a cone (see Fig.2.5). The vector around which orbits precess defines the local Laplace plane (normal to this vector). At Phoebe's orbit, all the dominant perturbations are solar, so the

local Laplace plane corresponds to the plane in which the Sun appears to move, Saturn's orbital plane. Close to Saturn, where the dominant perturbation is Saturn's oblateness, the local Laplace plane is Saturn's equatorial plane. Iapetus has the unique orbital property among satellites of existing at a distance where Saturnian and solar perturbations are comparable, and the local Laplace plane is intermediate, at about 11.5° to Saturn's orbital plane (see Ward 1981).

Because of this misalignment, although Iapetus will precess at approximately constant inclination to the normal to its local Laplace plane, its inclination relative to our reference plane (Saturn's orbital plane) will change as the orbit precesses (see Fig. 2.5). We therefore assumed uniform precession and coarsely averaged the probability calculation over an entire precessional cycle, sampling more finely when the inclinations of the particle and Iapetus were antiparallel and the collision probability was changing fastest.

Finally, as mentioned in Sec. 2.1, we averaged over the eight equally probable initial conditions that we integrated, yielding an overall cumulative probability of collision for the given particle size.

Apart from Iapetus, we also tracked collisions with Hyperion and Titan, as well as re-impacts into Phoebe. We therefore straightforwardly generalized the discussion above to not only update the cumulative probability of collision with Iapetus at each timestep, but also those with the other three moons. As is discussed below, Titan's large size renders it a sink for any long-lived dust particles that cross its path; thus, no other moons interior to it would receive appreciable amounts of dust and such bodies are therefore not tracked. As mentioned earlier, however, a significant fraction of the particles smaller than ~ 5 μm whose eccentricities all reach unity will strike Saturn or its rings within the first half

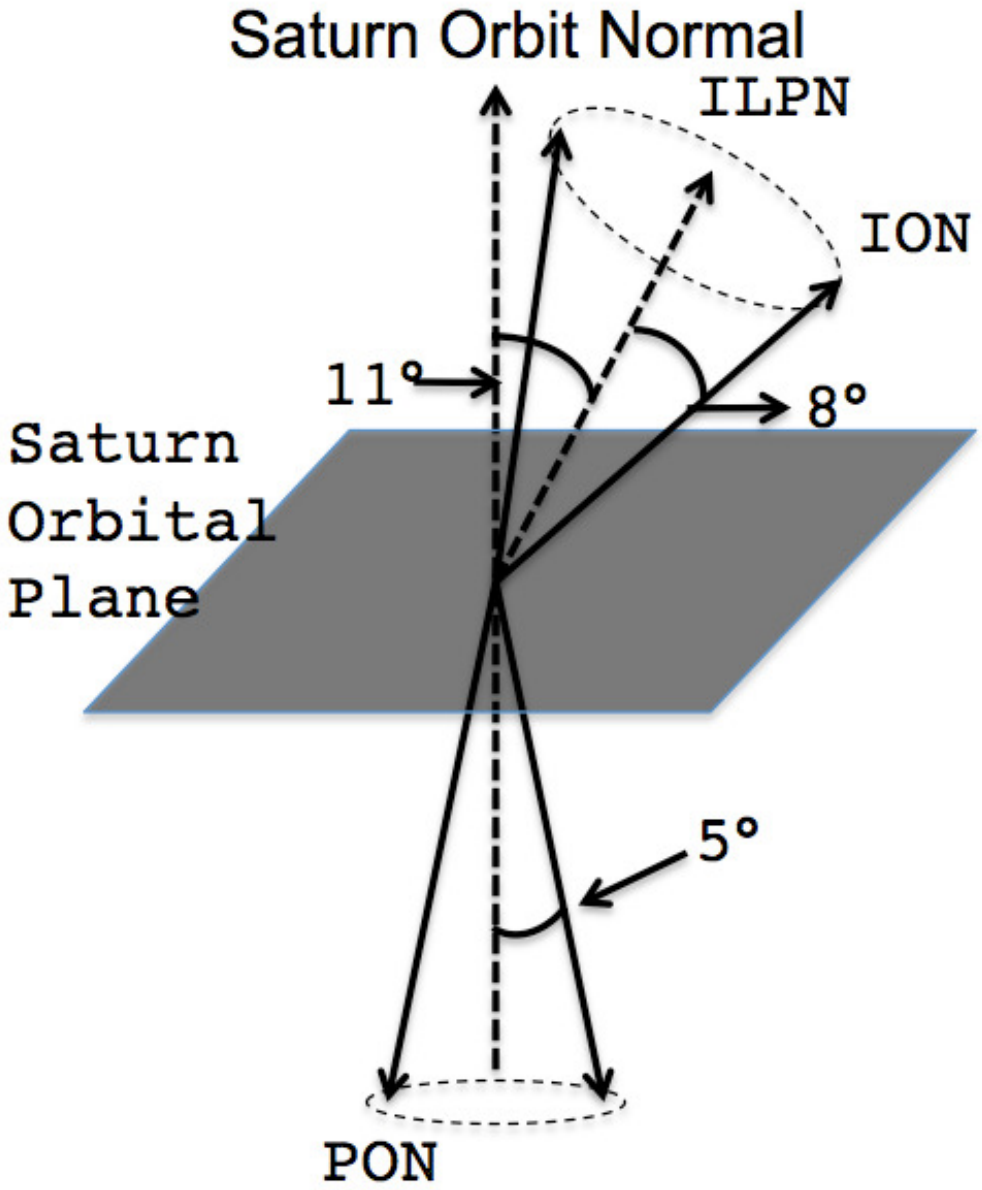

Figure 2.5: A schematic representation of the changing orientations of Iapetus' and Phoebe's orbits (represented by their respective orbit normals PON = Phoebe Orbit Normal and ION = Iapetus Orbit Normal). The moons' orbit normals precess at constant inclinations (5° and 8° for Phoebe and Iapetus, respectively) to the normal vector to their local Laplace planes, sweeping out a cone. Phoebe's Laplace plane coincides with Saturn's orbit normal, while Iapetus' local Laplace plane normal (ILPN) is inclined about 11° to Saturn's orbit normal.

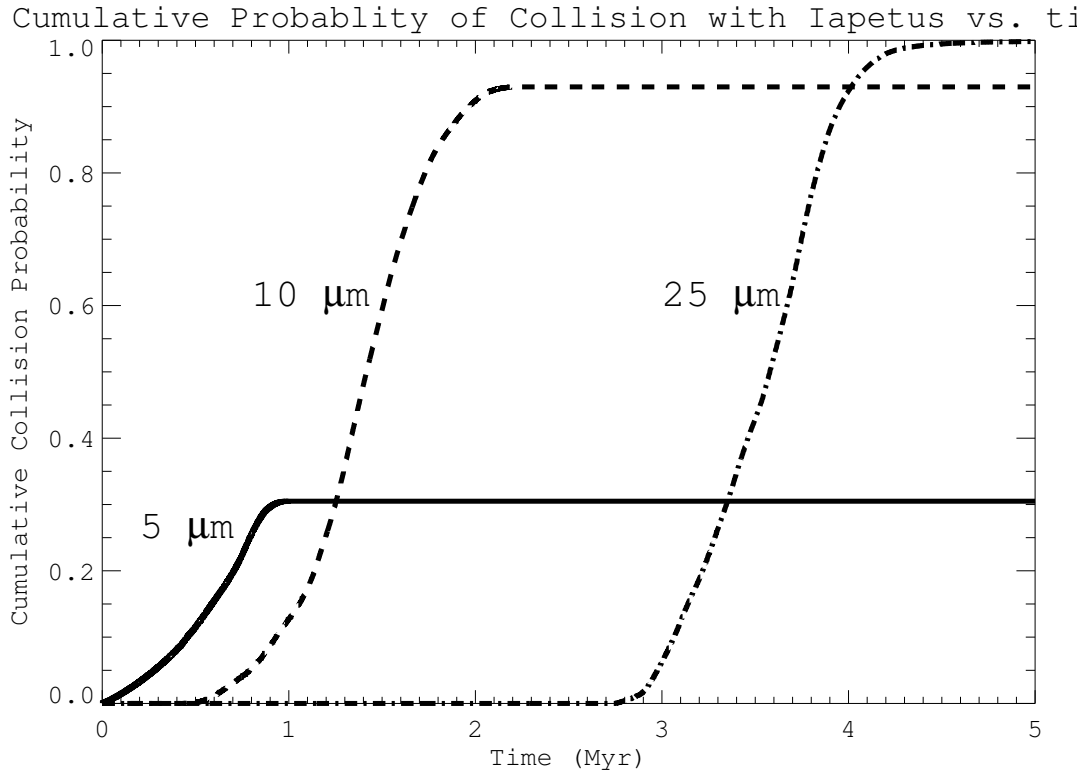

Figure 2.6: Cumulative collision probabilities vs. time for 5, 10 and 25 μm particles. Particles $\gtrsim$ 10μm almost all strike Iapetus, though larger particles take a longer time to do so.

Saturn-year.

2.2.3 Results

Figure 2.6 shows the calculated cumulative collision probability with Iapetus for 5, 10, and 25 μm grains.

Particles 10 μm and larger, being less affected by radiation forces, evolve inward via Poynting-Robertson drag so slowly (i.e., they execute many Iapetus-crossing orbits before crossing the orbits of Hyperion or Titan) that they almost

all eventually strike Iapetus. As stated before, particles smaller than about 4 μm quickly strike Saturn or escape the Saturn system. Therefore, of the longer-lived particles, *almost all* particle sizes are bound for Iapetus—only a very narrow size range (between about 4 and 10 μm for the chosen density) can miss and end up mostly on Titan, with a substantially smaller fraction striking Hyperion.

We mention that, while almost all particles larger than $\sim 10\,\mu$m would eventually strike Iapetus, it takes larger particles longer to evolve inward and hit the satellite. In particular, for particles in the geometrical optics limit (the peak wavelength in the solar spectrum $\sim 0.5\mu\text{m} \ll 2\pi r_{dust}$, satisfied for all particle sizes we consider), the Poynting-Robertson decay timescale grows linearly with particle size (see Burns et al. 1979). As a reference, assuming particles share Phoebe's density of 1.6 g/cm^3, 10 μm particles reach Iapetus in ≈ 1 Myr.

As particle sizes increase, one should expect to find a threshold where particles stop hitting Iapetus when the Poynting-Robertson decay timescale becomes longer than the timescale for the destruction of dust grains. Unfortunately, destruction lifetimes for dust in the outer Saturn system are not well constrained (cf. Burns et al. 2001). One mechanism for the destruction of dust grains is through mutual collisions. One can estimate the mean free time between particle collisions as

$$t_{MF} \sim \frac{P}{\tau} \tag{2.6}$$

where P is the particles' orbital period and τ the ring's normal optical depth. Taking the optical depth in the Phoebe ring, $\tau \sim 2 \times 10^{-8}$ (Verbiscer et al. 2009), this yields $t_{MF} \sim 100$ Myr, the Poynting-Robertson decay timescale corresponding to 1 mm grains; however, for each particle size, only collisions with particles of roughly the same size or larger affect the dynamics. This would act

to increase t_{MF}, but is dependent on the (currently unconstrained) particle size distribution. On the other hand, dust rings collisionally generated early in the Solar System likely had higher optical depths (Bottke et al. 2010), lowering t_{MF}. For this work we chose the maximum upper-size cutoff imposed by setting the Poynting-Robertson decay timescale equal to the lifetime of the Solar System. This yields a particle size of $\sim$ 1 cm. Improved estimates of collisional dust lifetimes in the Phoebe ring must await further observations.

As the introduction mentions, a large supply of dust has been available in the outer Saturn system over the course of the Solar System's history. The fact that particles $\gtrsim 10$ μm are virtually certain to strike Iapetus strongly implicates collisionally generated dust as the trigger to Iapetus' stark albedo dichotomy. An exogenous origin of the dark material explains why the pattern is centered on the apex of Iapetus' motion and, as shall be shown in Sec. 3, the dynamics predict a wrapping of dark material onto the trailing side consistent with that observed.

2.2.4 Titan, the gatekeeper to the inner Saturnian system

We now explain the sharp drop in the final fraction of particles that strike Iapetus between 5 and 10 μm, as seen in Fig. 2.6. This is due to the large eccentricities induced by radiation pressure, visible in Fig. 2.3. For the smallest particles, the eccentricities are high enough that before the dust grains' probabilities of striking Iapetus near certainty, their orbits begin to cross that of Titan. Saturn's largest moon is such a better interceptor of particles that the probability of striking Iapetus quickly stops increasing and levels off.

There are several reasons why Titan is highly efficient at eliminating dust particles. Most obviously, its sheer size makes its geometrical cross section larger than Iapetus' by a factor of about 12. Another reason is that collision rates depend on the objects' relative velocity, as this determines how frequently the objects can potentially encounter each other (see discussion following Eq. 2.32). Relative velocities between dust particles and Titan are substantially higher than those with Iapetus simply because in order to reach the further-in Titan, particles generally have to be on very eccentric orbits (e = 0.7-0.9), and will encounter Titan close to periapse.

One might have expected slow relative velocities to lead to enhanced collision probabilities due to strong gravitational focusing for slow encounters. In fact, gravitational focusing plays little role in this problem because the moon orbits are prograde while the dust orbits are retrograde, resulting in high relative velocities compared to the satellites' escape velocities ($v_{esc} = 0.572$ km/s for Iapetus, $v_{esc} = 2.639$ km/s for Titan). For typical encounter velocities, Iapetus' gravitational cross-section is about 0.5% greater than its geometrical cross-section ($\lesssim 10\%$ for Titan).

Though we account for gravitational enhancements to the collision cross section, in our orbit integrations we ignore close encounters with Titan (and all other satellites) on subsequent orbital paths. For typical relative velocities, the maximum scattering angle from a close encounter is $\approx 10^\circ$. The corresponding angle for Iapetus is $\approx 0.5^\circ$.

We postpone our discussion of the total amount of material that strikes Titan and the smaller Hyperion, along with its implications, until Sec. 5.

2.3 Coverage

Since much of the dust previously orbiting in the outer Saturnian system will eventually strike Iapetus, we ask where on Iapetus those particles would have landed. In particular, can the dynamics match the extent of Iapetus' dark side, Cassini Regio? The emplacement of dust could then trigger the thermal migration of ice thought to give Iapetus the striking appearance it has today (Spencer and Denk 2010).

Cassini Regio extends beyond Iapetus' leading side by tens of degrees onto the trailing side along the equator (see Fig. 2.7). As Burns et al. (1996) have suggested, dust eccentricities naturally explain the longitudinal extension of the dark material onto the trailing side.

If orbits were perfectly circular, dust particles would only strike Iapetus head-on, as both objects would be moving perfectly azimuthally in opposite directions; thus, only the leading face would be darkened since, as discussed at the end of Sec. 2.4, the encounter velocities make gravitational focusing negligible.

When particles have eccentric orbits, however, particle velocities are no longer perfectly azimuthal, and the radial components allow particles to strike the moon further along the equator (see Fig. 2.8). Eccentricities induced by radiation pressure therefore provide a natural mechanism for extending dust coverage onto the trailing side.

However, just as eccentricities act to extend coverage longitudinally, dust-orbit inclinations and Iapetus' varying orbital tilt should extend coverage lati-

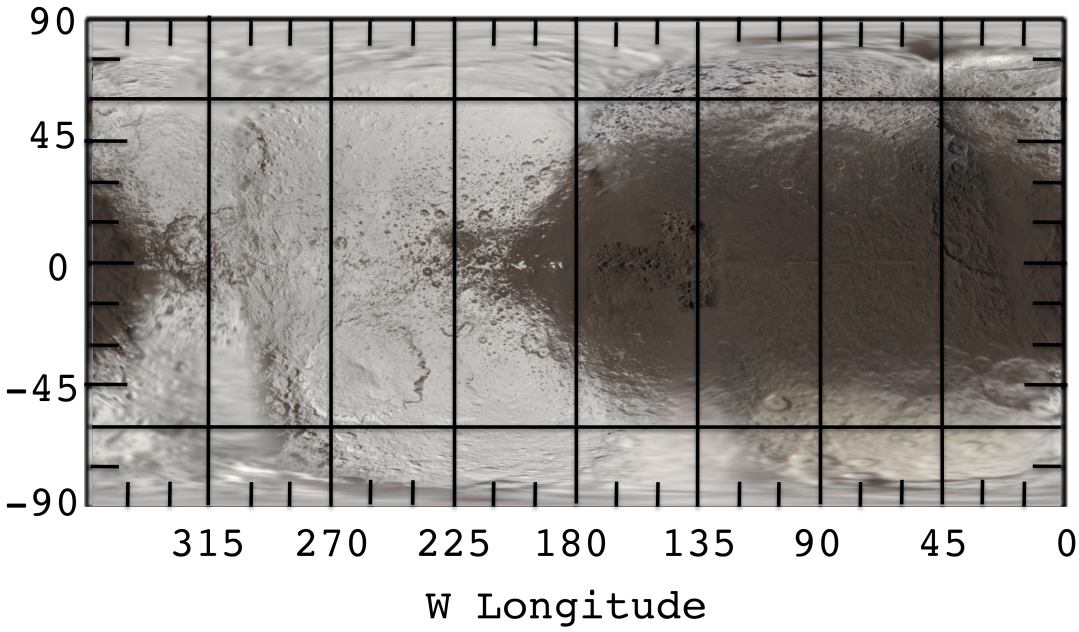

Figure 2.7: Global mosaic of Iapetus (from Albers 2008). Dark Cassini Regio is centered around the apex of Iapetus' motion, roughly at 90°W, and extends tens of degrees beyond 0° and 180°W onto the trailing side. The bright poles (beyond $\sim \pm 60°$ latitude) and sharp boundaries between light and dark terrain are likely the result of thermal ice migration (Spencer and Denk 2010).

tudinally over the poles (Burns et al. 1996, and see Fig. 2.5). Images of Iapetus, however, reveal bright, icy poles.

As previously mentioned, thermal ice migration provides a mechanism for brightening the poles (Spencer and Denk 2010). Icy patches on Iapetus darkened by exogenous dust increase in temperature as a result of their lowered albedo. Sublimation rates, which depend exponentially on temperature (e.g., Vyazovkin and Wight 1997), thereby increase sharply. This liberates bright ice and leaves behind an even darker surface. The further darkened surface's temperature rises further, and the cycle repeats in a self-accelerating process until a lag deposit forms with thickness of order the thermal skin depth Spencer and

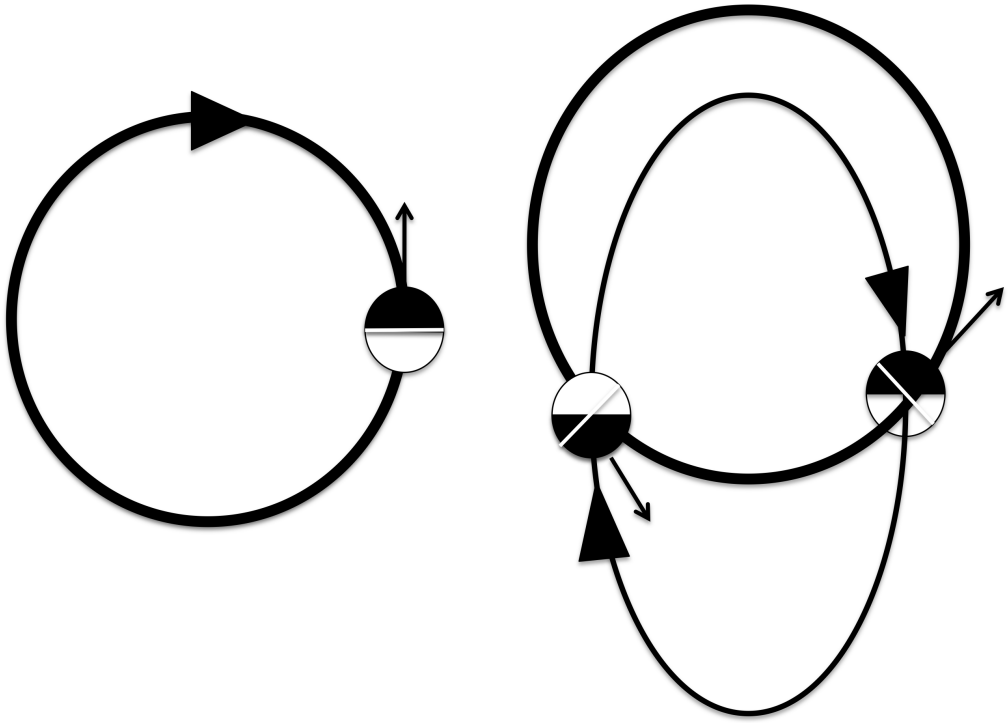

Figure 2.8: Iapetus is depicted as the circle moving on a prograde orbit, while the dust moves on retrograde orbits. The white lines separate Iapetus' leading and trailing sides. When orbits are circular (left), dust will solely darken the leading side, while the radial velocities of eccentric orbits allow dark material to reach part of the trailing side.

Denk (2010). The result is that warm, darkened areas become extremely dark and ice-free, while the sublimed ice settles on the coldest areas of the moon—the trailing side and the poles.

The distribution of dark material on the surface therefore holds several insights into ongoing processes on Iapetus as well as to the past and present prevalence of dark dust in the outer Saturnian system. Unfortunately, it is difficult to observationally determine the dark layer's depth. Bright-floored craters

from small impactors that punctured through the dark layer constrain the layer to being much thinner than the crater's depth $\sim$ 10 m (Denk et al. 2010), while radar measurements (Ostro et al. 2006) imply Cassini Regio is on the order of decimeters deep.

Given the above background, we wish to calculate the probability distribution for where on Iapetus dust would strike for three reasons:

a) One can convert a probability distribution to a depth distribution (Sec. 3.2) and compare the resulting global map to the observed Iapetus surface. Such a comparison tests the hypothesis that Iapetus is darkened by dust from Phoebe and can provide depths in areas where observations are not available.

b) Calculated polar deposition rates of dust yield an estimate of the minimum sublimation rate required to overwhelm dust deposition and keep the poles bright.

c) A global depth distribution provides the total volume of dark material on Iapetus. This volume, coupled with the collision probabilities of dust calculated in Sec. 2, provides a probe of the total amount of dust collisionally generated in the outer Saturnian system over its history (cf. Bottke et al. 2010).

We subdivide this problem by first calculating the collision probability distribution over the surface of Iapetus in Sec. 3.1. Then 3.2 converts this probability distribution to a depth distribution, and 3.3 estimates the sublimation rates required to keep the poles bright. We postpone discussion of point c) to Sec. 5.

2.3.1 Collision Probabilities as a Function of Latitude and Longitude

We now find the probability per unit area for particles striking Iapetus at latitude θ and longitude ϕ. Note that we can quickly determine the rough shape such a distribution should take in the limit of circular, uninclined orbits (a good approximation for large particles). In this limit, dust particles strike Iapetus' leading side head-on. Also, since $a_I \gg R_I$, we can approximate the orbits of Iapetus-striking particles as parallel straight lines. Finally, in this approximation, our assumed uniform distribution in the variables Ω and ω for both orbits (see Sec. 2.2) translates into a uniformly distributed bundle of quasi-parallel trajectories capable of striking Iapetus. In such a uniform field, the probability of an impact in a given area element simply is proportional to its projected area, given by $dAcos\psi$, where ψ is the angle between Iapetus' velocity vector and the outward normal vector to the area element. Equivalently, ψ is the angular distance from the apex of motion (see Fig. 2.9, in which Iapetus is moving to the left). In this simple case then, the probability per unit area is a simple function of ψ,

$$P(\theta, \phi) \propto cos\, \psi. \tag{2.7}$$

This approximation is good over most of the leading hemisphere, though it is clearly incapable of describing the extension of the dark material onto the trailing side and of quantifying probabilities in the interesting transition region from the dark to the light terrains. As described in Sec. 2.4, wrapping onto the trailing hemisphere cannot be the result of Iapetus' negligible gravitational fo-

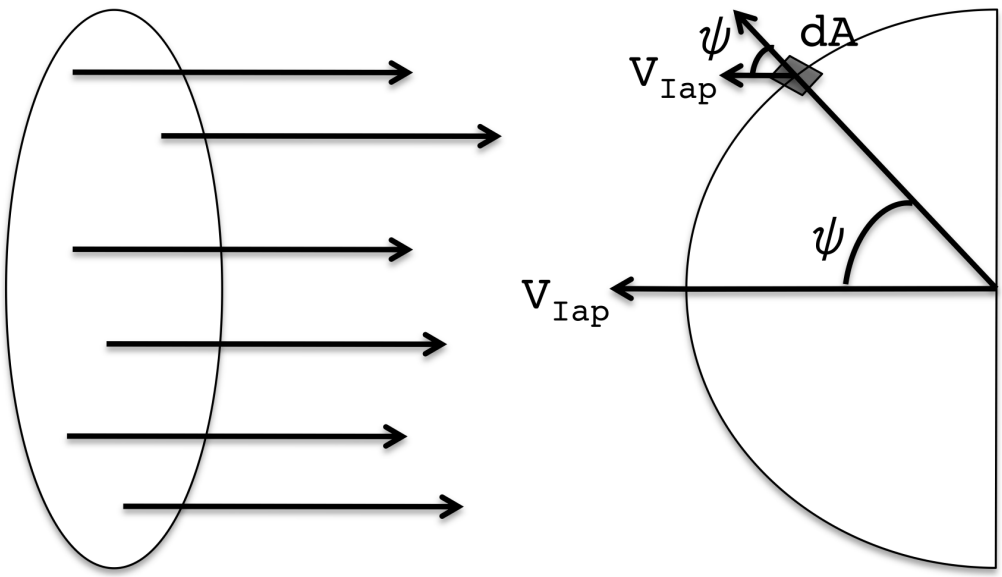

Figure 2.9: The orbits capable of striking Iapetus are well approximated by a uniform disk of parallel trajectories, shown on left. Probabilities are then simply proportional to the projected area, given by $dA\ cos\psi$. The apex of motion is at the leftmost point on the semicircle.

cusing of retrograde particles (the maximum deflection of a retrograde particle by Iapetus' gravity is $\sim 1^{\circ}$). Such extension is, however, a natural consequence of dust particles on eccentric orbits (see Fig. 2.8). We therefore now calculate the probability distribution in the more general case of eccentric, inclined particles.

Following Greenberg's formalism (1982), we express the probability distribution function (pdf) as an integral over all the uniformly distributed angles $(\Omega_I, \omega_I, \Omega_p, \omega_p)$, where the 'I' subscripts refer to Iapetus, and the 'p' subscripts to the dust particle. Figure 2.4 shows the geometry of an arbitrary orbit's three angular orbital elements i, Ω and ω.

As Greenberg (1982) notes, however, the problem's geometry does not depend on the values of Ω_I and Ω_p independently—the only geometrically meaningful quantity is their difference $\Delta\Omega$. Furthermore, an important simplification can be made by approximating Iapetus' orbit as circular (its actual eccentricity = 0.03 and for circular dust orbits would lead to extensions of only $\sim 1^\circ$ onto the trailing side). This obviates the need to specify ω_I, the position of pericenter in Iapetus' orbit. These two considerations reduce the phase space dimensionality from $(\Omega_I, \omega_I, \omega_p, \Omega_p)$ to $(\omega_p, \Delta\Omega)$, so that

$$\rho(\theta, \phi) = \int \rho(\theta, \phi, \omega_p, \Delta\Omega)\, d\omega_p\, d\Delta\Omega, \tag{2.8}$$

where the integral spans the region in $(\omega_p, \Delta\Omega)$ space in which collisions occur. $\rho(\theta, \phi, \omega_p, \Delta\Omega)$ can further be expressed in terms of the conditional pdf $\rho(\theta, \phi)$ *given* the set $(\omega_p, \Delta\Omega)$ multiplied by the probability density for $(\omega_p, \Delta\Omega)$,

$$\rho(\theta, \phi, \omega_p, \Delta\Omega) = \rho(\theta, \phi|\omega_p, \Delta\Omega)\rho(\omega_p, \Delta\Omega), \tag{2.9}$$

so

$$\rho(\theta, \phi) = \int \rho(\theta, \phi|\omega_p, \Delta\Omega)\rho(\omega_p, \Delta\Omega)\, d\omega_p\, d\Delta\Omega. \tag{2.10}$$

This simplifies the problem because $\rho(\omega_p, \Delta\Omega)$, the probability of striking Iapetus (anywhere) given ω_p and $\Delta\Omega$, is already available (Greenberg 1982). The problem is then reduced to finding $\rho(\theta, \phi|\omega_p, \Delta\Omega)$.

While analytically correct, Eq. (2.10) is a formidable integral to compute numerically due to the scale separation in the problem. The orbit is so large compared to the satellite that a minute change in ω_p or $\Delta\Omega$ shifts the location of impact drastically. This sensitivity of $\rho(\theta, \phi|\omega_p, \Delta\Omega)$ dictates extremely fine stepsizes in the integration. When combined with the fact that the calculation must be done for 10^4 separate timesteps, 8 initial conditions and 6 particle sizes, the scale separation indicates a brute force approach will be cumbersome at best.

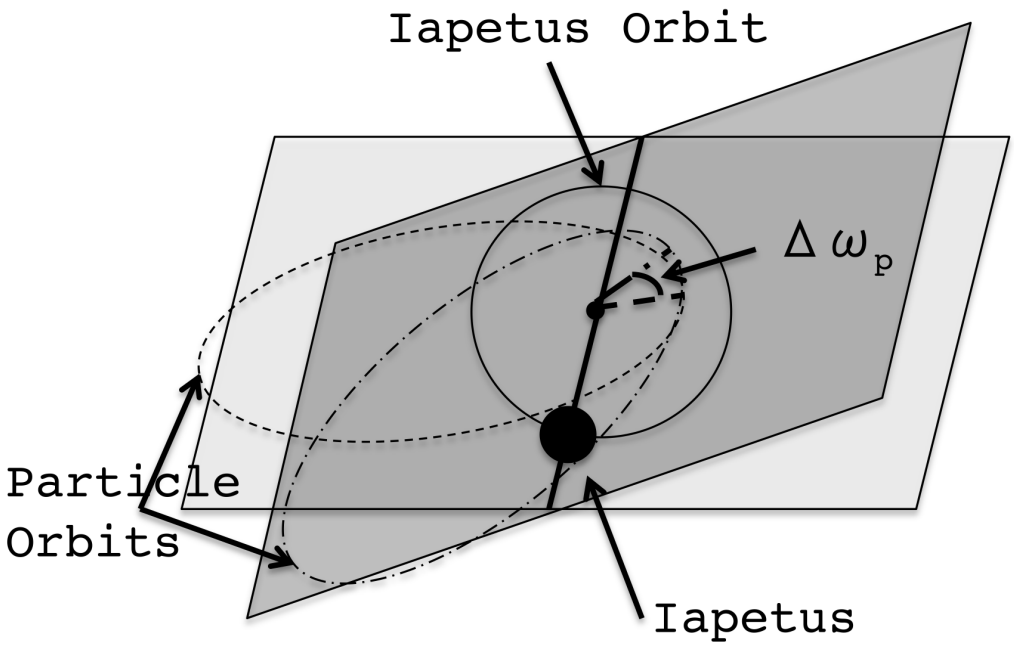

Figure 2.10: Orbits can only cross along the line that marks the intersection of both orbital planes (the line of nodes). Iapetus is depicted at one of the nodes, with its size greatly exaggerated. For the particle orbits, there is a range in the angle from the node to pericenter (ω_p) $\Delta\omega_p$ where collisions with Iapetus are possible. Similarly there is a collisional range in $\Delta\Omega$, the angle that rotates the line of nodes in the plane (not shown).

However, this approach considers each orbital orientation individually. The scale separation lets us consider well-defined *groups* of orientations. Consider an orientation where the orbits cross exactly, i.e., the particle would pass through the center of Iapetus. There is a range in $\Delta\Omega$ and ω_p around this orbital orientation where the orbits no longer exactly cross but are still close enough that the particle impacts Iapetus (Fig. 2.10).

As previously argued, the facts that $a_I \gg R_I$ and that gravitational focusing is

negligible mean that, near impact, we can approximate these orbits as a uniformly distributed disk of parallel trajectories. This approach allows one to coarsen stepsizes while retaining the symmetries in the problem and maintaining the fidelity of the final distribution.

With these considerations, the problem of calculating the distribution function is more tractable. Our approach will be to first find the latitude and longitude for exactly crossing orbits, and then to find how the disk of parallel orbits around the central orbit maps onto the spherical surface of Iapetus.

Given a particular $\Delta\Omega$, one can combine it with the inclinations to determine the orientation of the orbital planes relative to each other (see Fig. 2 in Greenberg 1982). The relative inclination i' is given by spherical trigonometry,

$$cos\, i' = cos\, i_I\, cos\, i_p + sin\, i_I\, sin\, i_p\, cos\, \Delta\Omega. \tag{2.11}$$

Within the particle's orbital plane, ω_p sets the orientation of the orbit. Having approximated Iapetus' orbit as circular, we do not have to consider the satellite's orientation within its orbital plane. From Fig. 2.10, it is clear that most particle-orbit orientations do not result in a crossing. Furthermore, if the two orbits are to cross, they must do so at either of the two nodes where Iapetus' orbit pierces the mutual line of nodes.

The facts that the orbits must cross at a node, and that those respective points on the orbits must therefore be equidistant from Saturn sets the possible values of ω_p (note that this would not be the case if both orbits were substantially non-circular). The angle from pericenter to the ascending node is, by definition, $-\omega_p$. From the equation for an ellipse, we therefore have the condition,

$$a_I = \frac{a_p(1-e_p^2)}{1+e_p\, cos(-\omega_p)}. \tag{2.12}$$

Rearranging,

$$cos\ \omega_p = \frac{1}{e_p}\left[\frac{a_p(1-e_p^2)}{a_I} - 1\right]. \tag{2.13}$$

Since cosine is an even function, Eq. (2.13) gives two solutions $\pm\omega_p$, reflecting the ellipse's symmetry across its long axis. Similarly, another pair of solutions are present at the descending node, located at an angle of 180 - ω_p from pericenter. In general, therefore, four orientations yield crossing orbits for a given $\Delta\Omega$ (see Fig. 1 in Wetherill 1967).

The imposed circularity of Iapetus' orbit means that these four orbits will strike symmetrically about the equator and about the longitude that corresponds to the apex of motion (this occurs because the satellite rotates synchronously). In other words, if we define the longitude in the direction of motion as 0°, the four exactly-crossing orbits will strike at $(\pm\theta, \pm\phi)$. These can later be adjusted to conform with the conventional longitude in the direction of motion—the zero-longitude meridians are currently under revision for Saturn's satellites (Roatsch et al. 2009). Given a $\Delta\Omega$, one therefore only has to compute (θ, ϕ) for one of the four orientations and then straightforwardly substitute for the other three. Here we choose to consider collisions at the ascending node.

The relevant vector to consider is the relative velocity vector in a coordinate system centered on the ascending node (see Fig. 2.11).

The spherical angles that define the direction of the particle's relative velocity vector in this system determine the location of impact on the Iapetus surface. The relative velocity vector is given by

$$\vec{\mathbf{v}}_{rel} = \vec{\mathbf{v}}_p - \vec{\mathbf{v}}_I. \tag{2.14}$$

Having approximated Iapetus' orbit as circular, $\vec{\mathbf{v}}_I$ is always azimuthal. $\vec{\mathbf{v}}_I$ can

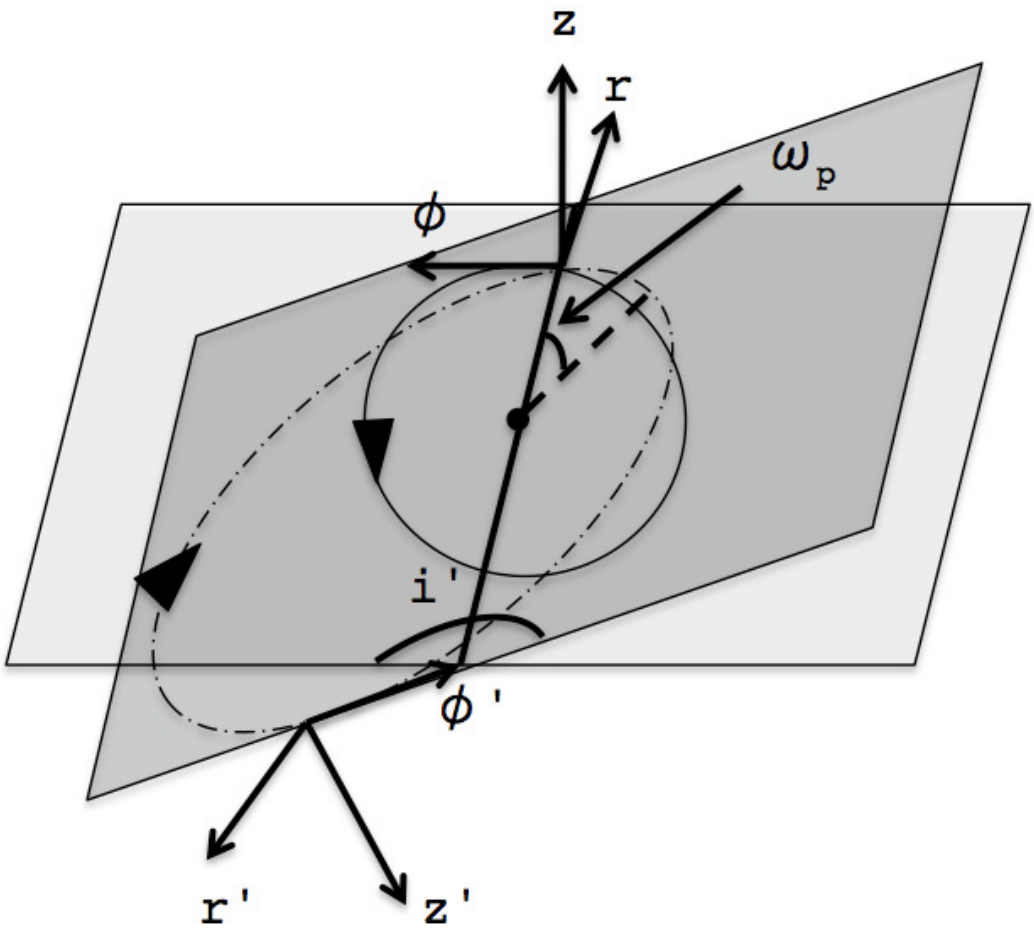

Figure 2.11: Iapetus' circular orbit is executed in the lighter horizontal plane, while the particle's orbit is carried out in the inclined darker plane, with the two crossing at the particle orbit's ascending node. We choose to work in a cylindrical coordinate system centered at the ascending node where the z direction is Iapetus' orbit normal. For simplicity, we first express the particle's velocity in its own orbital plane, where z' is the orbit normal. The relative inclination i' and argument of pericenter ω_p are also depicted.

therefore be simply written in terms of the uniform circular velocity,

$$\vec{\mathbf{v}}_I = \sqrt{\frac{GM_{Sat}}{a_I}} \begin{pmatrix} 0 \\ 1 \\ 0 \end{pmatrix}. \tag{2.15}$$

$\vec{\mathbf{v}}_p$ is given in the particle's orbital plane in cylindrical coordinates by Hamilton (1993),

$$\vec{\mathbf{v}}'_p = \sqrt{\frac{GM_{Sat}}{a_p(1-e_p^2)}} \begin{pmatrix} e_p sinf \\ 1 + e_p cosf \\ 0 \end{pmatrix}. \tag{2.16}$$

Since we are interested in the particle's velocity at the ascending node in particular, we plug in $f = -\omega_p$ (see Fig. 2.11). At the ascending node, the unit vectors r and r' align, but the remaining unit vectors are misaligned by the relative inclination i'. We therefore rotate $\vec{\mathbf{v}}_p$ by an angle $-i'$ around the r axis (see Fig. 2.11), yielding

$$\vec{\mathbf{v}}_p = \sqrt{\frac{GM_{Sat}}{a_p(1-e_p^2)}} \begin{pmatrix} -e_p sin\omega_p \\ cosi' \ (1 + e_p cos\omega_p) \\ sini'(1 + e_p cos\omega_p) \end{pmatrix}. \tag{2.17}$$

The relative velocity vector in Eq. (2.14) can then be obtained from Eqs. (2.15) and (2.17), plugging in for $cos\omega_p$ from Eq. (2.13). The latitude θ and longitude ϕ on Iapetus where the particle strikes are then given by,

$$\theta = Lat = -tan^{-1}\left(\frac{v_z^{rel}}{\sqrt{(v_x^{rel})^2 + (v_y^{rel})^2}}\right), \tag{2.18}$$

$$\phi = Long = tan^{-1}\left(\frac{v_y^{rel}}{v_x^{rel}}\right) - 180^\circ. \tag{2.19}$$

The symmetry described earlier can then be used to find the latitudes and longitudes for the other three orientations. We have thus determined the location

where particles on the four possible crossing orbits (for a given $\Delta\Omega$) would impact. The last piece is to include the disk of parallel trajectories around these crossing orbits that can still impact Iapetus (see Fig. 2.10).

As mentioned earlier, the scale separation in the problem allows us to consider all the orbits that can strike Iapetus close to the crossing orbit as parallel lines with a uniform probability distribution. The situation is analogous to the one presented at the beginning of the section, except with the $\psi = 0$ direction now interpreted as the incoming trajectory at latitude and longitude θ and ϕ, respectively. The probability is again proportional to the projected area, so normalizing the probability distribution we obtain

$$P(\psi) = \frac{cos\psi}{\pi {R_I}^2}, \tag{2.20}$$

which falls to 0 as ψ reaches 90° like it should. Obviously this only applies to the hemisphere facing the disk—for wherever $\psi > 90^\circ$, P(ψ) = 0. Again, this would not be the case with substantial gravitational focusing, but as a result of the high relative velocities due to dust orbits being retrograde, gravitational focusing is negligible (Sec. 2.4). The probability $P(\psi)$ can then be straightforwardly converted to a probability per $d\theta$ and $d\phi$ for substitution into Eq. (2.10).

This provides a prescription for numerically computing $\rho(\theta, \phi)$, the probability density function that we originally set out to find, as a function of latitude and longitude . Cycling over $\Delta\Omega$, at each step, we identify the four crossing orbits and their associated probabilities within the interval, using Greenberg (1982). Then, for each of the four crossing orbits, we "spread" the respective probability across the hemisphere defined by the crossing orbit through the distribution in Eq. (2.20).

Note that, since $\rho(\theta, \phi)$ depends implicitly on particle eccentricities (cf. Eq.

2.17), it will also be a function of particle size. We can write this explicitly, and straightforwardly convert $\rho(\theta,\phi)$ to a probability per unit area, by defining $P(r,\theta,\phi) = \rho(r,\theta,\phi)/cos(\theta){R_I}^2$. We choose to use $P(r,\theta,\phi)$, the normalized probability per unit area, in subsequent calculations.

2.3.2 Calculating Depths

Since radiation pressure produces different orbital histories and is particle-size dependent, different particle sizes have different pdfs. Fig. 2.12 shows the probability density functions for 5, 10, 50 and 500 μm particles, with each contour representing a successive 10-fold decay from the peak value at the apex of motion at the left-most point of each figure.

The figure shows that smaller particles extend farther onto the trailing side near the equator. This is due to their higher eccentricities, as discussed at the beginning of Sec. 3 (see Fig. 2.8). The distributions for particles $\gtrsim 50\mu$m quickly converge to the large-particle limiting distribution, depicted for 500μm particles. The eccentricities of these larger particles are too low to cause them to significantly wrap around the equator onto the trailing side; however, the coverage over the poles is dominated by the precession of Iapetus' orbit, which is independent of particle size.

We now use such probability density distributions $P(r,\theta,\phi)$ to estimate the depth of dust as a function of position on Iapetus' surface. The volume of dust particles within dr of size r that lands within an area A on Iapetus at latitude θ and longitude ϕ can be expressed as

$$Volume(r,\theta,\phi) = N(r) \times P(r,\theta,\phi) \times A \times V(r), \tag{2.21}$$

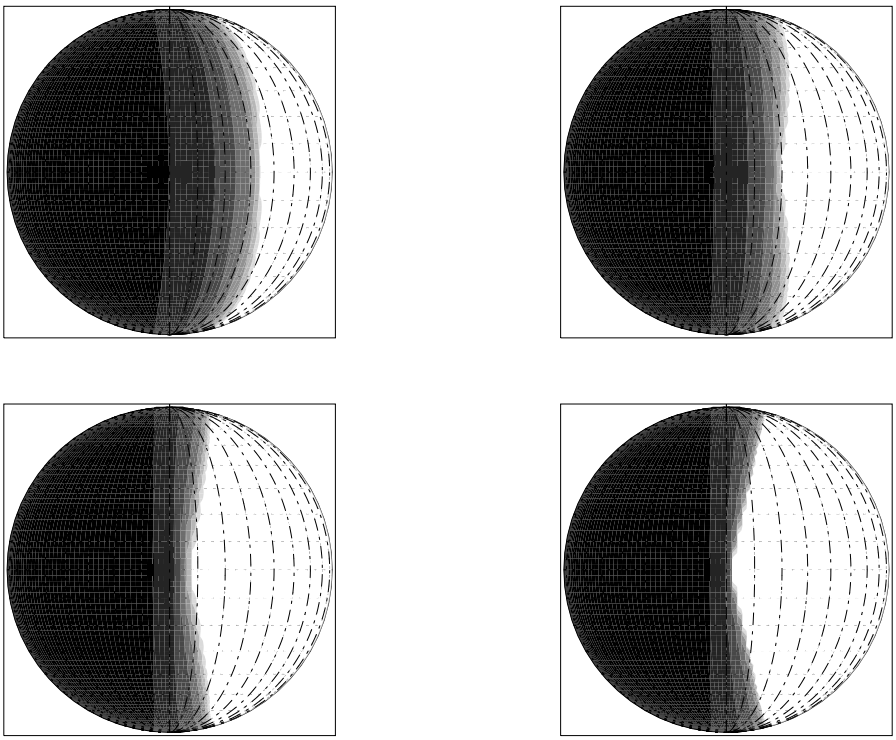

Figure 2.12: Moving from the top-left figure clockwise, probability density functions for 5, 10, 500 and 50 μm particles. Plots represent equatorial views where the vertical line in the center represents the boundary between leading and trailing sides. As such, the apex of motion is at the leftmost point on each figure. Contours represent successive 10-fold decays from the peak value at the apex of motion, down to 10^{-7} of the apex value. Dot-dashed lines are drawn every 10° in longitude.

where $N(r)$ is the number of dust particles within dr of radius r generated in the outer Saturnian system and $V(r)$ is the volume of a spherical particle of radius r. Unfortunately, the current (or past) particle size distribution N(r) is not well constrained observationally. We therefore consider a variety of exponents for distributions of the form,

$$N(r) = Dr^{-\beta}dr, \tag{2.22}$$

where D is a normalization constant, and β is the (negative) power law index of

the particle size-frequency distribution. Finally, the depth can be estimated (to within a packing efficiency factor) as the volume over an area element divided by the area of the surface element.

The final integration over the range of particle sizes to find the total dust depth is complicated by the fact that larger particles, being less affected by Poynting-Robertson drag, take longer to reach Iapetus from Phoebe. We can consider two limiting cases:

a) Most of the debris in the outer Saturnian system was generated early in the Solar System's history (i.e., the mass contribution from the Phoebe ring is negligible). In this limiting case, all the particles with Iapetus-collision timescales (and destruction lifetimes) smaller than the age of the Solar System will have had time to impact Iapetus and collision timescales across different particle sizes are irrelevant.

b) The mass in the outer Saturnian system has been generated at a constant rate over its history. In this case where particles are continuously resupplied, smaller particles that decay inward faster will have a larger effect than they would have in the first case.

We begin by considering case a) where we investigate all particles with collision timescales τ_C smaller than the age of the Solar System on an "even footing." Since dust particles' semimajor axes decay exponentially through Poynting-Robertson drag on a timescale τ_{PR}, and since the ratio of Phoebe's to Iapetus' semimajor axes is ≈ 3.6, particles that strike Iapetus do so on roughly a single e-folding timescale, i.e., $\tau_C \sim \tau_{PR}$. The P-R timescale is given by Eq. (2.2). This implies that the largest dust size to consider is ~ 1 cm, with corresponding

$\tau_{PR} \sim 1$ Gyr.

Integrating over all particle sizes,

$$Depth(\theta,\phi) \propto \int_{r_{min}}^{r_{max}} r^{3-\beta} \times P(r,\theta,\phi) dr. \tag{2.23}$$

For r_{min}, we use the smallest size of long-lived particles from Phoebe, approximately 5 μm (see Sec. 2.1). At the other limit, we use $r_{max} \sim 1$ cm. Should lifetimes from catastrophic collisions between particles or other processes (see Burns et al. 2001) be lower than ~ 1 Gyr, r_{max} must be considered more carefully.

We now address case b), where particles are continuously resupplied. In this circumstance we can consider each particle size to fall onto Iapetus at a characteristic rate,

$$Rate(r,\theta,\phi) = \frac{Volume(r,\theta,\phi)}{\tau_C}, \tag{2.24}$$

where τ_C is the characteristic collision timescale and is $\sim \tau_{PR}$. We can express the depth then as

$$Depth(r,\theta,\phi) \propto \frac{Rate(r,\theta,\phi) \times t}{A}, \tag{2.25}$$

where t is the interval over which dust has been accumulating. From Eq. (2.2), we find that $\tau_C \propto r$, so plugging in for the volume as was done in the first case, we find that

$$Depth(\theta,\phi) \propto \int_{r_{min}}^{r_{max}} r^{2-\beta} \times P(r,\theta,\phi) dr. \tag{2.26}$$

A comparison between Eqs. (2.23) and (2.26) shows that a constant rate of dust production simply acts to steepen the effective power-law index, because small particles will arrive at Iapetus more quickly than large ones. The effective power-law index will be intermediate between the limiting cases of Eqs. (2.23) and (2.26), and the depth can therefore be generally expressed as

$$Depth(\theta,\phi) \propto \int_{r_{min}}^{r_{max}} r^{3-(\beta+\gamma)} \times P(r,\theta,\phi)dr, \tag{2.27}$$

where γ is a number between 0 and 1 that parametrizes the constancy of dust production over the age of the Solar System. A γ of 0 and 1 would therefore, respectively, correspond to cases (a) and (b) introduced at the beginning of this section (3.2).

The constant of proportionality in Eq. (2.27) is *a priori* highly uncertain. An important, though poorly constrained, quantity is the time by which Iapetus had become tidally locked to Saturn. Iapetus' dichotomy could not have formed prior to this time, as a non-synchronously rotating Iapetus would receive dust equally on all sides. Furthermore, the thermal models required to explain its sharp albedo boundaries and bright poles require Iapetus' slow 79 day synchronous period Spencer and Denk (2010). Castillo-Rogez et al. (2007) estimate tidal locking occurred between 200 Myr and 1 Gyr after formation. Moreover, Bottke et al. (2010) argue that most of the dust in the outer Saturn system should have been generated in the first few 100 Myr. Case a) reflects a situation where most of the dust in the outer Saturn system was generated early and Iapetus was able to quickly achieve synchronous rotation so that this dust mass arrived after locking. If, on the other hand, the timescale for tidal evolution is long ($\sim$ 1 Gyr), one might expect the production of the relevant dust to be fairly constant—case b)—since any initial flurry of dust (should there have been one) would have arrived too soon. Despite these uncertainties, one can still normalize the depths over the surface *a posteriori* through a measurement of depth at a particular position (θ,ϕ).

In studying Iapetus with the Cassini radar instrument, Black et al. (2004)

found little hemispheric asymmetry in albedo at a wavelength of 13 cm, while Ostro et al. (2006) observed a strong dichotomy at 2 cm wavelength. Ostro et al. (2006) interpret these results as implying contamination of ice with dark material to a depth of one to several decimeters. The latter's measurement on the leading side of Iapetus was centered on (66° W, +39° N), but the beam size was comparable to the angular size of the satellite (beam/R = 1.36).

While this measurement is imprecise, it does set the order of magnitude of the dark material's depth. Figure 2.13 shows depth contours for three different choices of effective power law index, $\beta_{eff} \equiv \beta + \gamma$ in (25), *assuming* a peak depth of dust at the apex of motion (extreme left of each figure) of 0.5 m. Figure 2.14 provides depths following the equator and meridian passing through the apex of motion at $\sim 90°$ W for the same cases.

The top graph in Fig. 2.14 shows that one should expect extension of dark material $\sim 20 - 30°$ onto the trailing side for all expected particle-size distributions. Only small particles ($\lesssim 25\mu$m in size), having more eccentric orbits, can significantly reach onto the trailing side. As a result, the shallowest effective power-law index ($\beta_{eff} = 3$), having fewer small particles, yields a spatial distribution that extends onto the trailing side significantly less.

The bottom graph shows the extension over the poles. Far from Saturn, solar torques dominate torques from Saturn's oblateness and cause orbits' angular momentum vectors to precess, keeping the inclination roughly constant. Because the inclination is set by initial conditions (i.e., Phoebe's orbital inclination), and is independent of particle size, the graphs for all three power-law indices overlap. The extension over the poles ("latitudes" $> \pm 90°$ along the meridian onto the trailing side) is due to both particle-orbit inclinations and

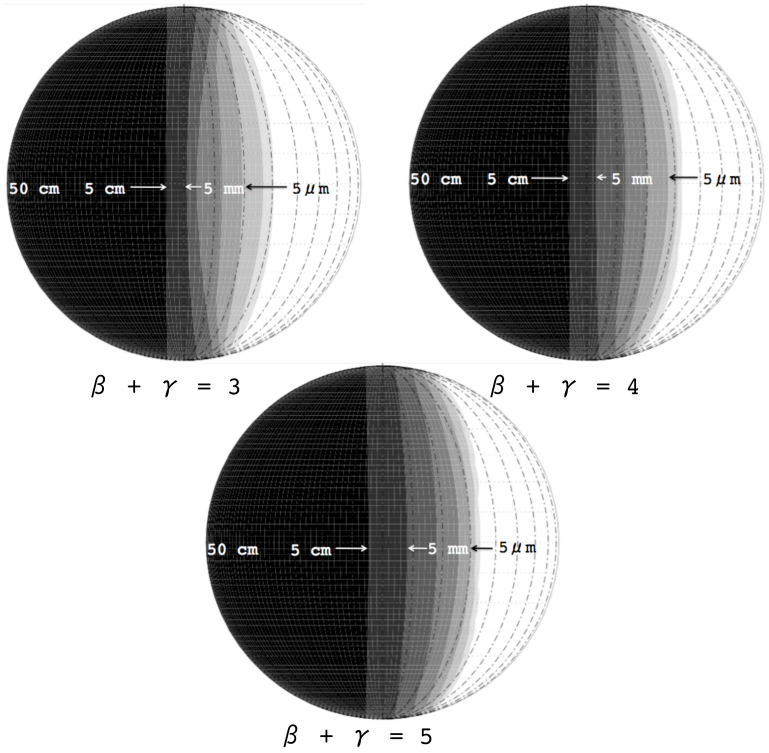

Figure 2.13: Depth contours representing 10-fold decays from the peak value (at the extreme left of the figure) for $\beta_{eff} = \beta + \gamma = 3, 4$ and 5, *assuming* a peak depth at the apex of motion (extreme left of each figure) of 0.5 m. Plots represent equatorial views where the vertical line in the center represents the boundary between leading and trailing sides. Dash-dotted lines are drawn every 10° in longitude.

Iapetus' orbital precession.

One should be careful in distinguishing measured depths of dark material (through radar or otherwise) from depths of dust accumulated over Iapetus' history. If the model of dust deposition and subsequent thermal ice migration is correct, the depth of dark material would be the sum of the contributions from exogenous dust and from the native lag deposit (see discussion in Sec. 3). As

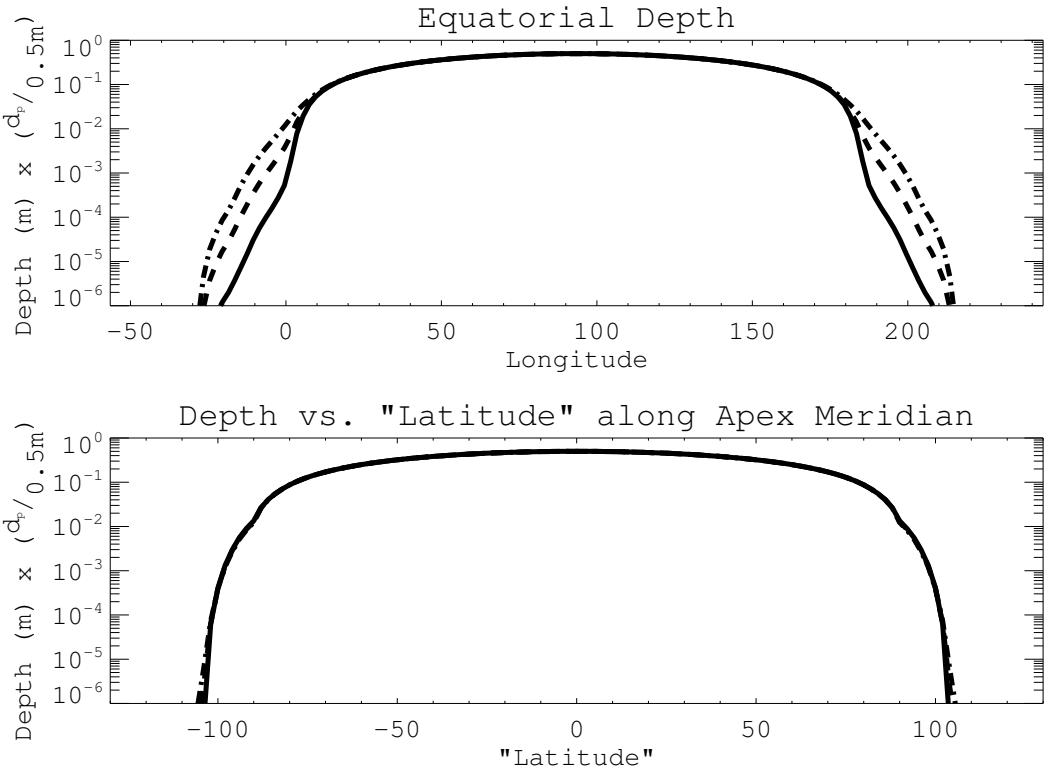

Figure 2.14: Top graph shows depth vs longitude along the equator for $\beta_{eff} = \beta + \gamma = 3$ (solid), $\beta_{eff} = 4$ (dashed), $\beta_{eff} = 5$ (dash-dotted). Bottom graph shows depth vs latitude along the meridian passing through the apex of motion (longitude $\sim 90^\circ$ W). The concept of latitude has been extended beyond $\pm 90^\circ$ along the corresponding meridian on the trailing side of Iapetus to show the extension of dark material over the poles.

long as the depth measured is substantially larger than the expected depth of the lag deposit, the distinction is minor. Figure 2.13 assumes a peak depth *of dust* of 50 cm–with no impact-gardening, this would imply an actual depth of dark material about 20% greater (with a 10 cm lag deposit). Should improved measurements of the peak dust depth become available, the contours on these maps could be straightforwardly rescaled.

The additional lag-deposit depths are not included in our modelling; how-

ever, since exogenous dust acts as the trigger to thermal ice migration, the maps above should be good tracers (at low latitudes) of which areas will be dark and which will be light. We can therefore attempt to predict the boundary of Cassini Regio.

While the figures show a rapid fall-off in depth on the trailing side, maps of Iapetus show no gradation in albedo. Areas initially darkened by infalling dust and receiving strong insolation become almost completely blackened. As a result, the equatorial regions of the leading side appear uniformly dark, while dust-free areas of the trailing side and the colder poles, where the ice that sublimated at lower latitudes settles, appear about ten times brighter.

Thus, if one ignores the contours, the plots above argue for a blackened leading side extending between twenty to thirty degrees in longitude onto the trailing side for $3 < \beta_{eff} < 5$. In fact, this holds true for all $\beta_{eff} > 3$ as shown in Fig. 2.15. At low latitudes, this matches maps of Iapetus' albedo well(see Fig.2.7). Deposition of exogenous dust therefore neatly explains the boundaries of the dark material at low latitudes for the entire range of likely power-law indices (accordingly, Spencer & Denk's (2010) model explains the sharp boundaries in albedo as well as the bright poles).

If indeed Iapetus was initially darkened by dust from the outer Saturnian system, the extension onto the trailing side seems to exclude the shallowest power-law indices in the particle size distribution, $\beta + \gamma < 3$. While it is encouraging that all $\beta_{eff} > 3$ are consistent with the observed distribution, the small slope in Fig. 2.15 for $\beta_{eff} > 3$ renders the longitudinal coverage on Iapetus a comparatively poor indicator of the responsible particle size distribution.

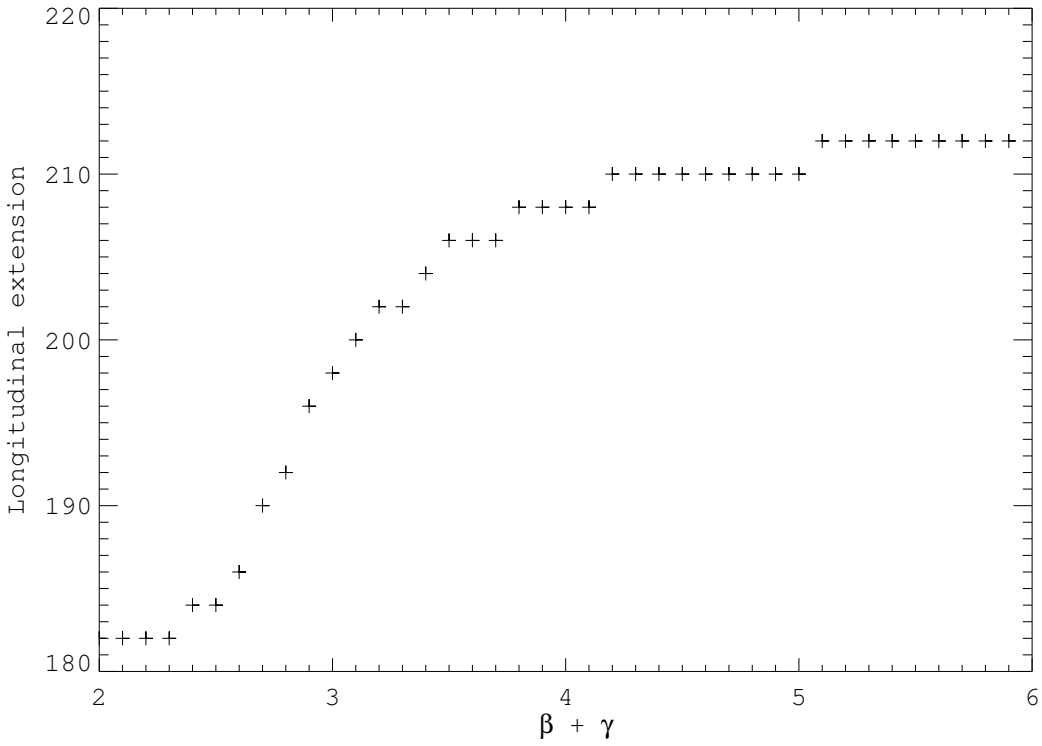

Figure 2.15: The extension in longitude onto the trailing side, chosen as the longitude at which the depth falls below 10^{-5} the peak value, for different values of $\beta_{eff} = \beta+\gamma$. The discrete steps are the result of the resolution of the calculation—2° in longitude.

Fig. 2.16 shows the distribution for $\beta = 3.5$, the power-law index for an idealized infinite collisional cascade (Burns et al. 2001). It assumes a constant supply of particles ($\gamma = 1$) and artificially accounts for thermal ice migration by brightening the poles down to the observed latitude of $\sim \pm 60^\circ$ and by completely darkening areas with depths greater than 5μm.

As previously mentioned, 5μm particles are the smallest Phoebe-generated particles that would strike Iapetus; therefore, this boundary for the anticipated depth is roughly where one should expect to transition from uniform darkness to the stochastic dalmatian patterns observed in the closest Cassini flyby of Ia-

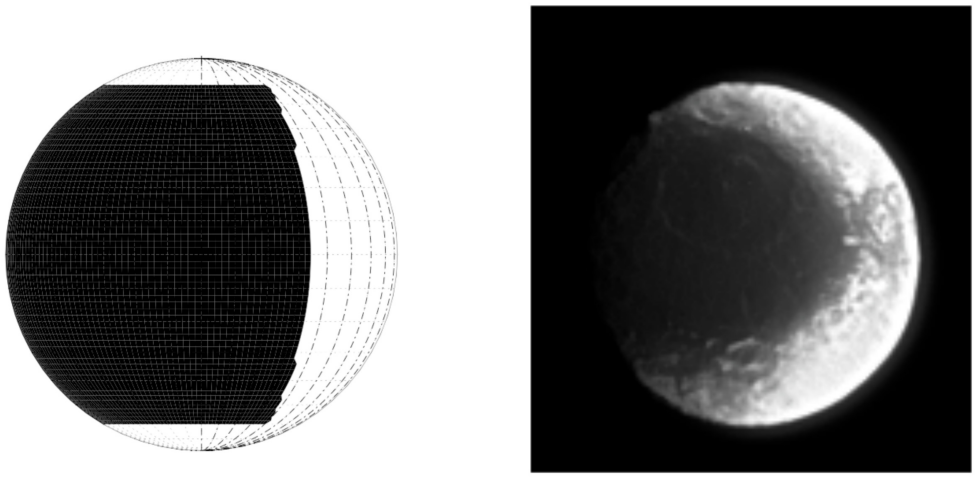

Figure 2.16: Model of the Iapetus surface assuming a peak depth of 50 cm, $\beta = 3.5$ and $\gamma = 1$. All areas with depths $> 5\mu$m have been uniformly darkened and the poles beyond $\pm 60^{\circ}$ latitude brightened to artificially account for thermal ice migration. On the right is an image taken by Cassini at roughly the same orientation for visual comparison (obtained from the Planetary Photojournal—PIA08273).

petus (Denk et al. 2010). This seems consistent with a visual inspection of maps (Fig. 2.7 and see also (Blackburn et al. 2011)) and images of Iapetus by Cassini like the one shown alongside in Fig. 2.16.

An important difference between the modeled surface and the observed distribution is that the theoretically derived dark terrain is concave, in the sense that if one follows a meridian on the boundary, one sees that the dark material extends further in longitude at higher latitudes. Cassini Regio is convex, as can be clearly seen in Fig. 2.7, which uses a simple cylindrical projection where meridians appear as vertical lines. Since temperatures should drop smoothly as one moves from equator to pole, perhaps the discrepancy results from ther-

mal ice migration. Indeed, such models (Spencer and Denk 2010) are able to reproduce this concavity.

Apart from the long-known albedo dichotomy on Iapetus, Denk et al. (2010) recently detected a new *color* dichotomy on Iapetus in which the leading side of Iapetus is substantially redder than the trailing side. The color dichotomy seems to extend farther pole-ward, and transitions more gradually onto the trailing side. Perhaps, as Denk et al. (2010) point out, the color dichotomy more faithfully traces where the dust landed while the albedo dichotomy reflects thermal ice migration's modification of the initial pattern of dust deposition. Further work is needed to ascertain quantitative agreement between observations of the color dichotomy and theoretical models like those presented here.

2.3.3 How Much Sublimation Is Required to Paint the Poles Bright?

Substantial amounts of dust should have struck Iapetus at high latitudes; however, the poles appear bright (Fig. 2.7). If the preceding section is correct, this means that bright, sublimed ice from lower latitudes must be settling on the polar regions faster than dark dust is landing on them. Our collisional flux then provides an opportunity to constrain sublimation rates.

We found in the previous section that the distribution at the boundary between the leading and trailing sides depends on the underlying particle size distribution of dust; however, farther from the boundaries, as argued at the beginning of Sec. 3.1, the depth (at low latitudes) should scale approximately as

cosψ independent of the particle size distribution, where ψ is the angular distance from the apex (cf. Eq. (2.20)).

Therefore, following the meridian that passes through the apex of motion (longitude $\approx 90^\circ$), at a latitude of 60° the depth should be roughly half that at the apex ($cos60^\circ = 1/2$). This point in the polar region would receive more dust than any other point at the same latitude as it has the minimum angular distance from the apex. The fact that this point in the polar region with maximum dust flux appears bright provides the strongest constraint on the minimum sublimation rate required to keep the poles bright. Assuming a peak depth of dust at the apex of 50 cm as done in the previous section based on radar measurements (Ostro et al. 2006), this implies an average rate for the minimum polar dust deposition of $\sim 25cm/5Gyr$ or $\sim 50\mu m/Myr$.

It is possible, however, that the average rate of deposition would not match the rate of sublimation. Maybe in the past (when deposition rates of dust in the outer Saturnian system were likely higher, Bottke et al. 2010), the poles of Iapetus were dark. Perhaps only recently did deposition of ice exceed that of dust and hide evidence of past dark poles. In that case the rate of ice sublimation required to keep the poles bright would be lower than the average dust deposition rate. Dark-ringed craters in the polar terrains could support such a conjecture, but current observations are unable to distinguish between these two general possibilities.

Therefore, given only the observation that Iapetus' poles are bright *today*, we now try to roughly constrain the current sublimation rate. We can estimate the deposition rate of the material coming from the Phoebe ring using its measured optical depth.

For lack of better information, we assume that the entire volume of the ring has the same particle size distribution. In this case, the rate of dust deposition at a latitude of 60° along the meridian passing through the apex (longitude ~ 90° W) can be directly obtained from Eqs. (2.24), (2.21), (2.22) and (2.2),

$$Rate(60^\circ, 90^\circ) \sim \int_{r_{min}}^{r_{max}} \frac{Dr^{-\beta}\, V_d\, P(r, 60^\circ, 90^\circ)\, \frac{4}{3}\pi r^3}{0.1\, r\, \frac{Myr}{\mu m}}\, dr, \tag{2.28}$$

where V_d is the volume of the disk and $P(r, 60^\circ, 90^\circ)$ is the probability per unit area for dust striking at the longitude corresponding to the apex ($\sim 90^\circ W$) and a latitude of 60°. In pursuing an order of magnitude estimate, we take all particle sizes in the Phoebe ring (i.e., $\gtrsim 5\mu$m) to have probability ~ 1 of striking Iapetus (cf. Fig. 2.6). Furthermore, we consider the depth distribution to be simply proportional to $cos\psi$ (Fig. 2.9), with depths of 0 on the trailing side. For the integrated probability to yield unity, $P(r, 60^\circ, 90^\circ) \approx 3 \times 10^{-7}$ km^{-2}.

We estimate V_d as the volume of a disk 300 R_S in radius and 40 R_S thick (as done by Verbiscer et al. 2009), or $\sim 2 \times 10^{21}$ km^3. This yields

$$Rate(60^\circ, 90^\circ) \sim 10^{16} \frac{km\, \mu m}{Myr} \int_{r_{min}}^{r_{max}} Dr^{2-\beta} dr. \tag{2.29}$$

The final integral here is provided by the definition of the normal optical depth,

$$\tau = \int_{l_{min}}^{l_{max}} \int_{r_{min}}^{r_{max}} n(r, l) Q_{ext} \sigma(r) dr dl, \tag{2.30}$$

where $Q_{ext} = Q_{abs} + Q_{scat}$. Following Verbiscer et al. (2009), we take values of $Q_{abs} = 0.8$ and $Q_{scat} = 0.2$. They estimate $\tau \sim 2 \times 10^{-8}$. Making again the simplifying assumption that the number density does not depend on the distance

along the line of sight l (trivializing the integration over l),

$$\frac{2 \times 10^{-8}}{40 R_S \, \pi} = \int_{r_{min}}^{r_{max}} D r^{2-\beta} dr. \tag{2.31}$$

If we are interested in the rate of deposition due to the material currently seen in the Phoebe ring (i.e., if we take the same limits of integration), the integral can then be plugged into Eq. (2.29), yielding a rate of dust deposition at the leading edge of the polar region of $\sim 50 \mu m/Myr$, which is of the same order as the average deposition rate calculated earlier. This estimate also agrees with that given by Verbiscer et al. (2009) of $\sim 40 \mu$m / Myr.

In either event, Iapetus must today be actively depositing on the order of tens of μm per Myr of sublimed ice onto the poles in order to keep them bright. This ice could originate from either the leading or trailing side. In Cassini Regio, with daytime temperatures of 130 K, ice will sublime over extremely short timescales—about 1000 μm in 8000 years (Spencer and Denk 2010). Very quickly, a dark layer thicker than the thermal skin depth will form, making it difficult for further ice to sublimate. In this case, the rate of impact gardening, which brings fresh ice to the surface, will determine the rate of sublimation from Cassini Regio. Unfortunately, impact gardening depths on Iapetus are not well constrained (Spencer and Denk 2010).

The temperature on the brighter trailing side indicates a sublimation rate of about $100 \mu m/Myr$ (Spencer and Denk 2010). Given that the area of the trailing side at latitudes $< 60^\circ$ is comparable to that of both polar regions combined, this sublimation rate seems capable of overwhelming polar dust deposition. Further data on the Phoebe ring will help further constrain the required sublimation rates, and improved modeling of the surface processes on Iapetus will ultimately dictate the consistency of these two pictures.

2.4 Dust from other Irregular satellites

A long-standing objection to Soter's model of dust infall from Phoebe has been that Cassini Regio's spectrum differs from that of Phoebe (e.g., Tholen and Zellner 1983; Cruikshank et al. 1983; Buratti et al. 2002). One possible resolution is that the surface compositions are in fact similar, but other effects such as Rayleigh scattering (Clark et al. 2008), cause the spectra to differ. Another possibility is that Iapetus has also been coated by dust from the irregular satellites other than Phoebe (Buratti et al. 2005; Tosi et al. 2010). Grav et al. (2003) and Buratti et al. (2005) find that many of these new irregular satellites have a reddish color similar enough to that of Hyperion and Cassini Regio to suggest a link between them.

Unlike the regular satellites (ignoring Iapetus) that move on low-eccentricity orbits close to Saturn's equatorial plane, the irregulars have widely varying inclinations and eccentricities. This implies a violent collisional history between irregular satellites as differing precession rates would have led to crossing orbits and consequent collisions (Nesvorný et al. 2003). By modeling this process of collisional grinding numerically, Bottke et al. (2010) estimate that $\sim 10^{20}$ kg of dust should have been generated in the outer Saturn system, particularly early in the Solar System's lifetime.

We therefore explore the likelihood that debris from these other irregular satellites would collide with Iapetus. Fig. 2.17 shows the probability that 10μm grains will strike Iapetus if they start with the orbits of the various irregular satellites known today, plotted against both today's value of the parent-satellite orbit's inclination and eccentricity. The orbits of the current irregular satellites

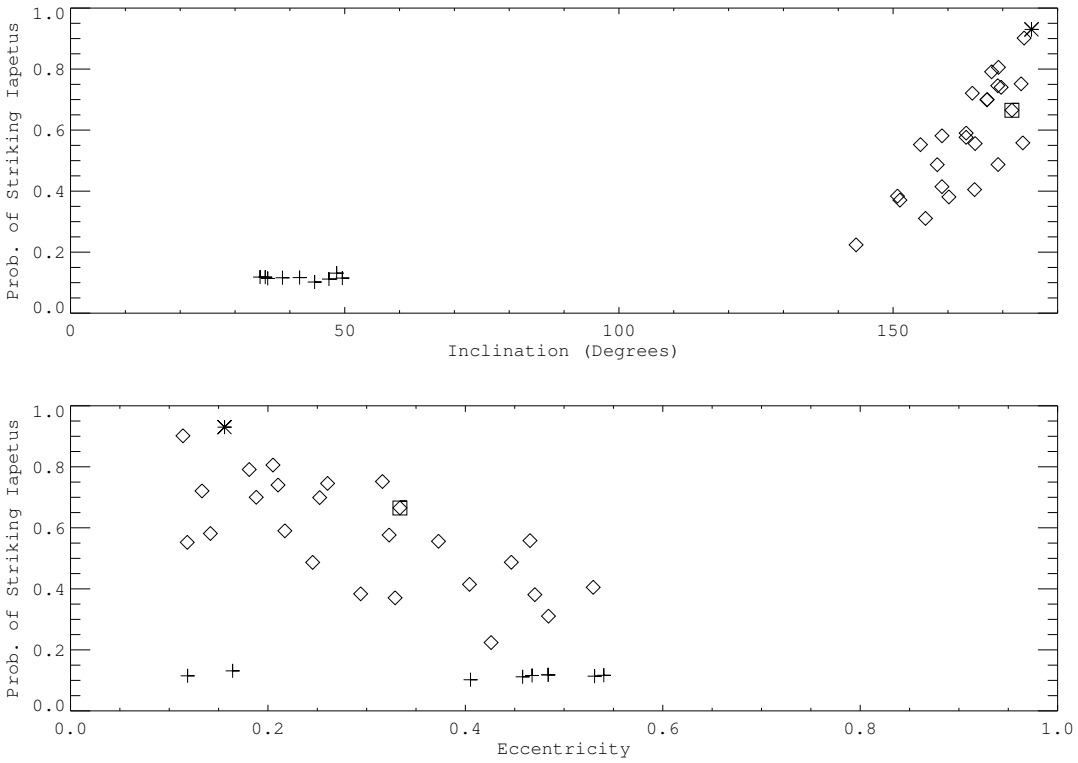

Figure 2.17: Collision probability with Iapetus for 10μm grains that start with the orbits of today's irregular satellites. Plus signs represent prograde irregulars, while open diamonds are retrograde. Inclinations are measured relative to Saturn's orbital plane. The asterisk represents Phoebe, and the boxed diamond Ymir (of importance below).

are not chosen to be necessarily representative of their orbits over the course of the Solar System's history—the irregular satellites seen today are likely the fragments of past satellites and are subject to increasingly strong gravitational perturbations from the Sun the further out in Saturn's Hill sphere they reside (Nesvorný et al. 2003; Turrini et al. 2008; Bottke et al. 2010). Rather, we chose the current orbits as a way of sampling the orbital phase space of irregular satellites.

The efficiency with which material is supplied to Iapetus differs markedly between the prograde (plus signs) and retrograde (diamond) satellites (Fig.

2.17). This can be understood through a simple particle-in-a-box estimate of the collision timescale, where the irregular-satellite and dust-particle orbits are taken to precess around the same axis (normal to Saturn's orbital plane):

$$T_{col} \sim \pi \left(sin^2 i_p + sin^2 i_I \right)^{\frac{1}{2}} \left(\frac{a_I}{R_I} \right)^2 \left(\frac{U_r}{U} \right) T_{orb}, \tag{2.32}$$

where the p subscript refers to the dust particle, i_p and i_I are inclinations measured relative to Saturn's orbital plane, R_I is Iapetus' radius and a_I its semimajor axis; U is the relative speed between the two objects, and U_r is the radial component of the relative velocity; finally, T_{orb} is the dust particle's orbital period (Öpik 1951; Hamilton and Burns 1994). Iapetus' orbit does not quite precess around the normal vector to Saturn's orbital plane, but rather around an axis (the normal to its local Laplace plane, see Fig. 2.5) $\sim 11^\circ$ away (Ward 1981); however, for our rough estimate this can be ignored.

Qualitatively, one should expect T_{col} to decrease as i_p approaches 0° (or 180°). As i_p approaches coplanarity, the phase space that the particle must explore before "finding" Iapetus is reduced. One should also expect prograde particles to have a substantially decreased chance of striking Iapetus compared to retrograde particles, as retrograde particles have a much larger relative velocity U than prograde particles. This occurs because for larger relative velocities, when one particle is passing through the node where collisions are possible, the other particle can initially be at a wider range of positions in its orbit and still reach the node "in time."

For prograde particles with low inclinations, the azimuthal component of U is mostly subtracted out so U_r/U is roughly 1, and nearly independent of the particle eccentricities (Hamilton and Burns 1994). For retrograde particles, on

the other hand, the azimuthal component of U dominates so U_r/U will be small and will increase with orbital eccentricity, which determines the departure of the dust orbit from being purely azimuthal. One should therefore expect that for retrograde particles, those with inclinations closest to coplanarity and with low eccentricities will have the shortest collision timescale and the highest collision probability (see Fig. 2.17).

We can also investigate this more quantitatively. The ratio U_r/U can be obtained from Eqs. (2.15) and (15), yielding

$$\frac{U_r}{U} = \left[1 + \frac{\alpha^2(1+\alpha^2-2\alpha\, cosi')}{e^2-(\alpha^2-1)^2}\right]^{-\frac{1}{2}}, \tag{2.33}$$

where i' is the mutual inclination between the particle's and Iapetus' orbits, e is the particle's eccentricity, and

$$\alpha^2 = \frac{a_p(1-e^2)}{a_I}. \tag{2.34}$$

We note that while particle orbits will perform small oscillations in their inclinations around their parent body's inclination, particle eccentricities will be substantially larger than those of the parent bodies due to radiation pressure. In this section we therefore take $i_p \approx i_{satellite}$ and select characteristic eccentricities from our numerical integrations. It is nevertheless generally true that source satellites with more eccentric orbits will yield particle orbits with higher eccentricities.

Since particles can only collide with Iapetus when their orbit's pericenter is smaller than a_I and their apocenter is greater than a_I, α^2 ranges between $1-e$ and $1+e$. Furthermore, from Eq. 2.11, i' varies between $i_p - i_I$ and $i_p + i_I$. Taking

$i' \approx i_p$ and $\alpha \approx 1$ as characteristic values, and expanding $cosi'$ to leading order,

$$\frac{U_r}{U} = \left[1 + \left(\frac{i_p}{e}\right)^2\right]^{-\frac{1}{2}}. \tag{2.35}$$

Since $sin^2 i_I \ll sin^2 i_p$ for Saturn's prograde irregular satellites ($35^\circ < i_p < 50^\circ$), we can approximate the first term in parentheses in Eq. (2.32) as simply $sini_p \approx i_p$. Therefore,

$$T_{col} \sim i_p \left[1 + \left(\frac{i_p}{e}\right)^2\right]^{-\frac{1}{2}} (prograde). \tag{2.36}$$

Over the range of prograde inclinations and the range of characteristic particle eccentricities found in our numerical integrations ($0.3 \lesssim e \lesssim 0.6$), T_{col} varies by a factor between $\sim 0.3 - 0.45$. This approximation agrees with the values from Eq. (prograde) to within 25% over the range of characteristic values for e, i_p and a_p for dust from the prograde satellites, and matches the small spread ($\lesssim 50\%$) in collision probability for the prograde satellites (plus signs) in Fig. 2.17.

For the retrograde satellites, again taking $i' \approx i_p$ and $\alpha \approx 1$, and noting that $\pi - i_p$ is small so that $cosi_p \approx -1 + (\pi - i_p)^2/2$,

$$T_{col} \sim (\pi - i_p)\left[1 + \frac{4}{e^2}(1 - \frac{(\pi - i_p)^2}{4})\right]^{-\frac{1}{2}}. \tag{2.37}$$

Thus, since $(\pi - i_p)^2/4 \ll 1$ for the retrograde satellites and $4/e^2 \gg 1$ for the range of characteristic eccentricities ($\gtrsim 0.3$),

$$T_{col} \sim (\pi - i_p)\,\frac{e}{2}\,(retrograde). \tag{2.38}$$

This agrees with the values from Eq. (2.38) to within 20% over the range of characteristic values of e, i_p and a_p for dust from the retrograde satellites. It also shows why the retrogrades have much higher collision probabilities. For the range of dust inclinations and eccentricities, the prograde to retrograde ratio of T_{col} using Eqs. (2.36) and (2.38) is always greater than unity and $\lesssim 25$.

Eq. (2.38) means that low-eccentricity moons (those that yield lower eccentricity particles) with inclinations close to 180° will have the shortest collision timescales, and therefore the largest collision probabilities with Iapetus. Fig. 2.18 shows the same probabilities as Fig. 2.17, but in two dimensions so as to separate the dependence on inclination and eccentricity. Darker squares represent larger collision probabilities. Thus one can see following rows of constant eccentricity that the probability increases as the inclination approaches 180°, whereas following columns of constant inclination, the probability decreases with increasing eccentricity. Tosi et al. (2010) find similar trends using a different method of evaluating collision probabilities. The two low-eccentricity, high-inclination moons on the bottom right of the plot with the highest probabilities are Suttungr and S/2007_S2.

2.4.1 Dust Generation Efficiencies

While the previous section addressed the likelihood of particles from different irregulars striking Iapetus once they are ejected, one must still determine the relative dust yield from the various satellites to infer the dominant sources of dust for Iapetus. Dust will be generated both in collisional break-up between the outer irregular satellites (Bottke et al. 2010) and in micrometeoroid bombardment from outside the Saturnian system (Burns et al. 1999). In both cases, the effectiveness of a satellite as a dust source is determined by the competition between a larger satellite radius raising the collision cross section and a larger satellite mass increasing the escape velocity (thus inhibiting dust from leaving the satellite).

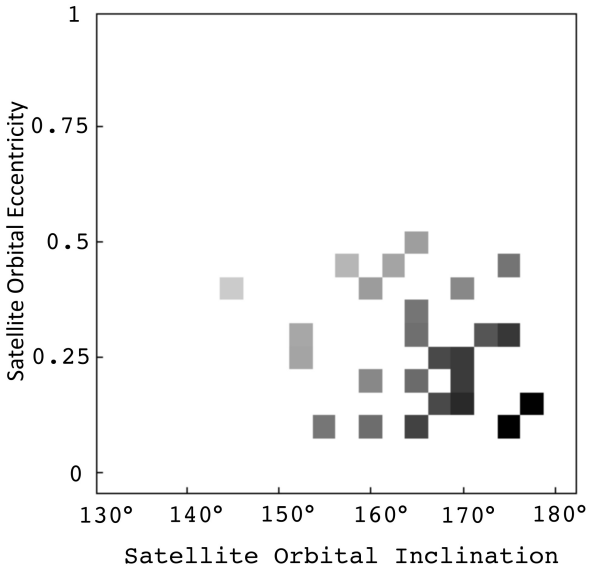

Figure 2.18: Numerically computed probabilities for 10-μm dust particles striking Iapetus as a function of parent (retrograde) satellite orbital inclination and eccentricity. Probabilities range from darkest (Suttungr = 0.9 and S/2007_S2 = 0.89) to lightest (Narvi = 0.22). Collision probability increases as the inclination approaches coplanarity (180°) and as the eccentricity decreases.

Burns et al. (1999) investigate this relationship in the Jovian system. For small moons, where gravity is not important, the rate at which mass is supplied to the ring by a satellite of radius R_i is simply proportional to R_i^2; however, beyond an optimum satellite size R_{opt} that depends on regolith properties, the dust production rate becomes almost flat, decreasing as $R_i^{-1/4}$. Burns et al. (1999) estimate that this optimum size should be about $5-10$ km in the Jovian system. Assuming similar results for the Saturn system, this implies that Phoebe ($R \sim$

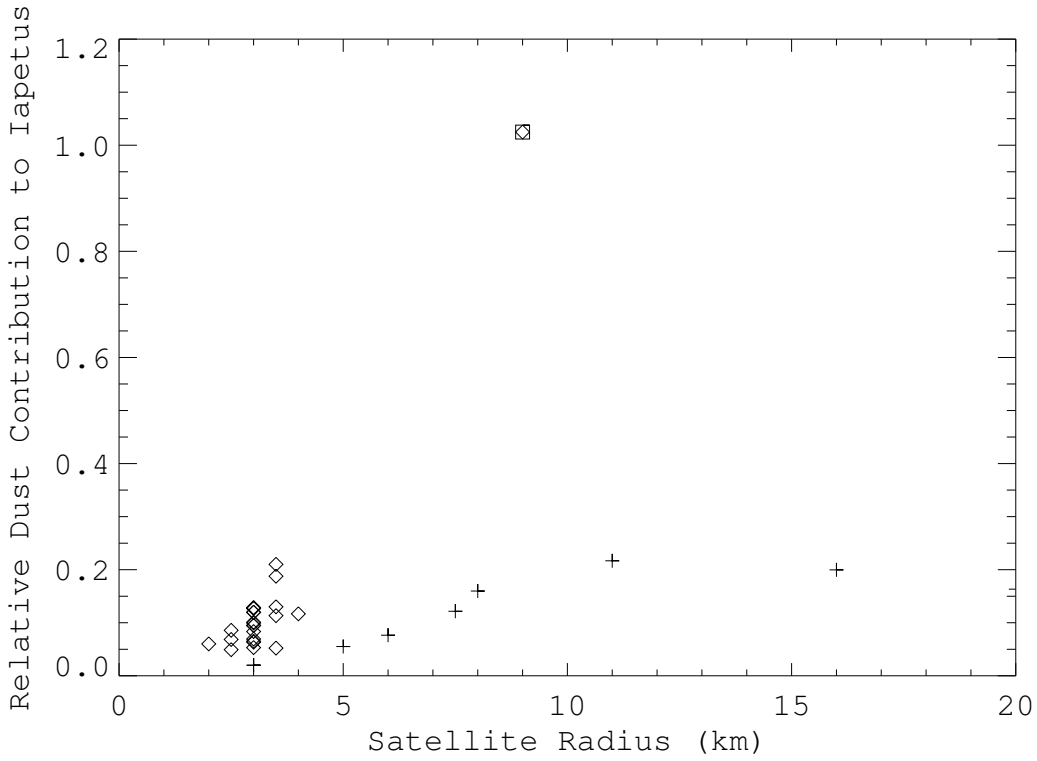

Figure 2.19: Dust supplied to Iapetus from each of the irregular satellites relative to the contribution from Phoebe, plotted vs. satellite radius. The relative contribution is calculated as the product of the collision probability for the particular satellite (Sec. 4) and the radius-dependent terms in the dust-generation efficiency factor of Burns et al. (1999), assuming an optimum satellite size of 10 km. Prograde satellites are represented by plus signs, and retrograde moons by open diamonds. Ymir is plotted as a boxed diamond (R_i =9 km) and has the largest contribution.

100 km) should produce no more (in fact slightly less) dust than any $\sim 5-10$ km irregular satellite. Fig. 2.19 shows the impact probabilities calculated in the previous section for each irregular satellite weighted by the R_i dependent terms in the dust-generation efficiency factor of Burns et al. (1999), assuming an optimum satellite size R_{opt} of 10 km.

Fig. 2.19 shows that Ymir (R_i = 9 km) should be roughly as important a contributor of dust to Iapetus as Phoebe (R_i = 107 km), though the summed contribution from the remaining moons is greater than that of either Ymir or Phoebe. This might help lessen the contradiction that the spectrum of Cassini Regio does not seem to match that of Phoebe (Buratti et al. 2005; Tosi et al. 2010).

But if Phoebe is not the dominant source of dust in the outer Saturnian system, why then is the only prominent dust ring generated by the irregular satellites associated with Phoebe? Satellites should generate dust rings of height $2asin\ i$, so one might expect to see a nested series of rings of differing heights. This is analogous to the dust bands observed in the zodiacal cloud, where the dimensions of the bands give away the orbital elements of the object that produced them (Dermott et al. 1984).

Perhaps the fact that Phoebe's orbit has the smallest semimajor axis and lowest inclination among the irregular satellites squeezes its modest share of dust into a more compact volume, yielding a higher optical depth than other satellite rings. The line-of-sight optical depth of a ring generated by satellite j, $\tau_j \sim n_j \sigma_j L_j$ where n_j is the number density, σ_j is the average particle cross-section and L_j is the distance along the line of sight. Focusing only on the parameters involving the satellites (as opposed to dust properties), and taking $L_j \sim a_j$, $\tau_j \sim M_j a_j / V_j$, where V_j is the volume of the ring associated with satellite j and M_j is the mass of dust within it. V_j should be proportional to $a_j^3 sini_j$, yielding

$$\tau_j \sim \frac{M_j}{a_j^2 sin\ i_j} \tag{2.39}$$

The mass M_j carries the same weighting factor used in Fig. 2.19. The optical

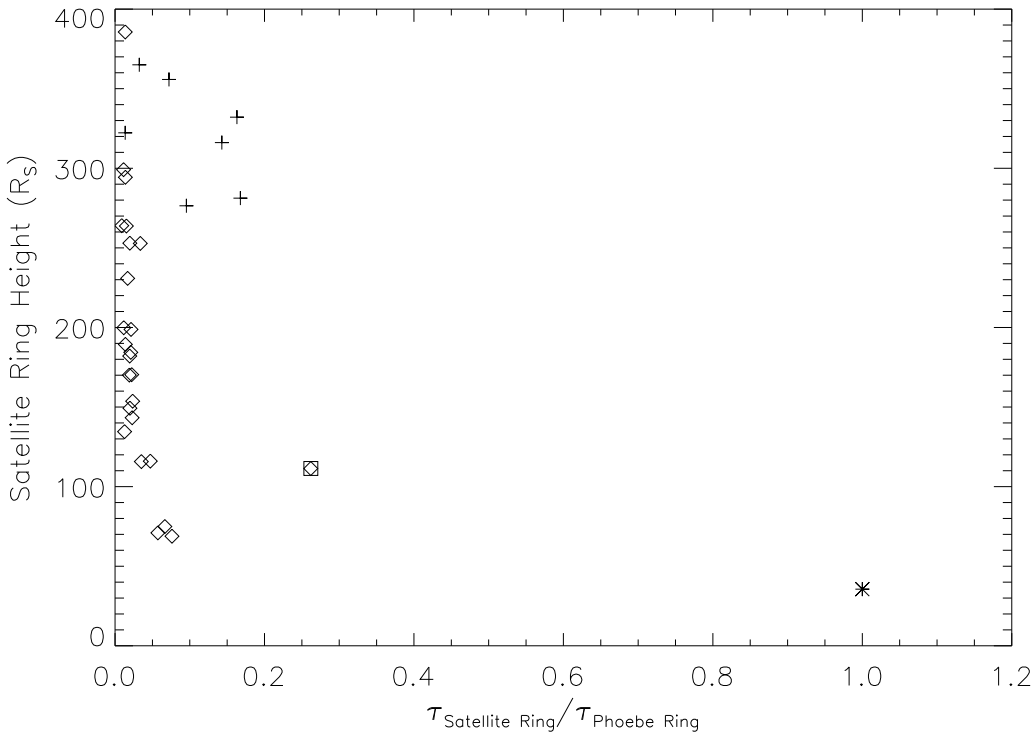

Figure 2.20: Estimated line-of-sight optical depth of rings created by the irregular satellites relative to the optical depth of the Phoebe ring, plotted vs. the height of the ring that the satellite would produce in Saturn radii. Phoebe (asterisk) generates the ring of highest optical depth with a thickness of $\sim 40\ R_S$, followed by Ymir (boxed diamond), which should produce a $\sim 110 R_S$-tall ring. Plus signs denote regular satellites, open diamonds irregular moons.

depth therefore carries an additional factor of $(a_j^2 sin\, i_j)^{-1}$. Fig. 2.20 plots the weighting factor in Eq. (2.39) relative to that for Phoebe vs. the expected ring height that would be produced by the particular moon ($2a sin\, i$) in Saturn radii.

The simple estimates illustrated in Figs. 2.19 and 2.20 suggest that irregular satellites other than Phoebe could contribute substantial amounts of dust to Iapetus, while the Phoebe ring (due to its compactness) would be the most

prominent dust ring generated by the irregulars. Perhaps in observations of the Phoebe ring, the flux from the various much taller, low-optical depth rings has been interpreted as part of the background. One might still, however, expect to be able to identify a dust ring associated with Ymir; it would be ~ 3 times taller, and have $\sim 1/4$ the line-of-sight optical depth of Phoebe's structure.

The fact that no other dust rings have yet been detected could be used to argue that other factors enhance Phoebe's dust production in the outer Saturn system. One possibility is that Phoebe's position as the innermost irregular satellite increases its collision frequency with other irregulars. Numerical studies (Nesvorný et al. 2003) suggest that Phoebe alone among the Saturnian irregulars likely suffered collisions with several now absent irregulars; while below the detection threshold of today's telescopes, the ejecta from these events would be excellent suppliers of debris. As such, there might be an increased amount of unseen collisional debris ($\lesssim 1$ km) sharing Phoebe's orbital elements, which, for a steep enough size distribution, could contribute significantly to the Phoebe ring. A more certain assessment will have to await further observations of the Phoebe ring and searches for separate dust bands. Our studies assume that Phoebe is the dominant dust source in the outer Saturn system. Should evidence to the contrary arise, further work would be required to assess the relative contributions to Iapetus, Hyperion and Titan.

2.5 Implications Beyond Iapetus

2.5.1 Iapetus as a Tracer of the Initial Dust Mass at Saturn

Bottke et al. (2010) argue that most of their estimated 10^{20} kg of collisionally generated dust in the outer Saturn system was created within a few hundred Myr of the capture of the irregular satellites. In this case, the whole range of particle sizes we considered should have had time to reach Iapetus, corresponding to the $\gamma \approx 0$ case discussed in Sec. 3.2. In this circumstance, since particles roughly larger than 10μm are almost certain to strike Iapetus, we should expect all the dust mass in sizes $\gtrsim 10\mu$m to be part of Cassini Regio.

Unfortunately, as Bottke et al. (2010) point out, 10^{20} kg would generate a dark layer on Iapetus that is kilometers thick. Taking the depth on the leading side to fall off as $cos\,\psi$, we can estimate the volume of dust on Iapetus as

$$V_{Iap} \sim \pi R^2\, d_{apex} \approx 850 \left(\frac{d_{apex}}{50cm} \right) km^3, \tag{2.40}$$

where d_{apex} is the peak depth of dust at the apex (not including any lag deposit from sublimation). Assuming 100% transfer efficiency (all particles $\gtrsim 10\mu$m), this would imply an initial dust mass $\sim 10^{15}$ kg.

The transfer efficiency could be reduced with a sufficiently steep size distribution (one that would cause essentially all of the dust mass to be in sizes $\lesssim 5\mu$m). These small particles would then be quickly eliminated from the system through radiation pressure and avoid Iapetus; unfortunately, the requisite power-law index is implausibly steep ($\gtrsim 5.5$).

The two results might also be reconciled if Iapetus achieved synchronous ro-

tation much later ($\gtrsim 1 Gyr$ after formation). In this case, the dark material would have been localized to the leading side only after the bulk of the influx had occurred. Such a scenario could help explain why even the bright hemisphere of Iapetus is darker than the surfaces of the other large icy satellites; however, it also poses the problem of why the masses of dust that would have blanketed Iapetus at all longitudes prior to synchronous rotation did not cause blackening everywhere when thermal migration (Spencer and Denk 2010) kicked in.

It seems for now that, unless the depth estimate derived from radar measurements (Ostro et al. 2006) is grossly in error, the amount of dark material on Iapetus implicates an initial dust mass in the outer Saturnian system about 5 orders of magnitude lower than that of Bottke et al. (2010). While the presence of ammonia could make a thicker layer of dark material appear shallow (Ostro et al. 2006), the discovery of small bright-floored craters close to the boundary of Cassini Regio support the idea of a thin dark deposit (Denk et al. 2010).

2.5.2 Hyperion

During Cassini's close fly-by, Cruikshank et al. (2007) and Thomas et al. (2007) found Hyperion to be segregated into a low-albedo unit mostly filling the bottoms of cup-like craters and a more widespread high-albedo unit. Furthermore, the spectra of the dark material show similarities to the material making up Cassini Regio, suggesting a common source (Cruikshank et al. 2007; Buratti et al. 2005).

Burns et al. (1996), in their dynamical study of the fate of Phoebe dust, had already argued that Hyperion should receive a significant fraction of Phoebe dust

grains. In their calculations, however, they considered collisions with Iapetus, Hyperion and Titan sequentially, when in fact—because of radiation-pressure-induced orbital eccentricities—dust grains can reach all three moons nearly simultaneously. As a result, Hyperion will receive a much-reduced fraction of the grains ($\sim$ 0.004 for both 5- and 10-μm grains vs. 0.18 according to Burns et al. (1996)). Furthermore, no grains $\gtrsim 10\mu$m reach Hyperion. The conclusion, however, is the same—Hyperion's surface layers should contain some dark material from Phoebe and the other irregular satellites. Furthermore, since Hyperion is chaotically rotating rather than tidally locked, an isotropic distribution of dust is expected (Burns et al. 1996).

We estimate the volume of material striking Hyperion relative to the volume hitting Iapetus as

$$\frac{V_{Hyp}}{V_{Iap}} \sim \frac{\int_{5\mu m}^{10\mu m} r^{3-(\beta+\gamma)} P_H(r) dr}{\int_{10\mu m}^{1cm} r^{3-(\beta+\gamma)} dr}, \tag{2.41}$$

where $P_H(r)$ is the probability for a particle of size r striking Hyperion (derived from our numerical simulations discussed in Sec. 2), V_{Iap} is given in Eq. (2.40), and we have approximated the probability of particles striking Iapetus as a step function at $r = 10\mu$m.

Calculated dust depths on Hyperion for $2 < \beta < 4$ in the limiting cases of $\gamma = 0$ and 1 (cf. Sec. 3.2) are given in Fig. 2.21 assuming isotropic coating and a spherical target of radius 135 km.

These extremely shallow depths of $\lesssim 1$ cm render it plausible that Hyperion might not be uniformly covered in dust, though the mechanism for segregating dark material to the bottoms of Hyperion's ubiquitous sharp-edged craters as

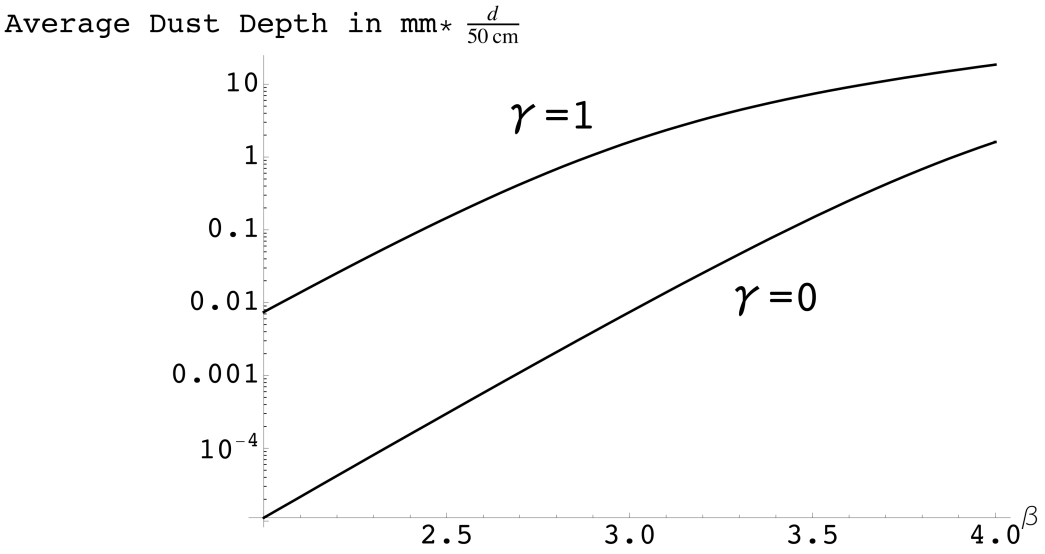

Figure 2.21: Average dust depth on Hyperion (in mm) vs power-law index β, for the limiting cases of $\gamma = 0$ (bottom curve) and 1 (top curve).

is observed remains unclear (Cruikshank et al. 2007). Constraints on the particle size distribution in the Phoebe ring from future observations may narrow estimates of the material delivered to Hyperion.

2.5.3 Titan

As discussed in Sec. 2.4, Titan's much larger cross-section causes it to efficiently sweep up almost everything that crosses its orbit. The slow inward migration of dust particles $\gtrsim 10\mu$m gives Iapetus enough time to collect most of them before they become Titan-crossing; our numerical simulations of Sec. 2, however, indicate that $\sim 70\%$ of 5μm particles strike Titan (and that smaller particles are so affected by radiation pressure that they either strike Saturn in the first half-

Saturn year or escape the system). As in the case with Iapetus, particles will strike Titan on its leading side; however, its atmosphere will distribute material around the entire moon and will fragment particles upon entry.

Using Cassini's measurements, Porco et al. (2005) report a detached haze layer at 500-km altitude on Titan. Since the sedimentation time in this layer is short, some process must continually replenish particles. Two hypotheses have been proposed (Tomasko and West 2009): the layer either represents a condensation region at a local temperature minimum (Liang et al. 2007) or occurs where aerosols produced at higher altitudes settle(Lavvas et al. 2009).

While this haze layer is likely due to the above-mentioned atmospheric effects, we can explore whether exogenous dust-infall might also be a significant contributor. We therefore derive the volume of particles striking Titan as we did for Hyperion (Eq. 2.41) assuming a present rate of dust production that is constant in time ($\gamma = 1$). Fig. 2.22 shows the results, expressed as a mass flux computed ~ 500 km above the Titan surface (i.e., $R = 3100$ km).

The calculated mass flux falls well short of the estimated 2.7-4.6 $\times 10^{-14}$ g cm^{-2} s^{-1} (Lavvas et al. 2009) required to replenish particles. Fortunately, the mechanisms listed above seem sufficient for explaining the haze layer (R. A. West, personal communication, 2010).

2.6 Conclusion

Our results show that out of the dust particles collisionally generated at Phoebe that are long-lived (grains $\gtrsim 5\mu$m), most larger than $\sim 10\mu$m will strike Iapetus

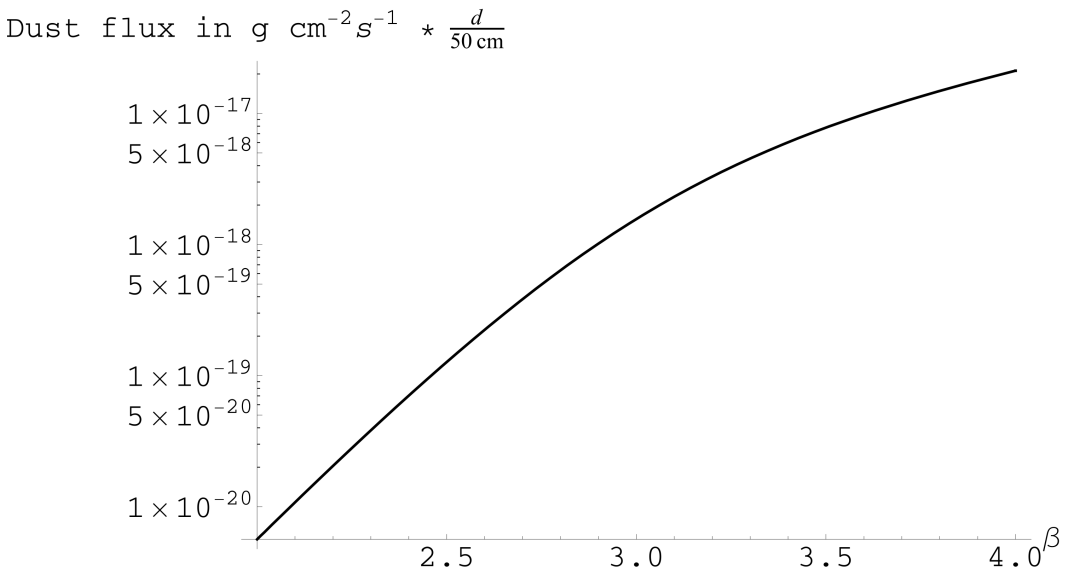

Figure 2.22: Dust flux into the Titan atmosphere at 500 km altitude (in $g cm^{-2} s^{-1}$) vs. power-law index β for the limiting case of $\gamma = 1$.

due to modifications of their orbits by perturbations from the Sun. The latter include Poynting-Robertson drag, solar radiation pressure and the Sun's tidal gravity in the Saturn system.

Our computed dust coverage on the Iapetus surface matches up well with the newly discovered color dichotomy on Iapetus that extends up to the poles (Denk et al. 2010). The calculated distribution also traces the shape of Cassini Regio well in the longitudinal direction, but realistic thermal modeling is required to explain both the bright poles and the sharp boundaries between bright and dark material.

Our orbital calculations for 10μm particles show that dust launched from other retrograde outer irregular satellites can have comparable likelihoods of striking Iapetus to those of dust launched from Phoebe. We argue this can con-

tribute to the differing spectra between Phoebe and Iapetus; however, the question of how much dust was generated by Phoebe relative to the other irregular satellites is still unclear.

By tracking the dust that strikes Hyperion, we find that just a veneer should have been laid down on its surface ($\lesssim$ 1 cm on average). This picture may be consistent with the observation that the surface is not uniformly coated. Cruikshank et al. (2007) and Thomas et al. (2007) find the dark material to be predominantly at the bottoms of Hyperion's ubiquitous cup-like craters. As opposed to Iapetus, which is tidally locked, Hyperion rotates chaotically, which can explain the presence of dark material throughout the surface.

We determine that effectively all long-lived dust particles that avoid Iapetus (i.e., a fraction of those between $\sim$ 5 and 10μm) are swept up by Titan. While these constitute a considerable mass flux into the Titan atmosphere, they are insufficient to account for the satellite's detached haze layer.

CHAPTER 3

FIRST OBSERVATIONS OF THE PHOEBE RING IN OPTICAL LIGHT

3.1 Introduction

Despite the present day's drastically reduced collision frequencies between irregular satellites, Verbiscer et al. (2009) discovered a vast dust disk around Saturn with the Spitzer Space Telescope. The height of a collisionally generated disk should correspond to its parent moon's vertical orbital excursions (e.g., Burns et al. 1999), and the disk's height of ≈ 40 Saturnian radii (R_S) implicates the largest irregular satellite Phoebe as the source (Verbiscer et al. 2009); however, other smaller satellites that also orbit close to Saturn's orbital plane may also contribute. This "Phoebe ring" is extremely diffuse, with a normal optical depth of $\sim 2 \times 10^{-8}$. Nevertheless, it provides an invaluable opportunity for understanding these circumplanetary debris disks. The Wide-field Infrared Survey Explorer (WISE) mission has recently obtained a more complete map of the Phoebe ring's emission at a similar wavelength (band 4, centered at 22 μm) as the 24-μm band on the Multi-Band Imaging Photometer aboard Spitzer (Skrutskie et al. 2011). However, more measurements at widely spaced wavelengths are needed to constrain the dust grains' properties, such as their wavelength-dependent albedo and emissivity. Tamayo et al. (2012a) observed the Phoebe ring with the Herschel Space Observatory at 70 and 130 μm; unfortunately, due to scattered light from Saturn, we were only able to set upper limits. In this paper we report the results from our efforts at shorter optical wavelengths. This is challenging because at these higher energies one measures sunlight scattered by dust into the detector, and one expects dust grains derived from Phoebe to ab-

sorb most of the incoming light given the parent moon's low geometric albedo of ≈ 0.085 across the visible spectrum (Miller et al. 2011). This strongly attenuates an already weak signal.

We executed the observations with the Imaging Science System's (ISS) Wide-Angle Camera (WAC) aboard the Cassini spacecraft, which has a unique vantage point as it orbits about Saturn. Relative to observations from Earth, this has the obvious advantage of placing the detector ~ 300 times closer to the target. However, this also implies that from Cassini's location, the full height of the Phoebe ring subtends $\approx 20^\circ$ in the sky. Thus, the debris disk presents a constant background of scattered light across the detector's field of view that cannot be directly measured. We circumvented this problem by exploiting the shadow cast by Saturn (and its dense rings), which extends behind the planet in a quasi-cylindrical tube. By capturing the full width of the shadow within a WAC field of view, we measured the scattered light *missing* from the region receiving no sunlight, thus indirectly probing the dust content.

3.2 Methods

3.2.1 Overview

As summarized above, we aim to measure the reduction in flux from the Phoebe ring region lying in Saturn's shadow, relative to the background. The quasi-cylindrical shadow cast by Saturn and its rings pierces the Phoebe ring on the side opposite the Sun, and its full width ($\approx 1^\circ$) can be contained in a single WAC field of view ($3.5^\circ \times 3.5^\circ$). We acquired 33 220-second WAC exposures

using clear filters (band centered at 635 nm Porco et al. 2004). All images were aimed at the same star field, capturing the section of the shadow from $\approx$ 130 R_S to $\approx$ 300 R_S from Saturn (for details of the data set see Sec. 3.2.2). Different pixels in the resulting image represent different lines of sight emanating from the detector that have different pathlengths through the shadow tube (see Fig. 3.1). Assuming a constant distribution of dust along the shadow, pixels should register a diminished flux in proportion to their associated pathlengths through the shadow. This approximation of constant dust density should be valid in the direction perpendicular to the tube's axis, as the shadow's transverse dimensions are much smaller than those of the Phoebe ring. The magnitude of the radial variation is not well constrained, though the measurements by Verbiscer et al. (2009) show the infrared flux is nearly constant on scales of tens of R_S, at least in the range 130-180 R_S from the planet (see their Fig. 3), so we proceed under this assumption for this initial study. By measuring the rate at which the flux decreases with increasing pathlength through the shadow, we thus probe the dust content along the tube, together with grain properties like the albedo and phase function. For details of how we determined the pathlengths through the shadow that correspond to each pixel, see Sec. 3.2.3. For an example of an image's modeled pathlengths, and thus of the signature we seek, see the bottom left panel of Fig. 3.2.

The sought signal is fainter than that from any ring yet detected in the Solar System. To motivate our detailed modeling and data analysis below, we first roughly estimate the expected brightness differences between shadowed and non-shadowed regions. We express all our data as values of I/F, which measures the specific intensity received at the detector relative to the incident solar flux at the Phoebe ring, such that an ideal, diffusely reflective surface would

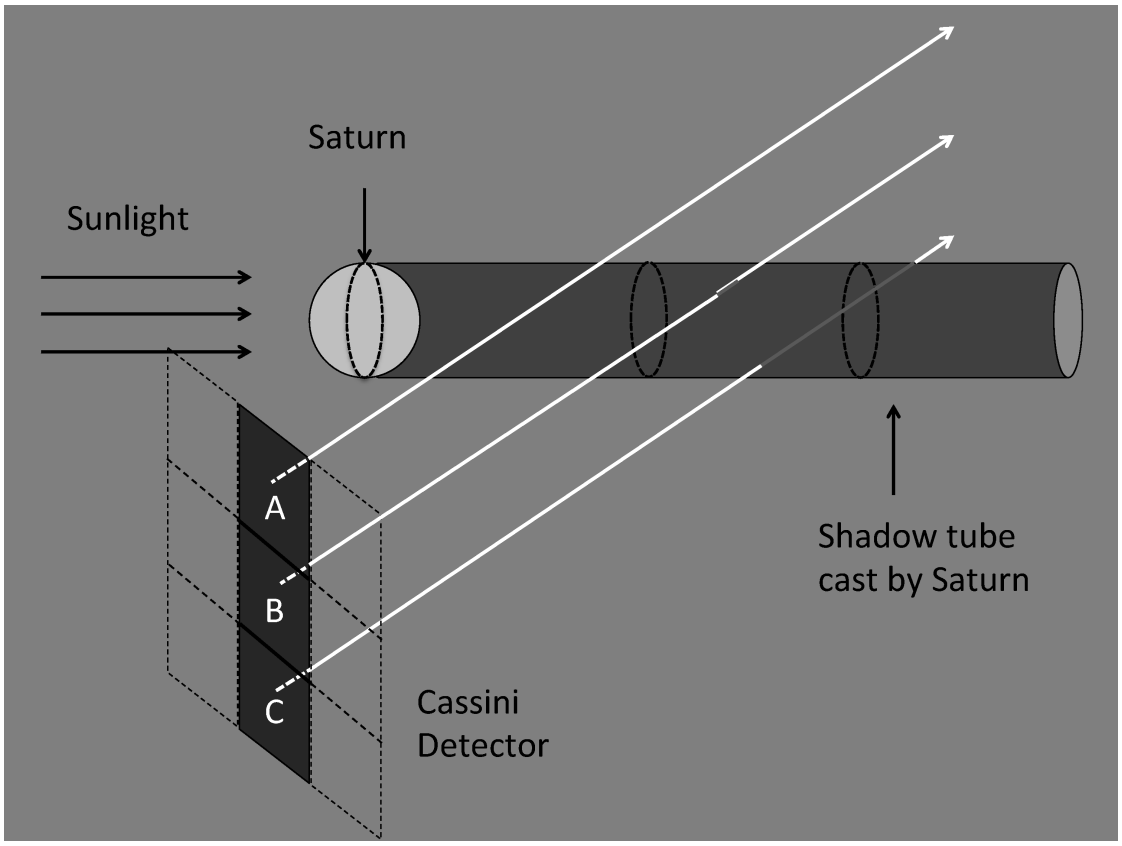

Figure 3.1: The shadow cast by the Saturn system (rings not shown) extends in a quasi-cylindrical tube behind the planet. Different pixels on the Cassini detector correspond to different lines of sight, shown in white. As drawn, the line of sight from pixel A misses the shadow tube completely. B grazes the shadow, so this pixel is only missing the scattered light from a short section of dust and should thus only show a slight brightness decrease relative to A. C has the longest pathlength through the shadow and should therefore be darkest. For clarity, the pixel sizes have been exaggerated and the number of pixels has been reduced. The distances and angles in the diagram are not to scale.

yield an I/F of unity.

We want to consider the photons that dust particles in the shadow tube *would* scatter into the detector were they not in shadow. Our pathlengths through the tube ($\lesssim 20R_S$) are comparable to the ring's height ($\approx 40R_S$), so we take the area filling-factor of dust grains along our line of sight to be roughly the ring's normal optical depth $\tau \sim 10^{-8}$ (Verbiscer et al. 2009). The I/F removed by the shadow is then roughly the product of the particles' albedo and this area filling-factor. Estimating an albedo ~ 0.1 (Phoebe's geometric albedo is ≈ 0.08, Simonelli et al. 1999), yields an I/F $\sim 10^{-10}$. To put this into perspective, typical I/F values measured from Saturn's extremely faint G-ring (undiscovered until the Voyager flybys) are three orders of magnitude larger than this.

Standard image processing techniques will fail to extract such a weak signal. We designed our observations to exploit the fact that, over the $\approx$ 12 hours of data collection, the spacecraft's motion causes the shadow to shift position on the field of view by a few tens of pixels, while the stars remain fixed. By filtering out faulty/noisy pixels (see Sec. 3.2.2) and then subtracting images, we attenuated the much brighter and complex background while retaining a signal from the shifted shadow (see Fig. 3.2). Rather than arbitrarily choosing one of our images as the reference for subtraction, we generated a mean image from our 33 files and subtracted this average field from each of our images.

We thus obtain 33 images with the mean field removed, like the one shown in the top right panel of Fig. 3.2. For each image we also calculate the signature expected from the shadow, i.e., the associated pathlength differences for each pixel (inverted since longer pathlengths through the shadow should yield darker pixels—see the bottom left panel of Fig. 3.2 for an example). Details of

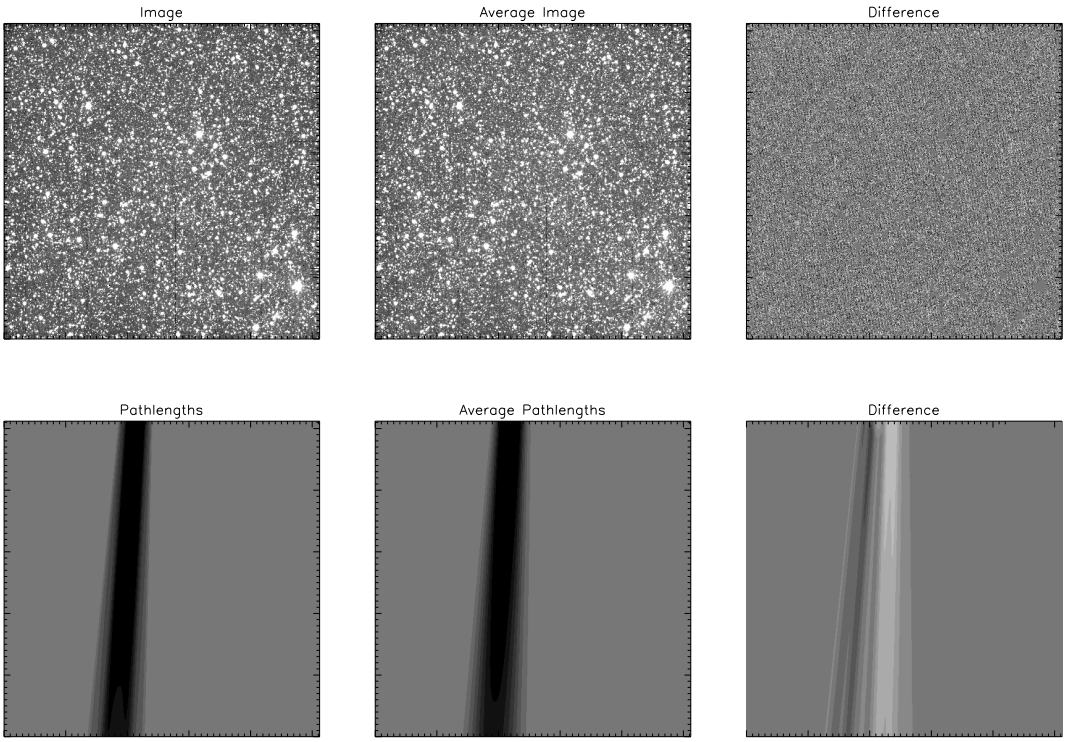

Figure 3.2: From left to right, the top row of panels shows one of our images, the mean of all 33 images, and the difference between the chosen image and the average (after applying the filtering process described in Sec. 3.2.2 and setting flagged pixels to zero). The grayscale in the first two images represents an I/F range of $[0, 10^{-7}]$, while the difference image is stretched an order of magnitude further, spanning $[-10^{-8}, 10^{8}]$. The subtraction reduces the background level substantially, though a signature is still not discernible by eye. By zooming in on the top right panel in the electronic version, one can see the filtered pixels in gray, mostly at locations corresponding to stars. The panels in the bottom row show the modeled pathlengths corresponding to the panels immediately above them (with the color scale inverted to reflect the fact that longer paths through the shadow should appear dark). The grayscale range for the pathlength plots is $[-30R_S, 30R_S]$.

this modeling can be found in Sec. 3.2.3. The signature expected in images that have had the mean field removed from them (bottom right panel of Fig. 3.2) is then simply the difference between the particular image's pathlength map (bottom left panel) and the mean pathlength map (bottom middle panel). Pixels with a longer path through the shadow than average should appear darker, while areas traversing less shadow should be brighter.

Even after applying the above procedure, a signal is not discernible by eye. However, we can associate a pathlength difference with the I/F measured in each pixel for all 33 images. We can then bin the $\sim$ 8 million pixels according to their associated pathlength differences, and look for a linear trend of decreasing I/F with increasing pathlength difference through the shadow. The interested reader can skip to Sec. 3.3 for our results. In the following two sections we provide details of our filtering process and shadow modeling.

We briefly mention that while our method (as we will see) allows us to extract a signal from the Phoebe ring, it imposes an important limitation. Because the shadow shifts its position between images, a given pixel whose line of sight pierces the shadow 150 R_S from Saturn in one image may cross the shadow at 165 R_S in another. This means that this pixel in the average image contains information about the shadow over a range of radial distances. This would confound our method if there were a strong radial gradient in dust concentration, as differences in I/F would no longer be solely determined by differences in path length through the shadow; they could instead reflect variations in the density of dust. In particular, our method is not well-suited for cases with edges, and WISE images reveal that the Phoebe ring extends to $\sim 270R_S$ (Hamilton et al. 2012). The radial range in our images varies, but extends from $\approx 130 - 300R_S$.

To avoid complicated edge effects, we therefore only used the half of each of our images that pointed closest to the planet in our analysis. This corresponds to a maximum radial distance from Saturn of $\approx 210 R_S$.

3.2.2 Filtering faulty/noisy pixels

On day 85 of 2012 (March 25$^{\text{th}}$), in Rev 163 (Cassini's 164$^{\text{th}}$ orbit about Saturn), we obtained 33 220-second WAC exposures over $\approx$ 12 hours, all aimed at right ascension (RA) $= 210.6^\circ$, declination (Dec) $= -7.75^\circ$[1] This pointing captured a section of Saturn's shadow tube $\approx 130 - 300 R_S$ from the planet while retaining the same star field across images (see Figs. 3.1 and 3.2). The data were collected in 2x2 summation mode, yielding images with 512x512 pixels. As a result, each of our image pixels subtends 1.2×10^{-4} rad on a side. We calibrated our images using the standard Cassini ISS Calibration (CISSCAL) routines (Porco et al. 2004; West et al. 2010) to remove instrumental effects, apply flat field corrections and convert the raw data to values of I/F.

Because the sought signal is so faint, it is crucial to pre-process the data to remove noisy pixels and cosmic rays. After using the CISSCAL calibration routines, we first scanned through each pixel in our 512x512 array and, for a given pixel location, examined the sample of values across our 33 collected images. We flagged pixels to be discarded if any of the following conditions were met: (1) the pixel lies on the border of the array, (2) the mean I/F across images was

[1]Image names W1711398010_1, W1711399340_1, W1711400670_1, W1711402000_1, W1711403330_1, W1711404660_1, W1711405990_1, W1711407320_1, W1711408650_1, W1711409980_1, W1711411310_1, W1711412640_1, W1711413970_1, W1711415300_1, W1711416630_1, W1711417960_1, W1711419290_1, W1711420620_1, W1711421950_1, W1711423280_1, W1711424610_1, W1711425940_1, W1711427270_1, W1711428600_1, W1711429930_1, W1711431260_1, W1711432590_1, W1711433920_1, W1711435250_1, W1711436580_1, W1711437910_1, W1711439240_1 and W1711440570_1.

less than 0, (3) any of the 33 values was exactly 0, (4) the mean I/F was above a specified brightness threshold. Condition (1) was implemented since edge pixels are known to misbehave. This removed 0.8% of our pixels. Condition (2) removes hot pixels that induce errors in the flat-field correction, and disqualified 0.5% of pixels. Several horizontal and vertical lines of zero-value pixels could be seen in our images, so we flagged these through condition (3), removing 0.2% of pixels. Finally, brighter pixels (in the proximity of stars in the field) have larger dispersions (across the 33 images), in part due to pointing jitter. We therefore tried a variety of brightness thresholds for condition (4) to optimize the tradeoff between maximizing the number of pixels retained and minimizing the average noise per pixel; we found that a threshold I/F of 6×10^{-8} yielded the lowest χ^2 values in our fits (see Sec. 3.3). This reduced the average pixel's standard deviation across images by a factor of 6.4, while flagging 20.2% of pixels. If we instead chose thresholds of 4×10^{-8} and 8×10^{-8}, this changed our result (the value of the slope we quote in Sec. 3.3) by less than 3%.

Since we point at a constant RA/Dec, we expect each pixel to exhibit a gaussian distribution about a well-defined mean across our 33 images. This spatial redundancy can be exploited to remove non-statistical outliers like cosmic rays. Using only pixels that were not flagged in the first step described in the previous paragraph, we first calculated the standard deviation across our 33 images at each pixel location. We then removed the largest absolute value from the sample, and recalculated the standard deviation. If the standard deviation changed by more than 20%, we flagged the anomalous pixel, and retained the rest. We then repeated the process until removing the largest value kept the standard deviation within 20%. The largest number of such iterations required by a pixel in our dataset was 11; however, if a pixel required more than 5 iterations, we

flagged the pixel as problematic over all 33 images. This removed an additional 1.7% of pixels. Choosing instead standard deviation thresholds of 10% and 30% change our results (the value of the slope we quote in Sec. 3.3) by less than 4%.

Given our sample of $\sim$ 8 million pixels, one would expect no pixels beyond six standard deviations if the distribution was Gaussian. Therefore, as a final step, we removed pixels with absolute values greater than six times our final distribution's standard deviation. There were 320 such pixels in our data, which represent $\approx 4 \times 10^{-3}\%$ of the total. In total, our combined filtering process removed 23.5% of pixels.

Figure 3.3 compares the distribution of brightnesses in our differenced images before and after applying our filtering process. Both panels include the best-fit gaussian distribution, shown as a dashed line. The pre-filter histogram (left) exhibits a substantial tail at negative values (removed by our brightness threshold), as well as an overabundance of values close to zero due to faulty pixels. The accompanying fit also appears skewed due to the presence of outliers at large positive values. The right panel plots the results after filtering. We obtain a gaussian distribution about zero that cannot be visually distinguished from the histogram. The filtered distribution is both tighter and taller because an average image is recomputed after removing problematic pixels that previously skewed the means. Upon subtracting this refined average field from each of the images, pixels have values closer to zero.

One might worry that as the shadow moves through our 33 images, a pixel which is in shadow in some images but not others might have a high dispersion and be unwittingly flagged by our filtering process. In fact, the expected lost signal due to the shadow is much smaller (a few times 10^{-10}) than the standard

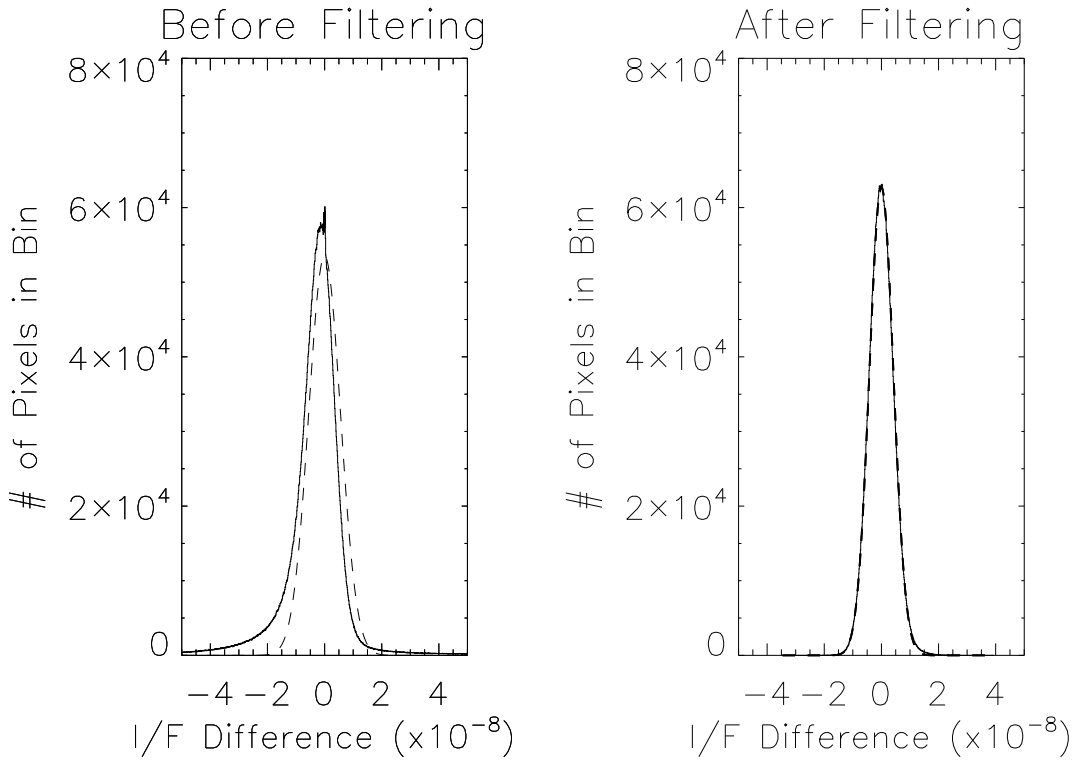

Figure 3.3: Left panel shows the distribution of I/F values in pixels from subtracted images with no filtering applied. The dashed line shows the best-fit gaussian to the data. Right panel shows results after filtering. The best-fit gaussian distribution is also plotted, but is visually indistinguishable from the data. The bin size is 10^{-10}.

deviation of the distribution (4.27×10^{-9}), so this is not an issue. For stronger signals, our procedure would have to be modified.

3.2.3 Modeling the Shadow

We begin by defining our variables and coordinate system. Let the shadowing function S be the fraction of the Sun's disk that is occluded by Saturn and its rings. This function will vary from 0 outside the shadow to 1 inside the umbra,

taking on intermediate values in the penumbra. We define a coordinate system centered on Saturn where $\hat{\mathbf{x}}$ points away from the Sun along the Sun-Saturn line, $\hat{\mathbf{z}}$ lies along Saturn's orbit normal, and $\hat{\mathbf{y}}$ completes a right-handed triad (Fig. 3.4a). In this frame tied to the Sun-Saturn line, the shadow cast by Saturn and its rings only varies with the Saturnian seasons, owing to the changing cross-section that the planet and annuli present to the Sun's rays. During our 12-hour observation, the shadow is effectively constant.

We then consider an arbitrary observer with coordinates (x, y, z). The shadowing function $S(x, y, z)$ is then given by the fraction of the solar disk occluded by Saturn at each position (x, y, z). We calculated S on a 1001×1001 pixel grid in the $y - z$ plane spanning 5 R_S in order to capture Saturn's A and B rings. We lightened the computational load along the x axis by noting that the shadow varies slowly in this direction over the distance range of interest of $120 - 300 R_S$. We therefore calculated the shadowing function only every 5 R_S along the x axis, yielding a $1001 \times 1001 \times 37$ grid. For a given x is it easiest to calculate the shadowing function in angular space, yielding $S(x, \theta_y, \theta_z)$, where $\theta_y \approx y/x$ and $\theta_z \approx z/x$ (see Fig. 3.4a).

As the observer moves to different values of (θ_y, θ_z), the angular position of Saturn will vary relative to the fixed stars. By contrast, the Sun is far enough away that the parallax effect is negligible given our effective pixel size of 1.2×10^{-4} rad. We therefore define a local coordinate system $(\hat{x}', \hat{y}', \hat{z}')$ at (x, y, z) with reference axes parallel to our previous ones centered on Saturn (see Fig. 3.4a). For all observers that we consider, then, the Sun lies along the $-\hat{x}'$ direction. We could construct a spherical coordinate system with the pole along the $-x'$ axis, but because θ_y and θ_z are small, we can approximate the problem in flat space,

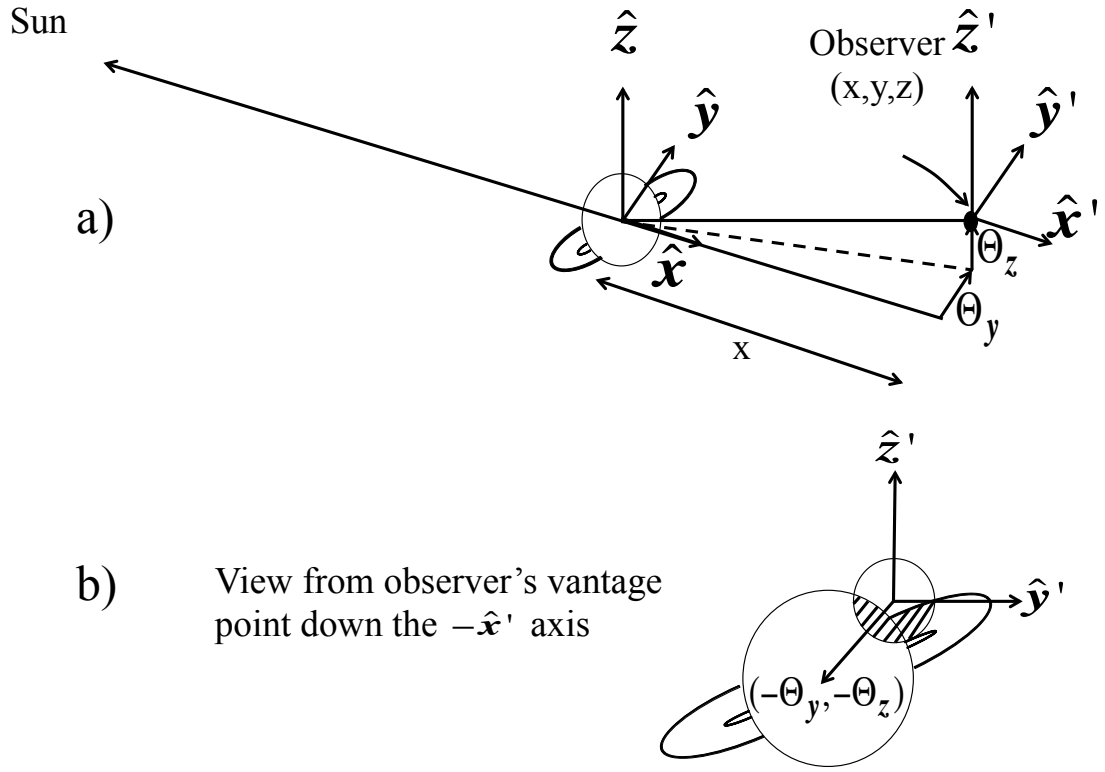

Figure 3.4: a) The geometry for an observer at position (x, y, z) (or angular coordinates (θ_y, θ_z) at distance x). The diagram is not drawn to scale. We construct a set of axes centered on the observer's position parallel to our coordinate system defined at Saturn (see text). b) The view, looking down the $-\hat{\mathbf{x}}'$ axis, from the observer's location. The Sun is far enough that the parallax effect is negligible, so it appears centered at the origin. The observer's displacement from the Sun-Saturn line causes Saturn's apparent angular position to shift by $(-\theta_y, -\theta_z) \approx (-y/x, -z/x)$. We calculate the shadowing function $S(x, \theta_y, \theta_z)$ by deriving the fraction of the Sun's disk that is occluded by Saturn and its rings at each observer location, e.g., the shaded region in b).

treating θ_y and θ_z as linear distances in the $y - z$ plane. Saturn, then, will be centered at $(-\theta_y, -\theta_z)$, see Fig. 3.4b.

To obtain $S(x, \theta_y, \theta_z)$, we then calculate the fraction of the Sun's disk that is

blocked by Saturn. We define a function $\odot(\theta'_y, \theta'_z)$ with value unity inside the solar disk (assumed uniform and circular) and 0 outside, and a similar function $♄(x, \theta'_y, \theta'_z)$ with value unity inside the cross-section of Saturn and its rings. As opposed to the Sun's angular size, which does not change appreciably as we vary x over the range of interest, Saturn's angular size will change substantially, so ♄ is a function of x. To calculate $S(x, \theta_y, \theta_z)$, we then simply offset $♄(x, \theta'_y, \theta'_z)$ by $(-\theta_y, -\theta_z)$, point-wise multiply $\odot$ and ♄, and integrate over all of (θ'_y, θ'_z) space (See Fig. 3.4b). Recalling that all angles are being approximated as linear distances in flat space, and expressing S as the fraction of the solar disk that is occluded,

$$S(x, \theta_y, \theta_z) = \frac{1}{A_\odot} \int \odot(\theta'_y, \theta'_z) ♄(\theta'_y + \theta_y, \theta'_z + \theta_z) d\theta'_y d\theta'_z, \tag{3.1}$$

where $A_\odot$ is the area of the Sun's disk, or $\pi {\theta_\odot}^2$, with $\theta_\odot$ the Sun's angular size $\approx 10^{-3}$ rad.

The computational method matches one's intuition that the umbra should narrow and the penumbra widen with increasing x. As the observer moves away from Saturn, the angular function ♄ scales as x^{-1}. Thus, as x increases, Saturn's angular size relative to the Sun shrinks, and Saturn does not completely block the solar disk over a larger area of (θ_y, θ_z) space, i.e., the penumbra becomes larger.

Because our Sun model is symmetric, i.e., $\odot(\theta'_y, \theta'_z) = \odot(-\theta'_y, -\theta'_z)$, we can write the shadowing function as a convolution by letting $\theta'_y = -\theta'_y$ and $\theta'_z = -\theta'_z$:

$$\begin{aligned} S(x, \theta_y, \theta_z) &= \frac{1}{A_\odot} \int \odot(-\theta'_y, -\theta'_z) ♄(\theta_y - \theta'_y, \theta_z - \theta'_z) d\theta'_y d\theta'_z & (3.2) \\ &= \frac{1}{A_\odot} \int \odot(\theta'_y, \theta'_z) ♄(\theta_y - \theta'_y, \theta_z - \theta'_z) d\theta'_y d\theta'_z & (3.3) \\ &= \frac{1}{\pi {\theta_\odot}^2} \odot * ♄. & (3.4) \end{aligned}$$

We thus have a compact way of calculating S that can be immediately converted to linear coordinates through $y = x\theta_y$ and $z = x\theta_z$. For the angular function $♄(x, \theta'_y, \theta'_z)$, we modeled the planet as an oblate spheroid, and included the A and B rings, assuming them to be perfectly opaque. We calculated the appropriate cross-section of our Saturn-system model perpendicular to the Sun-Saturn line using the Navigation and Ancillary Information Facility (NAIF) SPICE toolkit (Acton 1996).

We now briefly estimate the error on S. If the Sun were a point source, S would always be 0 or 1. Thus, the error on S in the penumbra is fundamentally set by our pixel size's ability to resolve the solar disk. The solar disk is spanned by $\approx$ 10 pixels, so the error in S is $\sim$ 10%. This base limitation allows us to ignore several complications not discussed above. We found that the following effects are unimportant at the 10% level: aberration of light, light travel time, atmospheric deviations in Saturn's shape from an oblate spheroid, the slight variations in the Saturn system's cross-section as viewed from different positions in our grid (x, y, z), and the fact that the A ring is slightly transmissive at the relevant incidence angle.

With our 3-dimensional model in hand, we then proceeded to calculate the pathlengths through the shadow for the various lines of sight corresponding to each of the pixels in our images. We first geometrically navigated the images using the stars in the field, and then calculated the RA/Dec coordinates for each of our pixels. Finally, for each pixel, we numerically integrated S along the line of sight to yield the associated pathlength through the shadow, generating 512x512 arrays like the ones displayed on the bottom row of Fig. 3.2.

3.3 Results

After the pre-processing described above, we bin our sample of $\approx$ 3.3 million surviving pixels according to their associated pathlengths through the shadow. Fig. 3.5 plots the mean value in each bin, with their associated standard errors. As can be surmised from the bottom panels of Fig. 3.2, most pixels ($\approx$ 2.5 million) correspond to lines of sight that do not pierce the shadow. This explains the extremely tight error bar on the zero bin. The bins from $\approx$ -10 to 10 R_S have $\sim 10^4$ values, thus improving on the error per pixel by a factor of $\sim$ Sqrt(10^4), and explaining why a clear signal is seen in the binned data despite the signature not being discernible in the images (Fig. 3.2).

As expected, there is a definite trend toward lower I/F values with increasing pathlength through the shadow. The best-fit slope is $m = -1.7 \pm 0.1 \times 10^{-11}/R_S$. The absolute value of this rate can be more straightforwardly interpreted as the I/F generated by dust grains in the Phoebe ring per R_S of the line-of-sight distance through the disk.

The reduced χ^2 from the fit is 1.38, with 26 degrees of freedom, so to be conservative we quote our statistical error on the slope multiplied by a factor of the square root of the reduced χ^2. We attribute this high χ^2 to radial variations in dust concentration along the shadow tube, which our simple model assumes do not exist. This is a difficult problem to disentangle. Since Cassini resides close to the planet ($\sim 20R_S$) and the Phoebe ring is far ($\sim 200R_S$), we are looking nearly down the axis of the shadow. While this helps to extract the exceedingly faint signal by providing longer lines of sight through the shadow, it also causes the loss of radial information since each pixel samples a column of dust over

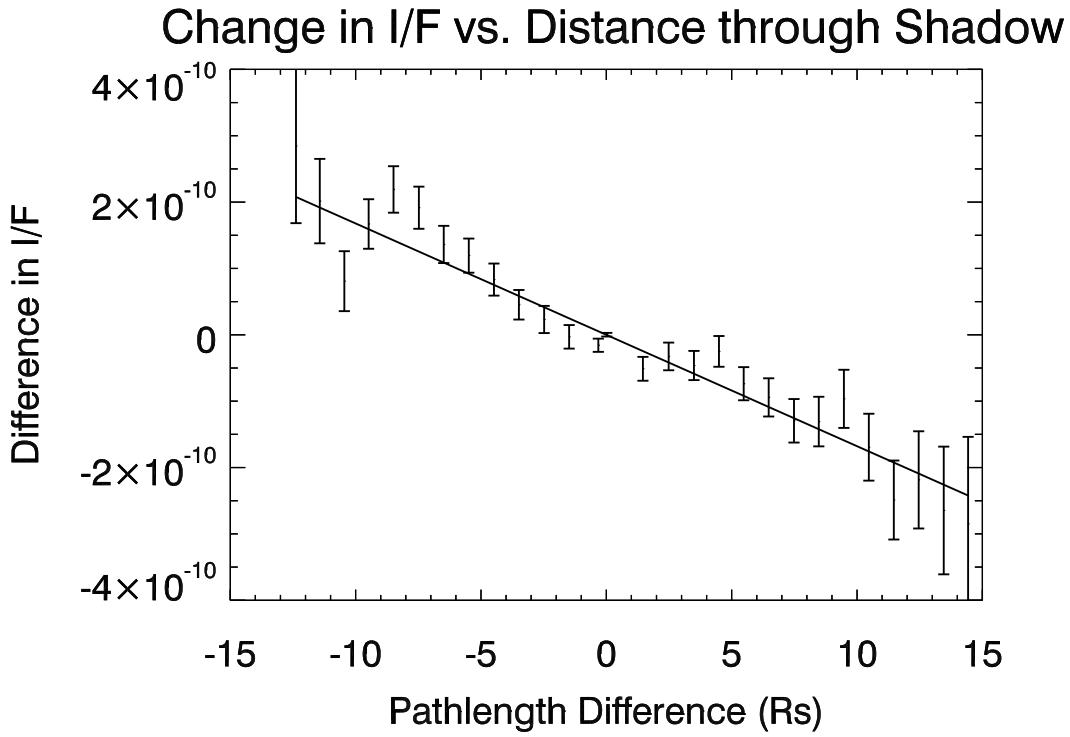

Figure 3.5: Differences in I/F vs. differences in pathlength through the shadow. As expected, pixels that see through more of the shadow than average have lower I/F values than pixels that see through less. The best-fit slope of a linear fit is $m = -1.7 \pm 0.1 \times 10^{-11}/R_S$. The reduced χ^2 is 1.38 with 26 degrees of freedom. We attribute this high χ^2 value to radial gradients in dust concentration in the Phoebe ring.

a range of distances from Saturn $\sim 20R_S$ long. Furthermore, as discussed in the previous section, by subtracting images from one another to attenuate the bright background, we sometimes compare measurements from radii varying by as much as $40R_S$.

To validate the robustness of our result, we perform the same analysis, but with the shadow model (see Fig. 3.2) offset to the right by 200 pixels—where, of course, there is no shadow. In this case we expect to see no correlation be-

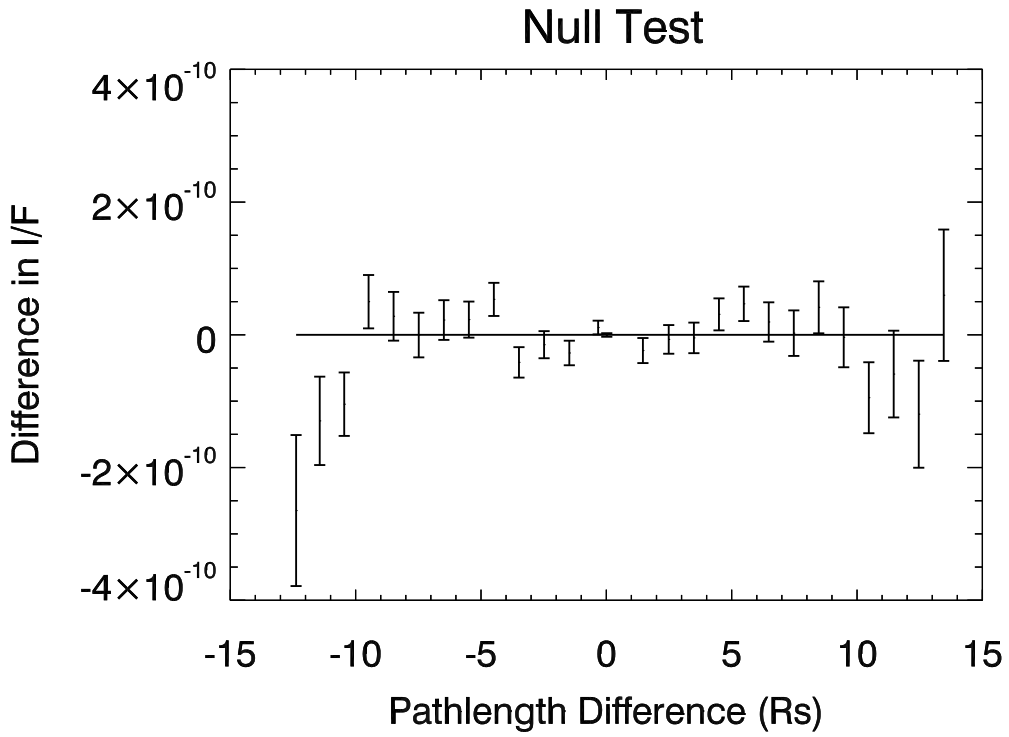

Figure 3.6: Null test performing the same analysis that led to Fig. 3.5, but with the shadow model offset by 200 pixels. As expected, there is no correlation in I/F deviations with pathlength differences through the incorrectly placed shadow model. A constant-value hypothesis provides the best reduced χ^2, and a linear fit gives a slope consistent with zero.

tween our modeled pathlengths and the measured deviations in I/F, as all the dust in this section of the field of view is in full sunlight. Figure 3.6 shows the analogous plot to Fig. 3.5. The reduced χ^2 for a constant-value model is 1.68 with 27 degrees of freedom, and a linear fit gives a slope consistent with zero (and a slightly higher reduced χ^2). We again attribute the correlated variations to radial gradients in the dust concentration that similarly affect our method in this part of the ring under full sunlight.

Since our shadow grid is only determined to within a pixel, we estimate the

systematic uncertainty in our modeling by offsetting the calculated pathlengths (bottom left panel of Fig. 3.2) by one pixel (along each of eight possible directions) and recalculating the slope from Fig. 3.5. The mean slope across these analyses is $m = -1.7 \times 10^{-11}/R_S$, identical to the value found above. The standard deviation is less than 1%, implying that pointing and modeling uncertainties do not dominate our errors.

3.3.1 Photometry

In order to estimate the disk's optical depth, Verbiscer et al. (2009) had to make assumptions about the Phoebe-ring grains' particle-size distribution, albedos, and emissivities. Our new measurement at optical wavelengths still leaves the problem underdetermined, but we can combine the optical and infrared data to place rough constraints on the particles' light-scattering properties. Since we only observe sunlight scattered almost directly backward at a Sun-ring-observer angle, or phase angle, of $\alpha \approx 6^\circ$, we ignore the diffracted component of light in our subsequent analysis. Furthermore, because particles with radii $s \lesssim 5\mu$m (assuming spherical grains) are quickly removed from the Phoebe ring by radiation pressure (Tamayo et al. 2011), particles are much larger than the optical wavelengths (λ) at which we observe, so we are in the geometric optics limit. Thus, the single-scattering albedo that we determine assumes a geometric cross-section $\sigma = \pi s^2$ to calculate the power incident on dust grains, and, when accounting for the outgoing power, ignores the light that is diffracted forward (at high phase) into a cone of angular width $\approx \lambda/(2s)$.

For low optical-depth clouds, the measured I/F is related to the line-of-sight

optical depth τ and the single-scattering albedo ϖ_0 (at 0.635 μm, where our band is centered) through

$$\frac{I}{F} = \frac{1}{4}\tau\varpi_0 P(\alpha), \tag{3.5}$$

where $P(\alpha)$ is the phase function (e.g., Burns et al. 2001). Since we are in the geometric optics limit, τ is a geometrical optical depth and, for low τ, is approximately the area filling-factor of dust along the line of sight. In our observations we obtain the differential change in I/F with distance, so we write $d\tau = \eta\, dl$, where dl is a differential length element along the line of sight and η is given by

$$\eta = \int n\sigma ds, \tag{3.6}$$

with $n\, ds$ the number density of dust grains with physical radii between s and $s + ds$ and σ the geometrical cross-section πs^2. We thus obtain

$$m \equiv \frac{d(I/F)}{dl} = \frac{\eta\varpi_0 P(\alpha)}{4}, \tag{3.7}$$

where m is our measured slope of $m = -1.7 \pm 0.1 \times 10^{-11}/R_S$.

In the case of the Spitzer observations at 24 μm, where one observes the grains' thermal emission, the particle sizes become important. A spherical blackbody in the Phoebe ring would have an equilibrium temperature of $\approx$ 90K and emit $\approx$ 90% of its energy in the wavelength range $\lambda = 10 - 100\mu$m. For typical particle-size distributions, one mostly observes the smallest grains (in this case $s \sim 5\mu$m) that dominate the population's surface area. Thus, the dimensionless parameter $X = 2\pi s/\lambda \sim 1$ over the wavelength range in which blackbody grains would preferentially emit, so real particles will have difficulty releasing energy at these long wavelengths. These small grains must therefore heat up beyond their equilibrium blackbody temperatures in order to release the energy they absorb.

Given our limited data, we follow the simple model of Verbiscer et al. (2009) using a constant infrared emissivity ϵ. Energy balance then requires

$$\pi F \pi s^2 (1 - A) = 4\pi s^2 \epsilon \sigma_B T^4, \tag{3.8}$$

where πF is the solar flux at Saturn, σ_B is the Stefan-Boltzmann constant, T is the equilibrium grain temperature, and A is the bolometric Bond albedo, which is integrated over all phase angles and wavelengths, and weighted by the solar spectrum. Since the solar spectrum peaks in the optical, and Phoebe's geometric albedo is flat across the visible spectrum (Miller et al. 2011), we can reasonably approximate the bolometric Bond albedo by the Bond albedo at 635 nm, where our observing band is centered. We can then relate A to the single-scattering albedo ϖ_0 through $A = \varpi_0 P(0) q/4$, where q is the phase integral. Rearranging Eq. 3.8,

$$T = \left(\frac{\pi F (1 - A)}{4 \epsilon \sigma_B} \right)^{\frac{1}{4}}. \tag{3.9}$$

The corresponding emission at Spitzer's 24 μm band is $\epsilon B_\nu(24\mu\text{m}, T)$, where B_ν is the Planck function. The ratio of the observed intensity with Spitzer to ϵB_ν then gives the area filling-factor of dust grains along the line of sight, or the geometrical optical depth τ. If we assume that the number density of dust grains does not vary within the Phoebe ring (the same assumption used in our above analysis), then $\tau = \eta L$, where L is the total pathlength through the disk. Given the Phoebe ring extends to $\sim 270 R_S$ (Hamilton et al. 2012), the Spitzer observations that pierce the disk edge-on at $\approx 150 R_S$ imply $L \sim 400 R_S$. Combining the above relations we obtain

$$\eta = \frac{I_{Sp}}{\epsilon B_\nu(T) L}, \tag{3.10}$$

where I_{Sp} is the intensity measured by Spitzer, and T is given by Eq. 3.9. Finally,

plugging η into Eq. 3.7 and rearranging we have

$$4\epsilon m L \frac{B_\nu(T)}{I_{Sp} P(\alpha)} = \varpi_0, \tag{3.11}$$

where T depends on ϖ_0 implicitly through Eq. 3.9.

If we treat Phoebe ring particles as isotropic scatterers ($P(\alpha) = 1$), the above relations are simplified, since in this case $A = \varpi_0$. If like Verbiscer et al. (2009) we then assume $\epsilon = 0.8$, we obtain $\varpi_0 \approx 0.2$. If instead we vary ϵ from 0.1-1, and L from $350 - 450 R_S$, ϖ_0 ranges from ≈ 0.2 (high emissivity, low pathlength) to $\approx$ 0.3 (low emissivity, high pathlength). This range is higher than the corresponding values inferred for Phoebe regolith particles from photometric modeling of Phoebe observations at 0.48 μm (Simonelli et al. 1999) and 0.9-1.4 μm (Buratti et al. 2008), which both yielded $\varpi_0 \approx 0.07$.

Several possibilities could account for this discrepancy. The assumption that particles are roughly isotropic scatterers is plausible. If one ignores the diffracted component of light (which causes the phase functions of small grains to rise at high phase angles), Pollack and Cuzzi (1980) found that irregularly shaped dust grains have approximately flat phase functions, and empirical fits to the phase function of particles in Saturn's faint G-ring also yield roughly isotropic scatterers (M.M. Hedman, 2013, private communication). If this accurately represents Phoebe ring particles, our high single-scattering albedo may point to the impacts that generated the disk having excavated brighter, subsurface material. Indeed, high-resolution images taken during the Phoebe flyby as Cassini approached Saturn reveal bright material lining crater walls (Porco et al. 2005). Buratti et al. (2008) report I/F values at 0.9 μm 4-5 times larger for the bright material relative to the predominantly dark surface. Further photometric modeling is required to quantitatively compare the bright material's surface re-

flectance with the single-scattering albedo of the regolith particles that make it up.

Alternatively, if the dust's phase function were not flat, but instead rose at small phase angles, our assumption above of isotropic particles would cause us to infer an artificially high single-scattering albedo, as our measurement at low phase would represent more than its fair share of the total scattered light. For example, if we assume a Henyey-Greenstein function (Henyey and Greenstein 1941) with parameter g = -0.35 (back-scattering), which in a Hapke model can reproduce Phoebe's photometry (Miller et al. 2011), we find $\varpi_0 \approx 0.06$ (taking the above nominal values of $\epsilon = 0.8$ and $L = 400\ R_S$). This is consistent with the modeled regolith albedo of $\varpi_0 \approx 0.07$ found by Simonelli et al. (1999) and Buratti et al. (2008).

Another possibility is that photometric model fits like those used in the above-quoted studies to obtain $\varpi_0 \approx 0.07$ do not accurately reproduce the light-scattering properties of the grains that form the Phoebe ring. Laboratory experiments by Shepard and Helfenstein (2007) show that Hapke models cannot reliably be used to uniquely infer regolith properties; however, they found that the single-scattering albedo of regolith particles is the most robust parameter extracted. It is therefore unlikely that this could fully account for the difference.

Finally, it is possible that smaller, brighter, irregular satellites also contribute to the Phoebe ring. The only observable currently connecting the disk to Phoebe is its vertical extent, which matches Phoebe's vertical excursions on its orbit. However, the moons Ymir, Suttungr, Thrymr, and Greip all have comparable orbital inclinations to Phoebe and are candidate sources. However, the albedos of irregular satellites that have been measured are low (Grav et al. 2013), so,

while these moons may nevertheless contribute to the "Phoebe" ring, they seem unlikely to substantially raise its albedo.

3.4 Conclusion

We have described the first measurements of the Phoebe ring in optical light. Extracting the exceedingly faint signal (I/F variations $\sim 10^{-10}$) was only possible by subtracting multiple images of the same star field, thereby attenuating the relatively bright background while retaining a signature from Saturn's shifting shadow. A careful statistical analysis then allowed us to indirectly measure the I/F generated by scattering Phoebe-Ring dust grains per unit pathlength through the disk. We obtained a value of $m = 1.7 \pm 0.1 \times 10^{-11} R_S$; thus, for example, a line of sight 100 R_S long would generate an I/F of $\approx 1.7 \times 10^{-9}$.

In Sec. 3.3.1 we then combined our measurement with the infrared intensity measured with Spitzer (Verbiscer et al. 2009) to constrain the grain albedos. Assuming particles to be isotropic scatterers, we derive albedo values higher than those obtained from photometric models applied to observations of Phoebe (Simonelli et al. 1999; Buratti et al. 2008). This may suggest that the impact(s) that generated the Phoebe ring are excavating bright sub-surface material, as observed on some of the moon's crater walls (Porco et al. 2005). Alternatively, our measurements can be brought into agreement if the phase function of dark Phoebe ring grains follows a Henyey-Greenstein function with parameter g = -0.35, which Miller et al. (2011) used to match the photometry of Phoebe using a Hapke model. The former hypothesis may implicate one or several larger collisions in the formation of the Phoebe ring, in order to effectively sample the

sub-surface. The latter is consistent with a roughly steady state of micrometeoroid bombardment.

Our measurements spanned the range $\approx 130-210R_S$. We plan to make future measurements of the Phoebe ring closer to Saturn with Cassini, and taking a larger number of exposures. The increased signal-to-noise should allow us to generate a radial profile of the disk, which may allow us to differentiate between a steady-state model of micrometeoroid bombardment and one invoking large, stochastic impacts. This would inform our interpretation of the grain properties discussed above.

We also plan to observe both inside and outside the orbital path of the two-faced moon Iapetus (at $59R_S$), to verify whether the satellite sweeps up most of the infalling debris (Tamayo et al. 2011). This would observationally settle a puzzle that has existed since the moon's discovery over 300 years ago. It is worth noting that this measurement can presently only be made by the Cassini spacecraft, given its favorable position about Saturn. The sought signal is so faint that scattered light from the planet should preclude currently planned Earth-bound telescopes from observing it inside $\sim 60-80R_S$.

CHAPTER 4

PROBING THE PHOEBE RING'S RADIAL STRUCTURE

4.1 Introduction

After proving the efficacy of our technique for indirectly observing the Phoebe ring using Saturn's shadow (Tamayo et al. 2014), we obtained several new datasets with the Cassini spacecraft; additional observations are planned over the next two years. This chapter presents our analysis to date on these new data.

We used the same techniques described in detail in Chap. 3; however, to increase the signal to noise ratio in our data, we modified our observation strategy. First, we sought out opportunities where the spacecraft was closer to the axis of Saturn's shadow, thus enhancing the pathlengths of our lines of sight through the shadow. Additionally, we took a larger number of exposures and we added a long pause in the middle of the observation. This last modification increased the distance the shadow moves in the field of view, thus enhancing the expected brightness differences between the first and second sets of images.

As shown in Fig. 4.1, the increased signal renders the Phoebe ring signature clearly visible in our data. The top left panel shows an average of our first 25 images of the same star field, and the panel below shows a model of the expected signal attenuation along the shadow. As can be seen from the I/F ranges labeled in the panel titles, the expected brightness dip along the shadow is $\sim$ three orders of magnitude smaller than the light levels in the images. As before, to attenuate the much brighter background, we exploited the fact that the stars are effectively fixed in inertial space, while the spacecraft's motion causes

the shadow's position to shift over time (see the shadow model for the second set of 25 images in the bottom middle panel). By subtracting the two average images, we therefore could eliminate most of the background signal, but retain a characteristic signature from the shadow (bottom right panel). Upon filtering out noisy pixels (using the techniques of Tamayo et al. 2014), rebinning and smoothing the data, we obtain the top right panel.

To quantitatively analyze the signal shown in Fig. 4.1, we adopted the procedure of Tamayo et al. (2014). Figure 4.2 shows our best-fit model when we take the Phoebe ring to be spatially homogeneous, as assumed by Tamayo et al. (2014). While the homogeneous model satisfactorily fit the noisier data of Tamayo et al. (2014), we can see that the new, improved, data deviate strongly from this model, particularly at large predicted I/F differences, i.e., lines of sight that have long pathlengths through the shadow in one image but short ones in others. Plotting the difference between our subtracted image (top right panel of Fig. 4.1) and our model signature (bottom right panel of Fig. 4.1), we see in Fig. 4.2 (right panel) that, while the model roughly agrees with the data at large distances from Saturn (top of image), there are substantial deviations closer to Saturn (bottom of image). We therefore now relax the homogeneity assumption and probe the Phoebe ring's radial structure (we assume there is no azimuthal variation across the shadow as the shadow's width represents less than 1% of the ring's circumference). We note that one might expect such radial variation given the ring's expected radial extent $\sim 60 - 250 R_S$—if there were comparable amounts of material at different radii, then the number density of particles would fall as grains get spread over annuli of increasing volume. We consider this more quantitatively in Sec. 4.3.

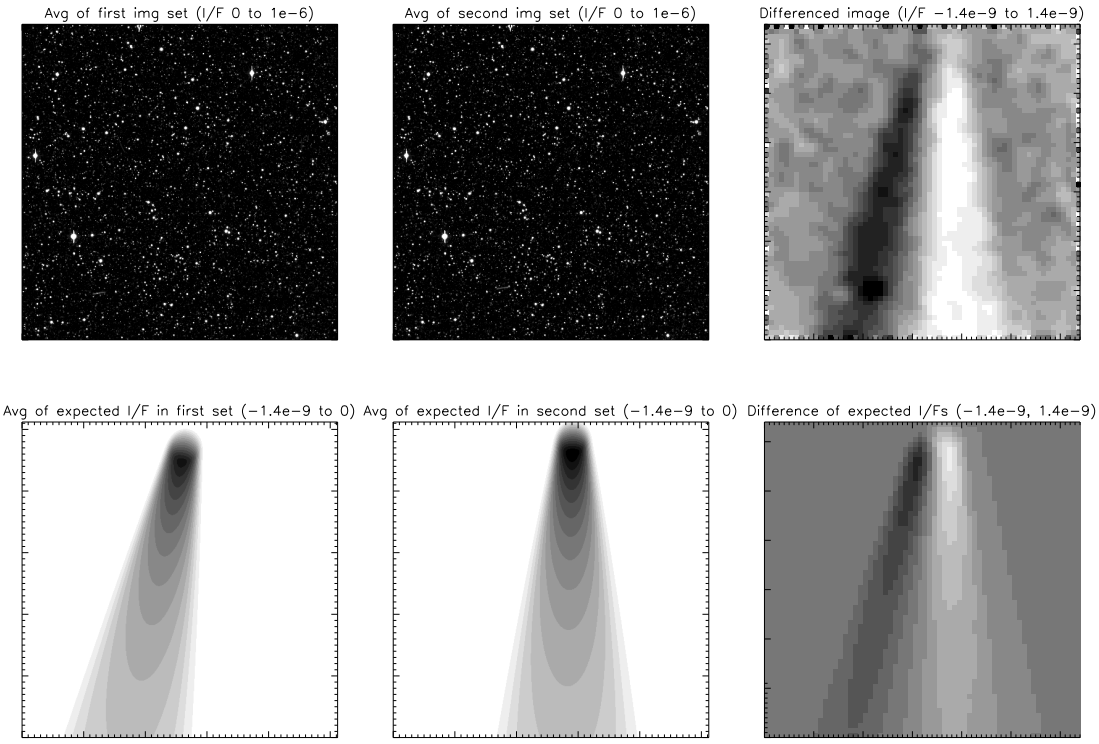

Figure 4.1: Top left and top middle panels show averages of the first 25 and second 25 images taken during our observation. The corresponding panels below show the expected dip in brightness along Saturn's shadow (note that the color scale varies by three orders of magnitude between the two, see the panel titles). By subtracting the two average images (top right panel), we attenuate the background signal while retaining the shadow signature shown in the bottom right panel. The model used to generate the predicted brightnesses in the bottom row is the best-fit model that assumes the Phoebe ring is spatially homogeneous (density does not change with distance from Saturn). The differences between the top and bottom right panels suggests the Phoebe ring is *not* homogeneous. The bright and dark spots in the central bottom part of the top right panel are the differenced signature of the irregular satellite Siarnaq, which happened to be in the field of view.

To incorporate radial structure in the Phoebe ring into our model, we no longer simply calculate the total path through the shadow. Instead, we calcu-

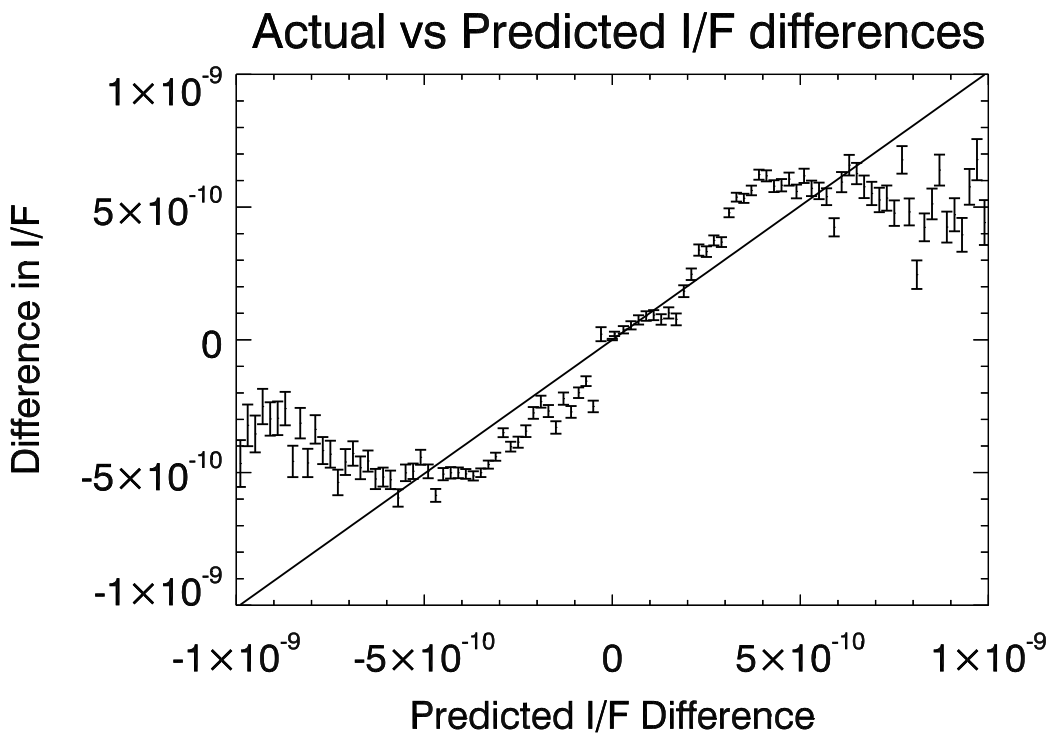

Figure 4.2: Predicted vs. observed I/F differences, assuming the best-fit spatially homogeneous model for the Phoebe ring. The strong disagreement at large I/F differences suggests the ring's radial structure is important.

late pathlengths through a suite of radial slices from Saturn. By assigning each slice its own I/F reduction per unit distance through it, m_i, we can again generate a predicted brightness difference image to compare with the observed I/F differences.

Figure 4.4 shows a model that is constant out to $130R_S$, and then falls off, following a power law with an index of negative two. This substantially improves the fit, though some obvious deviations remain.

Figure 4.5 shows the corresponding residuals for the radial profile described

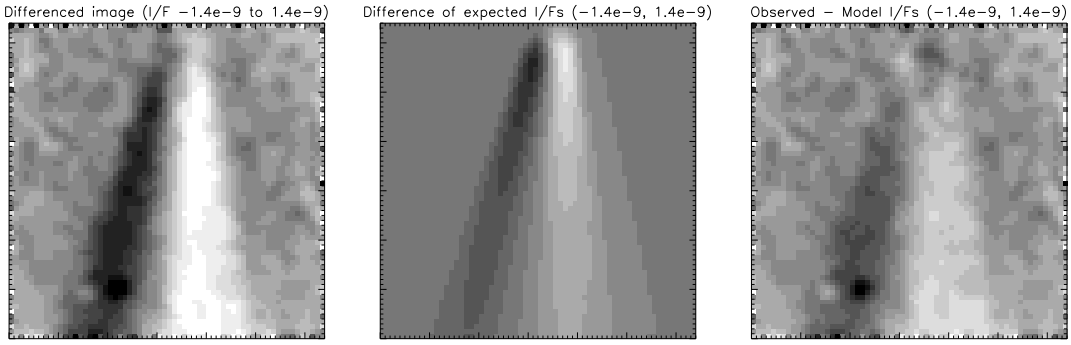

Figure 4.3: Left panel shows the real differenced data, corresponding to the top right panel of Fig. 4.1. The middle panel shows the prediction assuming the best-fit homogeneous model for the Phoebe ring, and the right panel shows the result of subtracting the middle panel from the left one. The residuals show that substantial signal remains closer to Saturn (toward the bottom of the panel).

above. This model performs substantially better (note that the image has been stretched by a factor of $\approx$ 5 relative to Fig. 4.3 to highlight differences). Some deviations are still discernible by eye, though it is possible that this is partly due to effects of the irregular satellite Siarnaq lying in the field of view (the bright and dark circles).

Future work is needed to further characterize the Phoebe ring's radial structure, which is difficult to disentangle since we look nearly down the axis of the

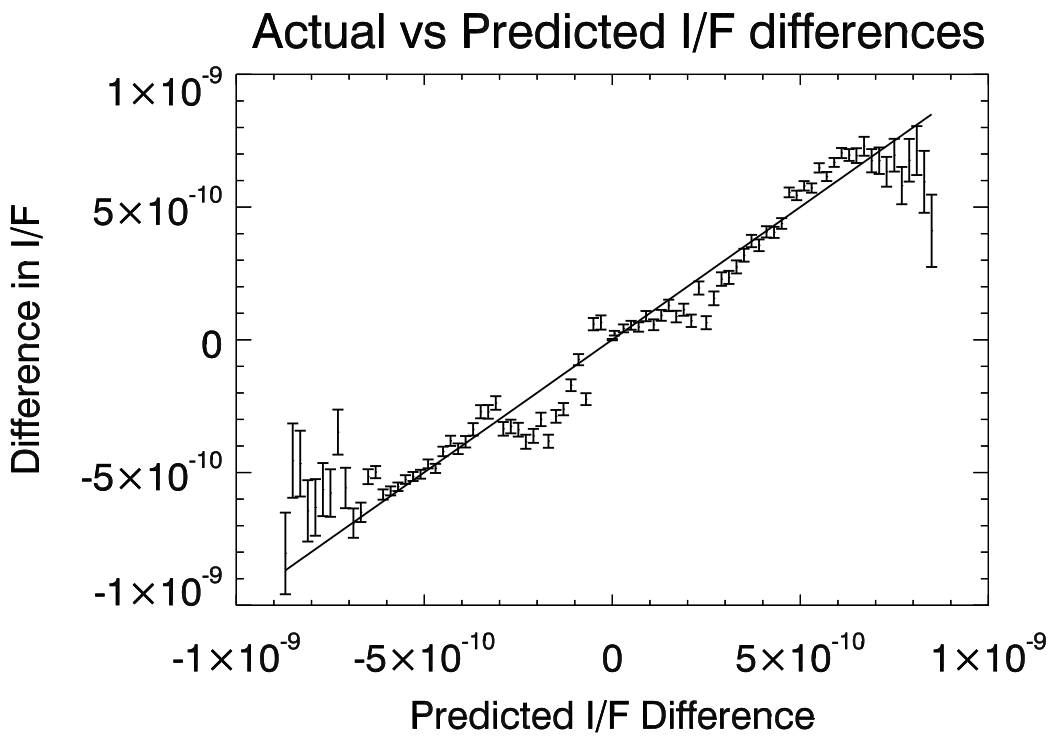

Figure 4.4: Predicted vs. observed I/F differences, assuming a constant Phoebe ring out to $130R_S$, followed by a power-law decay with index -2. This model provides an improved fit, but large deviations remain.

shadow (so we obtain an integrated measure of the amount of material present over a wide range of radii from Saturn). A more perpendicular geometry would be more favorable for detecting radial variations, but the reduced path through the shadow along each line of sight would greatly attenuate the already weak signal. We now move on to an investigation of what one might theoretically expect to observe in the data by modeling the 3-D structure of the Phoebe ring.

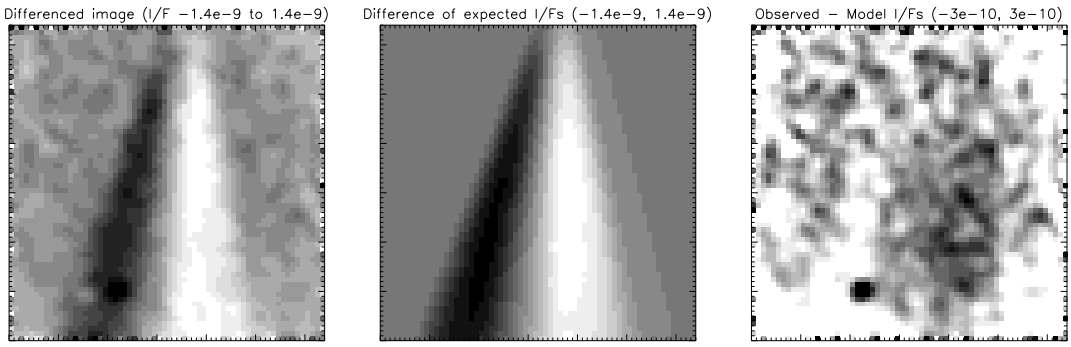

Figure 4.5: Similar to Fig. 4.3, but now the central panel assumes a radial profile that is constant out to $130R_S$, and then falls off, following a power law with an index of negative two. Note that the residuals in the right panel have a color scale that has been stretched by a factor of ≈ 5 relative to the corresponding panel in Fig. 4.3 to highlight structure (see panel titles).

4.2 Dynamics

A main goal of our observational campaign is to seek an inner edge to the Phoebe ring. As argued theoretically in Chap. 2, Iapetus should sweep up the majority of the infalling material, and finding such an inner edge would be an important verification of this model. However, an additional complication must be assessed.

The shadow cast by Saturn lies in the planet's orbital plane. But as dust grain orbits decay inward, they will follow the local equilibrium plane, which gradually shifts from Saturn's orbital to its equatorial plane (see Sec. 4.2.1). An infinitely thin Phoebe ring would therefore follow a warped surface like that shown in Fig. 4.6. The real Phoebe ring has a thickness about the equilibrium surface that is set by the orbital inclination that particles inherit from Phoebe (the thickness increases linearly with distance from Saturn, to a value of $\approx 40R_S$ at Phoebe's distance of $215R_S$). Because the ring lifts out of the plane probed by Saturn's shadow (the planet's orbital plane) as the planet is approached, it is possible that an apparently observed inner edge to the Phoebe ring using our technique may not point to Iapetus sweeping up material. Of course, in this case Iapetus might (and should) nevertheless be carving out an inner edge to the Phoebe ring; this would just occur in a plane inaccessible to our observation technique.

In order to address this issue, we now consider the dynamics of particle orbits as they decay inwards toward Saturn. We will use these results below to generate a Monte Carlo simulation of the Phoebe ring's 3-D structure. In particular, we study the evolution of dust-grain orbits under the simultaneous influence of radiation pressure, tidal solar gravity, and Saturn's oblateness. Note that we are ignoring the gravity of Iapetus, which could alter the dynamics at semimajor axes where the orbital periods of the particle and Iapetus form a near-integer ratio. In addition, we approximate Saturn's orbit as circular.

To make analytic progress, we assume that the evolutions of the eccentricity and the inclination are decoupled. In particular, we calculate the inclination evolution assuming a circular orbit, and evaluate the eccentricity evolution as-

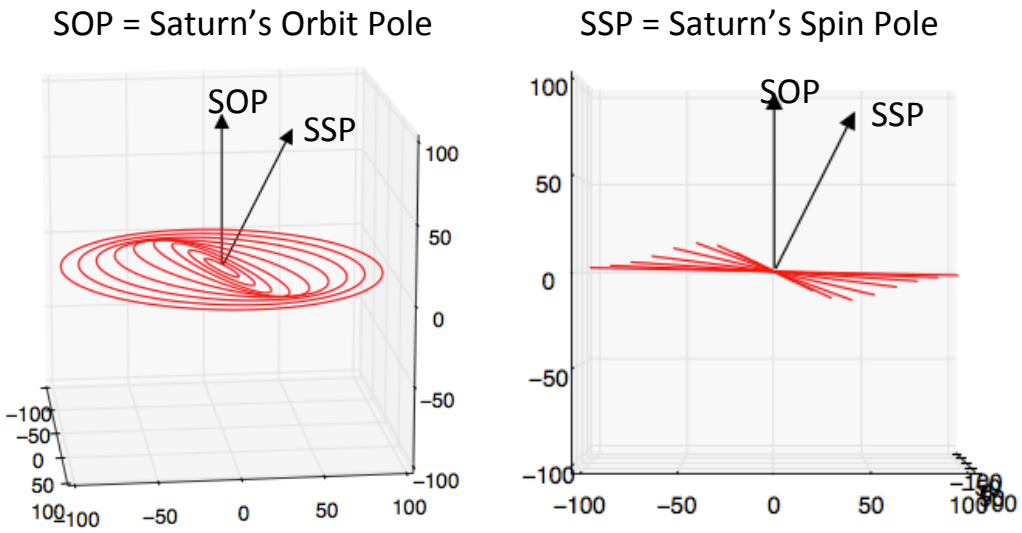

Figure 4.6: On the left is an oblique view from above of the warped equilibrium surface that an infinitely thin Phoebe ring would follow. On the right is an edge-on view. The horizontal plane in the edge-on view corresponds to Saturn's orbital plane, which is the plane in which Saturn casts its shadow. If Phoebe-ring material were spread evenly from Phoebe to the central planet, our method would observe an inner edge to the ring due to material tilting off the plane that is probed by Saturn's shadow. The only exception would be if the Sun happened to be aligned with the line along which Saturn's orbit plane intersects its equatorial plane (vantage point shown in right panel)—along this line, material would extend inward to the planet; however, in our data, the Sun lies at about 49° from this line of nodes. All distances are in Saturn radii.

suming a planar orbit. This amounts to ignoring second-order eccentricity terms in the equations of motion for the inclination evolution and vice-versa. These assumptions are only rigorously correct for circular orbits around a planet with

zero obliquity (so that all perturbations act in the same plane); however, they are reasonable approximations as long as the planet's obliquity is not too large (Saturn's obliquity $\approx 26.7^\circ$) and the orbital eccentricities are moderate. We will compare our analytic results to direct integrations below.

4.2.1 Inclination Evolution

Because, under the perturbations stated above, the inclination evolution is slow compared to both the particle's orbital timescale around Saturn and Saturn's orbital period about the Sun, one can profitably average over these fast oscillations. When considering only the effects of the quadrupole potentials from the planet's oblateness and the Sun's gravity, one then obtains the classical result that, for a given circumplanetary orbit's semimajor axis, an equilibrium plane exists between the planet's equatorial and orbital planes. Particle orbits in this so-called Laplace plane remain in the plane (in this sense it is an equilibrium plane), whereas inclined orbits will precess around the Laplace plane normal (see Fig. 5.1). The local Laplace plane represents a compromise between the oblateness perturbations that dominate close to the host planet and are symmetric about its equatorial plane, and the solar perturbations that dominate far out and are symmetric about the planet's orbital plane. Thus, the local Laplace plane nearly coincides with the planet's orbital plane for distant particle orbits (e.g., those of the irregular satellites), while progressively smaller orbits have their respective Laplace planes transition toward the planet's equatorial plane (see Fig. 4.6). The shift between these configurations occurs at approximately the Laplace radius r_L, where the torques from the two perturbations roughly balance (Goldreich 1966)

$$r_L{}^5 \approx 2J_2 R_p{}^2 a_p{}^3 (1 - e_p^2)^{3/2} \frac{M_p}{M_\odot}, \tag{4.1}$$

where J_2 is the quadrupole coefficient from an axisymmetric expansion of the planet's gravitational potential, R_p, M_p, a_p and e_p are the planet's radius, mass, orbital semimajor axis and eccentricity, respectively, and $M_\odot$ is the Sun's mass. Considering the contribution of the inner satellites to Saturn's effective J_2, r_L at Saturn is $\approx 55 R_S$ (Tremaine et al. 2009); Iapetus, at $59 R_S$, has a mean orbital plane set by the local Laplace plane's inclination to Saturn's orbital plane of $\approx 11.5^\circ$..

The inclusion of radiation pressure (which is symmetric about the planet's orbital plane) shifts the balance between the planet's oblateness and solar gravity. Because radiation-pressure induced precession of retrograde orbits opposes solar gravity precession, this is equivalent to a weakened effective solar gravity. Thus, for retrograde orbits, the transition of the equilibrium plane from the planet's orbital to equatorial planes occurs outside the classical Laplace radius given by Eq. 5.6. Conversely, radiation pressure enhances the solar-gravity induced precession of prograde orbits, so the transition radius moves inward (Tamayo et al. 2013a). Additionally, because radiation pressure is particle-size dependent, the local Laplace planes for grains of different sizes will vary.

Recently, Rosengren and Scheeres (2014) have performed a rigorous analysis of Laplace plane equilibria modified by radiation pressure. In Sec. 4.3 we use their Eq. 32 to calculate the equilibrium Laplace plane orientation for a given particle orbit's semimajor axis and particle radius.

4.2.2 Eccentricity Evolution

We now consider the evolution of the orbital eccentricity, assuming a planar orbit around a planet with zero obliquity (we will compare our results to direct integrations with a tilted Saturn below). As opposed to the orbital inclination, the orbital eccentricity of small grains will undergo large-amplitude oscillations over a single Saturn year (Burns et al. 1979). Moreover, such retrograde particle orbits that are begun on near-circular orbits will reach their maximum eccentricities when their pericenter is aligned with Saturn's shadow (where we make our observations). It is therefore important not to average over Saturn's orbit about the Sun in this application (but we still average over the much faster particle orbit around Saturn).

Hamilton and Krivov (1996) have studied this problem for prograde orbits. We now take their prograde solutions and apply symmetry arguments to derive the equations of motion for retrograde orbits.

In a frame centered on Saturn, the equations of motion for a prograde orbit can be written as

$$\begin{aligned} \frac{1}{n_\odot}\frac{d\varpi}{dt} &= A\sqrt{1-e^2}[1+5\cos 2(\varpi-\lambda_\odot)] + C\frac{\sqrt{1-e^2}}{e}\cos(\varpi-\lambda_\odot) + \frac{W}{(\sqrt{1-e^2})^2}, \\ \frac{1}{n_\odot}\frac{de}{dt} &= 5Ae\sqrt{1-e^2}\sin 2(\varpi-\lambda_\odot) + C\sqrt{1-e^2}\sin(\varpi-\lambda_\odot), \end{aligned} \tag{4.2}$$

where e is the particle's orbital eccentricity, ϖ is the longitude of the grain orbit's pericenter, $\lambda_\odot$ is the longitude of the Sun as it "orbits" around Saturn in the saturnocentric frame, $n_\odot$ is the Sun's angular rate, and A, C and W are constants capturing the strength of the sun's tidal gravity, radiation pressure, and

the planet's oblateness, respectively:

$$A \equiv \frac{3}{4}\frac{n_\odot}{n}, \qquad C \equiv \frac{3}{2}\frac{n}{n_\odot}\sigma, \qquad W \equiv \frac{3}{2}J_2\left(\frac{R_p}{a}\right)^2\frac{n}{n_\odot}, \tag{4.3}$$

where n is the particle's mean motion, a is the particle orbit's semimajor axis, and σ is the ratio of the radiation pressure force to the gravitational force of the planet on the body at a distance a[1].

The key idea is that a retrograde orbit is prograde in a frame where time runs backward, so we can immediately write down the equations of motion from Eq. 4.2 in this flipped frame. To be pedantic, we can write dt as dt^- to emphasize that it represents time in the flipped frame, and we can then obtain the equations of motion for a retrograde orbit in a frame where time runs forward by re-expressing the equations of motion in terms of the original variable t (through the simple relation $dt^- = -dt$). Note that in applications with non-zero inclination one must be careful to also write i^-, ϖ^- etc. when applying the prograde equations of motion and then re-express these in terms of i, ϖ etc. This is because when flipping the time, $i \to 180 - i$, the ascending node changes by 180°, and $\varpi = \Omega + \omega \to \Omega - \omega$.

Additionally, one might be tempted to write $\lambda_\odot = n_\odot t$ in Eq. 4.2, and have it flip sign upon these transformations; however, in the flipped frame the Sun moves backwards at a rate $-n_\odot t$, so one would write the equations in the flipped frame with terms involving, $\varpi + n_\odot t^-$, which would revert to $\varpi - n_\odot t$ when re-expressed in the original frame. Physically, the relevant terms in the differential equations only depend on the instantaneous position of the Sun, $\lambda_\odot$, not the direction in which it is moving, which is why we chose to write the right-hand sides of Eq. 4.2 in terms of $\lambda_\odot$.

[1] see Eq. 3 of Hamilton and Krivov (1996)

The above steps yield retrograde equations of motion with the signs on the right-hand sides of Eq. 4.2 negated. Following Hamilton and Krivov (1996), we now move to a frame where the x axis rotates with the Sun at a rate $n_\odot t$ so that the potential is stationary, as this will yield a conserved quantity. Note that this would not be true for a planet on an eccentric orbit (as the Sun would no longer "move" at a constant rate), or if the obliquity were nonzero (as the oblateness potential would become time-dependent). Denoting the longitude of pericenter relative to the Sun's position $\phi_\odot = \varpi - \lambda_\odot$, and plugging in for $d\varpi/dt$ from Eq. 4.2, we have the equations of motion for a retrograde orbit,

$$\begin{aligned} \frac{1}{n_\odot}\frac{d\phi_\odot}{dt} = \frac{1}{n_\odot}\frac{d\varpi}{dt} - 1 &= -A\sqrt{1-e^2}[1+5\cos 2(\phi_\odot)] - C\frac{\sqrt{1-e^2}}{e}\cos(\phi_\odot) - \frac{W}{(\sqrt{1-e^2})^2} - 1, \\ \frac{1}{n_\odot}\frac{de}{dt} &= -5Ae\sqrt{1-e^2}\sin 2(\phi_\odot) - C\sqrt{1-e^2}\sin(\phi_\odot). \end{aligned} \tag{4.4}$$

Following Hamilton and Krivov (1996), we can write these equations of motion using the semi-canonical equations

$$\frac{1}{n_\odot}\frac{de}{dt} = -\frac{\sqrt{1-e^2}}{e}\frac{\partial \mathcal{H}}{\partial \phi_\odot}, \qquad \frac{1}{n_\odot}\frac{d\phi_\odot}{dt} = \frac{\sqrt{1-e^2}}{e}\frac{\partial \mathcal{H}}{\partial e} \tag{4.5}$$

from a conserved "Hamiltonian"

$$\mathcal{H} = \sqrt{1-e^2} - \frac{1}{2}Ae^2[1+5\cos(2\phi_\odot)] - Ce\cos\phi_\odot - \frac{W}{3(1-e^2)^{3/2}}; \tag{4.6}$$

cf. Eq. 9 in Hamilton and Krivov (1996). Trajectories in this one degree-of-freedom problem thus move on level curves of constant $\mathcal{H}$.

Figure 4.7 compares these results to two direct integrations that include Saturn's obliquity and its orbital eccentricity. In both integrations, the particle were launched such that their orbits' pericenters coincided with the direction toward the Sun at $t = 0$, and both simulations were run for 100 years (i.e., more than

three Saturn orbits, and $\sim$ 7000 particle orbits (left panels) and $\sim$ 400 particle orbits (right panels). The top panels show the evolution of e and $\phi_\odot$ in polar plots, where the radial distance gives the eccentricity, and the angle from the positive x axis gives $\phi_\odot$. The top left panels is for a 2μm grain in an orbit with $a = 10R_S$ and initial eccentricity 0.3, in Saturn's equatorial plane (which is effectively coincident with the local Laplace plane at this semimajor axis). Despite the large eccentricities (reaching values greater than 0.5), the agreement is excellent. The bottom left panel shows the corresponding evolution of $\mathcal{H}$ (Eq. 4.6), which we verify is conserved to well within 1%.

The right panels are for a 20μm in an orbit with $a = 50R_S$, initial orbital eccentricity 0.156, and initial orbital inclination to Saturn's orbital plane of 165°, roughly half way between the orbital and equatorial planes. These values were chosen as representative of the grains we wish to simulate, at the point where our neglect of the coupling between eccentricity and inclination is most problematic; Phoebe's eccentricity (which grains are expected to inherit) is currently 0.156, and grains smaller than $\sim$ 3μm would be quickly eliminated by radiation pressure upon being liberated from Phoebe (Verbiscer et al. 2009). Again, the agreement is excellent, so we conclude that our analytic model is sufficient for analyzing the orbits of most grain sizes in the Phoebe ring size distribution. One should keep in mind, however, that the orbits of the smallest particles that survive immediate elimination by radiation pressure may exhibit important deviations from our results.

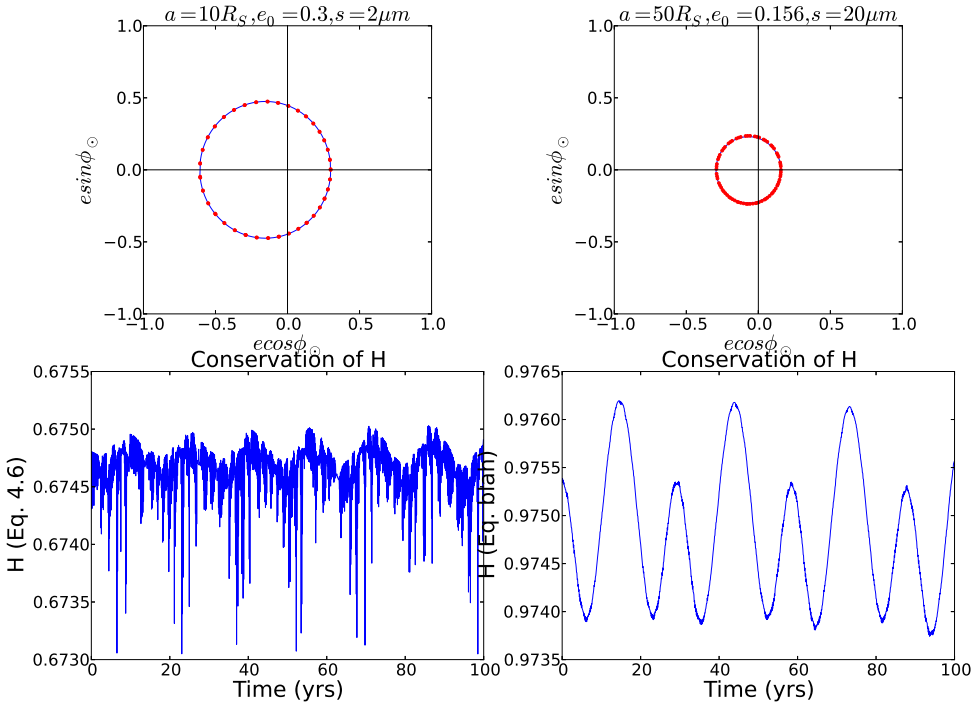

Figure 4.7: Top panels show comparisons of our analytical level curves (blue, calculated with Eq. 4.6) assuming a zero-obliquity planet in a circular orbit, and direct integrations (red) with Saturn's present eccentricity and obliquity. The discrete red points in the top left panel are due to a near integer ratio between the rate at which the orbit moves around the level curve, and the rate at which the integration was sampled. See text for the parameters of the two integrations. The bottom two panels show that $\mathcal{H}$ is conserved to within 1%.

4.3 Monte Carlo Simulations

With an approximate analytical model in hand, we can efficiently generate a Monte Carlo simulation of the Phoebe ring where we randomly sample particle positions in their orbital evolution, and see how many particles lie in Saturn's shadow at various radial distances from the planet. First we must connect our

model to the photometry.

For low optical depth clouds like the Phoebe ring, the I/F scattered by ring particles is related to the line-of-sight optical depth τ, the phase function $P(\alpha)$, and the single-scattering albedo ϖ_0 (at 0.635 μm, where our observing band is centered) through (Burns et al. 2001)

$$\frac{I}{F} = \frac{1}{4}\tau\varpi_0 P(\alpha). \tag{4.7}$$

Writing $d\tau = n\sigma dl$, where n is the number density of particles, σ is their geometrical cross-section, and dl is a differential length element along the line of sight, we define

$$m(r) \equiv \frac{d(I/F)}{dl} = \frac{n(r)\sigma\varpi_0 P(\alpha)}{4}. \tag{4.8}$$

The local quantity m thus quantifies how much I/F is gained per differential pathlength through the Phoebe ring. Since we only make measurements along Saturn's shadow, which subtends a small azimuthal angle, we take m to only be a function of the distance from the planet, r. For a given model of $m(r)$, one obtains the expected change in I/F in one of our pixels by integrating $m(r)$ along the path through the shadow.

Generalizing Eq. 4.8 to consider a range of particle sizes, we obtain that the differential contribution to m(r) from grains with radii between s and $s + ds$ is

$$dm(r,s) = \frac{\pi s^2 \varpi_0 P(\alpha) n(r,s) ds}{4}, \tag{4.9}$$

where $n(r,s)$, the differential number density for particles between size s and $s + ds$ lying between r and $r + dr$ from Saturn. It is important to consider an s-dependent $n(r,s)$, as radiation forces should lead to size-dependent radial distributions of material. The total $m(r)$ is then simply given by the integral of Eq. 4.9 over s.

We now estimate $n(r, s)$ using the results of our semi-analytical investigation of the grains' orbital dynamics from Sec. 4.2. We approximate Saturn's shadow as a rectangular prism with cross-section dimensions of $2R_S \times 2R_S$. By using radial bins of equal volume (spaced by $10R_S$), we ensure that the sought number density $n(r, s)$ is equal to the number of particles we find in each bin to within a normalization constant (which must be fit to the data anyway). We can therefore relate $dm(r, s)$ to $N(r, s)$, the number of particles in a Monte Carlo simulation lying in a radial bin centered at r, with sizes between s and $s + \Delta s$. Writing dm as Δm to emphasize the finite size of our bins, we have

$$\Delta m(r, s) \propto s^2 N(r, s) \Delta s, \tag{4.10}$$

where we have assumed that ϖ_0 and $P(\alpha)$ are the same for all particles (the phase angle α only varies by about a degree when looking at the nearest and farthest sections of the Phoebe ring).

The strengths of the various relevant perturbations vary with the particle orbits' semimajor axes, which decay according to

$$a = a_0 e^{-t/\tau_{P-R}}, \tag{4.11}$$

where a_0 is the original semimajor axis, and τ_{P-R} is the Poynting-Robertson decay timescale (Burns et al. 1979). Assuming particles share Phoebe's density of 1.6 g/cm^3,

$$\tau_{P-R} \approx \left(\frac{s}{7\mu\text{m}} \right) \text{Myr}, \tag{4.12}$$

where s is the particle radius (Tamayo et al. 2011). According to Eq. 4.11, approximately ln(215/60) Poynting-Robertson decay timescales are required for particles to approximately reach Iapetus' semimajor axis ($a \approx 60R_S$) from Phoebe ($a \approx 215R_S$). Because the semimajor axis evolution is the same for all

particle sizes if one rescales time through $t' = t/\tau_{P-R}$ (Eq. 4.11), we found it simplest to consider semimajor axes sampled at one hundred equally spaced t' intervals:

$$\Delta t' = \frac{\Delta t}{\tau_{P-R}} = \frac{\ln(215/60)}{100}, \tag{4.13}$$

where τ_{P-R} scales linearly with s (Eq. 4.12).

At each of these hundred semimajor axes, we first considered the motion of the particle's orbital angular momentum vector in a frame that uses the local Laplace plane as the reference plane (see Sec. 4.2.1). To a good approximation, the orbital angular momentum vector precesses around the Laplace plane pole at a constant angle given by the free inclination, which is an adiabatic invariant of the motion as the semimajor axis slowly decays (Ward 1981). Thus, at all semimajor axes, the free inclination is the same, and the longitude of the ascending node in this frame, Ω_{Lap}, is approximately uniformly distributed over $[0, 2\pi]$. We therefore randomly sampled Ω_{Lap}. To transform to a common reference frame for all semimajor axes (the frames coinciding with the local Laplace planes are tilted relative to one another as a varies), we calculated the inclination of the local Laplace plane to Saturn's orbit normal at each a (Rosengren and Scheeres 2014), and applied the appropriate rotation matrices.

With a, i and Ω (where orbital elements without subscripts are referenced to Saturn's orbital plane) in hand, we proceed to select the eccentricity e and argument of pericenter ω. The appropriate level curve that the eccentricity vector follows (Eq. 4.6) is set by the initial conditions. Since the escape velocity from Phoebe is small compared to its orbital velocity, and most ejecta is launched at velocities comparable to the escape speed (e.g., Farinella et al. 1993), dust grains will essentially inherit Phoebe's orbital elements at the time of impact. We set

the initial eccentricity to Phoebe's current value (which changes little) and considered eight equally spaced initial values of $\phi_\odot$ (Sec. 4.2.2).

As mentioned above, an orbit's angular momentum vector precesses with a constant free inclination about an equilibrium (the local Laplace plane's pole). Analogously, (to a good approximation) each orbit's pericenter precesses with a constant free *eccentricity* about another equilibrium (the forced eccentricity), i.e., in the polar plots in the top panels of Fig. 4.7, different initial conditions would move on level curves that to first order are concentric circles about the equilibrium forced eccentricity; the radius of the circle is then the constant free eccentricity. As in the inclination case with the shifting Laplace plane, the forced eccentricity changes as orbits decay and the relative perturbation strengths vary, and again, the free eccentricity is an adiabatic invariant as long as the semimajor-axis decay rate is slow compared to the precession timescale (which is always the case here).

For a given initial condition, we therefore first calculated the approximately conserved free eccentricity. Then, at each semimajor axis, we calculated the appropriate forced eccentricity numerically (by finding the point at which level curves collapsed to zero radius) , and randomly sampled e and $\phi_\odot$ from a uniform distribution along the perimeter of the level curve. Then, we obtained ω using the relationships $\phi_\odot \equiv \varpi - \lambda_\odot$ and $\varpi = \Omega - \omega$. Finally, we obtained the last orbital element by selecting the mean anomaly M from a uniform distribution.

With this procedure, for each of eight equally-spaced values of the initial condition for $\phi_\odot$, and for each of the hundred semimajor axis values, we obtained the orbital elements of particles, and calculated cartesian positions in a system where z points along Saturn's orbit normal, x points from Saturn to the

Sun (at the time of observation we are trying to model), and y completes a right-handed triad. In order to extract the number of particles along Saturn's shadow, we selected the particles whose positions lay inside the model shadow's rectangular prism, binned by their radial position along $-x$ in slices of length $10R_S$ from $0 - 250R_S$.

The probability of a particle's position falling inside the shadow decreases rapidly with distance from Saturn. In order to obtain reliable statistics, we therefore sampled more particles in distant orbits than in tight ones. In particular, we calculated the positions of 12500 particles for the innermost semimajor axis at $a = 60R_S$, and boosted the number of sampled particles at each semimajor axis by a factor of $(a/60R_S)^3$. For a fair comparison, when counting particles in each radial bin, we divided the number of particles from each semimajor axis by the same factor of $(a/60R_S)^3$.

We thus obtained radial distributions for each of our eight sampled particle sizes (5, 8, 20, 30, 45, 70, 100 and 1000 μm), for each of the 100 sampled semimajor axes. We denote $N(r_i, s_j, a_k)$ as the number of particles with semimajor axis a_k and size s_j that fell in the bin with radial distance r_i. The y-scale on our histograms is set by the number of particles for which we choose to calculate positions. The normalization of our histograms is thus arbitrary, but we obtain an accurate scaling with distance for each particle size.

The radial distribution of material as a function of particle size, $N(r_i, s_j)$, is then simply given by summing the contributions from each of the semimajor axes; however, knowledge of the relative amounts of material at each semimajor axis requires a model for the injection of particles into the Saturn system (which the data can then support or reject).

We consider here a steady-state model, where Phoebe is bombarded by micrometeorites at a constant rate, generating $d\dot{N}(s)$ particles with radii between s and $s + ds$ per second. In our discretized model, within a time Δt, Phoebe's semimajor axis will receive $N(a = 215R_S, s) = d\dot{N}(s) \times \Delta t$ particles. After another Δt, these particles will have moved to the next semimajor axis in (recall that our semimajor axis values were chosen to each be separated by the same Δt), and Phoebe's semimajor axis will have received a fresh set of particles. After another Δt, the chain is pushed one link further, until a steady state is reached. Thus, each *semimajor axis* (i.e., not necessarily each radius) should have the same number of particles. We can then simply build the *radial* distribution of particles of a given size $N(r_i, s_j)$ by taking the Monte Carlo simulations for grains of radius s_j, and for each radial bin adding up equal contributions of particles from each of the hundred sampled semimajor axes,

$$N(r_i, s_j) \propto \sum_k N(r_i, s_j, a_k). \tag{4.14}$$

Plugging this result into Eq. 4.10, we have

$$\Delta m(r_i, s_j) \propto \sum_k N(r_i, s_j, a_k) s_j^2 \Delta s_j. \tag{4.15}$$

Finally, to connect with the observed photometry, one must combine the $\Delta m(r_i, s_j)$ into a single $m(r_i)$ (Eq. 4.8). In addition to any intrinsic particle size distribution, because smaller particles evolve inward faster than large grains (Eq. 4.13), we must consider that a given semimajor axis will receive more small grains than large ones in a given time interval. To this end, we take the input *rate* of particles per unit time at Phoebe's semimajor axis (which is the same for all our a values in a steady state) to follow a power law distribution with index $-q$,

$$\dot{N}(s_j, a_k) \propto s_j^{-q} \Delta s_j. \tag{4.16}$$

Then, since each of our hundred sampled semimajor axes are separated by the same (size-dependent) Δt (Eq. 4.13), we can obtain the number of particles of size s_j of semimajor axis a_k $N(s_j, a_k)$ in our discretized model through

$$N(s_j, a_k) \propto \Delta t \times B s_j^{-q} \Delta s_j \propto s_j^{-(q-1)} \Delta s_j, \tag{4.17}$$

where the additional factor of s comes from the factor of τ_{P-R} (Eq. 4.11) in Δt from Eq. 4.13. Therefore, in combining particle sizes (assuming a steady state), one should weight the contribution from each grain radius by a factor $w_j = s_j^{-(q-1)} \Delta s_j$. Since w_j is independent of a we can obtain $m(r_i)$ directly from Eq. 4.15,

$$m(r_i) \propto \sum_{j=s_{min}}^{s_{max}} \Delta m(r_i, s_j) w_j \propto \sum_{j=s_{min}}^{s_{max}} \sum_k N(r_i, s_j, a_k) s^{3-q} \Delta s_j. \tag{4.18}$$

In summary, Eq. 4.18 relates the number of particles in each bin of our Monte Carlo simulations to the $m(r_i)$ that we use to convert our modeled pathlengths through each radial slice of the shadow into the expected brightness deficit in a particular pixel (see Fig. 4.1).

4.3.1 Simulation Results

Figure 4.8 shows, for different particle sizes, the profile of the number of shadowed particles in the Monte Carlo simulation as a function of radius ($N(r, s)$, Eq. 4.10). As one would expect, smaller particles are more spread out in radius, owing to their higher orbital eccentricities induced by radiation pressure. By contrast, large particles are relatively unaffected by radiation pressure and have similar distributions.

The inner edge around $65 R_S$ is due to material tilting off Saturn's orbital plane, so that the shadow no longer passes through the Phoebe ring. The re-

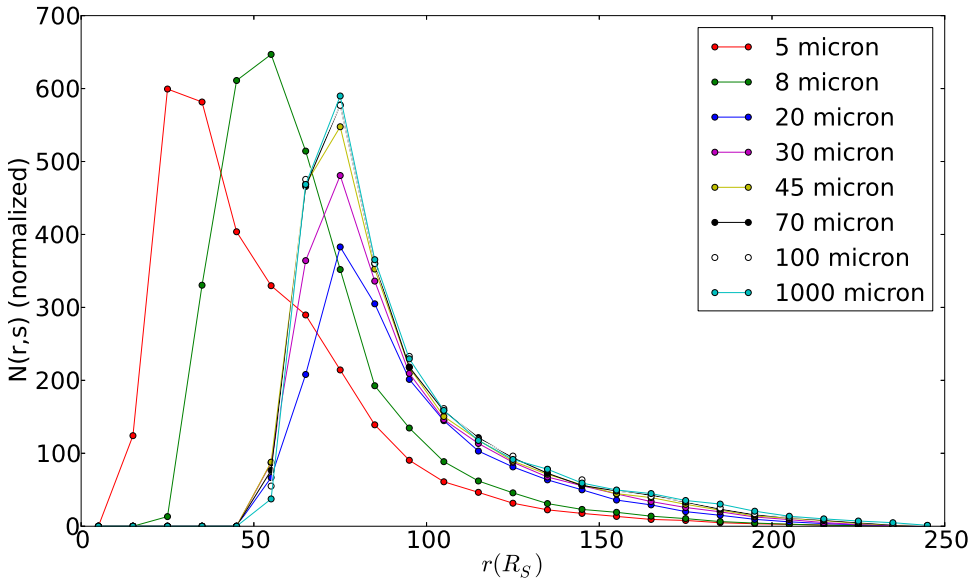

Figure 4.8: Number of shadowed particles in the Monte Carlo simulation as a function of radius, for different grain sizes. The inner edge around 65 R_S is due to material tilting off the orbital plane of Saturn, so that Saturn's shadow does not pierce it. As described in the text, particle numbers have been normalized to make up for the fact that we simulated more particles at large distances from Saturn (in order to have a similar chance of finding them in the shadow as grains on tighter orbits).

maining question is whether Iapetus would cut off the ring at larger radii than $65R_S$. As a limiting case, we imagine that Iapetus sweeps up all the material on orbits with pericenters inside Iapetus' semimajor axis (59 R_S). This is a good assumption for all but the smallest grains ($s \lesssim 10\mu m$, see Chap. 2). The result is shown in Fig. 4.9.

The inner edge resulting from the shifting Laplace plane remains in place. This suggests that our observation method will not be able to detect the true inner edge of the Phoebe ring. Nevertheless, we should extract important information. The extracted radial profile should allow us to either verify or rule out

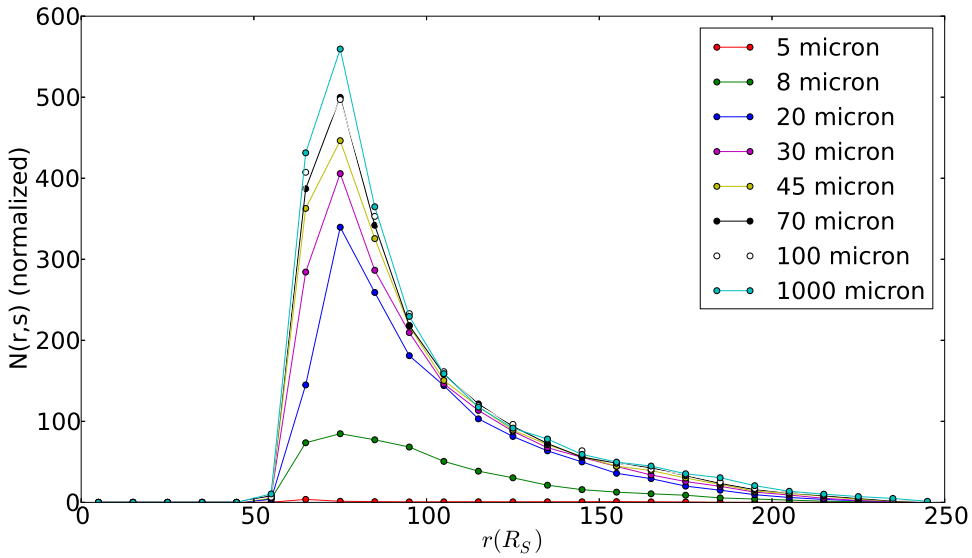

Figure 4.9: Number of shadowed particles in the Monte Carlo simulation as a function of radius, for different grain sizes. Any orbits that have pericenters interior to Iapetus' semimajor axis are removed from their respective bins.

such a steady-state model of dust production at Phoebe. If such a steady-state model prevails, that would allow us to constrain the micrometeoroid impactor population at Saturn, which was until recently poorly constrained(**?**). Alternatively, it is also possible that the Phoebe ring is instead the result of a larger isolated collision, which would result in a different radial profile depending on when in the past the impact occurred. This situation would allow us to probe the collision rates of the irregular satellites with sub-kilometer circumsaturnian bodies that current telescopes cannot detect. Future work will be directed at tackling these questions.

We can also connect these models to the data presented in Sec. 4.1. While these results are preliminary, we can make some general observations. The best-fit power law indices to the data in Figs. 4.8 are steeper (ranging from ≈ -3.7 for

the largest particles to ≈ -2.7 for 8μm grains) than the model used for Fig. 4.5 (-2); however, we find that steeper power-law fits to the data also work well (with different normalizations). We are currently working on determining the range of power law indices that we can rule out—because our method relies on looking nearly down the axis of the shadow to maximize our signal, each of our pixels registers a a "column density" of Phoebe ring material over a range of radial distances from the planet. Because we have many such pixels, we can extract some information about the radial distribution of material, but we are still characterizing how well we can resolve radial variations.

The data presented here (Sec. 4.1) only covers a radial range from $\sim 80 - 350 R_S$. As a result, we are unable to use it to probe an inner edge to the Phoebe ring. However, we have new data sets aimed closer to the planet that will help us address this question. The material presented in this chapter provides a framework for this future work.

CHAPTER 5

DYNAMICAL INSTABILITIES IN HIGH-OBLIQUITY SYSTEMS

5.1 Introduction

In this chapter I provide the theoretical framework for understanding the orbits of circum-uranian debris particles. It builds on the work of Tremaine et al. (2009) by incorporating the effects of radiation pressure. We additionally recast their work in terms of orbital elements, which makes it easier to connect the dynamics to the well studied Kozai effect, which I now introduce.

Satellites in inclined circumplanetary orbits that are subject to gravitational perturbations from the Sun can undergo large-amplitude eccentricity oscillations through the Kozai mechanism (Kozai 1962; Lidov 1962), often with catastrophic results (e.g., Carruba et al. 2002). As discussed below, such dramatic increases of eccentricity can occur as the pericenter slows its precession, allowing the solar tugs to systematically remove angular momentum from the orbit over part of the precession cycle. When the dominant perturbation is the Sun's gravity, this halting of the pericenter can only be achieved for highly inclined orbits ($\gtrsim 40^\circ$). In this paper we consider situations where additional perturbations are also important, thereby providing new ways to slow pericenter precession and to consequently generate large eccentricities.

An important additional potential to consider is that due to the central planet's oblateness. The study of this perturbation's effect on satellites in combination with the Sun's gravity dates back to investigations of Saturn's moon Iapetus by Laplace (1805), and later, by Tisserand (1896). Allan and Cook (1964)

subsequently generalized this analysis to an arbitrary number of perturbers. These works were limited to circular satellite orbits, for which the motion can be expressed in terms of elementary functions. In the general case of eccentric orbits, however, the evolution is no longer integrable. In the special circumstance where the obliquity is zero, Kozai (1963), found a class of solutions where the argument of pericenter librates around $\pm 90^\circ$, qualitatively similar to Kozai cycles. Lidov and Yarskaya (1974) tabulate and explore the integrable cases in the problem.

Kudielka (1994) and Vashkov'yak (1996) built on these works and discovered solutions where most or all of the orbital elements remained stationary. However, they limited their analysis to low obliquities, applicable to the Earth-Moon system. Tremaine et al. (2009), henceforth TTN, analyzed the full range of obliquities and found the stationary solutions for both circular and eccentric orbits. They further provide maps of the stability of these equilibria to eccentricity and angular momentum perturbations. Most importantly for this paper, they discovered that orbits around planets with obliquities $> 68.875^\circ$ undergo chaotic, large-amplitude oscillations in eccentricity and in inclination over the radial range from the planet where the two perturbations are comparable (see Fig. 9 in Tremaine et al. 2009). For a visualization of the effect, see the orbital histories shown in the figures below.

In this paper, we first investigate this case (including oblateness and gravitational solar perturbations) in a manner complementary to TTN. We use orbital elements in preference to TTN's vector approach, and we derive our results from the simple condition that the pericenter be able to halt, rather than from the stability of the Laplace surface. We thereby sacrifice some mathematical el-

egance and generality in order to provide a more physically intuitive picture. In Section 5.3 we extend the work of TTN, which only considers orbits in the equilibrium plane, to consider the general case of orbits inclined to this Laplace plane.

Although each added perturbation greatly increases the system's complexity, in Section 5.4 we incorporate radiation pressure so as to be able to study the motion of dust grains, for which such forces matter (Burns et al. 2001). Most importantly, radiation forces generate Poynting-Robertson (P-R) drag. P-R drag causes an orbit's semimajor axis to decay (Burns et al. 1979), allowing it to sweep through the radial range from the planet in which the eccentricity becomes unstable. We investigate whether radiation pressure's additional effects alter this unstable radial range or are even capable of stabilizing particle orbits against the instability found by TTN.

5.2 Evolution Under Perturbations from Solar Gravity and Planetary Oblateness

5.2.1 Kozai Oscillations

We start by reviewing the features of the Kozai mechanism that are essential to our work in order to motivate the strategy pursued in the rest of the paper. In our context, Kozai oscillations result solely from the Sun's gravitational perturbations on a body in an inclined circumplanetary orbit.

From a planetocentric perspective, the Sun "orbits" the planet in the latter's

orbital plane; to avoid confusion with the particle's orbital plane, we will hereafter refer to the planet's orbital plane as the "ecliptic" (even though the latter term strictly refers to the Earth's orbital plane). When interested in secular timescales much longer than the planet's and particle's orbital periods, one can time-average over the Sun's and particle's orbits and treat their masses as distributions smeared over their paths in the sky. Furthermore, since a circumplanetary particle lies much closer to the planet than to the Sun, it is usually sufficient to take only the leading quadrupole term in an expansion of the solar potential in powers of a/a_p, where a is the circumplanetary particle's semimajor axis, and a_p is the planet's semimajor axis. We point out, however, that Katz et al. (2011), Naoz et al. (2011) and Lithwick and Naoz (2011) have found that including the octupole term can introduce qualitatively different phenomena including flips from prograde to retrograde orbits, and eccentricities arbitrarily close to unity. In the limit where the circumplanetary particle's mass is negligible, they find that the octupole correction can be ignored when $\epsilon_M \ll 1$, where

$$\epsilon_M = \left(\frac{a}{a_p}\right)\left(\frac{e_p}{1-{e_p}^2}\right), \tag{5.1}$$

and e_p is the planet's orbital eccentricity. In this paper we consider only the Sun's quadrupole potential, and our results are therefore only applicable to cases where $\epsilon_M \ll 1$.

The secular problem truncated at quadrupole order was first analyzed by Kozai (1962) and Lidov (1962). We choose to work with the orbital elements $(a, e, i, \Omega, \omega)$. The equations of motion in these variables are given by (Innanen et al. 1997; Carruba et al. 2002, though see an erratum common to both papers in Carruba et al. 2003):

$$\frac{de}{dt} = \frac{15\epsilon_\odot n}{8} e(1-e^2)^{1/2}\sin^2 i_E \ \sin 2\omega_E, \tag{5.2}$$

$$\frac{di_E}{dt} = -\frac{15\epsilon_\odot n}{16} e^2(1-e^2)^{-1/2} \sin 2\omega_E \ \sin 2i_E, \tag{5.3}$$

$$\frac{d\omega_E}{dt} = \frac{3\epsilon_\odot n}{4}(1-e^2)^{-1/2}\Big[2(1-e^2) + 5\sin^2\omega_E(e^2 - \sin^2 i_E)\Big], \tag{5.4}$$

where n is the particle's mean motion, e is the particle orbit's eccentricity, ω_E its argument of pericenter, and i_E its inclination to the ecliptic, in which the Sun moves. The subscript E has been added to the angular quantities to emphasize that they are measured relative to the ecliptic plane. The quantity $\epsilon_\odot$ characterizes the strength of the solar perturbation relative to the dominant planetary gravity and depends on the distance from the planet; it is given by

$$\epsilon_\odot = \frac{M_\odot a^3}{M_p a_p^3 (1-e_p^2)^{3/2}}, \tag{5.5}$$

where M_p and $M_\odot$ are the planet's and Sun's masses, respectively.

The fact that the Sun has been averaged over its orbit and that the potential it creates is therefore time-independent means that energy (and thus a) is conserved. Furthermore, Kozai (1962) realized that the problem's symmetry guaranteed the conservation of the component of angular momentum perpendicular to the ecliptic, $L_z = \sqrt{GM_p a(1-e^2)}\cos i_E$, where G is the gravitational constant. This renders the system a one-degree-of-freedom, integrable system in the (e, ω_E) plane, i.e., one can divide Eq. 5.2 by Eq. 5.4, eliminate i_E using L_z, and solve for e as a function of ω_E. For initial values of $\Theta = \sqrt{1-e^2}\cos i_E < 3/5$ ($i_E > 39.2^\circ$ for $e \ll 1$), a stable equilibrium solution exists where e, i_E, and ω_E are stationary. In this case, the phase portrait in the (e, ω_E) plane consists of two types of solutions: 1) ones that trace out paths around the stationary point so that ω_E librates between minimum and maximum values, and 2) ones where ω_E

circulates. For $\Theta > 3/5$, no stationary point exists, and only circulating solutions are possible. These behaviors can be seen in Figs. 2-8 of Kozai (1962) and Fig. 2 of Carruba et al. (2002).

More qualitatively, Eq. 5.2 indicates that the pericenter's orientation within the orbital plane (given by ω_E) determines whether the eccentricity grows or shrinks. Normally ω_E circulates swiftly, as the term in brackets in Eq. 5.4 is roughly constant for small e and i. This results in a small-amplitude eccentricity oscillation (due to the $\sin 2\omega_E$ term in Eq. 5.2). However, if $d\omega_E/dt$ ever approaches zero in an orientation where $\sin 2\omega_E > 0$, the eccentricity can grow to large values. This can occur in the Kozai problem whenever the relative inclination, i_E, between the particle's orbit and the distant perturber's orbit is significant. For small eccentricities, Eq. 5.4 indicates that $d\omega_E/dt$ equals zero for some values of ω_E when $\sin^2 i_E > 2/5$ (i.e., $i_E > 39.2^\circ$).

Large inclinations to the ecliptic therefore provide one way for the eccentricity of circumplanetary orbits to grow to large values; however, adding other perturbations may allow for additional possibilities.

5.2.2 Adding Planetary Oblateness (J_2)

A planet's oblateness, represented by its J_2 coefficient, causes pericenter precession but does not produce secular effects on an orbit's eccentricity or inclination (e.g., Danby 1962). One can therefore imagine that orbital configurations may exist in which the ω_E precession from J_2 cancels that from the Sun, making ω_E constant and allowing the eccentricity to grow to large values according to Eq. 5.2.

The conservation of L_z mentioned in the previous section is due to the quadrupole potential's azimuthal symmetry, and this causes the eccentricity and inclination evolution to be coupled (Kozai 1962). But when one adds planetary oblateness, which is invariant about a different axis (the planet's spin pole), this symmetry of the classical Kozai case is destroyed. Hence, the eccentricity and inclination become decoupled, and the optimal choice of a reference plane from which to measure all angles is no longer obvious.

An appropriate choice is the local Laplace plane, which lies between the planet's equatorial plane and the ecliptic. If a particle on a circular orbit has its orbital plane align with this equilibrium plane, the torques from the Sun and J_2 balance so that the orbit's angular momentum vector remains fixed, and the orbital plane does not precess (Allan and Cook 1964). A circular orbit *not* aligned with the local Laplace plane will have its orbital axis precess around the equilibrium Laplace plane axis (see Fig. 5.1). This represents a compromise between the particle orbit attempting to precess around both the planet's spin axis and the Sun's orbital axis.

More generally, the orbit normals of eccentric orbits will wobble as they undergo their precession cycle since their changing distance from the planet means they "sense" a range of Laplace planes. We note that even in cases where the *orbital plane* itself does not precess, the *pericenter* may still precess within that orbital plane. It is specifically the ability of the *pericenter* to halt that gives rise to large eccentricities, as argued in the first paragraph of this section.

Because the strengths of the two relevant perturbations vary differently with distance from the planet, the local Laplace plane shifts as the particle's semi-major axis varies. Near the planet, where the torques on the orbit are pre-

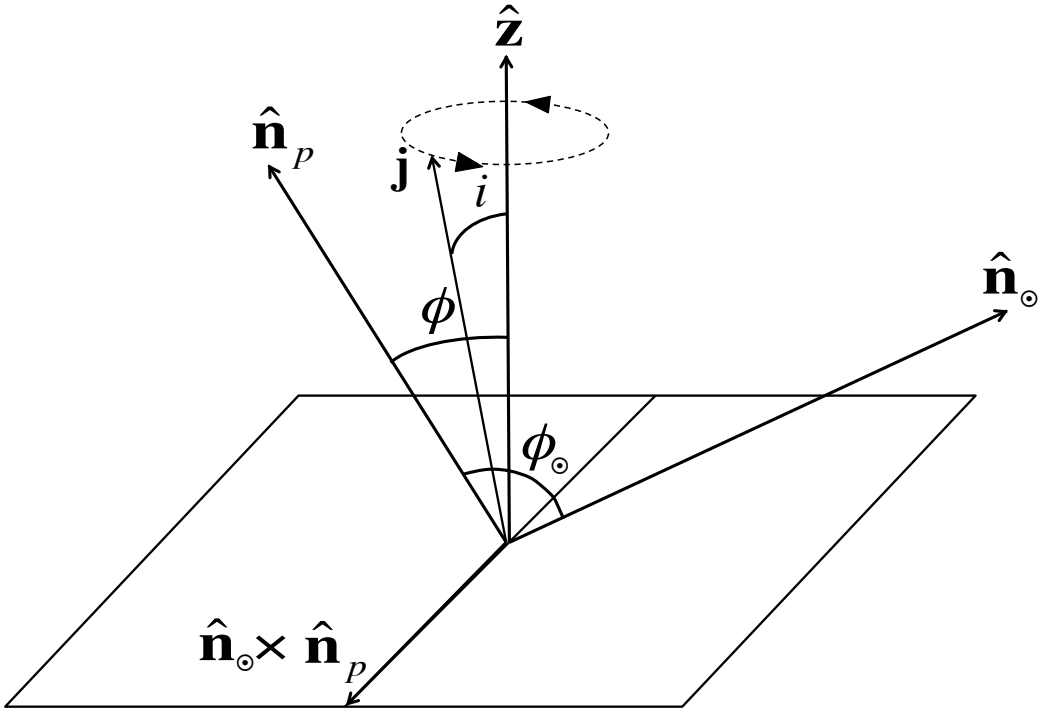

Figure 5.1: Normal to the local Laplace plane $\hat{\mathbf{z}}$ lies between, and is coplanar with, the planet's spin pole $\hat{\mathbf{n}}_p$ and the ecliptic normal $\hat{\mathbf{n}}_\odot$. The normal to an arbitrary particle's orbit plane $\mathbf{j}$ will precess around $\hat{\mathbf{z}}$ at approximately constant inclination i, sweeping out a cone. The obliquity $\phi_\odot$ is simply the angle between the vectors $\hat{\mathbf{n}}_p$ and $\hat{\mathbf{n}}_\odot$, and ϕ represents the angle between $\hat{\mathbf{n}}_p$ and the $\hat{\mathbf{z}}$ axis. As the semimajor axis changes and the relative strengths of the Sun's and planet's perturbations vary, the Laplace plane will shift, and ϕ will vary.

dominantly caused by oblateness, the Laplace plane nearly coincides with the planet's equatorial plane. Far from the planet, where solar torques dominate, the Laplace plane aligns closely with the ecliptic (in which the Sun "moves"). Between these limits, the Laplace plane takes on intermediate orientations, generating a warped Laplace surface. The Laplace plane at a given semimajor axis is the tangent plane to the Laplace surface. The transition of the Laplace surface

from the ecliptic to the equatorial plane occurs approximately at the distance where the torques from the solar tides and J_2 are equal. Omitting factors of order unity, this distance is often referred to as the Laplace radius and is given by Goldreich (1966),

$$r_L{}^5 = J_2 R_p{}^2 a_p{}^3 (1 - e_p^2)^{3/2} \frac{M_p}{M_\odot}, \tag{5.6}$$

where R_p and M_p are the planet's radius and mass, and $M_\odot$, a_p and e_p were previously defined. For particles orbiting at large distances from any existing inner satellites, one can treat the inner moons' effect as a further contribution to the planetary J_2, where (see, e.g., TTN),

$$J_2' R_p^2 \equiv J_2 R_p^2 + \frac{1}{2} \sum_{i=1}^{n} a_i^2 m_i / M_p, \tag{5.7}$$

where J_2' is the effective J_2, and the a_i and m_i are the moons' semimajor axes and masses, respectively. Any subsequent references to a planet's J_2 in this paper should be understood as the effective J_2 that includes any inner satellites' contribution to the quadrupole potential.

An important dynamical feature for particle orbits decaying slowly compared to the precession timescale (e.g., through P-R drag) is that the orbital inclination to the local Laplace plane remains roughly constant (Goldreich 1965). This means that a decaying particle orbit starting far from the primary in the planet's orbital plane (which coincides here with the local Laplace plane) will have its orbital plane follow the Laplace plane as the latter shifts on its way inward toward the planet.

Following TTN, we neglect any variations in $\hat{\mathbf{n}}_\odot$, as well as the precession of $\hat{\mathbf{n}}_\mathbf{p}$ due to the torques on the equatorial bulge from the Sun and other planets. The latter timescale is generally much longer than a circumplanetary orbit's precession period, in which case it can be safely ignored (Goldreich 1965).

5.2.3 The Disturbing Potential

We now derive the disturbing potential using orbital elements and TTN's notation. The obliquity $\phi_\odot$ and the variable ϕ are defined in Fig. 5.1, whereas the remaining quantities are shown in Fig. 5.2.

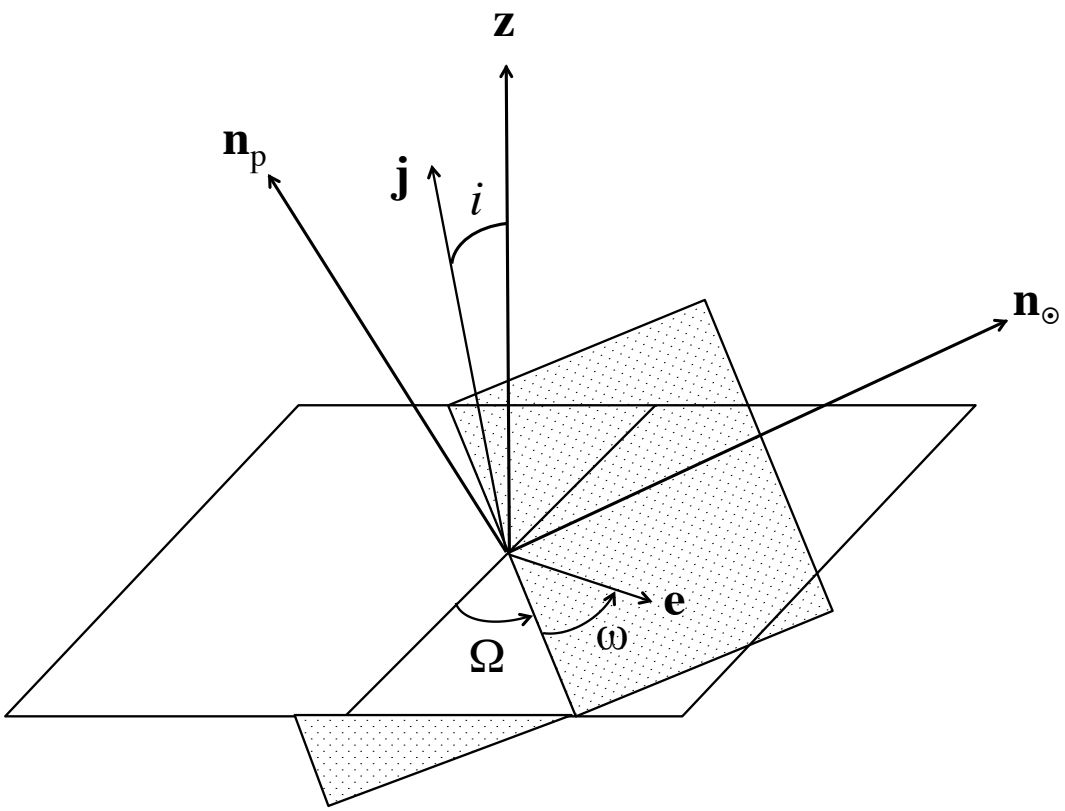

Figure 5.2: Reference plane (white) is the local Laplace plane. $\hat{\mathbf{n}}_\mathbf{p}$ is the planet's spin pole and $\hat{\mathbf{n}}_\odot$ the ecliptic pole. The particle's orbital plane (shaded) is defined by its orbit normal $\mathbf{j}$, which can be given in terms of the orbit's inclination i and longitude of the ascending node Ω. The orientation of the orbit (not shown) within the orbital plane is defined by the so-called eccentricity vector, which points toward pericenter $\mathbf{e}$, and is parametrized by the argument of pericenter ω, measured along the shaded orbital plane, from the line of ascending node. We choose to measure the longitude of the ascending node Ω from the direction defined by $\hat{\mathbf{n}}_\odot \times \hat{\mathbf{n}}_\mathbf{p}$. Note that $\mathbf{j}$ and $\mathbf{e}$ are not unit vectors.

The eccentricity vector **e** points toward pericenter and has a magnitude given by the orbit's eccentricity. The vector **j** lies along the orbit normal and has a magnitude chosen as $\sqrt{1-e^2}$, so that $\mathbf{j}\cdot\mathbf{e} = 0$ and $j^2 + e^2 = 1$. We choose to measure the longitude of the ascending node Ω from the direction along $\hat{\mathbf{n}}_\odot \times \hat{\mathbf{n}}_\mathbf{p}$.

The perturbing potentials (averaged over both the particle and solar orbits) are (see Eq. 12 in TTN):

$$\begin{aligned} \Psi_p &= \frac{\epsilon_p}{4(1-e^2)^{5/2}}[1 - e^2 - 3(\mathbf{j}\cdot\hat{\mathbf{n}}_\mathbf{p})^2] \\ \Psi_\odot &= \frac{3\epsilon_\odot}{8}[5(\mathbf{e}\cdot\hat{\mathbf{n}}_\odot)^2 - (\mathbf{j}\cdot\hat{\mathbf{n}}_\odot)^2 - 2e^2], \end{aligned} \tag{5.8}$$

where Ψ_p and $\Psi_\odot$ represent potentials non-dimensionalized by the factor GM_p/a. The quantity $\epsilon_\odot$ was defined in Eq. 5.5 and ϵ_p is given by

$$\epsilon_p = \frac{J_2 R_p^2}{a^2}. \tag{5.9}$$

Since our aim is to approach the problem using orbital elements, we employ them to rewrite the three scalar products in Eqs. 5.8. This is perhaps easiest to do by first writing **j**, $\hat{\mathbf{n}}_p$, $\hat{\mathbf{n}}_\odot$ and **e** in terms of their Cartesian components. This process yields

$$\begin{aligned} \mathbf{j}\cdot\hat{\mathbf{n}}_p &= (1-e^2)^{1/2}(\cos\phi\cos i + \sin\phi\sin i\cos\omega) \\ \mathbf{j}\cdot\hat{\mathbf{n}}_\odot &= (1-e^2)^{1/2}[\cos(\phi_\odot - \phi)\cos i - \sin(\phi_\odot - \phi)\sin i\cos\Omega] \\ \mathbf{e}\cdot\hat{\mathbf{n}}_\odot &= e[\sin(\phi_\odot - \phi)(\cos i\cos\Omega\sin\omega + \cos\omega\sin\Omega) + \cos(\phi_\odot - \phi)\sin i\sin\omega]. \end{aligned} \tag{5.10}$$

Substituting into Eqs. 5.8, we obtain the dimensionless disturbing function $R = -(\Psi_p + \Psi_\odot)$,

$$\begin{aligned} R = -\frac{3\epsilon_\odot}{8}\Bigg\{ & \frac{2}{3(1-e^2)^{3/2}}\left(\frac{r_L}{a}\right)^5[1 - 3(\cos\phi\cos i + \sin\phi\sin i\cos\Omega)^2] + \\ & 5e^2[\sin(\phi_\odot - \phi)(\cos i\cos\Omega\sin\omega + \cos\omega\sin\Omega) + \cos(\phi_\odot - \phi)\sin i\sin\omega]^2 - \\ & (1-e^2)(\cos(\phi_\odot - \phi)\cos i - \sin(\phi_\odot - \phi)\sin i\cos\Omega)^2 - 2e^2\Bigg\}, \end{aligned} \tag{5.11}$$

where we have written the potential only in terms of $\epsilon_\odot$ in order to explicitly bring out the dependence on the semimajor axis a relative to the Laplace radius r_L (note that from Eqs. 5.6, 5.9 and 5.5, $\epsilon_p/\epsilon_\odot = (r_L/a)^5$).

Implicit in Eq. 5.11 is a relation between a, ϕ and $\phi_\odot$, since the semimajor axis sets the location of the local Laplace plane and therefore of the $\mathbf{z}$ axis (see Fig. 5.2). Changing a therefore alters ϕ. The transcendental equation that connects these quantities is (Tremaine et al. 2009)

$$\tan 2\phi = \frac{\sin 2\phi_\odot}{\cos 2\phi_\odot + 2\left(r_L/a\right)^5}. \tag{5.12}$$

Equation 5.12 has four solutions in a 2π interval: ϕ, $\phi + \pi$, and $\phi \pm \pi/2$. The solution corresponding to the classical Laplace equilibrium has the property $\phi \to \phi_\odot$ for $a \gg r_L$. Orbits locally aligned with this surface are stable to small perturbations in their orientation. The other two solutions 90° away are always unstable: if the orbit plane is displaced slightly from either of these directions, it will precess about the stable solutions; we therefore do not discuss them further (see TTN).

Eq. 5.11 is equivalent to the disturbing function in Eq. 1.3 of Lidov and Yarskaya (1974), which is instead referenced to the ecliptic. The two are simply related by a rotation by $\phi_\odot - \phi$ about the x-axis, where ϕ is given by Eq. 5.12.

5.2.4 Dynamics in the Laplace Plane

While orbits in the classical Laplace plane are always stable against perturbations to their orbit normal, they are not always stable to small changes in their eccentricity. We now find the radial distance at which the Laplace plane be-

comes unstable to such eccentricity perturbations by considering the limit $i \to 0$. As the orbital plane approaches the Laplace plane, however, Ω becomes ill-defined. One therefore typically switches to the variable $\varpi = \Omega + \omega$, which smoothly approaches the angle between $\hat{\mathbf{n}}_\odot \times \hat{\mathbf{n}}_\mathbf{p}$ and pericenter (see Fig. 5.2).

Before continuing, we wish to relate the angular variables to ω_E, since Eq. 5.2 shows that it is specifically the halting of ω_E that can create large eccentricities. Careful inspection of Fig. 5.2 shows that orbits in the Laplace plane (the white reference plane) must intersect the ecliptic plane (not shown but perpendicular to $\hat{\mathbf{n}}_\odot$) along the vector $\hat{\mathbf{n}}_\odot \times \hat{\mathbf{n}}_\mathbf{p}$. If we make the same choice of $\hat{\mathbf{n}}_\odot \times \hat{\mathbf{n}}_\mathbf{p}$ as the arbitrary reference direction in the ecliptic plane, this means that orbits in the Laplace plane always satisfy $\Omega_E = 0$. The angle ω_E is then just the angle from $\hat{\mathbf{n}}_\odot \times \hat{\mathbf{n}}_\mathbf{p}$ to pericenter, or ϖ. Therefore, for orbits in the Laplace plane, we set $i = 0$ in Eq. 5.11 and, writing $\Omega + \omega = \omega_E$, we obtain

$$R = -\frac{3\epsilon_\odot}{8}\left\{\frac{2}{3(1-e^2)^{3/2}}\left(\frac{r_L}{a}\right)^5\left(1-3\cos^2\phi\right)+5e^2\sin^2(\phi_\odot-\phi)\sin^2\omega_E-(1-e^2)\cos^2(\phi_\odot-\phi)-2e^2\right\}. \tag{5.13}$$

We can now employ Lagrange's planetary equations to find the orbital elements' time evolution. The equation for the eccentricity is (cf. Murray and Dermott 1999, p. 251, noting that we have non-dimensionalized R and that over-dots denote time derivatives),

$$\frac{\dot{e}}{n} = -\frac{(1-e^2)^{1/2}}{e}\frac{\partial R}{\partial \varpi} = -\frac{(1-e^2)^{1/2}}{e}\frac{\partial R}{\partial \omega_E}, \tag{5.14}$$

where we have ignored a term involving the mean longitude at epoch that disappears in our orbit-averaged equations. Plugging Eq. 5.13 into this equation,

$$\frac{\dot{e}}{n} = \frac{15}{8}\epsilon_\odot e(1-e^2)^{1/2}\sin^2(\phi_\odot-\phi)\sin 2\omega_E. \tag{5.15}$$

Since we are considering orbits in the Laplace plane, $\mathbf{j}$ lies along $\hat{\mathbf{z}}$ in Fig. 5.1, and

since i_E refers to the angle between $\mathbf{j}$ and the ecliptic axis $\hat{\mathbf{n}}_\odot$, $i_E = \phi_\odot - \phi$. Hence Eq. 5.15 matches the classical Kozai result (Eq. 5.2). This is what one would expect as the planet's oblateness does not contribute secularly to the eccentricity evolution (e.g., Danby 1962).

The precession of pericenter *is* altered by the planet's oblateness, however. The appropriate equation is (cf. Murray and Dermott 1999, p. 251),

$$\frac{\dot{\omega}_E}{n} = \frac{\dot{\varpi}}{n} = \frac{(1-e^2)^{1/2}}{e}\frac{\partial R}{\partial e}, \tag{5.16}$$

where we have omitted a term $\propto \partial R/\partial i$ that vanishes in the limit $i \to 0$. Again substituting for R from Eq. 5.13,

$$\frac{\dot{\omega}_E}{n} = \frac{3\epsilon_\odot(1-e^2)^{1/2}}{4}\left\{2-5\sin^2(\phi_\odot-\phi)\sin^2\omega_E-\cos^2(\phi_\odot-\phi)-\frac{1}{(1-e^2)^{5/2}}\left(\frac{r_L}{a}\right)^5[1-3\cos^2\phi]\right\}. \tag{5.17}$$

In the limit $a \ll r_L$, $\phi \to 0$, and $\dot{\omega}_E \to (3/2)\epsilon_p(1-e^2)^{-2}$ (where, once again from below Eq. 5.11, $(r_L/a)^5 = \epsilon_p/\epsilon_\odot$). This matches the rate of precession $\dot{\varpi}_p$ for the longitude of pericenter relative to the planet's equatorial plane due to oblateness (Danby 1962). In the limit $a \gg r_L$, $\phi_\odot \to \phi$ (Eq. 5.12) and $\dot{\omega}_E \to (3/4)\epsilon_\odot(1-e^2)^{1/2}$. Since we have restricted ourselves to orbits in the Laplace plane, this does not agree with Eq. 5.4; rather it provides the rate one would obtain solely from solar perturbations after imposing the Laplace-plane condition that $\Omega_E = 0$ (see the paragraph preceding Eq. 5.13).

Recall that inducing large eccentricity amplitudes relies on the pericenter precession rate approaching zero, i.e., keeping ω_E constant (cf. Eq. 5.2). In the above two limiting cases, $\dot{\omega}_E > 0$, so if $\dot{\omega}_E$ is to cross through zero, it must do so at intermediate semimajor axes. To find the least stringent condition for the pericenter to lock, one can pick the most unstable configuration (i.e., the orientation that generates the largest negative terms). As in the Kozai case, this

corresponds to $\sin^2 \omega_E = 1$, i.e., $\omega_E = \pm 90^\circ$. Setting $\dot{\omega}_E = 0$ in Eq. 5.17 with $\omega_E = \pm 90^\circ$ yields, to first order in e,

$$\frac{3\epsilon_\odot}{4}\left\{1 - 4\sin^2(\phi_\odot - \phi) - \left(\frac{r_L}{a}\right)^5 [1 - 3\cos^2\phi]\right\} = 0. \tag{5.18}$$

One cannot analytically find a solution for a since ϕ, $\phi_\odot$ and a are all related through the transcendental relation in Eq. 5.12. But one can see that $4\sin^2(\phi_\odot - \phi)$ will only be large for ϕ far from $\phi_\odot$, and the last term (from J_2) is only negative for $\phi \gtrsim 55^\circ$. Since ϕ is bounded to be between zero and the obliquity $\phi_\odot$ (see Fig. 5.2), this suggests that high obliquities are required for $\dot{\omega}_E$ to drop below zero. It also means that the roots of Eq. 5.18 (if they exist) should be close to r_L, since this is where the Laplace plane transitions and is the only situation where $\phi_\odot - \phi$ and r_L/a are simultaneously appreciable.

When Eq. 5.18 is solved numerically for various $\phi_\odot$, no solution appears for $\phi_\odot < 68.875^\circ$. Below this obliquity, orbits are therefore always stable. Beyond this threshold obliquity, however, the pericenter can halt for a range in a, thereby generating large-amplitude eccentricity oscillations; our value for the critical $\phi_\odot$ agrees with that derived differently by TTN.

5.2.5 Uranus: A case study

Uranus is a solar system example with an extreme obliquity ($\phi_\odot \approx 98^\circ$) beyond the threshold value of 68.875°. Hence, circumplanetary particles within a certain semimajor axis range will generate large eccentricity values. This unstable range is depicted in Fig. 5.3, which prescribes the minimum non-dimensionalized precession rate $\dot{\omega}_E/n$ as given by Eq. 5.17 for low eccentricities and $\omega_E = \pm 90^\circ$, plotted vs. semi-major axis (using Eq. 5.12 to solve for ϕ).

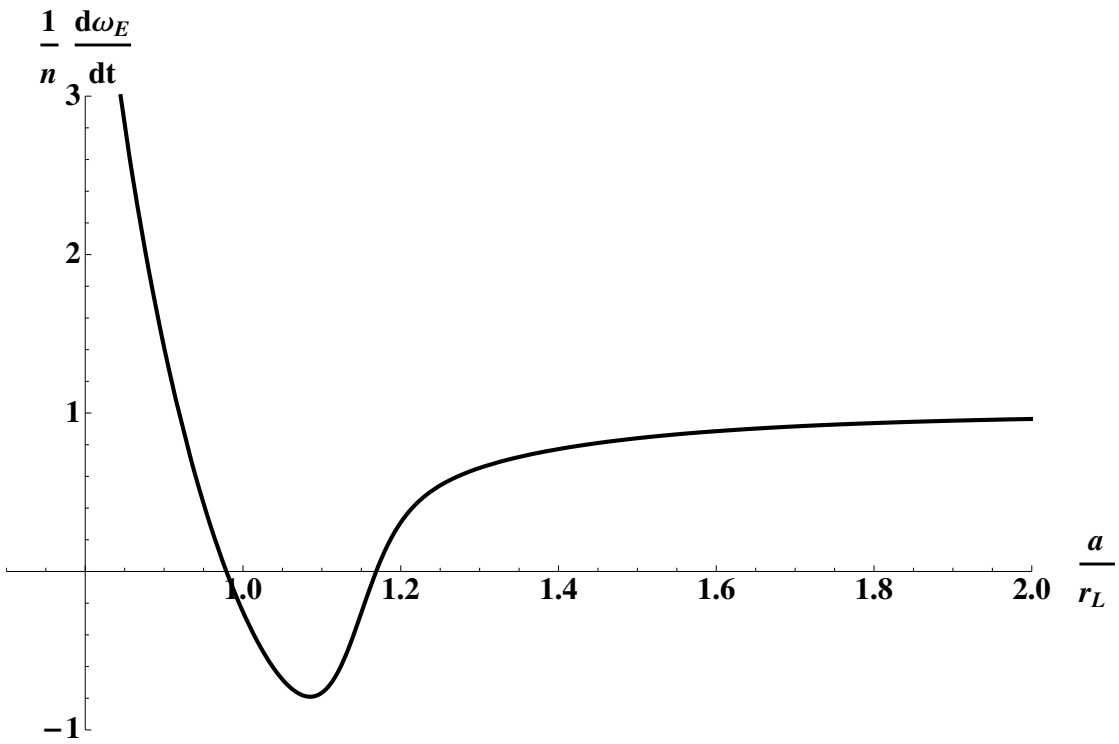

Figure 5.3: For low eccentricities, the minimum $\dot{\omega}_E/n$ (at $\omega_E = \pm 90^\circ$ in Eq. 5.17) as a function of semimajor axis. The semimajor axis is in units of the Laplace radius $r_L \approx 64R_p$ for Uranus (Eq. 5.6). The non-dimensionalized precession rate is expressed as a fraction of the rate for $a \gg r_L$ ($\dot{\omega}_E/n = 3\epsilon_\odot/4$). In the radial range where $(\dot{\omega}_E/n)_{min} < 0$, $\dot{\omega}_E/n$ will cross through 0 for certain values of ω_E. In this radial range, the Laplace plane is unstable to eccentricity perturbations.

Fig. 5.3 shows that a circular orbit lying in the classical Laplace plane will be unstable in the approximate range $0.93r_L < a < 1.17r_L$. In the case of Uranus, the effective J_2 including the contribution of the inner satellites is approximately 0.019 (Eq. 5.7), $r_L \approx 64R_p$, and the unstable range translates to $59.5R_p < a < 74.9R_p$.

Fig. 5.4 displays a numerical integration of a nearly circular orbit (initial eccentricity of 10^{-6}) started far from the planet in the ecliptic (coincident with

the local Laplace plane). The particle is then slowly brought inward according to $a = a_0 e^{-t/\tau}$, where $\tau = 2.5$Myr. This interval is much longer than the secular timescale on which the orbit evolves of ~ 0.01Myr. The functional form for the semimajor-axis decay was chosen to match that for P-R drag (Burns et al. 1979); this is simply for consistency with Sec. 5.6 where we consider small particles that are subject to this dissipative force. Uranus' orbit is taken as circular, and the whole third body effect of the Sun is included. As our later integrations will include radiation pressure, we used the well-established dust integrator dI for all our numerical simulations (Hamilton 1993; Hamilton and Krivov 1996; Hamilton 1996; Hamilton and Krüger 2008; Tamayo et al. 2011; Jontof-Hutter and Hamilton 2012a,b).

Since the particle starts in the ecliptic, the inclination relative to the ecliptic i_E begins at zero. As the orbit approaches the Laplace radius (64 R_p), the inclination follows the local Laplace plane toward Uranus' equatorial plane. However, both the eccentricity and inclination become unstable immediately upon entering the unstable range at $\approx 74.9 R_p$. One can see this corresponds to the point where ω_E (bottom panel) stops precessing (at the maximally unstable orientation of 270°). The reason the eccentricity does not grow the first time $\dot{\omega}_E$ drops to zero at $a \approx 77 R_p$ is that ω_E is just above 270°, where according to Eq. 5.2, the eccentricity shrinks. The second time $\dot{\omega}_E < 270°$, so $\dot{e} > 0$. Once the eccentricity grows, e eventually becomes large enough that the second-order eccentricity contribution to the last term of Eq. 5.17 becomes important and causes precession to resume, i.e., the particle gets close enough to Uranus at pericenter that J_2 re-initiates precession.

As mentioned at the beginning of Sec. 5.2.2, this behavior differs from that of

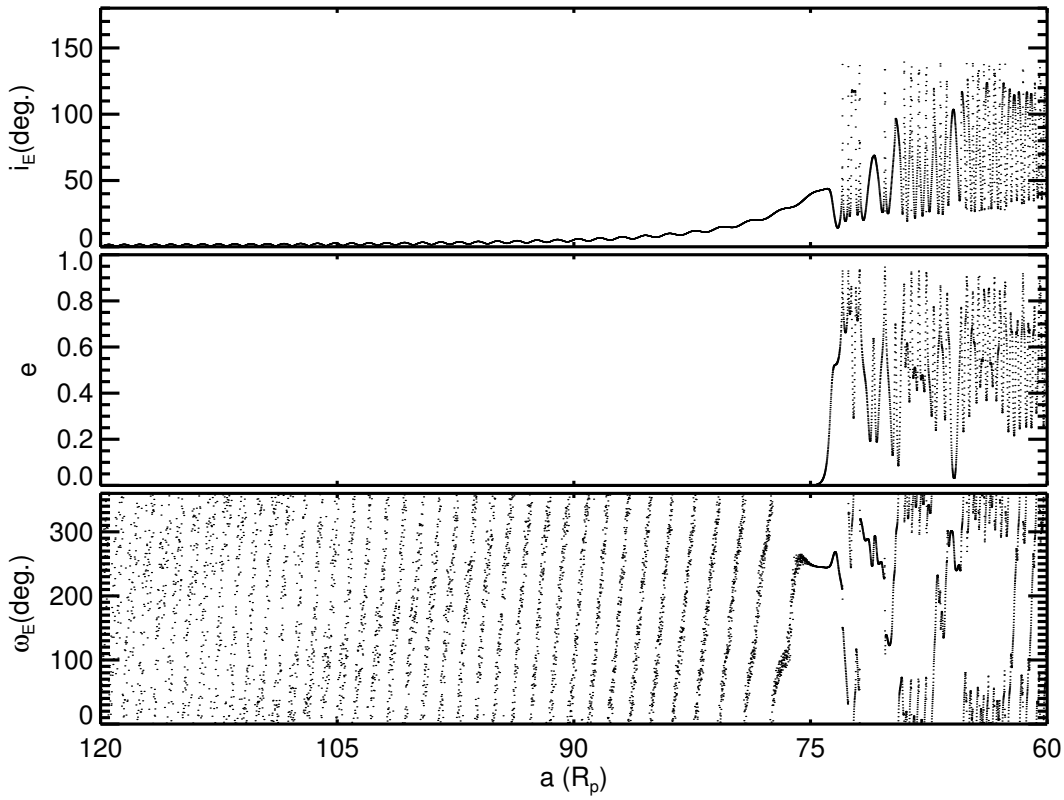

Figure 5.4: Numerical integration of an initially nearly circular orbit started in the ecliptic at $120R_p$ and slowly brought inward. The top panel plots inclination referenced to the ecliptic, so initially $i_E = 0$. The middle plot displays the eccentricity history, and the bottom plot shows the evolution of ω_E. The eccentricity and inclination become unstable when the semimajor axis reaches $\approx 74.9R_p$. Note also that this is the point where ω_E remains constant, near the most unstable orientation $\omega_E = 270^\circ$.

Kozai cycles. The oscillations are not regular and the eccentricity and inclination are not coupled. In the Kozai case this coupling was due to the conservation of angular momentum along the ecliptic axis. The planet's oblateness spoils this symmetry from the Kozai problem because it allows the particle to exchange substantial angular momentum with the planet at pericenter along that previously conserved direction. Note that when the eccentricity becomes large and the particles at pericenter approach the inner moons, the approximation used in

our calculations and simulations of treating the inner satellites as a contribution to the planet's J_2 is no longer an appropriate assumption. However, one would expect collisions to remove particles shortly after their orbits cross those of these large satellites.

We also point out that even though the classical Laplace plane is defined only for circular orbits, eccentric Laplace equilibria also exist (TTN). The circular and eccentric equilibria bifurcate when the circular solution becomes unstable, and a decaying particle-orbit can transfer onto the eccentric-equilibrium track. However, TTN find that the eccentric equilibrium becomes unstable almost immediately upon bifurcating from the circular solution (see Fig. 6 of TTN). This is especially true for particles starting far from the planet and evolving inward through the unstable region (rather than starting close and evolving outward). The point at which the classical Laplace plane becomes unstable (found above) is therefore a good proxy for when a circular orbit originally in the Laplace plane destabilizes.

5.3 Dynamics in 3 Dimensions

By restricting the above discussion to orbits that lie in the local Laplace plane, we reduced the dimensionality of the problem to two dimensions. We now address the general situation where orbits are inclined to the local Laplace plane. Then the problem is inherently three-dimensional, and the enlarged phase space makes it difficult to provide detailed general results. Accordingly, we do not pursue a complete analytical theory and instead limit ourselves to a qualitative description of orbital behavior based on our understanding derived from the

above analysis as well as various numerical integrations. There are some integrable cases considered by Lidov and Yarskaya (1974); however, in the case of interest with finite eccentricity and $a \sim r_L$, these only apply to obliquities of zero and ninety degrees, or to polar orbits with the orbital axis pointing along the intersection between the planet's orbital and equatorial planes.

We can first gain some insight by investigating the equations of motion relative to the ecliptic plane. Since J_2 perturbations have no secular effect on e, the eccentricity evolution depends only on solar perturbations; it is therefore given simply by Eq. 5.2. In Eqs. 5.3 and 5.4 for di/dt and $d\omega_E/dt$, one would have to add the complicated effect of J_2 referenced to the ecliptic plane. This is obtained by taking the J_2 contribution to R in Eq. 5.11, i.e. the term involving $(r_L/a)^5$, setting $\phi = \phi_\odot$, appending a subscript E to all angular variables, and applying (cf. Danby 1962, recalling that our disturbing potential is non-dimensional)

$$\begin{aligned} \frac{\dot{i_E}}{n} &= -\frac{1}{\sqrt{1-e^2}}\left\{ \csc\, i_E \frac{\partial R}{\partial \Omega_E} - \cot\, i_E \frac{\partial R}{\partial \omega_E} \right\} \\ \frac{\dot{\omega}_E}{n} &= \frac{\sqrt{1-e^2}}{e}\frac{\partial R}{\partial e} - \frac{1}{\sqrt{1-e^2}} \cot\, i_E \frac{\partial R}{\partial i_E}. \end{aligned} \tag{5.19}$$

The resulting equations are complex and difficult to pursue analytically. One can, however, gain insight from investigating the effect of a non-zero inclination on the solar perturbations that dominate the particle's early evolution far from the planet, before the J_2 terms become important.

From Eq. 5.4, a larger inclination acts to lower $d\omega_E/dt$, bringing the orbit closer to instability. This leads to Kozai oscillations for sufficiently large i_E in this limit that ignores J_2. In this sense, the previous section's situation where a particle begins far from the planet in the Laplace plane (where $i_E = 0$) furnishes the best-case scenario for stability; $d\omega_E/dt$ would have to be substantially decreased by J_2 in order for $d\omega_E/dt$ to drop to zero. One should therefore expect

that, if a circular orbit starting in the Laplace plane becomes unstable, any orbit initially inclined to the ecliptic will also destabilize. Furthermore, inclined orbits should become unstable earlier during their inward evolution than their uninclined counterparts would.

Numerical integrations support this assertion. Figure 5.5 shows the evolution of nearly circular orbits that are slowly evolved inward after beginning far from Uranus at various initial inclinations to the ecliptic. One sees that more inclined orbits become unstable earlier in their inward migration. We point out, however, that the orderly progression in Fig. 5.5 results from starting all the integrations with the same initial conditions (other than the inclination). In the general 3-D case, all the orbital elements affect the dynamics. Altering the initial conditions changes the phase in the elements' evolution at which they enter the unstable range in a that we found in the 2-D case; this can change the semimajor axis at which the eccentricity grows by $\sim 10\%$. It nevertheless remains true that for a given set of initial conditions, increasing the inclination destabilizes the orbit earlier in its inward evolution.

Changing the initial e, however, does not have a strong effect on the location at which the pericenter halts and the orbit undergoes large-amplitude eccentricity oscillations. This can be seen from Eq. 5.17. A non-zero e enhances the J_2 contribution, pushing outward the location at which e grows slightly; however, this term's steep dependence on semimajor axis of $(r_L/a)^5$ allows a small change in a to accommodate a large initial eccentricity. The edge of the unstable region therefore shifts by less than a few percent for $e \lesssim 0.3$.

A more complete investigation of inclined orbits is beyond the scope of this paper. We note, however, that the threshold obliquity of 68.875° found by TTN,

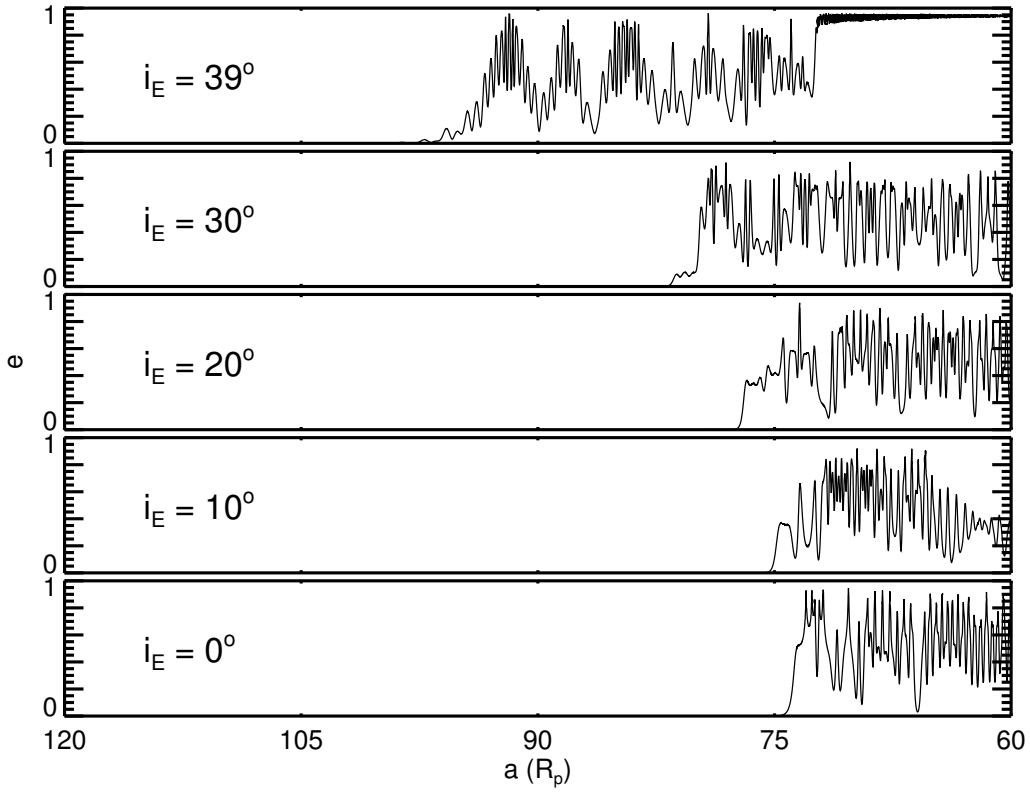

Figure 5.5: Orbital eccentricity histories for particles begun far from Uranus ($120R_p$) with $e = 10^{-6}$ at varying inclinations to the ecliptic. Like Fig. 5.4, the semimajor axis is brought inward according to $a = a_0 e^{-t/\tau}$, with $\tau = 2.5$Myr. The figure plots eccentricity vs. semimajor axis, where constant offsets have been added to the eccentricities to separate the different plots. Higher-inclination orbits are inherently less stable and undergo large-amplitude eccentricity oscillations sooner in their inward evolution.

and derivable from Eq. 5.18, applies to orbits in the Laplace plane, i.e., the most stable configuration. For orbits initially inclined to the Laplace plane, the threshold obliquity would be lower. An inward-evolving object with an initial inclination close to the threshold value for Kozai oscillations ($\approx 39.2^\circ$ for low eccentricities) could undergo large-amplitude eccentricity oscillations in systems with more modest obliquities. We have verified this, finding that for a hypo-

thetical planet with obliquity $\phi_\odot = 60^\circ$, orbits begun with $e = 0$ and $i_E \gtrsim 7^\circ$ undergo eccentricity oscillations in the transition region. The maximum eccentricity attained increases with initial inclination, varying from $e_{max} \approx 0.35$ for initial $i_E = 10^\circ$ to $e_{max} \approx 0.95$ for $i_E = 35^\circ$. Even at Saturn ($\phi_\odot \approx 27^\circ$), initially circular orbits started with $i_E = 35^\circ$ undergo oscillations with a maximum eccentricity of ≈ 0.2.

5.4 The Effects of Non-gravitational Forces

The mechanism discussed in this paper occurs when the effects of planetary oblateness and solar gravity balance at $a \sim r_L$ (Eq. 5.6) so as to halt pericenter precession. It is therefore appropriate to consider whether additional perturbations might instead keep the pericenter moving, thereby stabilizing the orbit. While the previous discussion applies to objects of arbitrary size and mass, we now consider radiation forces, which are most important for small dust grains.

Radiation forces are of particular interest because they provide a natural mechanism (P-R drag) for the semimajor axis of dust-grain orbits to decay in toward the planet and reach the unstable range in a (Burns et al. 1979). Two further effects that are generally important for dust grains are direct solar radiation pressure (Burns et al. 1979) and electromagnetic forces due to the planetary magnetic field (Hamilton 1993; Hamilton and Krivov 1996; Burns et al. 2001).

At all the solar system's planets except Jupiter, the instability occurs beyond the magnetopause, rendering perturbations from the planetary magnetic field irrelevant. Furthermore, radiation pressure (discussed below) can remove small particles by pumping their eccentricities close to unity. Particles then either

crash into the primary or escape the system entirely (see Hamilton and Burns 1992). For dust grains starting far from the planet ($\sim 200R_p$), only particles larger than roughly a few microns in radius survive (see below). For particles of this size and larger, even inside the magnetosphere, the planetary magnetic field is not important (cf. Fig. 11 in Burns et al. 2001); we therefore ignore it.

5.4.1 Radiation Pressure

Solar radiation pressure, however, can have powerful effects. This perturbation has been extensively studied, usually by approximating the planetary orbit as circular and averaging over the particle's orbit, which generally changes much faster than the planet's orbital period (Burns et al. 1979; Hamilton 1993; Juhasz and Horanyi 1995). Mignard and Henon (1984) found an exact solution under these assumptions in a frame rotating with the Sun, employing several changes of variables; unfortunately, the inverse transformations to the orbital elements that we have utilized are complicated. We therefore choose to instead work in the same inertial system we employed above and to find approximate equations sufficient for our needs.

Upon averaging over the particle's orbit, two fundamental timescales remain. The first is the secular rate at which the orbital elements change ($\sim nF_{rad}/F_g$, where n is the particle's mean motion and F_{rad} and F_g are the radiation pressure and planet's gravitational forces, respectively); the second is simply the Sun's mean motion about the planet $n_\odot$. The dynamics are set through their ratio $Z \equiv (3nF_{rad})/(2n_\odot F_g)$, where the factor of $3/2$ results from the exact form of the equations of motion (Burns et al. 1979). Note that since we will later

be interested in higher-order eccentricity terms, we have removed the changing factor of $\sqrt{1-e^2}$ from the definition of Burns et al. (1979) so that Z is constant (at a given semimajor axis). One can express Z as

$$Z = 0.86 Q_{pr} \left(\frac{1 \text{ g cm}^{-3}}{\rho} \right) \left(\frac{1 \, \mu\text{m}}{s} \right) \left(\frac{M_\odot}{M_p} \right)^{1/2} \left(\frac{a}{a_p} \right)^{1/2}, \tag{5.20}$$

where Q_{pr} is the radiation pressure coefficient averaged over the central star's spectrum, ρ is the particle density and s is the particle radius. Note that smaller particles, with larger surface-area-to-volume ratios, are more affected by radiation pressure (i.e., have higher Z). However, once particles shrink below the scale of the star's peak emission wavelength, they lose the ability to couple to the radiation field and Q_{pr} drops to zero; this occurs at $\sim 0.1 \, \mu$m for solar-type stars.

If Z approaches one, radiation pressure pumps a particle's orbital eccentricity to unity, most often resulting in collision with the planet. This provides a minimum particle size to consider. However, because Z increases with a, this limit would vary with initial location from the planet. This is because the importance of radiation pressure relative to the dominant planetary gravitational field increases the farther out one orbits in the primary's gravitational well. For a more detailed analysis of this threshold and the ultimate fate of these grains, see Hamilton and Burns (1992).

The inclusion of radiation pressure introduces high-frequency variations to all the orbital elements at the Sun's orbital rate about the planet, $n_\odot$ (Burns et al. 1979). Since these rates are much faster than the precession rates due to J_2 and solar tides, one can average over these fast solar oscillations. As shown in the next section, to first order in the eccentricity, no secular change in ω_E occurs. For orbits in the Laplace plane with low eccentricities, Eq. 5.18 therefore re-

mains the *averaged* condition for the pericenter to halt (at $\omega_E = \pm 90^\circ$). Thus, as we argued following Eq. 5.18, $\dot{\omega}_E$ will still only cross through zero at approximately the semimajor axis where the Laplace plane transitions from the ecliptic to the equatorial plane. However, we will show in Sec. 5.4.3 that by inducing a slower secular change in Ω, radiation pressure shifts this transition location. Again using the Uranian system as an example, Fig. 5.6 shows the numerical integration of a $Z = 0.1$ particle started at $80R_p$ with a small seed eccentricity and inclination to the ecliptic. The inclination follows a modified Laplace plane (cf. Fig. 5.4) as P-R drag slowly decreases the semimajor axis, and ω_E only becomes stationary when this transition occurs at $a \approx 54R_p$.

5.4.2 Secular Precession Rates

Although the equations of motion become more difficult to solve with each added perturbation, we can make some analytic progress for small eccentricities and inclinations to the ecliptic. The relevant equations of motion, subject to the simplifications mentioned at the beginning of this section, are provided by Hamilton (1993). The elements are referenced to the ecliptic plane (as there is no ambiguity, we henceforth omit the 'E' subscripts), and since we limit ourselves to low inclinations (ignoring terms of order i^2), we switch from ω to the variable $\varpi = \Omega + \omega$. This yields

$$\begin{aligned} \dot{e} &= -n_\odot Z \sqrt{1-e^2}\, \sin(n_\odot t + \delta - \varpi), \\ \dot{\varpi} &= \frac{n_\odot Z \sqrt{1-e^2}}{e} \cos(n_\odot t + \delta - \varpi), \\ \dot{\Omega} &= -\frac{n_\odot Z e}{\sqrt{1-e^2}} \sin(\varpi - \Omega) \sin(n_\odot t + \delta - \Omega), \end{aligned} \tag{5.21}$$

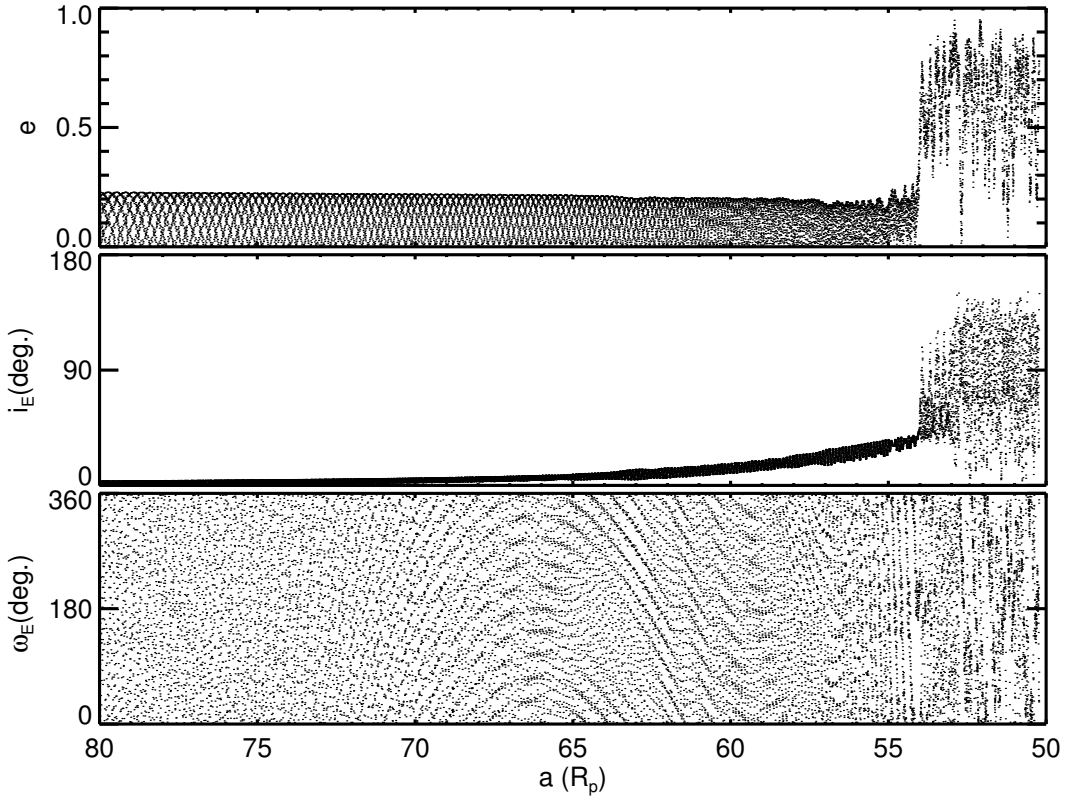

Figure 5.6: Orbital integration of a $Z = 0.1$ particle begun at $80R_p$ from Uranus with $e = 10^{-6}$ and $i_E \approx 0.06^\circ$. Radiation pressure has caused the location of the Laplace plane's transition to shift inward from $a \approx 75R_p$ to $a \approx 55R_p$ (cf. Fig. 5.4).

where δ is the angular location of the Sun at $t = 0$ relative to the inertial reference direction. We approach this system of coupled differential equations through the method of successive approximations. Expanding Eqs. 5.21 in powers of e, we begin by ignoring the terms of order e and higher. In this limit, Ω is constant, and the solution for the first two equations is given by Burns et al. (1979) in terms of the new variables $k = e\cos\varpi$ and $h = e\sin\varpi$:

$$\begin{aligned} k &= k_0 - Z\cos(\delta) + Z\cos(n_\odot t + \delta) \\ h &= h_0 - Z\sin(\delta) + Z\sin(n_\odot t + \delta), \end{aligned} \tag{5.22}$$

where in their solution, the time $t = 0$ has been redefined so that $\delta = 0$. These solutions have a readily-visualized geometric interpretation. The system evolves at a rate $n_\odot$ along the locus of points defined by a circle of radius Z. The center of this circle is offset from (k_0, h_0) away from the Sun's initial position δ (see Fig. 5.7). One can visualize the evolution of e and ϖ from such a representation since the orbital eccentricity at a particular point in h, k space is given by the distance from the origin, and ϖ by the polar angle. The Sun's initial location therefore determines the range of eccentricities explored by setting the location of the circle's center.

We now refine our solution by including terms of order e in an expansion of Eqs. 5.21 in powers of e. Omitting the first equation, which is unchanged,

$$\begin{aligned} \dot{\varpi} &= \dot{\varpi}_0 - \frac{1}{2} n_\odot Z e \cos(n_\odot t + \delta - \varpi) \\ \dot{\Omega} &= -n_\odot Z e \sin(\varpi - \Omega) \sin(n_\odot t + \delta - \Omega), \end{aligned} \tag{5.23}$$

where $\dot{\varpi}_0$ is the zeroth-order rate employed in our first solution. Expanding the trigonometric functions in the equation for $\dot{\Omega}$, and using the substitutions $k = e\cos\varpi$ and $h = e\sin\varpi$, one obtains,

$$\dot{\Omega} = -n_\odot Z(h\cos\Omega - k\sin\Omega)[\sin(n_\odot t + \delta)\cos\Omega - \cos(n_\odot t + \delta)\sin\Omega]. \tag{5.24}$$

We now feed our zeroth order solution back into the above equation. In particular, we treat Ω as constant, and use Eqs. 5.22 for h and k. Since we are interested in how radiation pressure interacts with solar tides and oblateness on long secular timescales, we additionally average over a solar cycle from $t = 0$ to $t = 2\pi/n_\odot$. This then yields the simple expression

$$< \dot{\Omega} > \approx -\frac{n_\odot Z^2}{2}. \tag{5.25}$$

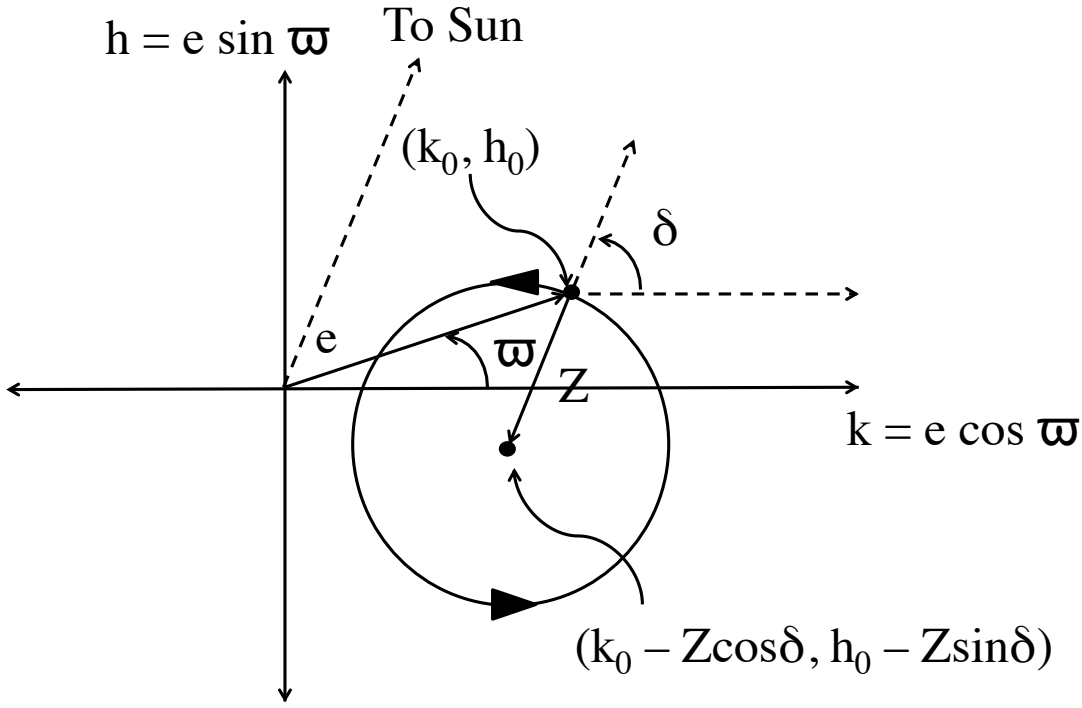

Figure 5.7: Geometrical representation of Eqs. 5.22. The system begins at (k_0, h_0) and evolves along the perimeter of the circle of radius Z at a constant rate $n_\odot$. The orbit's eccentricity e and ϖ can be read as the system point's distance from the origin and polar angle, respectively. The circle's center relative to (k_0, h_0) is set by the Sun's initial position, δ, and lies at the point $(k_0 - Z\cos\delta, h_0 - Z\sin\delta)$.

For small values of Z, this expression is consistent with our previous assumption that Ω evolves at a rate much slower than $n_\odot$ and matches numerical integrations well. As Z approaches unity, our approximations worsen.

Applying the same procedure of inserting the zeroth-order solution and averaging over a solar cycle in the expression for $\dot{\varpi}$ in Eq. 5.23 yields the same

value

$$< \dot{\varpi} > \approx -\frac{n_{\odot} Z^2}{2}. \tag{5.26}$$

Since $\varpi = \Omega + \omega$, this means that the secular change in ϖ is entirely due to Ω. Therefore, to our level of approximation, ω does not move secularly. This justifies our claim from Sec. 5.4.1 that Eq. 5.18 still represents an averaged condition for the halting of pericenter with radiation pressure included. However, as we argue in the next section, radiation pressure can change the semimajor axis at which the eccentricity becomes unstable by modifying the Laplace surface.

5.4.3 The Modified Laplace Surface

We showed in the previous section that, to first order in e, ω does not move secularly; therefore Eq. 5.18 still holds as a condition for the eccentricity to grow to large values. However, the regression of Ω in the ecliptic plane induced by radiation pressure (Eq. 5.25) spoils the Laplace equilibrium between solar tides and planetary oblateness given by Eq. 5.12. Radiation pressure creates a modified Laplace surface (on which the torques from all three perturbations balance) and shifts the location where the local equilibrium plane transitions from the ecliptic to the equatorial plane.

For prograde particles, and to first order in e and i, the secular regression of the node due to solar tides is given by $\dot{\Omega} = -(3/4)\epsilon_{\odot} n$ (e.g., Carruba et al. 2003). Radiation pressure thus enhances the nodal regression induced by the Sun. As a result, the semimajor axis at which these torques balance those from the planet's oblateness (i.e., the point at which the Laplace plane shifts) must move inward, where the effects of the zonal harmonics are stronger.

We do not calculate the detailed warp of the Laplace plane in this paper—for references on the process in the classical case of the competition between solar gravity and planetary oblateness, see Ward (1981) and Dobrovolskis (1993); Allan and Cook (1964) treat the general case of an arbitrary number of non-interacting perturbers in independent planes; for the different case of radiation pressure offsetting planetary oblateness, see (Hamilton 1996, cf. Fig. 18 of Burns et al. 2001). In our case involving all three perturbations, we limit ourselves to estimating the transition location of the Laplace plane where we expect the orbit to become unstable and execute large-amplitude eccentricity oscillations. More concretely, this will approximately correspond to the distance at which the nodal precession rates from the solar tides and radiation pressure balance that due to planetary oblateness: $\dot{\Omega}_{Sun} + \dot{\Omega}_{Rad} = \dot{\Omega}_{J2}$. One can understand this as an approximate condition that the torques from forces directed out of the orbital plane cancel (see Eq. 38 in Burns 1976). The nodal rate due to J_2, now referenced to the planet's *equatorial* plane and again to first order in the inclination, is $\dot{\Omega}_{J2} = -(3/2)\epsilon_p n$ (e.g., Murray and Dermott 1999, p. 270). The nodal rate due to solar gravity is $\dot{\Omega}_{Sun} = -(3/4)\epsilon_\odot n$ (e.g., Carruba et al. 2003).

Substituting for $\epsilon_\odot$ and ϵ_p from Eqs. 5.5 and 5.9, the condition for the balance of precession rates is

$$\frac{3}{4}\frac{M_\odot a_T^3}{M_p a_p^3} + \frac{1}{2}Z(a_T)^2\left(\frac{M_\odot a_T^3}{M_p a_p^3}\right)^{1/2} = \frac{3}{2}J_2\frac{R_p^2}{a_T^2}, \tag{5.27}$$

where a_T is the approximate semimajor axis at which the Laplace plane transitions. For $Z = 0$, the equation can be solved analytically, yielding $a_T = 2^{1/5} r_L$. At Uranus, this corresponds to $74.7 R_p$, which can be seen from Fig. 5.4 to be approximately the location where the inclination is intermediate between 0 and

Uranus' obliquity of 98°. It furthermore quite accurately matches the location at which the eccentricity grows rapidly, and is therefore a slightly more accurate estimator than the dimensionally obtained r_L.

One can roughly estimate the particle size-range in which radiation pressure is important at the Laplace plane transition by setting $\dot{\Omega}_{rad} \sim \dot{\Omega}_{Sun}$, or $n_{\odot} Z(r_L)^2 \sim \epsilon_{\odot} n(r_L) = n_{\odot}^2 / n(r_L)$, where r_L is the Laplace radius from Eq. 5.6. This will generally yield a small value of Z since $Z = 1$ would correspond to a Laplace radius equal roughly to the Hill radius. In the Uranian example previously discussed, this corresponds to $Z \sim 0.05$, or for particles with a density of $1 \mathrm{g/cm}^3$, to $s \sim 70 \mu$m. Figure 5.8 shows numerical integrations of particles around Uranus with radii $s = 20\mu$m-80μm, with the corresponding a_T (numerically obtained) marked as a vertical line.

The modified location of the Laplace-plane's transition from Eq. 5.27 matches the onset of instability to within $\approx 10\%$. As the particle size decreases and Z increases, our approximations worsen, and one can see in the fourth panel that the behavior is beginning to change; the eccentricity first decreases, and later rises in two steps. Our results should therefore be applied with caution beyond $Z \gtrsim 0.2$. We find that for large values of Z, some particles retain low orbital eccentricities as they traverse the unstable region. We note, however, that this range in Z represents a narrow size range since $Z \propto s^{-1}$. In this example, the range $Z = 0.2 - 1$ only corresponds to $s \approx 20\mu$m-4μm (particles with $Z \gtrsim 1$ need not be considered as they would have been immediately removed). If interested in these smallest particles, one must carry out suites of numerical integrations over a wide range of initial conditions to capture the full dynamics.

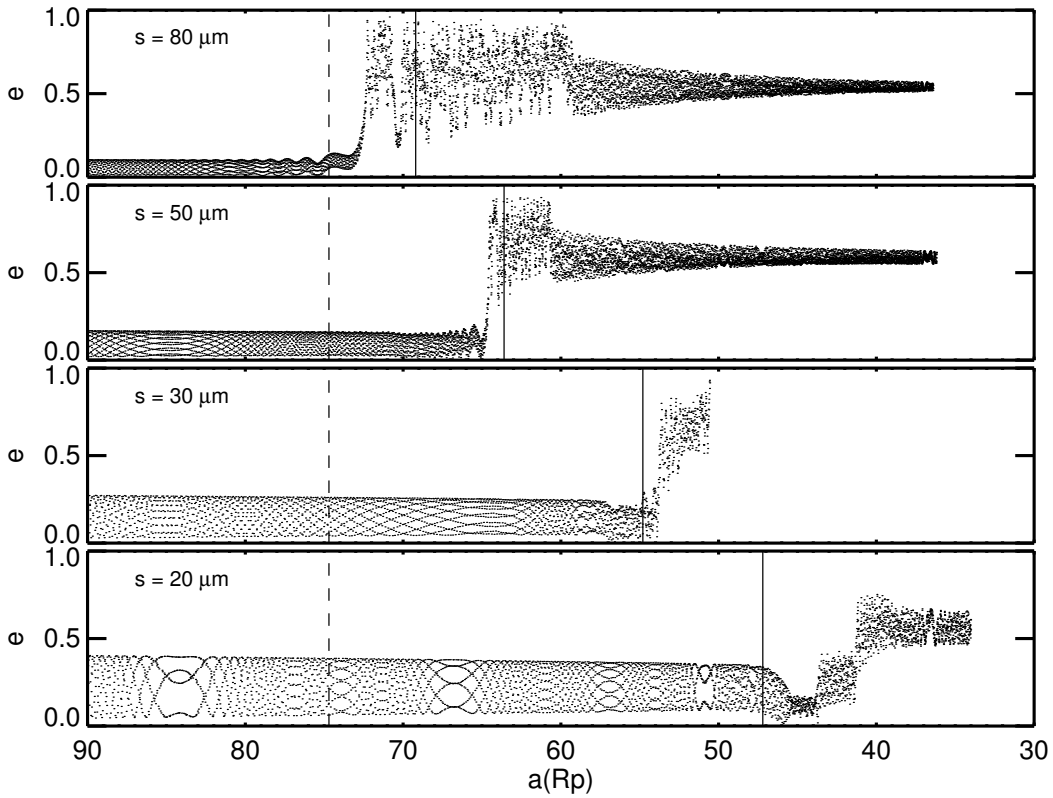

Figure 5.8: Orbital integrations of particles with various radii s orbiting Uranus. The four panels, from top to bottom, correspond to values of Z (at $a = 75R_p$) of 0.04, 0.07, 0.11, and 0.17. Particles were started at $a = 90R_p$ with a seed eccentricity and inclination of $e = 10^{-6}$ and $i = 0.06^\circ$, respectively. The vertical solid lines denote the transition locations of the Laplace plane for each size computed from Eq. 5.27. The dashed lines denote the transition location in the absence of radiation pressure. This predicted position matches the location where the eccentricity destabilizes to within $\approx 10\%$.

5.4.4 Retrograde Orbits

We now briefly consider retrograde orbits, which interestingly can exhibit qualitatively different behavior. For retrograde orbits, $\dot{\Omega}_{Sun}$ and $\dot{\Omega}_{J2}$, which both contain a $\cos i$ dependence, switch sign. One can obtain $\dot{\Omega}_{rad}$ by rederiving the results of Sec. 5.4.2 starting from the equations given by Hamilton (1993) with

$i \approx 180^\circ$ instead of Eqs. 5.21; alternatively, one can employ a symmetry argument similar to ones presented in Hamilton (1994).

One can change a retrograde orbit into a prograde orbit by rotating the coordinate system by 180° around the $\hat{x}$ axis, so that $\hat{z} \rightarrow -\hat{z}$. One can then immediately write down the solution found above for prograde orbits, except in this coordinate system the Sun now moves retrograde, so one must make the transformation $n_\odot \rightarrow -n_\odot$. This yields $\dot{\Omega}^-_{rad} = +n_\odot Z^2/2$, where the superscript minus sign denotes that these are elements in the $-\hat{z}$ coordinate system. The final step is to relate Ω^- to Ω^+, the longitude of the ascending node in the original coordinate system. Since, by the right-hand-rule, the directions in which angles increase in the $+\hat{z}$ and $-\hat{z}$ coordinate systems are opposite in direction, $\Omega^+ = -\Omega^-$. That actually is not quite right, since upon flipping the conventional "up" direction, the ascending and descending nodes switched places, so $\Omega^+ = 180 - \Omega^-$. This yields $\dot{\Omega}^+ = -\dot{\Omega}^- = -n_\odot Z^2/2$; therefore, while the rates due to solar tides and planetary oblateness flip sign for retrograde orbits, the rate due to radiation pressure does not. This is because, while planetary oblateness and solar tides (after averaging over a solar orbit and smearing the Sun's mass into a ring) are symmetric under $\hat{z} \rightarrow -\hat{z}$, radiation pressure is not, due to the Sun's motion changing sense.

The condition for the three torques to balance therefore becomes $|\dot{\Omega}_{Sun}| - |\dot{\Omega}_{rad}| = |\dot{\Omega}_{J2}|$. In this case radiation pressure *detracts* from the solar rate, so the transition location will move outward, where weaker oblateness perturbations are sufficient to offset the reduced combination. There is the further possibility that $|\dot{\Omega}_{rad}|$ overwhelms $|\dot{\Omega}_{Sun}|$, in which case the balance condition cannot be satisfied. Since $|\dot{\Omega}_{Sun}| \propto a^{3/2}$ while $|\dot{\Omega}_{rad}| \propto a$, there will always exist an a at which

the solar rate overtakes the rate due to radiation pressure; however, if that a lies beyond the particle's initial semimajor axis (which is constrained to be smaller than the Hill radius), radiation pressure will always dominate. In this case there is no Laplace equilibrium and the inclination does not transition to the equatorial plane. The instability is thereby avoided. The threshold Z where this occurs is given by the condition $|\dot{\Omega}_{rad}| = |\dot{\Omega}_{Sun}|$. We considered the balance of these two rates at the Laplace radius in the prograde case; the result evaluated at a_0 yields the threshold value of Z, $Z_t \approx [3n_\odot/(2n)]^{1/2}$. Using Eq. 5.20 to solve for the threshold particle size s_t,

$$\frac{s_t}{1\,\mu\text{m}} \approx 0.70 Q_{pr} \left(\frac{1\text{ g cm}^{-3}}{\rho}\right) \left(\frac{M_\odot}{M_p}\right)^{1/4} \left(\frac{a_p}{a}\right)^{1/4}. \tag{5.28}$$

The threshold size in the Uranian case with $a_0 = 140R_p$ is $s_t \approx 46\mu$m. Fig. 5.9 shows the range of behaviors discussed in the previous paragraph for the Uranian case with the same particle sizes as in Fig. 5.8. The direct integrations match our analytic predictions well for our low chosen values of Z. The irregular behavior in the 50μm case is presumably the result of its proximity to the threshold size from Eq. 5.28, but we do not investigate this further in this paper.

5.5 Conclusion

We have shown that the unstable range in semimajor axis around planets with high obliquities found by Tremaine et al. (2009) can be understood as a modification of Kozai oscillations. Furthermore, we extended their work (which focused on orbits lying in the local Laplace plane) and provided equations valid for arbitrary inclination. Although it is difficult to give precise general results, we showed that orbits with inclinations off the Laplace plane are less stable. We

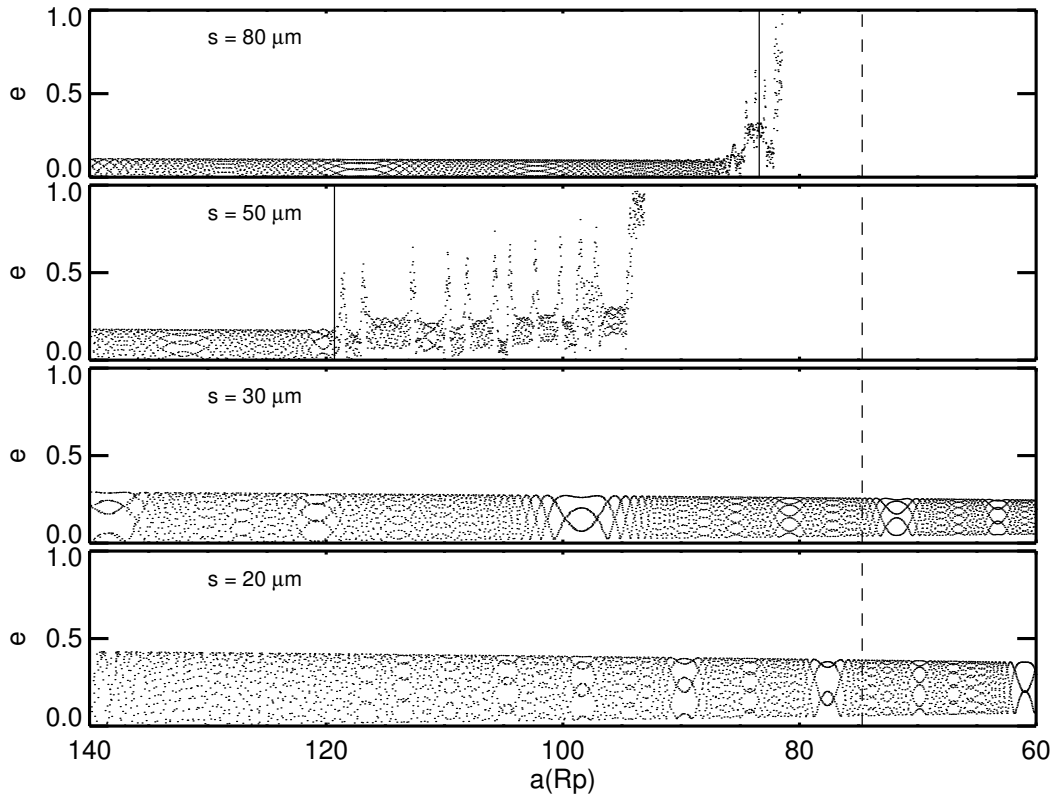

Figure 5.9: Orbital integrations of retrograde particles with various radii s orbiting Uranus. The four panels, from top to bottom, correspond to values of Z (at $a = 75R_p$) of 0.04, 0.07, 0.11, and 0.17. Particles were started at $a = 140R_p$ with a seed eccentricity and inclination of $e = 10^{-6}$ and $i = 179.91^\circ$, respectively. The vertical solid lines denote the transition locations of the Laplace plane for each size computed from the appropriate condition for retrograde orbits discussed in the text. The dashed line denotes the transition location in the absence of radiation pressure. For the bottom two panels, the transition locations are at $a = 751R_p$ and $a = 3803R_p$, the latter of which is beyond the Hill sphere. In these two cases, the Laplace plane does not transition to the equatorial plane and the eccentricities remain stable.

therefore argued that the threshold obliquity of 68.875° found by Tremaine et al. (2009) is an upper limit—inclined orbits can become unstable around planets with lower obliquities.

We then investigated the instability as it applies to dust grains. Dust grains are subject to Poynting-Robertson drag, which provides a natural mechanism to sweep the semimajor axis inward toward the unstable region. However, one must also consider the additional effects of radiation pressure on dust-particle orbits. We found that radiation pressure modifies the classical Laplace surface, and that this shifts the unstable range of semimajor axis. For prograde particles, this chaotic region is shifted inward, while for retrograde particles it is shifted outward, and can even disappear for small particles. We estimated the threshold grain size at which orbital eccentricities remain stable for retrograde particles in Eq. 5.28. For the smallest particles with $Z \gtrsim 0.2$ (cf. Eq. 5.20), or particles with large initial inclinations or eccentricities, our analytical approximations break down. We found in simulations that in such cases, for a minority of initial conditions, even prograde orbits can remain stable. Suites of numerical simulations spanning the range of initial conditions are therefore required to fully characterize a population of dust evolving in toward a high-obliquity planet.

This work can be applied both in the solar system and beyond. Bottke et al. (2010) have proposed that, at each of the giant planets, a vast supply of dust generated by the irregular satellites once existed. At least in the case of Saturn, this supply persists today (Verbiscer et al. 2009). Many irregular satellites have inclinations close to the low-eccentricity threshold for Kozai oscillations, $i \approx 39.2^\circ$ or 150.8°. These orbits are very unstable, and dust originating from such objects might undergo large-amplitude eccentricity oscillations even around planets with modest obliquities. At Uranus, all but the smallest particles will do so, and this might explain the color dichotomies common to the outer four regular satellites observed by Buratti and Mosher (1991). Tamayo et al. (2012a) have

started toward such an explanation, which we will pursue elsewhere. More generally, this instability could be applied to myriad classes of circumstellar binary objects, such as binary KBOs and asteroids. Finally, having incorporated radiation forces, one could consider debris disks in systems with an interior planet (providing an effective J_2) and a highly-inclined companion.

CHAPTER 6

CHAOTIC DUST DYNAMICS AND IMPLICATIONS FOR THE HEMISPHERICAL COLOR ASYMMETRIES OF THE URANIAN SATELLITES

6.1 Introduction

As discussed in the introduction, Buratti and Mosher (1991) found that all five of the primary Uranian satellites, excluding the innermost Miranda, exhibit systematic leading-trailing color asymmetries of roughly 2-23% that increase with distance from the primary. In particular, the leading hemispheres of these tidally locked satellites (pointing in the direction of motion) are redder than their respective trailing hemispheres. Explaining the origin of this phenomenon is challenging. We briefly consider several exogenic possibilities, dismissing endogenic alternatives due to the difficulty of geological processes producing an effect coinciding with the satellite's apex of motion. Exogenic hypotheses can be divided into two categories: sources from within the Uranian system, and sources from beyond.

For explanations that rely on particles that come from beyond the Uranian system, we consider alteration by: (i) interplanetary dust particles (IDPs) (see Cook and Franklin 1970, for an analysis of the Saturnian system), (ii) interstellar dust particles (ISDPs) (Landgraf 2000), (iii) solar radiation (Hodyss et al. 2009), and (iv) cosmic rays (Johnson 1990). A tidally locked satellite on a circular orbit (like the primary Uranian satellites, to an excellent approximation) rotates on its axis once per orbit at a constant rate. For (iii) and (iv), the incoming particle velocity is large enough that the satellite's motion is negligible. Furthermore,

the paths of these satellites over an orbital period ($\lesssim$ 2 weeks) are small compared to the distances over which the incoming particles travel. If one therefore ignores the moon's orbital motion and simply imagines it rotating in place, one can see that the leading and trailing sides will spend an equal amount of time facing each inertial direction. Thus, a distribution of fast incoming particles like solar photons and cosmic rays cannot generate a hemispherical leading/trailing asymmetry.

On the other hand, if the incoming particles have speeds comparable to a satellite's orbital speed ($\sim$ 5 km/s), the moon's motion introduces a detectable asymmetry. Like a car's windshield, the satellite's leading side will accumulate more material relative to its trailing side the faster it ploughs through the rain of particles. This is certainly the case for IDPs, whose speeds relative to the satellites is $v_{Rel} \sim 10$ km/s, and less so for ISDPs ($v_{Rel} \sim 30$ km/s). However, this argument predicts that inner satellites with faster orbital velocities should exhibit stronger asymmetries, which is opposite to the trend found by Buratti and Mosher (1991). Furthermore, gravitational focusing by Uranus would intensify the flux of IDPs and ISDPs nearer to the planet, which again runs counter to the observed pattern. Thus, (iii) and (iv) cannot produce leading/trailing asymmetries, and while (i) and (ii) in principle could, they would generate the opposite trend with semimajor axis to what is observed. It therefore seems unlikely that the source of the Uranian regular satellites' leading/trailing asymmetries lies beyond the Uranian system.

Explanations from within the Uranian system include magnetospheric effects (see Schenk et al. 2011, for a discussion in the Saturnian system), and the infall of dust that originates at the irregular satellites. Though resonant

phenomena could in principle complicate the picture, magnetospheric effects would generally incorrectly predict a larger effect on inner moons, since all the satellites are beyond the co-rotation radius and the magnetic field strength falls off rapidly with semimajor axis (Buratti and Mosher 1991). We are therefore left with the last hypothesis, dust from the irregular satellites, which we evaluate in the remainder of this paper. In fact, though the currently known Uranian irregular moons lay undiscovered at the time, Buratti and Mosher (1991) argued that such dust from unseen outer satellites could account for the observed hemispherical differences.

6.1.1 The Irregular Satellites

To date, nine irregular satellites have been found around Uranus, and many more around the other giant planets. In contrast to the large regular satellites nestled close to their planets, the irregular satellites are a separate population of distant, small moons. These bodies, rather than forming in a circumplanetary disk, are thought to have been captured by their respective planets' gravity (perhaps with the aid of drag forces) early in the Solar System's history (see Nicholson et al. 2008, and references therein). As a result, the irregulars' orbits form a distant swarm of mutually inclined, highly elliptical, crossing orbits. This suggests an intense collisional history that would have generated much debris and dust, particularly at early times (Bottke et al. 2010). Furthermore, micrometeoroid bombardment of the irregular satellite surfaces would contribute further dust over the age of the Solar System.

Dust particles of radius 10μm will then slowly migrate inward through

Poynting-Robertson (P-R) drag on a timescale of five million years, with the timescale for larger particles scaling linearly with grain radius (Burns et al. 1979). Upon reaching the inner Uranian system, this dust will coat the regular satellites. We evaluate the dust grains' ability to generate leading/trailing asymmetries below. Figure 6.1 shows this process schematically. Note that the irregular satellites, which are dominantly affected by solar perturbations, lie (very roughly) symmetrically about the planet's orbital plane, while the regular satellites lie in the planet's equatorial plane, which, due to Uranus' extreme obliquity, is 98° away! The diagram also displays a chaotic range in semimajor axis that is more fully described below.

We pause to caution that several important aspects of these processes are poorly constrained. For example, the lifetimes of dust particles orbiting planets in the outer Solar System are very uncertain. The main mechanisms for grain destruction are sputtering, shattering by micrometeoroids, and sublimation. The last of these is not thought to be important at Uranus and Neptune, and Burns et al. (2001) give sputtering and shattering timescales of $\sim 10^{5\pm2}$ and $\sim 10^{6\pm2}$ years for 1-micron particles orbiting Uranus in its magnetosphere, respectively. However, dust from the irregular satellites lives out its life in a very different environment to typically-considered circumplanetary grains. Because the irregular satellites ($\sim 200-800$ Uranian radii, R_p) reside far beyond the magnetopause ($\sim 20R_p$), sputtering should be much less important. Also, far out in the Uranian gravity well, IDPs and ISDPs are not as gravitationally focused and have reduced orbital speeds, resulting in longer collision timescales. However, depending on the optical depth of the generated dust cloud, one may have to consider mutual collisions between grains (Tamayo et al. 2011). Given our crude knowledge, it is not clear whether lifetimes of such particles can be very long

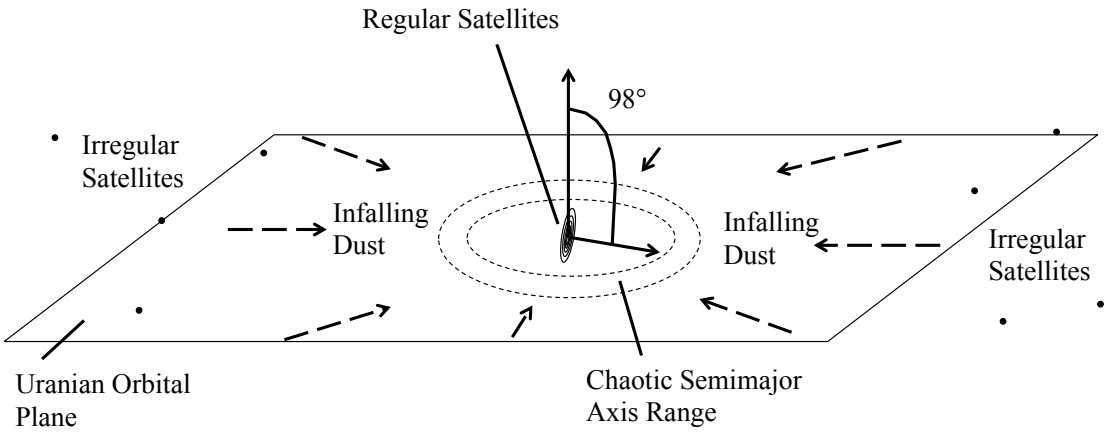

Figure 6.1: Schematic diagram showing the geometry of the Uranian system. The regular satellite orbits lie in the planet's equatorial plane, which is inclined by 98° to the planet's orbital plane, shown by the surrounding rectangle. The irregular satellites (black dots) lie at large distance from the planet on inclined orbits to the planet's orbital plane. They have only been drawn on the left and right for clarity, but there would also be moons at phases in their orbit such that they lie at the bottom and top edges of the plane pictured. Dust from these satellites will spiral inward over millions of years through P-R drag, eventually entering a chaotic semimajor axis range schematically depicted by two concentric, dashed rings. Upon doing so, the dust orbits will undergo chaotic large-amplitude oscillations in eccentricity and inclination. See Sec. 6.1.2 for details.

($\sim$ 100 Myr), or whether large particles will be eroded into smaller particles that evolve inward faster and have longer collisional lifetimes (Burns et al. 2001).

A second uncertainty is the total supply of dust available from the irregular satellites. If this quantity is much smaller than the mass of IDPs striking the regular satellites, it would seem dubious to suppose that the irregulars could be responsible for the color asymmetries. Cuzzi and Estrada (1998) estimate an IDP mass flux $\sim 5 \times 10^{-16}$ kg m^{-2}s^{-1} of IDPs in the outer Solar System. This corresponds to $\sim 10^{14}$ kg on each of the regular satellites over 5 Gyr. As for the irregulars, Bottke et al. (2010) estimate that, over the Solar System's history, these satellites would produce $\sim 10^{20}$ kg of dust solely through mutual collisions (this number would be enhanced by micrometeoroid bombardment). This value, however, is very uncertain since it assumes a number and distribution of primordial irregular satellites that is poorly constrained (it draws initial conditions from models of irregular satellite capture during a Nice-model reshuffling of the planets). Furthermore, as discussed above, it is then not clear what fraction of this dust will survive on its way inward. Nevertheless, we find below that the vast majority of surviving grains will strike one of the regular satellites; it therefore seems plausible that irregular satellite debris represents the dominant source of micrometeoroids impacting the regular satellites.

Finally, the precise mechanism through which incoming dust particles alters the satellites' surface color is unclear. Does the altered color represent a contribution from the dust material? Is the satellite's regolith mineralogy altered by the micrometeoroid impacts due to vaporization and/or melting? Or is it something else? Presumably the answer involves all three.

In the end, we take the view that the above considerations are unfortunately

too uncertain to be of much guidance. Yet if, as we have argued, other sources are unable to account for the hemispheric asymmetries and if, as we will try to show, irregular satellite dust can, then perhaps this provides constraints on these quantities that are so difficult to estimate, like the grain lifetimes and the total dust mass generated by the irregulars.

6.1.2 Dynamics

Buratti and Mosher (1991) favored an infalling-dust explanation of the hemispherical asymmetries by analogy to arguments for the Saturnian satellite Iapetus (Soter 1974; Tosi et al. 2010; Tamayo et al. 2011), which seems to display a much more extravagant hemispherical albedo pattern as a result of subsequent runaway water ice sublimation (Spencer and Denk 2010). This analogy has been strengthened by the recent discovery on Iapetus of a color dichotomy similar to those observed on the Uranian satellites Denk et al. (2010). However, a closer look at investigations in the Saturnian system reveals an important difficulty.

Tosi et al. (2010) and Tamayo et al. (2011) find that Iapetus, the outermost Saturnian regular satellite, intercepts the vast majority of dust grains from the irregular satellites. This should also be the case in the Uranian system. Because the collision time with each satellite ($\tau_{Col} \sim 10^5$yrs) is much shorter than the P-R decay timescale on which the dust moves inward ($\tau_{P-R} \sim 5 \times 10^6$ yrs for the smallest particles), one would expect almost no dust to penetrate inside the orbit of the outermost moon Oberon—yet three moons further in are observed to also exhibit leading/trailing asymmetries. The key breakdown in the analogy between the two planetary systems is a dynamical instability in a chaotic range

of semimajor axes that occurs owing to Uranus' extreme obliquity of 98°. The goal of this paper is to investigate the effects of this instability to assess whether it is consistent with the observed hemispherical color asymmetries.

Tremaine et al. (2009) study the dynamics of circumplanetary-particle orbits under the combined effect of the quadrupole potentials due to the planet's oblateness and the solar tide. They find that around planets with obliquities exceeding 71.072°, particles with orbits starting far from the primary in the planet's orbital plane that are slowly brought inward become unstable over a range of semimajor axes. In this unstable region, orbits undergo chaotic, large-amplitude oscillations in eccentricity and inclination on a secular timescale that is $\tau_{Sec} \sim 10^4$ yrs for circumuranian particles. The unstable range roughly coincides with the location where the strengths of the two perturbations are comparable, which around Uranus, is $\sim 75R_p$ (Tamayo et al. 2013b).

This provides a possible mechanism for creating the color dichotomies observed on the four outermost Uranian satellites. Instead of slowly drifting past Oberon through P-R drag, the grains' pericenters abruptly plunge inward upon entering the unstable semimajor axis range. This would (nearly simultaneously) spread dust across all the inner moons rather than predominantly concentrating it on the outermost satellite. However, the dynamical results of Tremaine et al. (2009) cannot be immediately applied to dust particles, as dust grains are also strongly perturbed by radiation pressure (Burns et al. 1979).

Tamayo et al. (2013b) investigate the orbital modifications created by this additional force. The first important consequence of radiation pressure is that it induces a variation in the particle's orbital eccentricity and pericenter location on Uranus' orbital timescale of $\sim$ 100 years (Burns et al. 1979). We are interested

in much longer secular timescales ($\tau_{\rm Sec} \sim 10^4$ yrs), so these fast oscillations can be averaged out. However, radiation-pressure effects are stronger for smaller particles, leading to larger-amplitude eccentricity variations. Below a threshold particle size, the eccentricity reaches unity within the first half of a Uranian year, and the grain either collides with the planet or escapes the system. Integrations show that this threshold size is $\sim 5\mu$m; we therefore only consider particles of radius 10μm and larger. Tamayo et al. (2013b) also find that radiation pressure shifts the position of the chaotic zone for most orbits with low initial eccentricities and inclinations to the planet's orbital plane. While these analytic results furnish good intuition, the Uranian irregular satellites (and therefore the dust grains they generate) lie on high-eccentricity and high-inclination orbits, forcing our detailed investigation to be primarily numerical. The equation of motion we integrate in our simulations is

$$\ddot{\mathbf{r}} = -\frac{GM_p}{r^3}\mathbf{r} + \frac{SAQ_{pr}}{mc}\hat{\mathbf{S}} - \frac{SA}{mc^2}Q_{pr}[(\dot{\mathbf{r}}\cdot\hat{\mathbf{S}})\hat{\mathbf{S}} + \dot{\mathbf{r}}] - \frac{GM_\odot}{2a_p^3}\nabla[r^2 P_2(\hat{\mathbf{n}}_\mathbf{p}\cdot\hat{\mathbf{r}})] + GM_p R_p^2 J_2' \nabla\left(\frac{P_2(\hat{\mathbf{s}}_\mathbf{p}\cdot\hat{\mathbf{r}})}{r^3}\right), \tag{6.1}$$

where overdots denote time derivatives, and the right-hand terms, in sequence, are due to the dominant Uranian gravity, solar radiation pressure, Poynting-Robertson drag, the Sun's tidal gravity, and Uranus' effective J_2, treating the inner satellites' averaged gravity as a contribution to the planet's quadrupole field. G is the gravitational constant, M_p the planetary mass, r the dust particle's distance from Uranus, S the solar flux at the grain's position, A the particle's cross-sectional area, Q_{pr} the grain's radiation pressure efficiency factor, m the particle mass, c the speed of light, a_p the semi-major axis of Uranus (assumed to be on a circular orbit about the Sun) and P_2 the second Legendre polynomial. The remaining vectors can be seen in Fig. 6.2; $\mathbf{r}$ is the particle's displacement vector from Uranus, $\hat{\mathbf{S}}$ is the unit vector from the Sun to the particle position, $\hat{\mathbf{n}}_\mathbf{p}$

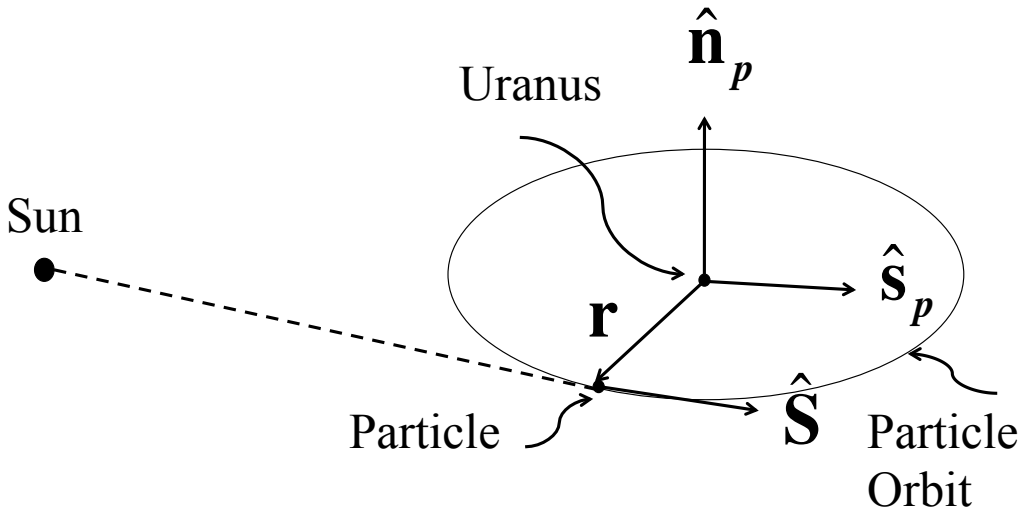

Figure 6.2: Diagram showing the various vectors in Eq. 6.1. The unit vectors $\hat{\mathbf{n}}_\mathbf{p}$ and $\hat{\mathbf{s}}_\mathbf{p}$ point along Uranus' orbit normal and spin axis, respectively. The unit vector $\hat{\mathbf{S}}$ points along the line from the Sun to the particle, and the vector $\mathbf{r}$ is the particle's displacement vector from Uranus.

is the unit vector along the planet's orbit normal, and $\hat{\mathbf{s}}_\mathbf{p}$ is the unit vector along Uranus' spin axis. The effective J_2 including the contribution from the inner satellites is denoted by J_2', and is given by

$$J_2' = J_2 + \frac{1}{2}\sum_{i=1}^{5}\left(\frac{m_i}{M_p}\right)a_i, \tag{6.2}$$

where J_2 is the planetary J_2 coefficient, and m_i and a_i are the ith satellite's mass and semimajor axis, respectively.

In order to demonstrate the viability of the creation of the Uranian color di-

chotomies through dust infall from the irregular satellites, we aim to show four properties of the process: (i) the dynamics are capable of spreading dust across the four outermost satellites, rather than concentrating grains on the outermost moon Oberon, (ii) the innermost regular satellite Miranda is not exposed to a comparable effect, (iii) there is an increasing trend with target satellite semimajor axis, and (iv) the incoming dust-particle distribution creates hemispherical leading/trailing asymmetries. The last point is certainly not obvious in view of Uranus' peculiar obliquity, coupled with the fact that the chaotic orbital evolution of the dust particles generates large-amplitude ($\gtrsim 90^\circ$) swings in the grains' orbital inclinations, allowing them to strike the regular satellites from any direction. The distribution of impacting grains over the regular satellite surfaces is therefore *a priori* highly uncertain.

6.2 Methods

To characterize the dust-transfer efficiency from the irregulars to Uranus' regular satellites (Miranda, Ariel, Umbriel, Titania and Oberon), one would ideally integrate a representative sample of dust particles along with the regular satellites, checking for collisions at each timestep. Unfortunately, the orbital phase space occupied by the irregulars (and the dust particles they create) is enormous. One can reduce the computational load by observing that the satellites' and dust particles' pericenters and their relative nodes circulate rapidly and are roughly uniformly distributed from 0 to 2π. We verified this for our integrations, though our simulations approximate the motion of the regular satellites as a contribution to the planetary quadrupole (Tamayo et al. 2013b), and therefore ignore the effects of orbital resonances (we note that orbits almost exclu-

sively destabilize prior to encountering the first-order resonance regions with the regular satellites). After integrating a dust particle orbit, at each timestep we use the formalism of Greenberg (1982), with corrections from Bottke and Greenberg (1993), to calculate collision probabilities with each of the regular satellites. These formulae calculate a weighted collision probability assuming the pericenters and relative node to be uniformly distributed. The values calculated from a single integration are thus equivalent to an average over a much larger population of orbits so distributed. Finally, we use the methods Tamayo et al. (2011) applied in the Saturnian system to combine the probabilities at each timestep into aggregate values. This approach renders the phase space of initial conditions more tractable. We believe that the errors introduced by this approximation are not significant relative to the uncertainty in the dust grains' physical and orbital parameters. In addition to calculating collision probabilities, we further use the techniques in Tamayo et al. (2011) to calculate the ratio of material striking the leading vs. the trailing side of each satellite. We performed all our integrations with the well-established dust integrator dI (Hamilton 1993) using a Bulirsh-Stoer time-stepper with adaptive stepsize.

Most dust particles escaping irregular-satellite surfaces should have ejection speeds comparable to the satellites' escape velocities (Farinella et al. 1993). Since these escape speeds are much smaller than the satellites' orbital velocities, dust grains should inherit their parent satellites' orbital elements. While our method outlined above circumvents having to sample a variety of pericenter and node positions, the irregular satellites also span a wide range in semimajor axis (a), eccentricity (e) and inclination (i) (Brozovic and Jacobson 2009). In this paper, we limit ourselves to studying the effects of varying a single initial condition with all other parameters fixed. For reference initial conditions, we took the approx-

imate mean values across the known irregular satellites: $a_0 = 460R_p$, $e_0 = 0.35$ and $i_0 = 155^\circ$—where in averaging we have excluded the single prograde irregular, Margaret, and the inclination is measured relative to the Uranian orbital plane (Brozovic and Jacobson 2009). These values should not be taken as necessarily representative of the irregular satellite population over time, as collisions and gravitational perturbations would alter the distribution; rather, they were chosen as sensible (albeit somewhat arbitrary) values for comparison. We chose a reference particle radius s of 50μm, which is large enough to be only moderately affected by radiation pressure, and adopted a particle density equal to that of Saturn's irregular satellite Phoebe, the only irregular satellite for which a density has been directly determined ($\rho = 1.6$g cm^{-3}, Porco et al. 2005).

Taking the above parameters, we performed three suites of integrations, each of which varied a separate initial value. The first sampled the observed range of irregular-satellite orbital eccentricities (e_0 =0.05, 0.2, 0.35, 0.5, 0.65). The second spanned a range of inclinations i_0 ($5^\circ, 15^\circ, 25^\circ, 35^\circ, 145^\circ, 155^\circ, 165^\circ, 175^\circ$), and the last varied s (10, 20, 30, 50, and 100μm). We ignore the intermediate inclinations between $\approx 40-140^\circ$ that will undergo Kozai oscillations since the importance of their contribution is unclear, and our methods cannot adequately handle them. The Kozai effect generates large-amplitude oscillations in the orbital eccentricity. If its eccentricity amplitude is high-enough, an irregular satellite will collide with a regular satellite on a short timescale, preventing it from generating dust with similar orbital elements. It is therefore unclear how much these satellites would contribute to the total dust budget. The reason our methods cannot handle such orbits is that our assumption that the pericenter orientation is uniformly distributed between $[0, 2\pi]$ becomes poor. Beyond a critical inclination that depends on the initial eccentricity, new solutions appear where the peri-

center orientation oscillates around a fixed value (librating solutions), whereas circulating solutions cycle at significantly non-uniform rates. Nevertheless, as discussed in the next section, we expect the behavior of particles undergoing circulating Kozai cycles to match our high-eccentricity cases.

We then calculated the collision probabilities and leading/trailing ratios every 450 yrs. This choice of timestep carefully samples the secular evolution ($\tau_{\rm Sec} \sim 10^4$yrs) and changing collision probabilities ($\tau_{\rm Col} \sim 10^5$yrs), though only captures the fast radiation-pressure induced evolution ($\tau_{\rm RP} \sim 100$yrs) in an average sense.

We started all particles with values of zero for the longitude of ascending node (measured from Uranus' vernal equinox), argument of pericenter, and true anomaly. While it is true that within a single integration the pericenter and relative node (with any given satellite) are roughly uniformly distributed, the chaotic dynamics in the unstable region mean that slightly different initial choices for these values will yield divergent evolution through the chaotic region. Performing the collision probability calculations on orbital histories of initially nearby orbits would then yield different (but equally valid) results. To try and capture this chaotic effect statistically, we instead varied the initial position of the Sun, which also determines the amplitude of the eccentricity oscillation induced by radiation pressure on the fast Uranian orbital timescale (Burns et al. 1979; Tamayo et al. 2013b). Thus, in addition to creating divergent orbital evolution through the chaotic region, this angle choice affects which inner moons can be reached at a given time by changing the amplitude of the fast eccentricity oscillation that is superimposed on the secular evolution. For each of the eighteen combinations of orbital elements given above (five varying e, eight varying

i and five varying s), we ran integrations for sixteen equally-spaced initial solar positions, yielding a total of two hundred and eighty-eight orbital integrations.

6.3 Results

For each group of simulations, we plot the ratio of particles striking the leading vs. trailing hemispheres of each satellite, as well as the "intrinsic" collision probability, defined as the probability of striking a particular moon divided by its total surface area. To see why this might be a better indicator for the generation of hemispherical asymmetries than a total collision probability, imagine that the infalling dust had an equal probability of striking two moons. The two satellites would therefore receive equal quantities of dust; however, if one moon were larger than the other, one would expect a larger effect on the smaller satellite since each area element on its surface is subject to a greater quantity of dust. Normalizing the collision probabilities by the satellite surface areas therefore provides a better comparison.

The results can be qualitatively understood as arising from a competition between three different timescales. The longest is the P-R timescale over which the semimajor axis (and therefore the pericenter distance) slowly decays. In the geometric optics limit, this timescale varies linearly with particle size (Burns et al. 1979), and for the Uranian system is $\tau_{\text{P-R}} \sim s \times 10^6$ yr, with s in microns. Next is the much faster secular timescale on which the eccentricity changes when the instablility is reached, $\tau_{\text{Sec}} \sim 10^4$yrs. Finally, τ_{Col} is the typical timescale on which a dust grain collides with a regular satellite once the particle's orbital pericenter dips below the moon's orbital radius, allowing collisions. While the latter colli-

sion time depends on the particle's orbital elements, our numerical calculations show that $\tau_{\text{Col}} \sim 10^5$yrs, intermediate between τ_{Sec} and $\tau_{\text{P-R}}$.

Figures 6.3a) and 6.3b) show two representative cases. In 6.3a), the unstable zone is reached at $t \approx 20.5$ Myr, at which point the orbit's pericenter abruptly plunges inward and the particle strikes Uranus. However, prior to that at $\sim$ 15 Myr, the pericenter occasionally crosses the orbit of the outermost regular satellite Oberon, due to the large orbital eccentricities ($e_0 = 0.65$, which radiation pressure periodically drives even higher). Then, the pericenter slowly drifts past Oberon on a timescale $\tau_{\text{P-R}} \gg \tau_{\text{Col}}$, allowing that satellite to sweep up most dust particles before they can reach the next moon Titania. By contrast, in panel 6.3b), e_0 is low (0.05), and when the orbit reaches the unstable zone at $t \approx 24 Myr$, the pericenter still lies beyond Oberon's orbit. On the short timescale τ_{Sec}, the pericenter then plunges inside the orbit of several regular satellites, leading to a more equitable distribution of collision probabilities among the inner moons.

We expect that particles undergoing circulating Kozai cycles (not integrated), should roughly match the high ($e = 0.65$) case, concentrating most material on Oberon. Kozai oscillations will periodically drive the eccentricity to high values, allowing the pericenter to cross Oberon's orbit prior to the semimajor axis reaching the unstable range, like in the $e = 0.65$ case. Librating solutions reach lower maximum eccentricities, so this case is more complicated. It is unfortunately not clear what fraction of irregular satellites would be captured onto librating vs. circulating Kozai trajectories, or how significant the Kozai population is to the total budget of dust generated by the irregular satellites. If the Kozai population is found to be important, one would have to use alternate methods to ours for the estimation of collision probabilities, (e.g., Vokrouhlickỳ et al. 2012).

While panels 6.3a) and 6.3b) showed cases on the extremes of our initial eccentricity distribution, panel 6.3c) displays the combined results from all integrations varying e_0 (see caption description). The intrinsic collision probability with Oberon (red) increases substantially for high initial eccentricities, due to the effect discussed in the previous paragraph. At lower eccentricities, the distribution is more equitable due to the interaction of two factors. On the one hand, all other aspects being equal, one would expect inner satellites to intercept more dust due to their higher orbital speeds. Higher relative velocities lead to more frequent encounters between the moon and dust particles, providing more chances for collision. On the other hand, all other aspects are *not* equal, due to the "random" distribution of successive minima in the pericenter distance upon entering the unstable region (panel 6.3b). A smaller fraction of these minima dip low enough to strike an inner moon than an outer one, leading to a fractionation of collision probability. Finally, we note that orbital pericenters rarely dip low enough to reach Miranda. As a result, the intrinsic collision probabilities with Miranda are always much smaller than those with the other moons, consistent with the non-detection of a hemispheric color asymmetry on Miranda by Buratti and Mosher (1991).

Panel 6.3d) plots the ratio of material striking the leading vs. trailing side of each moon. With Uranus' equatorial plane nearly perpendicular to the ecliptic, it is not *a priori* clear what leading/trailing ratio one would expect, particularly since the instability also scatters the orbital inclination over a wide range. The plotted values are averaged over the sixteen initial solar positions, weighted by their corresponding collision probabilities. Thus, the leading/trailing ratio in an integration where Miranda receives 0.03% of dust matters proportionately less than that in a simulation where the collision probability is 3%. The standard

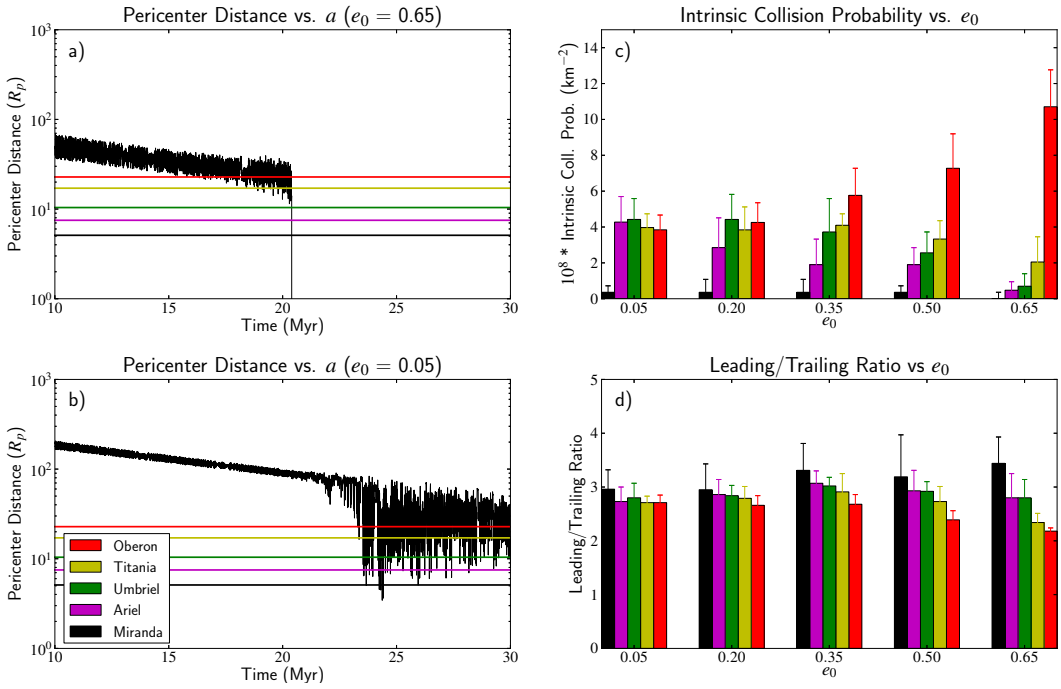

Figure 6.3: Integrations varying e_0 (0.05, 0.2, 0.35, 0.5, 0.65) with $a_0 = 460R_p$, $i_0 = 155^\circ$, and $s = 50\mu$m. Panels a) and b) plot the pericenter distance vs. time for a typical orbit with $e_0 = 0.65$ and $e_0 = 0.05$, respectively. The semimajor axes of the five regular satellites are plotted as horizontal lines, see the color legend on the figure's bottom left (used in all panels). Panel c) shows the intrinsic collision probabilities with each target (total collision probability divided by satellite surface area) for the five values of e_0. The bars over each value of e_0 are offset and arranged from left to right in order of increasing distance from Uranus. Thus, Miranda (left) is in black, and Oberon (right) is in red. Each of the five sets of bar graphs represents an average over sixteen equally spaced initial conditions for the solar position, and the error bars correspond to the standard deviation across those sixteen integrations. Panel d) displays the ratio of material striking the leading vs. the trailing side of each satellite.

deviations are similarly weighted. The calculated leading/trailing ratios range between $\approx 2-4$. Our numerical calculations show a definite preference for material striking the leading sides of all the regular satellites. This is mostly due to the fundamental asymmetry induced by the satellite's motion discussed in the introduction for IDPs and ISDPs. It is analogous to the increase in rain striking a car's windshield at faster speeds through a storm. The slight decrease in the leading/trailing ratio with satellite distance from Uranus seems to be a peculiarity of the chosen initial inclination ($i_0 = 155^\circ$), as revealed by our next set of integrations (Fig. 6.4d).

Figure 6.4 shows our results upon varying the initial inclination. Ignoring for a moment the curious behavior for $i_0 = 35^\circ$ in panel 6.4c), the collision probabilities do not seem to depend strongly on i_0, though systematic differences occur between prograde and retrograde orbits. The distribution is more equitable for prograde particles, while for retrograde particles the intrinsic collision probabilities increase with the target's distance from Uranus. This is due to a difference in the manner the chaotic region is approached, visible in panels 6.4a) and 6.4b). For prograde particles (panel a), the orbital eccentricity spikes abruptly upon entering the unstable region, and the pericenter plunges. The dust can thereby access all the moons on a single $\tau_{\rm Sec}$, leading to a flatter probability distribution among the satellites. By contrast, the eccentricities of retrograde particles undergo gradual growth as the chaotic regime is approached. The pericenter distance is thereby often able to dip inside Oberon's orbit (panel 6.4b) prior to being exposed to the remainder of the moons, concentrating the collision probability on the outermost satellite. We note that each individual excursion inside Oberon's orbit is significant since $\tau_{\rm Col}$ is not much longer than $\tau_{\rm Sec}$, the relevant timescale on which the eccentricity evolves.

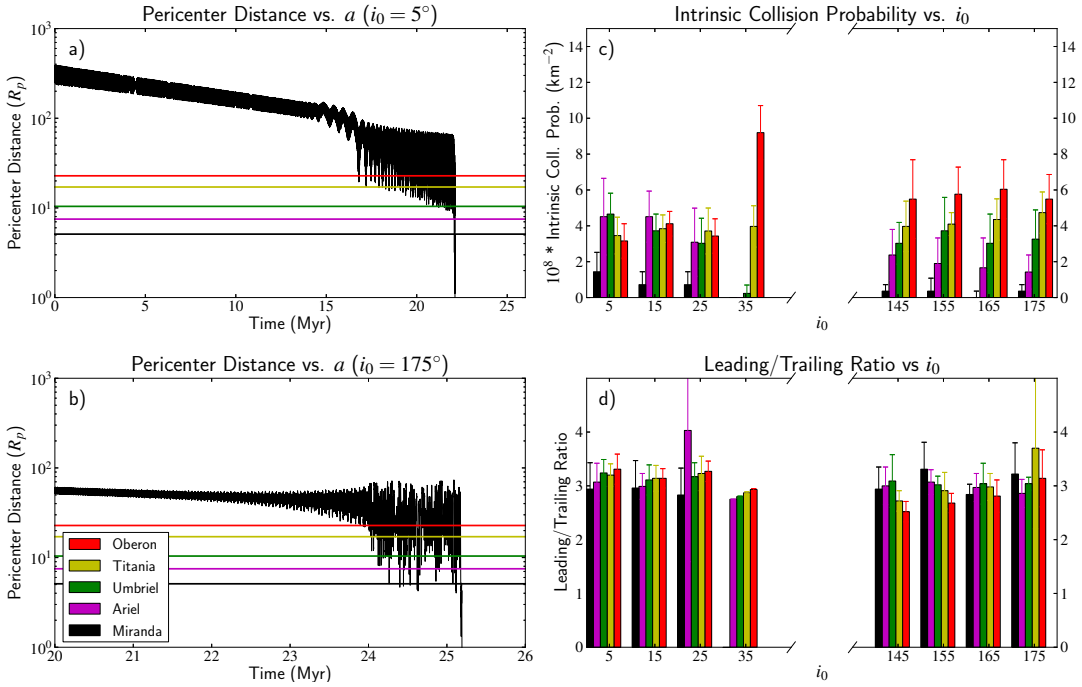

Figure 6.4: Integrations varying i_0 $(5°, 15°, 25°, 35°, 145°, 155°, 165°, 175°)$ with $a_0 = 460R_p$, $e_0 = 0.35$, and $s = 50\mu$m. Panel a) shows the pericenter distance vs. time for a typical orbit in the prograde group with initial inclination $i_0 = 5°$. Panel b) shows a typical orbit in the retrograde group with $i_0 = 175°$. For an explanation of panels c) and d), see the caption to Fig. 6.3.

The dynamical cause of this prograde/retrograde asymmetry is not clear. Similarly curious is the high collisional likelihood on Oberon for $i_0 = 35°$. We find upon inspection of our integrations that at such high inclinations below, but approaching, the critical i_0 at which Kozai oscillations occur ($i_0 = 43.5°$ for $e_0 = 0.35$), the system undergoes nearly regular Kozai-like oscillations prior to reaching the chaotic semimajor axis regime. These high eccentricities bring the pericenter inside Oberon's orbit, but outside the orbital radii of the remaining moons, thus concentrating material on Oberon. The same does not occur for highly inclined retrograde orbits. An analysis of the dynamics in this rich and highly non-linear regime is beyond the scope of this paper. Low-eccentricity or-

bits close to the equilibrium Laplace plane are treated by Tamayo et al. (2013b).

As in the case varying e_0, the leading/trailing ratio ≈ 3, independent of i_0 (panel d of Fig. 6.4). There is no systematic trend with target distance from Uranus.

Figure 6.5 shows our results for various grain sizes. Smaller particles, more affected by radiation pressure, have larger-amplitude eccentricity oscillations ($\tau_{\rm RP} \sim 100$ yrs) superimposed on their secular evolution. Radiation pressure also shifts the position at which orbits become unstable (Tamayo et al. 2013b). Panel c) shows that the collision probability distribution for 50 and 100μm grains are qualitatively similar. Due to the enhanced effects of radiation pressure, we find that the orbital eccentricities of 20 and 30μm particles reach unity within one to a few $\tau_{\rm Sec}$ of entering the unstable region (panel b), and they strike Uranus. The available time for impact with satellites is thus drastically reduced. While in all of the previously discussed cases the fraction of particles striking Uranus was $\lesssim 5\%$, approximately 30% and 40% of particles strike the planet in the 20μm and 30μm cases, respectively. For 10μm particles, and for some 20μm grains, the rapid eccentricity oscillations induced by radiation pressure ($\tau_{\rm RP} \sim 100$ yrs) are of such large amplitude that for some initial solar positions the pericenter dips inside Oberon's orbit before the semimajor axis reaches the unstable region (see panel a). This concentrates the probability distribution on the outermost satellite. We note that, especially for the 10μm particles, the orbital behavior varies substantially across different initial solar positions. The above statement nevertheless remains qualitatively valid.

From panel d), one can see that the leading/trailing ratio remains ≈ 3 for $s \gtrsim 30\mu$m. While we cannot simply explain the decreased asymmetry for smaller

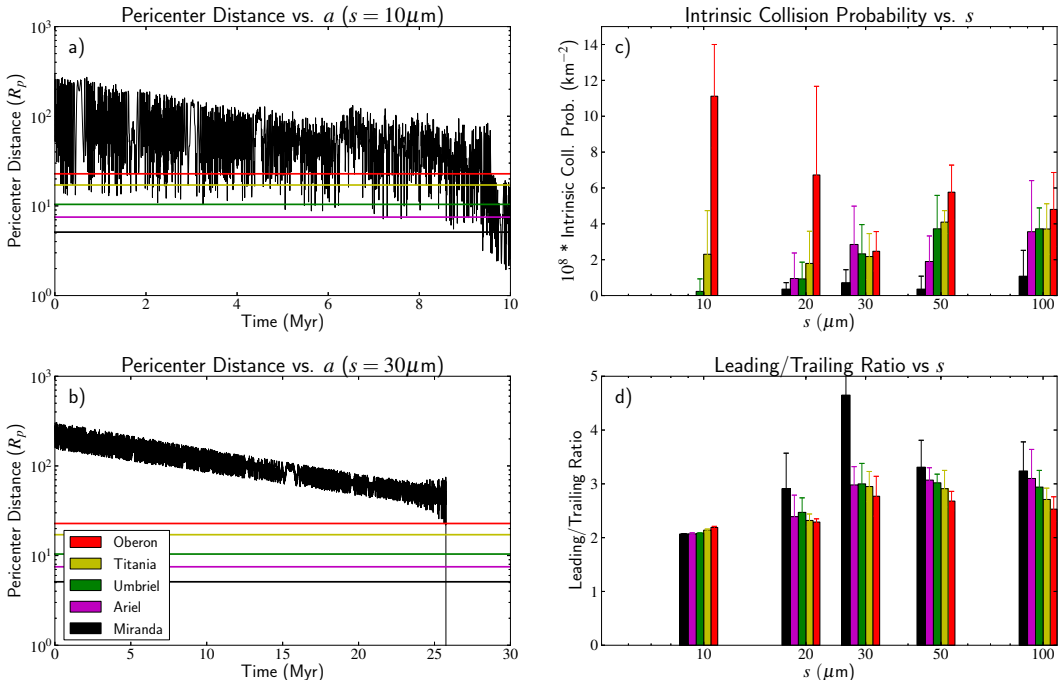

Figure 6.5: Integrations varying s (0, 20, 30, 50, and 100μm) with $a_0 = 460R_p$, $e_0 = 0.35$, and $i_0 = 155^\circ$. Panel a) shows the pericenter distance history vs. time for a typical 10μm particle orbit. Panel b) shows a typical 30μm grain orbit. For an explanation of panels c) and d), see the caption to Fig. 6.3.

particles, it remains true that dust grains will preferentially strike the leading sides of the regular satellites. We performed analogous integrations for prograde particles ($i_0 = 25^\circ$, not plotted) of varying sizes, and found the distributions to be qualitatively similar in all the respects discussed above, with the exception that the anomalously high leading/trailing ratio on Miranda for 30μm particles disappeared, and similar spikes occurred for Titania at $s = 20\mu$m and Ariel at $s = 50\mu$m. In all cases, the standard deviations are large, so we do not believe them to be observationally important.

6.4 Conclusion

In this paper we have tried to find a mechanism capable of explaining the hemispherical asymmetries on the Uranian regular satellites found by Buratti and Mosher (1991). We argued that various sources beyond the Uranian system and magnetospheric effects are either incapable of producing leading/trailing differences, or in cases where they might create asymmetries, that the effect should be largest for the inner satellites. This predicted trend is opposite to what is observed. Innermost Miranda has no detectable asymmetry, and hemispherical differences grow with semimajor axis for the outer four moons (Buratti and Mosher 1991).

We then investigated the dynamics of infalling dust from the irregular satellites as a possible mechanism. This process is complicated by the fact that Uranus' extreme obliquity causes chaotic large-amplitude variations in particles' orbital eccentricity and inclination over a range of semimajor axes (Tremaine et al. 2009; Tamayo et al. 2013b). We found that: (i) dust reaches the outermost four satellites, contrary to the expectation (in the absence of this dynamical instability) that the vast majority of dust would be concentrated on the outermost moon Oberon, (ii) dust-orbit pericenters rarely reach the semimajor axis of Miranda, consistent with the fact that this innermost moon shows no hemispherical asymmetry (cf. panel c of Figs. 6.3-6.5), (iii) for retrograde dust particles, the intrinsic collision probability with each satellite tends to increase with semimajor axis (panel c of Figs. 6.3-6.5), and (iv) despite the unusual Uranian geometry and the fact that the mentioned instability leads to chaotically varying orbital inclinations, approximately three times more dust strikes the leading hemispheres of each of the regular satellites than their respective trail-

ing hemispheres, independent of initial conditions ($\approx$ 2 times for the smallest dust grains); see panel d) of Figs. 6.3-6.5.

We point out that not all initial conditions generate collision probabilities that increase with the semimajor axis of the target satellite. Most notably, only retrograde particles with moderate-to-high orbital eccentricity do. The directionality fits well with the fact that retrograde irregular satellites are more dynamically stable than prograde moons and are therefore longer-lived (Carruba et al. 2002; Nesvorný et al. 2007). Today, out of nine known Uranian irregulars, only Margaret is prograde. The eccentricity requirement does not preclude a population of low-eccentricity impactors (that would tend to produce comparable color asymmetries across the satellites)—it only requires that a significant fraction of the dust population be born on moderate-to-high eccentricity orbits to produce the trend. If the current irregular satellite orbital eccentricity distribution is any indicator of this historical average, this seems plausible.

We therefore conclude that, despite the uncertainties, infall of dust from the irregular satellites furnishes the best explanation for the color asymmetries on the Uranian regular satellites. If this hypothesis is correct, it implies that the lifetimes of dust grains orbiting Uranus at large semimajor axes ($\sim 100R_p$) are much longer ($\gtrsim$ 10 Myr) than in typical planetary magnetospheres. It would also require that irregular-satellite dust infall overwhelm the flux from sources that would generate the opposite trend with semimajor axis, in particular, IDPs. The flux of IDPs over the Solar System's history is quite uncertain, but one can obtain a rough lower limit for the total interplanetary dust mass intercepted by the Uranian satellites by extrapolating the current flux backward in time. Using estimates for the current flux of IDPs in the outer Solar System by Cuzzi and

Estrada (1998), this demands a dust mass generated by the irregulars $\gtrsim 10^{14}$kg over the system's history. While no current dust ring associated with the irregular satellites has been detected thus far around Uranus, the production of dust through mutual collisions between irregulars should have been been strongly concentrated in the first few hundred Myr after the capture of the irregular satellites (Bottke et al. 2010). An analogous diffuse dust ring has been discovered around Saturn with the Spizer Space Telescope; it is generated by the irregular satellite Phoebe (Verbiscer et al. 2009). This Phoebe ring has an estimated mass $\sim$ 3 orders of magnitude smaller than our lower limit of 10^{14} kg. Thus, if our hypothesis is correct, the irregular satellites must have generated a substantial amount of dust in the past.

CHAPTER 7

CONSEQUENCES OF AN ECCENTRIC ORBIT FOR FOMALHAUT B

7.1 Introduction

Fomalhaut b is currently the least massive, directly imaged exoplanet candidate (Kalas et al. 2008). Kalas et al. (2005) had predicted the existence of such a planet due to their discovery that the system's circumstellar debris disk was eccentric ($e \approx 0.1$). This was significant since one expects collisional dissipation to circularize the orbits of bodies in the belt of debris. However, Laplace-Lagrange secular theory shows that planets on elliptical orbits can force similarly eccentric orbits in test particles. Quillen (2006) performed an in-depth study determining that not only could an unseen planet induce the belt's observed eccentricity, it could also explain the disk's observed sharp inner edge as the boundary of the planet's chaotic zone where mean motion resonances overlap and particle orbits are quickly depleted. It was therefore exciting when, using optical images from the Hubble Space Telescope (HST), Kalas et al. (2008) discovered Fomalhaut b at approximately the predicted projected separation from the star in an orbit that seemed capable of explaining the disk's eccentricity (Chiang et al. 2009).

However, Fomalhaut b's planetary status has been controversial. While Currie et al. (2012) and Galicher et al. (2013) performed independent analyses of the optical HST data that confirmed the detection of Fomalhaut b, searches in the infrared (Kalas et al. 2008; Marengo et al. 2009; Janson et al. 2012) did not recover the putative planet. This implies that rather than directly imaging the planet, optical images are detecting starlight scattered by a vast dust cloud, which has led some (e.g., Janson et al. 2012) to discard the planetary interpretation com-

pletely. In this case, however, one must posit an additional unseen perturbation to force the debris disk's observed eccentricity.

Kalas et al. (2008) instead interpreted the dust as lying in an optically thick protosatellite disk about a planet. In principle, this could simultaneously explain both the observed flux and the debris-disk dynamics; however, it is unclear whether such a disk could persist for the system's age of 440 ± 40 Myr (Mamajek 2012). Kennedy and Wyatt (2011) instead suggested that a more diffuse and extended circumplanetary cloud of debris would be a natural consequence of the planet hosting a population of irregular satellites—small, captured moons at the outskirts of a planet's sphere of gravitational influence. Each of the Solar System's four outer planets hosts many such satellites, suggesting they could be a general feature of giant planets (see reviews by Jewitt and Haghighipour 2007; Nicholson et al. 2008). Furthermore, an analogous vast dust ring sourced by the irregular satellite Phoebe persists around Saturn (Verbiscer et al. 2009). While this Saturnian disk is faint, the Solar System's irregular satellite size-distribution suggests that when the Sun was as young as the central star Fomalhaut A, the dust clouds around the giant planets would have been much brighter (Bottke et al. 2010), perhaps yielding comparable fluxes to those observed from Fomalhaut b (Kennedy and Wyatt 2011). Thus, a circumplanetary dust cloud sourced by irregular satellites plausibly explains the observations, and a massive planet on a low-eccentricity orbit ($e \approx 0.1$) can account for the otherwise puzzling elliptical circumstellar debris disk.

However, Kalas et al. (2013)'s (hereafter K13) recent analysis of two additional epochs of HST observations complicate the story further. They find that Fomalhaut b does not move on a low-eccentricity path interior to the circum-

stellar debris disk as previously thought; instead, the orbit has an extreme eccentricity of 0.8 ± 0.1, and crosses the debris disk (in projection). This renders the previous low-eccentricity Laplace-Lagrange secular analyses (Quillen 2006; Chiang et al. 2009) inapplicable to Fomalhaut b. One must now ask not only why the circumstellar debris disk is eccentric, but also how it has managed to survive the gravitational perturbations of an object on such an extreme orbit. One would expect such a crossing orbit to both smear the boundaries of the belt and to puff up its vertical extent, through both secular effects and close encounters. Instead, one observes sharp inner (Kalas et al. 2005) and outer (Boley et al. 2012) edges of a disk that is vertically confined to an opening angle of 1.5° (Kalas et al. 2005). The seeming incongruity between the debris disk's dynamically cold state and Fomalhaut b's highly elliptical orbit may therefore set important constraints on the putative planet's mass and lifetime on its present orbit.

In order to understand the limits imposed by Fomalhaut b's revised orbit, K13 performed numerical simulations for several possible scenarios. In this paper, I perform deeper studies of what I consider to be the most important configurations, probing larger sets of initial conditions and pushing toward longer times. In particular, while K13 focused mostly on orbital timescales, I probe the longer secular timescales on which the orbits of particles in the debris disk can change dramatically. I find this provides valuable new constraints.

I organize my investigation around the need to account for the circumstellar debris disk's observed eccentricity. There are three broad classes of explanation for its elliptical geometry: interactions with other stars, hydrodynamical instabilities within the disk, and planetary perturbations.

First, the central star Fomalhaut A is part of a wide binary. As the two stars undergo a close approach when the companion Fomalhaut B crosses pericenter, one would expect an initially circular debris disk to develop tightly wound, eccentric spiral arms that qualitatively resemble the observed disk (Larwood and Kalas 2001). But as K13 point out, successive pericenter passages would scramble this structure, and the system has undergone many such events over its lifetime. The companion is also too widely separated to induce secular dynamical variations in the disk, as these would have periods of $\sim$ 100 Gyr (K13). Recently, a second companion star has been discovered (Mamajek et al. 2013), though it too is far enough away that its gravitational effect is negligible. Looking beyond the system, Deltorn and Kalas (2001) searched for past close encounters with a sample of $\approx$ 20000 stars whose space motions could be ascertained. They found an F7V star imparted the strongest perturbation 474^{+20}_{-19} Myr ago, with a closest-approach distance of $1.15^{+0.41}_{-0.34}$ pc. However, this is probably too far to excite the observed eccentricity in the belt, and may have predated the belt itself.

In the second class, Lyra and Kuchner (2013) have recently proposed a hydrodynamical mechanism that obviates the need for an external perturber. They find that debris disks with small quantities of gas can spontaneously develop narrow eccentric rings through clumping instabilities. This is a promising possibility, but requires further observational and theoretical investigation. Currently, only upper limits exist on the gas content in the Fomalhaut belt (Liseau 1999), and current simulations do not produce rings that are wide or eccentric enough to match the observed disk. While the disk could be made up of a large number of narrow, unresolved rings, only a fraction of annuli become elliptical in the simulations of Lyra and Kuchner (2013). Resolutions to these problems are beyond the scope of this paper so I do not pursue this possibility further.

Given the above limitations, I investigate the third scenario, namely, that gravitational perturbations from planets are responsible for the belt's elliptical geometry. I treat two limits. In Sec. 7.2, I assume that Fomalhaut b is the only massive object interacting with the disk, and perform numerical simulations to ascertain parameters and dynamical histories consistent with the belt's observed eccentricity. I then consider the alternate possibility of an additional unseen planet dominantly forcing the disk's elliptic geometry. As Quillen (2006) and Chiang et al. (2009) showed, such a planet orbiting interior to the disk can plausibly explain the observed disk geometry, and current infrared surveys (Kalas et al. 2008; Marengo et al. 2009; Janson et al. 2012) have only probed down to masses $> 1 M_J$. Following K13, I dub this hypothetical planet Fomalhaut c. Assuming this configuration, in Sec. 7.3 I investigate how long different-mass Fomalhaut bs could move on their on their present orbit without disrupting the disk, and in Sec. 7.4 I describe some difficulties for a transient-dust-cloud interpretation of Fomalhaut b in light of the revised eccentric orbit. I conclude in Sec. 7.5 by comparing the relative likelihoods of these three scenarios, and by summarizing testable predictions that could differentiate among them.

7.2 If only Fomalhaut b interacts with the disk, what is Fomalhaut b's maximum lifetime on its present orbit?

It is important to point out that if Fomalhaut b is solely responsible for the debris disk's eccentricity, it must be $\sim$ Neptune-mass or larger. This is because Fomalhaut b can only drive the dynamics in the debris disk if its mass is comparable to or larger than the mass in the belt. Estimates of the disk mass are uncertain,

but range from $\sim$ 3 Earth-masses ($M_\oplus$) (Chiang et al. 2009) to $\sim 30 M_\oplus$, though the upper limit could be as large as $\sim$ 1 Jupiter mass if there are objects with radii $\gg$ 1km embedded in the disk (Wyatt and Dent 2002). Following Quillen (2006) and Chiang et al. (2009), I assume the disk's self-gravity is negligible, but as observations better constrain the problem, this approximation may need to be reevaluated.

I focus on the putative planet's effect on the parent bodies in the belt that inject mass at the top of the collisional cascade, thereby generating the dusty disk. We cannot observe such parent bodies directly, but the visible debris they generate through collisions will approximately inherit their parent bodies' orbits (Chiang et al. 2009). Radiation pressure will subsequently modify the orbits of small dust grains (Burns et al. 1979); however, it is reasonable to assume that if Fomalhaut b were to disrupt the cohesion between parent-body orbits, the dust belt would be similarly dispersed. This greatly simplifies the analysis, since it allows one to only consider only gravitational perturbations, ignoring radiation pressure and other non-gravitational forces. Furthermore, it means that one can safely ignore collisions, since, by definition, parent bodies undergo a single collision over the system's lifetime. This was the approach taken by Quillen (2006).

Chiang et al. (2009) tested the above assumption. In addition to considering large parent bodies, they included the effects of radiation pressure on the dust grains that are generated. They found that the scattered light profile derived from dust generated by a sharply confined population of parent bodies is smoothed radially. Nevertheless, Chiang et al. (2009) found that the inner edge of the scattered-light profile matches that of the parent-body population to within 5 % (cf. Figs. 3 and 5 in their work). This claim was verified observa-

tionally with ALMA observations that are instead sensitive to millimeter grains (Boley et al. 2012). These grain sizes are negligibly affected by radiation pressure and are thus excellent tracers of parent bodies. As expected, Boley et al. (2012) find a sharp inner edge at a location consistent with the optical observations. I therefore conclude that we are justified in only considering parent-body orbits.

As for the effects of Fomalhaut b, one might expect that a massive object would disrupt the belt through scattering events during close encounters. This is true for planetary masses $\gtrsim 1 M_J$; for lighter planets, however, the fraction of the belt's circumference that undergoes strong perturbations while Fomalhaut b crosses the disk is small (Tamayo and Burns 2013). K13 also found this in their numerical simulations spanning 2-4$\times 10^5$ yrs (see Fig. 29 in their work). But pushing to longer times, I find that the secular evolution generates a more drastic, global effect. On a timescale of $M_\star/M_p$ parent-body orbital periods, test-particle orbits undergo large-amplitude eccentricity oscillations approaching unity. I therefore focus on this slower, secular evolution. I now describe the simulations and initial conditions in detail. Readers only interested in the results can skip ahead to Figs. 7.1 and 7.2.

A challenge in dynamically modeling the system with Fomalhaut b's orbit only roughly constrained is that the phase space of initial conditions to sample is large. But by focusing on the secular evolution, we additionally benefit from a reduced dimensionality of this space. A classic result by Gauss is that, to first order in the masses, the secular problem is equivalent to smearing out the orbiters' masses along their respective paths in proportion to the time spent at each longitude. The secular problem can thus be formulated as the interaction between the Fomalhaut b "mass ring" and the "rings" corresponding to each of

the parent bodies. In this process, one integrates out the problem's dependence on the orbiters' longitudes. Furthermore, each average is done over a closed orbit in a time-independent, conservative potential; thus, each object's orbital energy, and therefore each of the semimajor axes, is conserved.

Considering only Fomalhaut b and an individual parent body, I have reduced the phase space of initial conditions by two by ignoring their respective longitudes. Furthermore, since the semimajor axes are constant, I can consider their constant ratio as a single parameter. A final simplification obviates the need to sample a range of planetary masses. Since I only treat Fomalhaut b as massive, and work to linear order in this mass, I factor out the planet's mass from the perturbing Hamiltonian $\mathcal{H}_p$ acting on each test particle,

$$\mathcal{H}_p = M_p \mathcal{H}'_p, \tag{7.1}$$

where $\mathcal{H}_p$ is the perturbing Hamiltonian, and $\mathcal{H}'_p$ is the "Hamiltonian" with M_p, the mass of Fomalhaut b, factored out. The change of the orbital elements, expressed in canonical variables, is of the standard Hamiltonian form

$$\frac{d\rho}{dt} = \pm M_p \frac{\partial \mathcal{H}'_p}{\partial \sigma}, \tag{7.2}$$

where ρ is a canonical coordinate or momentum (this choice determines the appropriate sign), and σ is the conjugate variable to ρ. I now absorb the dependence on M_p by introducing a dimensionless time $t' = t/\tau_{Sec}$ with

$$\tau_{Sec} = \frac{M_\star}{M_p} P, \tag{7.3}$$

where $M_\star$ is the mass of the central star, $1.92 \pm 0.02 M_\odot$ (Mamajek 2012), and P is the test-particle's orbital period (which is constant since it is given by the test particle's semimajor axis through Kepler's third law). This yields,

$$\frac{1}{P}\frac{d\rho}{dt'} = \pm M_\star \frac{\partial \mathcal{H}'_p}{\partial \sigma}, \tag{7.4}$$

which is independent of M_p. This means that if a given M_p yields a given orbital history, one can immediately generate an orbital history for a different M'_p by stretching the time axis by the ratio M_p/M'_p. This is a familiar feature of a test particle undergoing Kozai oscillations, which is a specialized case of secular dynamics with a single perturber.

Since the test particles have no mass with which to affect Fomalhaut b, the latter's orbit remains fixed throughout the simulation. I therefore construct my coordinate system around Fomalhaut b's fixed path. I first choose the planet's orbital plane as the reference plane. Thus, Fomalhaut b's orbital inclination $i_p = 0$. Furthermore, I choose the direction toward the planetary orbit's pericenter as the x axis, which sets the planetary orbit's longitude of pericenter to 0. Thus, the only remaining (constant) parameters, are Fomalhaut b's orbital semimajor axis a_p, and eccentricity e_p. I sampled e_p over the range $[0.05, 0.95]$ in increments of 0.1, and a_p from 60 to 340 AU in steps of 20 AU, the latter range covering approximately two standard deviations around the best-fit value of a_p found by K13. I thus performed 150 separate simulations for each possible combination of a_p and e_p.

Finally, for each simulation, I must choose the initial orbital elements for the test particles. I assign particles orbital eccentricities of 0.1, the approximate value observed for the debris disk (Kalas et al. 2005), and the semimajor axis corresponding to the belt's brightness peak of 142 AU (K13). I take only a single test-particle orbital semimajor axis and vary the planet's a_p since, as mentioned above, the dynamics only depend on the ratio of these two values. One can therefore take my final results and translate them to other values of a by adequately scaling a_p.

I sampled the test-particle orbital angles as follows. K13 find that, to 95% confidence, the disk's inclination (i) relative to Fomalhaut b's orbital plane is under 45° (see Fig. 22 in their work). K13 also find that 90% of the orbits that can fit the data are apsidally aligned with the disk to within 36° (see Fig. 23 in their manuscript). However, partly in order to make my results applicable to the general problem of radially crossing orbits, I chose to independently sample both the longitude of the ascending node (Ω) and the argument of pericenter (ω). Of course, the apsidally aligned case still is a subset of my initial conditions. In each simulation, I generated one thousand initial conditions for all combinations of ten equally spaced values of i in the range $[0, 45^\circ]$, and ten equally-spaced values for both Ω and ω in the range $[0, 360^\circ]$.

I performed all the numerical integrations with the secular integrator smpGauss (Touma et al. 2009). A numerical difficulty for integrating radially overlapping orbits is that as the orbits precess, two orbits can intersect at a point. In such an event, the mutual forces suffer a discontinuity that is difficult for integrators to handle. The integrator smpGauss circumvents this difficulty by using softened gravity. This approximation reflects the reality that collisions are unlikely even in cases where two orbits intersect at a point, since the probability that both objects will cross the intersection point at the same time is generally small. One would therefore expect that the softened secular solution should match a full integration until the test-particle suffers a close encounter with the planet. I used a softening length of 0.01 AU, and verified that the secular integration matched a full N-body integration to within $\sim 1\%$, though only for about one secular timescale τ_{Sec} (cf. Eq. 7.3). I found that this is due to the secular dynamics being chaotic for overlapping orbits, with neighboring trajectories diverging after $t \sim \tau_{Sec}$. This limitation is acceptable, since below I only consider

a single secular period to constrain Fomalhaut b's properties.

I then performed the numerical integrations for the described suite of initial conditions, searching for regions of (a_p, e_p) parameter space in which the particles' orbital eccentricities remained low on secular timescales. The observed belt has a width $\sim 20AU$, or $\sim 15\%$ of its semimajor axis. In principle, this could be explained through parent bodies with a single semimajor axis and an eccentricity dispersion ~ 0.15. To be conservative, I take twice this value ($e = 0.3$) as a threshold beyond which eccentricities are incompatible with observations. Figure 7.1 shows the percentage of the thousand initial conditions that stayed below $e = 0.3$ over a single secular cycle in each simulation and are therefore nominally consistent with observations. The solid white lines are the boundaries of the region of parameter space where Fomalhaut b's orbit would radially overlap the test particle's path if one approximated the latter orbit as circular. Above these lines, Fomalhaut b's orbit is eccentric enough to cross the test particle's path.

To within the resolution of the grid, all initial conditions are driven to high eccentricities in configurations where Fomalhaut b overlaps the test-particle's orbit (above the two curved solid white lines). This result is general—a massive body on an eccentric orbit that crosses a belt of test particles on near-circular orbits will globally drive the latter onto similarly elliptical paths on secular timescales (not just particles that suffer close encounters). This agrees with the intuition from low eccentricity and inclination Laplace-Lagrange secular theory; however, the result was not clear *a priori* since a) the high eccentricities and inclinations mean that additional terms in the disturbing function are important (e.g., Murray and Dermott 1999), and b) the disturbing function's expansion is

itself predicated on the assumption that the orbits do not cross.

The dashed white lines in Fig. 7.1 bound the region of phase space that is consistent with the observed deprojected distance of Fomalhaut b from the central star of 119 AU (Kalas et al. 2008); below these lines, Fomalhaut b orbits too close (far) to reach its observed position at apocenter (pericenter). The cross represents the best-fit value of (a_p, e_p) from K13, with their marginalized 1-σ error bars. The figure shows that the region of phase space where Fomalhaut b's orbit is consistent with its observed distance from the star (above the dashed white lines) and does not drive parent bodies onto high-eccentricity orbits (lighter shades in grayscale) is narrow, restricted to small eccentricities, and inconsistent with the orbit determined by K13 (solid white cross)—see also Fig. 7.2.

I note that one cannot argue that we are observing the belt at a low eccentricity as part of a long-lived, larger-amplitude cycle. As mentioned previously, the secular evolution is chaotic on a timescale $\sim \tau_{Sec}$; we would therefore see different belt particles at widely varying phases along the cycle, forming a much more radially extended disk than is observed.

The evolution is also rapid compared to the age of the system (440 Myr). Fig. 7.2 shows the same grid as Fig. 7.1, but assumes that Fomalhaut b has a mass equal to Saturn's, and the color scale represents the median time required for parent bodies in the given grid point to reach $e = 0.3$ (out of the initial conditions that did so). Only grid points where more than 90% of the initial conditions were driven to high eccentricities (see Fig. 7.1) were coded in this way—other grid points were colored white to indicate they may be dynamically stable. The times in the figure can be immediately translated to a different-mass Fomalhaut

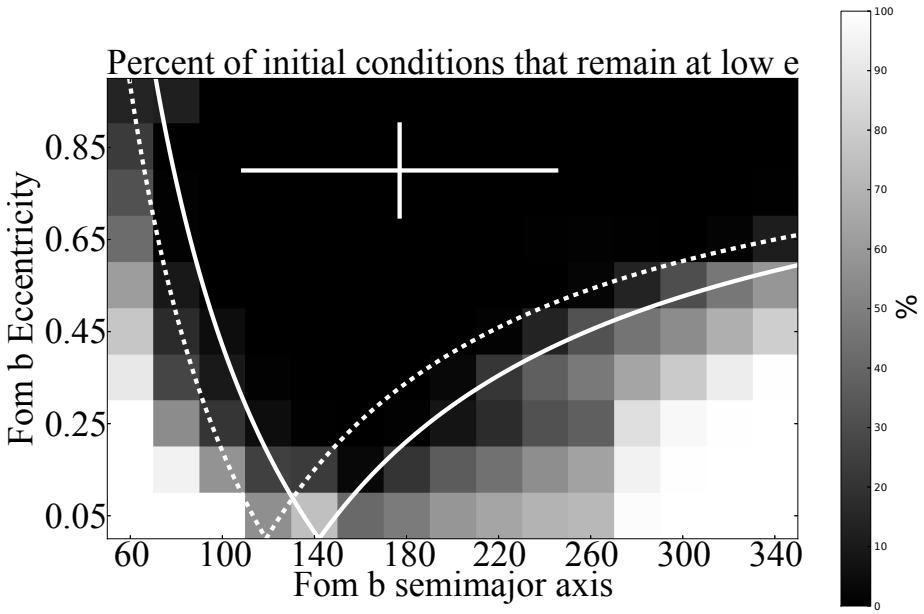

Figure 7.1: Each grid point, representing a combination of Fomalhaut b's semimajor axis and eccentricity, contains 1000 equally-spaced initial conditions for test particles representing parent bodies in the debris disk. The gray-scale represents the percentage of those initial conditions that remained at low eccentricity over one secular cycle and are possibly consistent with the observed disk. The region above the solid white line roughly represents Fomalhaut b orbits that cross the debris disk in projection (the debris disk is assumed circular and at 142 AU). To within the resolution of our grid, Fomalhaut b orbits that cross the debris disk push nearly all parent bodies onto high-eccentricity orbits. The region below the dashed white line is inconsistent with the deprojected distance of Fomalhaut b from the central star of 119 AU (Kalas et al. 2008). The white cross gives the marginalized 1-σ error bars for Fomalhaut b's orbit from K13.

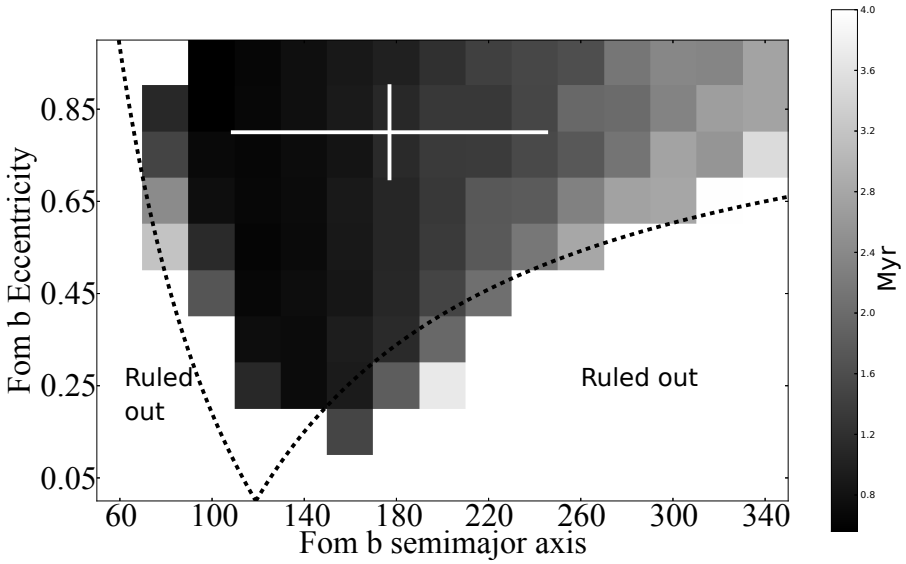

Figure 7.2: Grid and simulations depicted are the same as in Fig. 7.1. The gray-scale now represents the median time required for parent-body orbits in the given grid point to reach $e = 0.3$, assuming Fomalhaut b has Saturn's mass (timescales for other planet masses can be straightforwardly obtained, see text). Grid points where more than 10% of initial conditions remained at low eccentricity are plotted white. The region below the two dashed black lines corresponds to the area of phase space that is ruled out by the fact that Fomalhaut b would never reach its current observed distance from the central star of $\approx 119AU$ (Kalas et al. 2008). The white cross gives the marginalized 1-σ error bars for the orbit determination of Fomalhaut b from K13.

b by multiplying the values by the ratio of Saturn's mass to the mass of interest (see Eq. 7.3). One can also interpret Fig. 7.2 as the rough times Fomalhaut b would require to raise an initially circular debris disk to its present eccentricity of $e \approx 0.1$.

An important additional constraint is the observed alignment between the pericenters of the debris disk and Fomalhaut b. It is also unclear whether the

disk would retain a coherent shape as the eccentricities rise to the observed value of $e \approx 0.11$ (Kalas et al. 2005). To test this, I created a massless debris disk of 10^4 parent bodies that is initially centered at 142 AU, 20 AU. I assumed the initial random velocities in the debris were low and isotropic, drawing initial eccentricities and inclinations from uniform distributions over $[0, 0.01]$ (with inclinations in radians). I then gave Fomalhaut b the mass of Saturn, and took K13's marginalized best-fit elements of an orbital semimajor axis of 177 AU, eccentricity 0.8 and inclination to the disk of 17°. I took the mutual line of nodes to coincide with Fomalhaut b's major axis—this orientation is difficult to determine observationally since the mutual inclination is low. Snapshots of the evolution are shown in Fig. 7.3. The left panels show a top-down view (looking down Fomalhaut b's orbit normal), while the right panels show an edge-on view to Fomalhaut b's orbit—the dashed line represents Fomalhaut b's orbital plane. The stars represent the central star, while the plus signs show the instantaneous center of the debris disk, averaged over all test particles.

By t = 0.4 Myr (second row), the parent-body orbits have evolved in near-unison to eccentricities of 0.14, comparable to the mean belt eccentricity measured by Kalas et al. (2005) of 0.11. This can be seen in the offset (plus sign) in the center of the debris disk from the central star (a low-eccentricity orbit is an offset circle to lowest order). The longitudes of pericenter, measured relative to Fomalhaut b's pericenter are narrowly distributed around 84.7° (standard deviation is 2.5°). The eccentricities then continue to rise, accompanied by a dramatic secular inclination evolution. By t = 4.4 Myr (third row), the orbits have rotated about their respective major axes into nearly polar orbits, and the eccentricities have reached their maximum value of ≈ 0.95. The orbits then continue rotating about their major axes, rendering them retrograde. By the time

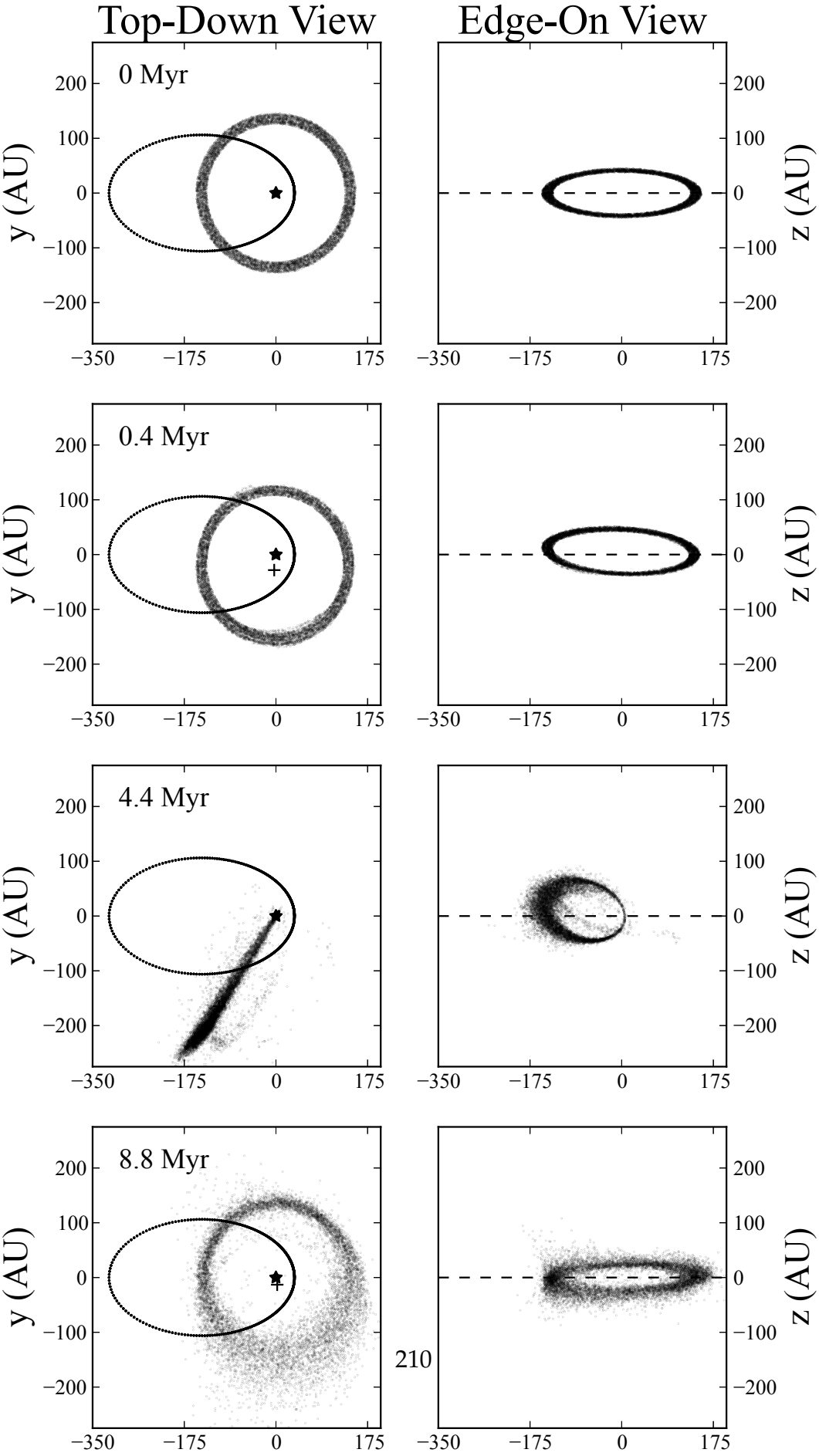
Top-Down View
Edge-On View
0 Myr
0.4 Myr
4.4 Myr
8.8 Myr
y (AU)
z (AU)
200
100
0
−100
−200
−350
−175
0
175

the eccentricities decrease once again to values ~ 0.11 (t = 8.8 Myr, bottom row), the mean inclination of the disk-particle orbits to Fomalhaut b's orbital plane is similar to the corresponding epoch at 0.4 Myr (second row), except in a *retrograde* sense. However, because the orbital evolution is chaotic on these secular timescales, the particle orbits have by this time diverged from one another, rendering the disk both radially and vertically extended, inconsistent with observations. Over longer timescales than those plotted, particle orbits diverge further, and continue flipping between prograde and retrograde orbits. Such flips are qualitatively very similar to those analyzed by Li et al. (2013) while studying the effect of an outer eccentric perturber on an inner test particle that is also on an eccentric orbit; however, their analytical work cannot be directly applied to the present case where the orbits cross.

I tested the robustness of the above results by trying seven other equally spaced orientations for the line of nodes—in all cases, similarly eccentric disks were formed at 0.4 Myr, the mean longitude of pericenter was within ten degrees of 90°, and orbits flipped back and forth between prograde and retrograde senses. This behavior is consistent with that reported first by Beust et al. (2013) (see note following the acknowledgements).

This predicted near-right angle between the disk's and Fomalhaut b's pericenters is largely ruled out by the data; however, since fits to the data with such large misalignments do exist (see the green points at near-right angles to the disk's major axis in Fig. 24 of K13), I briefly consider the consequences of such a scenario.

Figure 7.4 shows the secular evolution of four debris disk particles with similar initial conditions, drawn from the grid point in Fig. 7.1 closest to Fomalhaut

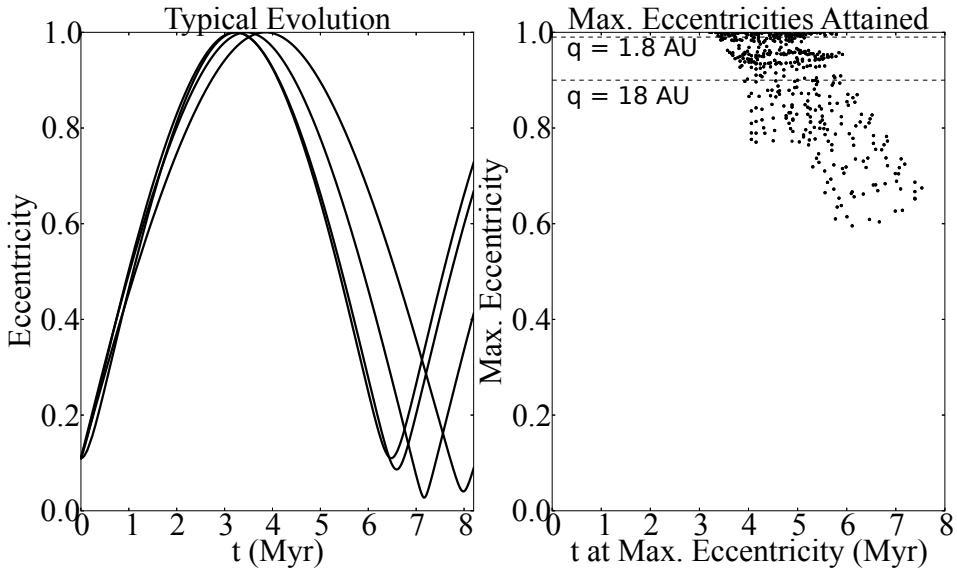

Figure 7.4: Left panel: Secular evolution of four debris disk particles with similar initial conditions, drawn from the grid point closest to Fomalhaut b's best-fit orbit from K13 in Fig. 7.1 (a=180 AU, e=0.85). All four particles reach eccentricities near unity, and begin to diverge after $\sim$ 1 secular oscillation as mentioned in Sec. 7.2. The simulation assumes Fomalhaut b has the mass of Saturn. Right panel: Maximum eccentricity attained by each of the thousand initial conditions for the same grid point mentioned above, plotted vs. the time at which the maximum value was achieved. The dashed lines mark pericenter distances of $q = 1.8$ and $q = 18$ AU, showing that a large fraction of objects will reach the innermost Fomalhaut system.

b's best-fit orbit from K13 (a=180 AU, e=0.85). It assumes Fomalhaut b has the mass of Saturn, but one can simply scale the time for a different mass M_p by multiplying all the times by the factor M_{Sat}/M_p (see Eq. 7.3).

The right panel of Fig. 7.4 shows the maximum eccentricities attained in the first secular cycle for the thousand initial conditions in the same grid point of Fig. 7.1 identified above. The dashed lines represent pericenter distances of 1.8 and 18 AU. I find that 66% of initial conditions drop below 18 AU, and 30% fall

below 1.8 AU. These values vary by about 15% between adjacent grid points. Thus, within the next few Myr, the inner Fomalhaut system would be injected with a large number of high-eccentricity impactors. If the Fomalhaut system harbors interior planets, they would then undergo a violent period perhaps analogous to the Solar System's hypothesized Late Heavy Bombardment 4.1-3.8 Gyr ago, when the impact rate on the Moon and other terrestrial planets may have spiked (Hartmann et al. 2000).

The main conclusion of this section is that it is unlikely that Fomalhaut b is a Neptune-mass or larger planet if it is the only body interacting with the debris disk. Not only would Fomalhaut b need to have scattered into its present orbit in the last $\sim 1-10$ Myr to not have disrupted the disk, current data largely rules out the predicted $\sim 90^\circ$ misalignment between the disk's and planet's pericenters. On the other hand, the deleterious gravitational effects from a Fomalhaut b roughly less massive than Neptune would be attenuated by the disk's self-gravity. In this case, however, one must invoke an alternate mechanism for producing the observed eccentricity of the debris disk. I thus turn in the next two sections to the alternate possibility that an unseen planet is dominantly responsible for forcing the debris disk's observed eccentricity and shaping its sharp inner edge.

7.3 If an unseen planet dominantly forces the eccentricity in the debris disk, what is Fomalhaut b's maximum lifetime on its present orbit?

I argued in the introduction that if Fomalhaut b cannot force the debris disk's observed eccentricity (because it is either too light or scattered into its present orbit too recently), then the best explanation for the belt's elliptical geometry is an unseen planet (Fomalhaut c) orbiting interior to the disk. Importantly, the addition of a second planet relaxes the constraints from the previous section. If Fomalhaut c's mass (M_c) is larger than that of Fomalhaut b (M_b), the former can dominate the secular dynamics and test particles can be partially shielded from the latter's extreme effects. Nevertheless, the fact that we observe the belt as dynamically cold sets important limits on Fomalhaut b's mass and on its lifetime in its current orbit.

My numerical experiments, detailed below, are similar to ones performed by K13 (see their Sec. 9.3.3). The key difference is one of timescale. K13 were interested in showing that physical crossings of Fomalhaut b through the disk would not destroy the belt structure. They therefore chose the most damaging configuration—namely, a coplanar system where Fomalhaut b plows through the disk every orbit. They found that, indeed, Fomalhaut b does not interact with enough of the disk's circumference to erase its structure for $M_b \lesssim 1 M_J$. However, the coplanar arrangement limited their integrations to less than 0.5 Myr, since eventually Fomalhaut b and Fomalhaut c would scatter and the system would no longer be coplanar. But these timescales are too short to probe the dramatic secular effects we found in Sec. 7.2. I therefore simulate longer times

in a non-coplanar configuration, consistent with the observation that Fomalhaut b's orbit is likely mutually inclined with the disk (K13).

Perhaps the most constraining feature of the debris disk is its narrow vertical extent. The radial extent of the belt could support a comparatively wide range of semimajor axes and eccentricities, but the relative inclinations between particles must unambiguously remain small. Photometric models by Kalas et al. (2005) give an opening angle of $\approx 1.5^\circ$. For $M_b \ll M_c$, one expects test particles to remain coplanar with Fomalhaut c, but as M_b approaches M_c, the inclined Fomalhaut b (marginalized best-fit value $i \approx 17^\circ \pm 12^\circ$, see Fig. 22 in K13) should pull particles out of the plane on secular timescales. The conclusions from this section should hold as long as Fomalhaut b's inclination to the debris disk is $\gtrsim$ the disk's opening angle.

Since these secular timescales are shorter than the age of the system for $M_b \gtrsim 1 M_\oplus$, we must once again conclude that Fomalhaut b scattered onto its present path relatively recently. I artificially simulate this event by injecting Fomalhaut b into its current orbit only after letting Fomalhaut c dynamically shape the disk's inner edge and allowing the belt to reach a quasi-steady state. I then recorded the time required for Fomalhaut b to disrupt the disk, as a function of planet mass. Infrared surveys to date that have failed to detect planets in the Fomalhaut system have been sensitive to planet masses $> 1 M_J$ (Kalas et al. 2008; Marengo et al. 2009; Janson et al. 2012). I therefore assign Fomalhaut c a mass of $1 M_J$—the best-case scenario for shielding the belt from Fomalhaut b and thus for system stability. I will argue that Fomalhaut b's lifetime on its present orbit must be much shorter than the system's age (making it unlikely to observe the planet at this special time), so lower Fomalhaut c masses would only exacerbate

the problem. The model is purposefully simple since there are currently too many unknowns to perform an in-depth dynamical study spanning the space of possible initial conditions.

My detailed initial conditions were as follows (results are in Figs. 7.5 and 7.6). I take Fomalhaut c to be on the orbit that Chiang et al. (2009) found to best fit the disk's morphology for a $1M_J$ planet, and Fomalhaut b to be approximately on the best-fit orbit found by K13. Specifically, for Fomalhaut c, I adopted $a_c = 109AU$ and $e_c = 0.123$, where the c subscript corresponds to Fomalhaut c (Chiang et al. 2009)[1]. I reference the coordinate system to Fomalhaut c's *initial* orbit (which will change once Fomalhaut b is introduced), so at first $i_c = 0$ and the longitude of pericenter is 0. I then introduce 10^4 test particles representing the parent bodies in the debris disk. For each orbit, I randomly assign $125 < a < 155$ AU, $0^\circ < i < 1.5^\circ$, $0^\circ < \Omega < 360^\circ$, and $\omega = -\Omega$ so that the orbits are apsidally aligned with Fomalhaut c (the longitude of pericenter $\varpi = \Omega + \omega = 0$). The orbital eccentricities were set to the forced values calculated from Laplace-Lagrange secular theory (see Eq. 13 in Chiang et al. 2009). I chose the semimajor axis range to roughly match the observed disk's radial extent, though it extends further inward so that I can numerically determine the boundary of the planet's chaotic zone where particles should be depleted. The inclination range was chosen to match the photometric models of Kalas et al. (2005).

I then integrated Fomalhaut c and the 10^4 test particles for 100 Myr, in order to numerically establish the inner boundary of the planet's chaotic zone and

[1]Subsequent to the work of Chiang et al. (2009), Fomalhaut A's mass has been revised downward by $\approx$ 20% by Mamajek (2012). Thus, I am using elements that would correspond to a $1.2M_J$ planet. This is a minor effect, especially given my other uncertainties, since the planet mass' main effect is in setting the location of the disk's inner edge, and I determine this numerically by integrating test particles for 100 Myr prior to introducing Fomalhaut b.

establish realistic initial conditions. This follows the approach taken by Chiang et al. (2009), and I find that the 100-Myr timescale is sufficient for the system to reach a quasi-steady state where the particle population is approximately constant. For the integrations I used the package SWIFTER, written by D.E. Kaufmann, which is based on SWIFT (Levison and Duncan 1994). I chose to use the integration scheme SyMBA within SWIFTER (Duncan et al. 1998; Levison and Duncan 2000), as it allowed me to accurately integrate close encounters with Fomalhaut c while ignoring interactions among test particles. Particles were removed from the simulation if they physically collided with Fomalhaut c, or if they moved inside 0.008 AU or outside 1000 AU. After 100 Myr, 7433 particles remained, and, like Chiang et al. (2009), I find an inner edge at approximately 131 AU, with inclinations largely unchanged, except at locations corresponding to mean-motion resonances with Fomalhaut c.

With this quasi-steady state of initial conditions, I then introduced Fomalhaut b on its extreme orbit. To be consistent with K13's best-fit orbit, I chose an apsidally aligned configuration ($\Omega = 0, \omega = 0$) with $a = 177$ AU, $e = 0.8$, $i = 15^\circ$. The a and e values are the marginalized values found in the same study, and i is slightly smaller than the best-fit value of the mutual inclination (17°).

Figure 7.5 shows snapshots in time of the inclination distribution for a Neptune-mass Fomalhaut b, which confirm the expectations presented at the beginning of this section. Initially (following the 100 Myr integration without Fomalhaut b), the standard deviation of the parent-bodies' orbital inclinations was 3.4° (biased beyond 1.5° by inclinations excited at mean-motion resonances as mentioned above—many points lie off-screen at higher inclinations). By 10 Myr, the mean inclination has risen, the standard deviation has doubled, and

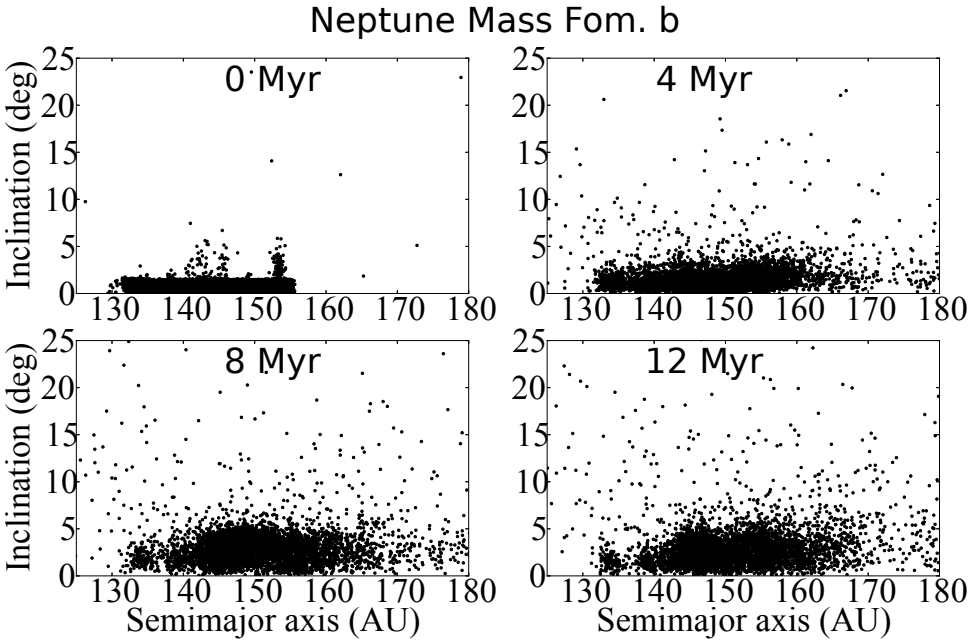

Figure 7.5: Snapshots in time of the inclination distribution of parent bodies vs. semimajor axis. The hypothetical unseen planet Fomalhaut c has a mass of 1 Jupiter-mass, and Fomalhaut b has a mass of 1 Neptune-mass. By $\approx$ 10 Myr, the mean inclination has changed, and the inclination dispersion has doubled from its initial value, inconsistent with observations.

the distribution is clearly inconsistent with observations.

The main result of this section is the left panel in Fig. 7.6, which shows a summary of the results of our simulations where Fomalhaut b has masses of either 1 $M_\oplus$, 3 $M_\oplus$, 10 $M_\oplus$, Neptune (17$M_\oplus$), Saturn (95 $M_\oplus$), Jupiter (318 $M_\oplus$), or 1000 $M_\oplus$. I took the maximum lifetime of Fomalhaut b on its present orbit to be the time required for the standard deviation of the inclinations to double (cf. Fig. 7.5). The dashed line (normalized to the value for Jupiter) shows the expected scaling $\propto M_p^{-1}$, where M_p is the planet's mass, that one expects from secular behavior (see Eq.

7.3). The trend may have continued for slightly smaller values than $M_p = 10M_\oplus$,

but in my runs with $1M_\oplus$ and $3M_\oplus$, the integration was long enough that Fomalhaut b suffered a close encounter with Fomalhaut c and was ejected from the system. Thus, for objects with $M_p \ll M_c$, the maximum lifetime is set by the close-encounter timescale with Fomalhaut c.

To quantify this ejection time in the limit $M_p \ll M_c$, I performed an integration using SyMBA (Duncan et al. 1998) with the same Fomalhaut c, and 10^4 hypothetical Fomalhaut b test particles that do not interact with each other. These candidate planets were given the same $a = 177$ AU, $e = 0.8$ and $i = 15^\circ$, but their longitudes of ascending node, arguments of pericenter and true anomalies were randomly drawn from a uniform distribution in the range $[0, 360]$. The solid line in the right panel of Fig. 7.6 shows the number of surviving Fomalhaut b's vs. time. It is well-fit by an exponential decay (dashed line) with an e-folding timescale of ≈ 48 Myr. This value is plotted as the solid horizontal line in the left panel.

So while K13 found that a Neptune-to-Saturn-mass Fomalhaut b would not disrupt the disk on orbital timescales (see their Fig. 29), I conclude that such a planet must have scattered onto its present orbit more recently than the secular timescale of ~ 10 Myr ago. This is essentially the same result I obtained in the previous section's scenario where Fomalhaut b was the only object interacting with the disk. It should not be surprising as they are both measuring the secular timescale of perturbations from Fomalhaut b. Sub-Neptune Fomalhaut b masses would also be consistent, since then the disk's self-gravity (which I have ignored) would become important, and Fomalhaut b's secular effects on the belt are mitigated. However, on a timescale $\tau_{Scat} \approx 48$ Myr, Fomalhaut b would undergo a close encounter with Fomalhaut c and be ejected. This constraint

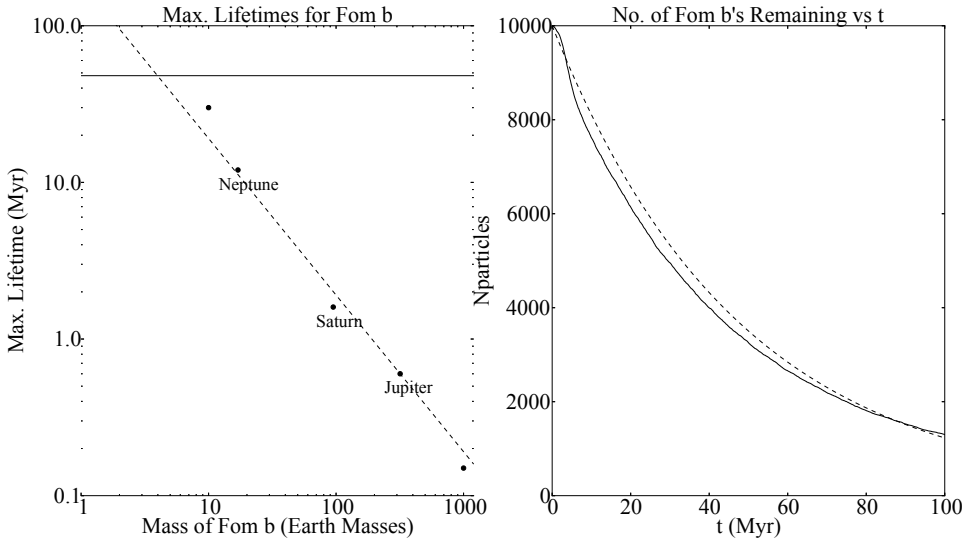

Figure 7.6: Left panel: Summary of simulations with a Jupiter-mass Fomalhaut c. The plot shows Fomalhaut b's maximum lifetime on its present orbit (defined as the time required for the planet to cause the debris disk's inclination dispersion to double), as a function of Fomalhaut b's mass. The dashed line shows the expected scaling $\propto M_p^{-1}$ that one expects from secular behavior, normalized to the maximum lifetime of Jupiter. Planets in the limit $M_p \ll M_c$ are ejected on a timescale $\sim \tau_{Scat} = 48$ Myr, shown by the solid horizontal line. Right panel: Number of initial Fomalhaut b orbits surviving vs. time (solid line). The trend is well fit by an exponential decay with $\tau_{Scat} = 48$ Myr (dashed line). On a timescale τ_{Scat}, objects suffer a close encounter with Fomalhaut c and are ejected from the system. See text for initial conditions.

is relaxed with lower masses for Fomalhaut c, since closer encounters become necessary for ejection, so τ_{Scat} rises. For example, in a parallel simulation to that displayed in the right panel of Fig. 7.6 using a Saturn-mass Fomalhaut c, I find $\tau_{Scat} = 194$ Myr.

I conclude that if there exists an unseen Fomalhaut c orbiting interior to the debris disk and forcing its observed eccentricity as described by Quillen

(2006) and Chiang et al. (2009), then either (a) Fomalhaut b is massive enough ($\gtrsim$ Neptune-mass) to dominate the disk's self-gravity and must have scattered into its present orbit within the last $\sim$ 10 Myr, or (b) Fomalhaut b's mass is small relative to the debris disks's and can thus be long-lived without destroying the disk's structure. The latter case is more likely for Fomalhaut c masses $\sim$ 1 Saturn-mass, as then the timescale for close encounters between Fomalhaut b and c leading to ejection of Fomalhaut b is comparable to the age of the system. But if one considers the possibility that Fomalhaut b's mass is low enough that its secular effect on the debris disk is negligible, one should also investigate other low-mass scenarios—perhaps Fomalhaut b is nothing more than an isolated, transient dust cloud. I consider this general class of low-mass scenarios for Fomalhaut b in the next section.

7.4 A Low-Mass Fomalhaut b?

Before considering specific possibilities, I begin by making two general points about any models that claim that Fomalhaut b's mass is low enough ($\lesssim$ Neptune-mass) that it does not influence the secular dynamics in the debris disk. First, by emasculating Fomalhaut b, one pushes the burden of explanation for the circumstellar disk's measured eccentricity onto an unidentified perturbation, such as an unseen planet. Second, it is difficult to explain why Fomalhaut b and the disk seem to be roughly apsidally aligned (to within at least $\sim 25^\circ$, K13). By the above definition, a low-mass Fomalhaut b cannot be forcing the alignment; it is perhaps possible that instead the disk's gravity forces Fomalhaut b's pericenter, though one would also have to consider the secular effects from Fomalhaut c (or whatever other perturbation is responsible for the disk's

forced eccentricity). I leave such an analysis for future work when more data is available and the problem is better constrained. Of course, the alignment could also be purely fortuitous (probability $\lesssim 10\%$).

The next important constraint for a low-mass Fomalhaut b is the object's large observed flux at optical wavelengths. Because Fomalhaut b has not been detected in the infrared, optical images must be detecting starlight scattered from a vast cloud of dust. One can envision a variety of explanations for such dust, which I deal with in turn. In all cases, the main question is whether such a dusty structure would be long-lived enough, or such dust-producing events frequent enough, to render it plausible that we would observe Fomalhaut b today.

By assuming the dust is optically thick, Kalas et al. (2008) estimated the minimum-size disk of dust that could explain the observed flux as $\sim$ 300 Earth-radii. While a primordial protosatellite disk of this size would be plausible around a gas giant during planet formation, it is unlikely that a super-Earth would host such a disk 440 Myr after formation. Circumplanetary disks from giant impacts like the ones thought to have formed the Moon (e.g., Salmon and Canup 2012) and Charon (e.g. Canup 2011) are also highly implausible, since such disks are much smaller than 300 Earth-radii and should only last $\sim$ 100 yrs (Salmon and Canup 2012).

A more promising idea proposed by Kennedy and Wyatt (2011) is that we are observing dust produced in a collisional cascade among a swarm of irregular satellites around Fomalhaut b. Such populations are observed around each of the Solar System's giant planets, and fill a large fraction of their parent planets' Hill spheres (inside which the planet can keep satellites in orbit in the face of

the Sun's tidal gravity). Such a dust distribution would be more extended and optically thin, though still unresolvable by HST, since the Hill radius of a 2 $M_\oplus$ Fomalhaut b on the nominal orbit from K13 would be $\approx$ 0.4 AU and the Hubble Space Telescope's ACS/HRC has a point spread function with a full-width half-max corresponding to $\approx$ 0.5AU (Kalas et al. 2008). Note that to estimate Fomalhaut b's Hill sphere on its eccentric orbit, it is important to evaluate the Hill radius at pericenter (e.g., Hamilton and Burns 1992). Using a simple model, Kennedy and Wyatt (2011) argue that the minimum planet size that can host such a collisional cascade of irregular satellites is set by the requirement that the orbital speeds be fast enough for collisions between irregular satellites to be destructive. They find that for the collisional cascade to generate the observed flux for the age of the Fomalhaut system, Fomalhaut b must have a mass $\gtrsim$ a few $M_\oplus$. Thus, subject to the caveats mentioned at the beginning of the section for all low-mass Fomalhaut b scenarios, this provides a possible, though finely tuned explanation: Fomalhaut b is a super-Earth with enough mass to drive a collisional cascade of irregular satellites (M $\gtrsim$ a few $M_\oplus$) but too little to drive the secular dynamics of the debris disk (M $\lesssim$ Neptune-mass).

However, once one posits that Fomalhaut b is of such low mass that its dynamical influence on the system is negligible, it is tempting to throw out the planetary interpretation completely and argue that Fomalhaut b is simply a transient dust cloud. Such a scenario was considered by Galicher et al. (2013), but the revised eccentric orbit of Fomalhaut b provides new constraints.

One might ask whether a cloud of dust could naturally be driven to high eccentricity through radiation pressure. This is appealing as it could in principle account for Fomalhaut b's anomalously high eccentricity through a collision

between objects on near-circular orbits. Objects moving on such paths should be much more numerous (particularly in the circumstellar debris disk), so one would expect many more such collisions compared to ones involving eccentric orbits. However, on short sub-orbital and size-variable timescales, radiation pressure would disperse such a dust cloud to several AU in extent (Burns et al. 1979). Fomalhaut b would have thus been easily resolved in the original HST observations, which it was not (Kalas et al. 2008). Galicher et al. (2013) argue that Fomalhaut b may be marginally resolved in the same HST data, though the inferred size of the dust cloud $\approx$ 0.5 AU is still far too small. One might argue that the collision could have taken place recently (close to Fomalhaut b's current position) so that the dust would not have had time to disperse beyond $\sim$ 0.5 AU. But such a scenario also fails, as dust released from nearly circular orbits would move on orbits whose pericenters are close to their location of release (Burns et al. 1979). However, Fomalhaut b's pericenter is more than 90° away from its present position (see Fig. 20 in K13). Fomalhaut b's eccentricity is therefore not caused by radiation pressure; rather, it must be inherited from one (or both) of its parent bodies.

The requirement that the putative Fomalhaut b dust cloud be smaller than 0.5 AU in radius (to be unresolved or marginally resolved) further constrains any impact event to have occurred recently. If the resulting dust cloud is unbound to a massive central object, K13 find that Keplerian shear smears the cloud along the orbit into a structure that is resolvable by HST within $\approx$ 1000 years. K13 further determine that one can prevent such shearing by placing the cloud in orbit around a parent central body with mass $\gtrsim 5 \times 10^{21}$ kg (roughly 5 times Ceres' mass). Perhaps, therefore, dust around a dwarf planet could render the configuration long-lived (without disturbing the disk, see Fig. 7.6). How-

ever, as I argued above, such an impact-generated circumplanetary cloud like the one thought to have produced Pluto's moon Charon Canup (2011) would be far too compact and short-lived to explain Fomalhaut b. Finally, unbound dust from such an impact would disperse even faster than in the isolated dust-cloud scenario. The escape speed from objects $\gtrsim 5 \times 10^{21}$ kg is $gtrsim$0.5 km/s. Taking the unbound debris to collectively be moving at this minimum escape speed (this is really a three-body problem, but the two-body escape speed sets the right scale), or at $\gtrsim 0.1$ AU/yr, the cloud would be resolved by HST within $\lesssim 20$ years.

I conclude that since the lifetimes of clouds of debris that are either isolated or bound to low-mass objects are so short, the probability of observing a specific such dust cloud is exceedingly low. However, one must balance this against the rates of collisions that produce such objects. Previous estimates of these frequencies yielded reasonable values of ~ 1 dust cloud per 200 yrs (Galicher et al. 2013), but they assumed that the impactors originated in the densely populated debris disk. This scenario must be re-evaluated in light of Fomalhaut b's revised eccentric orbit. It is difficult to see from simple conservation laws how an impact between comparably sized bodies in the belt could simultaneously yield a low angular momentum (to provide a large eccentricity) and a high orbital energy (to raise a from the disk's value of ≈ 140 AU to Fomalhaut b's $a \sim 180$ AU). For example, a prograde-retrograde collision between comparably sized objects could generate an appropriately low angular momentum, but would yield a low orbital energy and thus a *smaller* semimajor axis. One seems to require the rarer event of an object first scattering onto Fomalhaut b's orbit, and then impacting a much smaller body in the debris disk so that the total energy and angular momentum is dominated by the former projectile; the resulting dust cloud would

then follow the same eccentric orbit.

I briefly note that if the potential scattered object does not cross the debris disk, the collision probability plummets. The particle-in-a-box impact timescale between two isolated bodies is $\sim (a/R)^2$ orbital times, where a is the semimajor axis and R is the impactor radius (e.g., Hamilton and Burns 1994). The observed flux from Fomalhaut b corresponds to a dust mass equivalent to that in a $\sim$ 10 km body (Kalas et al. 2008). If one considers a collision between two such objects with semimajor axes $\sim$ 100 AU, one obtains an impact timescale of $\sim 10^{21}$ yrs. Even if there were many such candidate pairs of objects to collide, this is prohibitively long.

In conclusion, the only long-lived explanation for a low-mass Fomalhaut b considered above is a collisionally grinding swarm of irregular satellites around a super-Earth with $\sim$ a few $M_\oplus \lesssim M \lesssim$ Neptune-mass. Other impact scenarios all have short dust lifetimes $\lesssim$ 1000 yrs. This can be counterbalanced if the frequency of such impacts is large. I argued that plausible impacts require an original impactor on a similarly eccentric orbit that physically crossed through the debris disk (not just in projection). Currently, only $\approx$ 12% of the orbits that fit the data do so (K13), but this will be an important test as the orbit is further refined with additional observations. This assumes that Fomalhaut b's orbit has not changed appreciably since the impact, which is reasonable since the dust-cloud lifetime of $\sim$ 1 Fomalhaut-b orbit about the central star does not give the orbit time to change appreciably. In both the long-lived irregular-satellite swarm and the frequent transient dust-cloud scenarios, we require the existence of an undetected giant planet Fomalhaut c orbiting interior to the observed debris disk (or a different undetermined mechanism) to force the belt's eccentricity. An ade-

quate explanation must also account for the seeming apsidal alignment between Fomalhaut b and the disk (K13).

7.5 Conclusion

In this article, I have considered three scenarios: (1) Fomalhaut b is a giant planet and is the only object dynamically interacting with the debris disk, (2) Fomalhaut b has enough mass ($\gtrsim$ 1 Neptune mass) to secularly affect the disk, but the belt's eccentricity is instead dominantly forced by an additional unseen planet Fomalhaut c, and (3) Fomalhaut b is a low-mass object—either a super-Earth generating dust through collisions between its irregular satellites, or perhaps simply a transient dust cloud—and again the belt's eccentricity is set by an unseen Fomalhaut c (or a different unidentified perturbation).

Case (1) makes the important diagnostic prediction that the pericenters of Fomalhaut b and the debris disk should be at roughly right angles (Sec. 7.2, Fig. 7.3). This was found recently by Beust et al. (2013) (see the note following the acknowledgements). Currently, such a scenario is largely inconsistent with observations. Additional epochs of observation should be able to rule out the few orbital fits that are consistent with this scenario; however, in the event that such fits are instead supported by additional data, one expects disk particles to reach eccentricities approaching unity within $\sim$ 10 Myr (Fig. 7.4). If the Fomalhaut system harbored planets close to the central star, such planets would undergo a period analogous to the hypothesized Late Heavy Bombardment in our own Solar System (Sec. 7.2).

In case (2), where the debris disk's observed eccentricity is instead domi-

nantly forced by an unseen planet Fomalhaut c, a $\sim$ Neptune-mass or larger Fomalhaut b would have to have scattered into its present orbit within the last $\sim$ 10 Myr (see Fig. 7.6 in Sec. 7.3). This timescale is short compared to the system's age of 440Myr, rendering it unlikely that we would witness the event in process.

Lower masses than $\sim$ 1 Neptune-mass for Fomalhaut b (case 3) mean that Fomalhaut b's gravitational effect on the debris disk will be small compared to the disk's self-gravity, and the disk's structure can be maintained on long timescales. However, such explanations require an undetected Fomalhaut c (or a different undetermined mechanism) to force the debris disk's observed eccentricity, and must simultaneously account for the large amount of dust implicated in Fomalhaut b's observed optical flux (Kalas et al. 2008).

One plausible explanation is that the dust is maintained through a collisional cascade among a swarm of irregular satellites, which exist around each of the Solar System's giant planets. However, Kennedy and Wyatt (2011) find that only planets $\gtrsim$ a few Earth masses have fast enough circumplanetary velocities for collisions between irregulars to be sufficiently destructive to maintain the dust over the Fomalhaut system's lifetime. Thus, a planetary interpretation for Fomalhaut b only is plausible within a narrow range of masses between a few and $\sim$ 20 Earth-masses.

Alternatively, Fomalhaut b could merely be a transient dust cloud, the result of one of many, frequent impacts. I argued in Sec. 7.4 that Fomalhaut b's revised eccentric orbit requires an impact between a body previously scattered into Fomalhaut b's orbit that collides with a much smaller object. It is otherwise difficult to explain Fomalhaut b's low angular momentum, high energy

orbit. I also argued that for such an impact to be plausible, it must have occurred recently, and Fomalhaut b's orbit must pass directly through the debris disk—currently only $\approx 12\%$ of the orbits that fit the data do so (K13). It is also difficult under this scenario to understand the observed apsidal alignment between Fomalhaut b and the debris disk, since Fomalhaut b has no effect on the disk, and the dust cloud's lifetime ($\sim$ 1 Fomalhaut b orbit) is not long enough for the disk or Fomalhaut c to secularly affect Fomalhaut b's orbit. In this case, apsidal alignment would have to be the orientation under which Fomalhaut b's orbit intersects the debris disk, which the current data do not support.

The Fomalhaut system thus provides a complex set of constraints on Fomalhaut b. The best explanation found in this paper is that Fomalhaut b is a super-Earth hosting a large population of irregular satellites, and that there exists an undetected Fomalhaut c orbiting interior to the disk in the range $a \approx 100 - 120$ AU and $e \approx 0.11 - 0.14$—the orbit Fomalhaut b was previously thought to move on, which can naturally explain the debris disk's observed eccentricity (Quillen 2006; Chiang et al. 2009). A super-Earth mass is large enough to drive a collisional cascade among the irregular satellites to generate the observed dust, yet low enough so as to preserve the debris disk's structure on long timescales. This narrow mass range is somewhat uncomfortable, but future observations should help elucidate Fomalhaut b's mysterious nature.

One way to falsify this hypothesis would be to resolve Fomalhaut b's emission and obtain an estimate of the dust's extent. The dynamically stable region in which irregular satellites can orbit over long timescales is inside roughly half of the planet's Hill sphere (e.g. Nesvorný et al. 2003). This scenario then predicts that the dust emission should be confined to a cloud with radius $\lesssim 1\%$ of

Fomalhaut b's pericenter distance $\sim 0.5AU$. This roughly corresponds to the resolution of the original images taken by Kalas et al. (2008) with the Hubble Space Telescope. Interestingly, Galicher et al. (2013) find that Fomalhaut b may be resolved at 0.8 μm. Further observations should help elucidate this picture.

In particular, JWST's NIRCAM should be in a powerful position to constrain the Fomalhaut system both by pushing to higher sensitivity and resolution in the infrared, and by extending the temporal baseline over which Fomalhaut b is tracked, thus refining its orbit. The major questions are: (i) Can JWST detect Fomalhaut b in the near infrared, confirming it as a giant planet? (ii) Can it resolve Fomalhaut b, suggesting it is instead an expanding/shearing cloud of dust? (iii) Can it find a Fomalhaut c orbiting interior to the disk (iv) Does Fomalhaut b's orbit physically cross through the debris disk, rendering it plausible for a collision between two low-mass objects to generate Fomalhaut b?

Of one thing we can be certain—as new observations come in, the Fomalhaut system will remain a rich and lively topic of debate.

CHAPTER 8

CONCLUSIONS AND FUTURE WORK

The overarching conclusion of this thesis is that the irregular satellites have transferred a substantial amount of material onto the surfaces of the outermost regular satellites of each of the giant planets. This is significant as remote sensing of these regular satellites is only sensitive to the topmost surface layer, i.e., to a thickness of a few times the wavelength of the observation. Thus, even a thin layer of contamination can completely obscure the underlying indigenous material. This is an important consideration for any interpretation of the possible surface geochemistry.

More specifically, Chap. 2 showed that most of the long-lived dust that decays inward from Saturn's irregular satellites should strike Iapetus. Furthermore, the predicted distribution of material on the moon's surface matches observations well, with the wrapping of dark material onto the trailing side explained through orbital eccentricities induced by radiation pressure.

Chapters 3 and 4 detailed a novel technique for indirectly probing the Phoebe ring with the Cassini spacecraft. These data, when combined with the data in the infrared from Verbiscer et al. (2009), allowed for the estimation of the grain albedos, and the increased radial coverage allowed for the determination of the disk's radial structure.

The next two chapters addressed the transfer of material between irregular and regular satellites in the Uranian system. Chapter 5 provided the theoretical framework for understanding the evolution of dust grain orbits as they transition from a high-obliquity planet's orbital plane to its equatorial plane, pass-

ing through a chaotic zone that plunges their pericenters close to the planet. This work built on the work of Tremaine et al. (2009) by considering the additional effects of radiation pressure. Chapter 6 then investigated the Uranian case in particular, finding that infall of irregular satellite dust could both generate leading-trailing hemispherical dichotomies, and reproduce the observed increase in color asymmetry with increasing distance from the planet.

Finally, Chap. 7 investigated the implications of the newly revised, highly eccentric orbit for Fomalhaut b. It shows that this development sets stringent constraints on Fomalhaut b. The only plausible scenario found was one where Fomalhaut b is in the super-Earth regime (massive enough to host a swarm of irregular satellites to generate the observed scattered flux, but not massive enough to disrupt the dynamically cold circumstellar debris disk over the age of the system), with an additional unseen giant planet orbiting interior to the debris disk, and carving out its inner edge.

The research carried out also poses important questions that provide directions for future work. Is the amount of dark material in Iapetus' Cassini Regio (constrained by radar observations of the layer's depth (Ostro et al. 2006) to be $\sim 10^{15}$ kg) indicative of the amount of dust ground up by collisions between the irregular satellites at Saturn? This estimate is orders of magnitude lower than that suggested theoretically by Bottke et al. (2010). It may thus be that fewer irregular satellites are captured by Saturn than would be predicted by the Nice model. This would constrain both possible migration histories of the giant planets and the surface density of planetesimals in the disk.

Alternatively, it is possible that the dominant fraction of material is immediately lost to Saturn and its rings. As discussed in Chap. 2, particles smaller

than $\sim 5\mu$m have their orbital eccentricities pumped up to unity within a single Saturnian year. This should predominantly lead to collisions with Saturn's rings at pericenter (which have a larger surface area than the planet). Since the Poynting-Robertson decay timescale is long ($\gtrsim 1 Myr$), at early times when collisions are frequent and the disk's optical depth is higher, there should be many inter-particle collisions before orbits have time to migrate inward toward Iapetus. It may thus be that particles are continually ground down to smaller and smaller size until reaching the minimum threshold of 5μm and impacting Saturn's main rings. This would then predict a low flux of leftover material that slowly migrates inward to Iapetus. This scenario would also impose additional constraints. Saturn's main rings are constituted of remarkably pure water ice. The requirement that the main rings not be contaminated by dark material would set an upper limit on the amount of initial mass in the irregular satellites, or alternatively, argue that the rings are young, i.e., that they postdate a few hundred Myr after the capture of the irregular satellites, in order to avoid the influx of the majority of this material. Future modeling should be able to address this question.

More work on Cassini observations of the Phoebe ring could also yield important insights into its radial structure. Work should be focused on improving the model of the shadow cast by Saturn and its rings, which currently has difficulty fitting the data closer to the planet. Additionally, I hope to tie the modeled radial profile together with theoretical models of the Phoebe ring's 3-D structure.

The dynamics in Chap. 5 suggest applications across a broad range astrophysical settings. Hierarchical stellar triple systems with a large inclination be-

tween the tight binary's orbital plane and that of the outer companion would similarly create a chaotic zone in which orbiting bodies would undergo chaotic large-amplitude eccentricity and inclination cycles (where the tight binary acts like an effective oblateness for a single planet). This would generate a "forbidden zone" at a range of distances from the tight binary where one does not expect to find any bodies, as their high eccentricities would have led to impact with one of the stars. An important application in the solar system is Pluto, which will be visited by New Horizons in July 2015. In both of these cases, the formalism of Chap. 5 must be modified to account for the tight secondary (Charon for Pluto), but the effect should be qualitatively unaltered.

Finally, more detailed dynamical investigations of the Fomalhaut system will need to await further data to better constrain Fomalhaut b's orbit, as well as to settle the question of whether the object is marginally resolved. In Chap. 7 I detailed important questions for future observations to address.

BIBLIOGRAPHY

Acton, C.H., 1996. Ancillary data services of NASA's Navigation and Ancillary Information Facility. Planet. Space Sci. 44, 65–70.

Albers, S., 2008. http://laps.noaa.gov/albers/sos/saturn/iapetus/iapetusmac_rgb_cyl_www.jp .

Allan, R.R., Cook, G.E., 1964. The long-period motion of the plane of a distant circular orbit. Royal Society of London Proceedings Series A 280, 97–109.

Beust, H., Augereau, J.C., Bonsor, A., Graham, J., Kalas, P., Lebreton, J., Lagrange, A.M., Ertel, S., Faramaz, V., Thebault, P., 2013. An independent determination of Fomalhaut b's orbit and the dynamical effects on the outer dust belt. ArXiv e-prints 1311.5035.

Black, G.J., Campbell, D.B., Carter, L.M., Ostro, S.J., 2004. Radar detection of Iapetus. Science 304, 553–553.

Blackburn, D.G., Buratti, B.J., Ulrich, R., 2011. A bolometric bond albedo map of iapetus: Observations from¡ i¿ cassini¡/i¿ vims and iss and¡ i¿ voyager¡/i¿ iss. Icarus 212, 329–338.

Boley, A.C., Payne, M.J., Corder, S., Dent, W.R.F., Ford, E.B., Shabram, M., 2012. Constraining the Planetary System of Fomalhaut Using High-resolution ALMA Observations. ApJ 750, L21. 1204.0007.

Bottke, W.F., Greenberg, R., 1993. Asteroidal collision probabilities. Geophys. Res. Lett. 20, 879–881.

Bottke, W.F., Nesvorný, D., Vokrouhlický, D., Morbidelli, A., 2010. The irregular satellites: The most collisionally evolved populations in the Solar System. AJ 139, 994–1014.

Bottke, W.F., Vokrouhlický, D., Nesvorný, D., Moore, J.M., 2013. Black rain: The burial of the Galilean satellites in irregular satellite debris. Icarus 223, 775–795.

Brozovic, M., Jacobson, R.A., 2009. The orbits of the outer Uranian satellites. AJ 137, 3834–3842.

Buratti, B.J., Hicks, M.D., Davies, A., 2005. Spectrophotometry of the small satellites of Saturn and their relationship to Iapetus, Phoebe, and Hyperion. Icarus 175, 490–495.

Buratti, B.J., Hicks, M.D., Tryka, K.A., Sittig, M.S., Newburn, R.L., 2002. High-resolution 0.33-0.92 μm spectra of Iapetus, Hyperion, Phoebe, Rhea, Dione, and D-type asteroids: How are they related? Icarus 155, 375–381.

Buratti, B.J., Mosher, J.A., 1991. Comparative global albedo and color maps of the Uranian satellites. Icarus 90, 1–13.

Buratti, B.J., Soderlund, K., Bauer, J., Mosher, J.A., Hicks, M.D., Simonelli, D.P., Jaumann, R., Clark, R.N., Brown, R.H., Cruikshank, D.P., Momary, T., 2008. Infrared (0.83 5.1 μm) photometry of Phoebe from the Cassini Visual Infrared Mapping Spectrometer. Icarus 193, 309–322.

Burns, J.A., 1976. Elementary derivation of the perturbation equations of celestial mechanics. AmJPhys 44, 944–949.

Burns, J.A., Hamilton, D.P., Mignard, F., Soter, S., 1996. The contamination of Iapetus by Phoebe dust, in: Gustafson, B.A.S., Hanner, M.S. (Eds.), ASP Conference Series Vol, 104, Physics, Chemistry, and Dynamics of Interplanetary Dust, University of Chicago Press. pp. 179–182.

Burns, J.A., Hamilton, D.P., Showalter, M.R., 2001. Dusty rings and circumplanetary dust: Observations and simple physics, in: Grün, E., Gustafson, B. A. S., Dermott, S., & Fechtig, H. (Ed.), Interplanetary Dust, Springer, Berlin. pp. 641–725.

Burns, J.A., Lamy, P.L., Soter, S., 1979. Radiation forces on small particles in the solar system. Icarus 40, 1–48.

Burns, J.A., Showalter, M.R., Hamilton, D.P., Nicholson, P.D., de Pater, I., Ockert-Bell, M.E., Thomas, P.C., 1999. The formation of Jupiter's faint rings. Science 284, 1146–1150.

Canup, R.M., 2011. On a Giant Impact Origin of Charon, Nix, and Hydra. AJ 141, 35.

Canup, R.M., Ward, W.R., 2002. Formation of the galilean satellites: Conditions of accretion. The Astronomical Journal 124, 3404.

Carruba, V., Burns, J.A., Nicholson, P.D., Gladman, B.J., 2002. On the inclination distribution of the jovian irregular satellites. Icarus 158, 434–449.

Carruba, V., Burns, J.A., Nicholson, P.D., Gladman, B.J., 2003. Erratum to "on the inclination distribution of the jovian irregular satellites"[Icarus 158 (2002) 434-449]. Icarus 162, 230–231.

Castillo-Rogez, J., Matson, D., Sotin, C., Johnson, T., Lunine, J., Thomas, P., 2007. Iapetus' geophysics: Rotation rate, shape, and equatorial ridge. Icarus 190, 179–202.

Chiang, E., Kite, E., Kalas, P., Graham, J.R., Clampin, M., 2009. Fomalhaut's Debris Disk and Planet: Constraining the Mass of Fomalhaut b from disk Morphology. ApJ 693, 734–749. 0811.1985.

Clark, R.N., Curchin, J.M., Jaumann, R., Cruikshank, D.P., Brown, R.H., Hoefen, T.M., Stephan, K., Moore, J.M., Buratti, B.J., Baines, K.H., Nicholson, P.D., Nelson, R.M., 2008. Compositional mapping of Saturn's satellite Dione with Cassini VIMS and implications of dark material in the Saturn system. Icarus 193, 372–386.

Cook, A., Franklin, F., 1970. An explanation of the light curve of Iapetus. Icarus 13, 282–291.

Cruikshank, D.P., Bell, J.F., Gaffey, M.J., Brown, R.H., Howell, R., Beerman, C., Rognstad, M., 1983. The dark side of Iapetus. Icarus 53, 90–104.

Cruikshank, D.P., Dalton, J.B., Ore, C.M.D., et al., 2007. Surface composition of Hyperion. Nature 448, 54–56.

Ćuk, M., Burns, J.A., 2004. Gas-drag-assisted capture of himalia's family. Icarus 167, 369–381.

Currie, T., Debes, J., Rodigas, T.J., Burrows, A., Itoh, Y., Fukagawa, M., Kenyon, S.J., Kuchner, M., Matsumura, S., 2012. Direct Imaging Confirmation and Characterization of a Dust-enshrouded Candidate Exoplanet Orbiting Fomalhaut. ApJ 760, L32. 1210.6620.

Cuzzi, J.N., Estrada, P.R., 1998. Compositional evolution of Saturn's rings due to meteoroid bombardment. Icarus 132, 1–35.

Danby, J., 1962. Fundamentals of Celestial Mechanics. New York: Macmillan.

Deltorn, J.M., Kalas, P., 2001. Search for Nemesis Encounters with Vega, ϵ Eridani, and Fomalhaut, in: Jayawardhana, R., Greene, T. (Eds.), Young Stars Near Earth: Progress and Prospects, p. 227. arXiv:astro-ph/0105284.

Denk, T., Neukum, G., Roatsch, T., et al., 2010. Iapetus: Unique surface properties and a global color dichotomy from Cassini imaging. Science 327, 435–439.

Dermott, S., Nicholson, P., Burns, J., Houck, J., 1984. Origin of the solar system dust bands discovered by IRAS. Nature 312, 505–509.

Dobrovolskis, A.R., 1993. The Laplace planes of Uranus and Pluto. Icarus 105, 400–407.

Dohnanyi, J.S., 1969. Collisional Model of Asteroids and Their Debris. J. Geophys. Res. 74, 2531.

Duncan, M.J., Levison, H.F., Lee, M.H., 1998. A Multiple Time Step Symplectic Algorithm for Integrating Close Encounters. AJ 116, 2067–2077.

Farinella, P., Gonczi, R., Froeschle, C., Froeschle, C., 1993. The injection of asteroid fragments into resonances. Icarus 101, 174–187.

Galicher, R., Marois, C., Zuckerman, B., Macintosh, B., 2013. Fomalhaut b: Independent Analysis of the Hubble Space Telescope Public Archive Data. ApJ 769, 42. 1210.6745.

Gladman, B., Kavelaars, J.J., Holman, M., Nicholson, P.D., Burns, J.A., Hergenrother, C.W., Petit, J., Marsden, B.G., Jacobson, R., Gray, W., Grav, T., 2001. Discovery of 12 satellites of Saturn exhibiting orbital clustering. Nature 412, 163–166.

Goldreich, P., 1965. Inclination of satellite orbits about an oblate precessing planet. AJ 70, 5.

Goldreich, P., 1966. History of the lunar orbit. Rev Geophys Space Phys 4, 411–439.

Grav, T., Holman, M., Gladman, B., Aksnes, K., 2003. Photometric survey of the irregular satellites. Icarus 166, 33–45.

Grav, T., Mainzer, A., Bauer, J., Masiero, J., Nugent, C., Stevenson, R., 2013. Albedo, size and taxonomy of the small body populations outside the main belt, in: AAS/Division for Planetary Sciences Meeting Abstracts.

Greenberg, R., 1982. Orbital interactions - A new geometrical formalism. AJ 87, 184–195.

Hamilton, D., 1994. A comparison of Lorentz, planetary gravitational, and satellite gravitational resonances. Icarus 109, 221–240.

Hamilton, D.P., 1993. Motion of dust in a planetary magnetosphere - Orbit-averaged equations for oblateness, electromagnetic, and radiation forces with application to Saturn's E ring. Icarus 101, 244–264.

Hamilton, D.P., 1996. The Asymmetric Time-Variable Rings of Mars. Icarus 119, 153–172.

Hamilton, D.P., Burns, J.A., 1991. Orbital stability zones about asteroids. Icarus 92, 118–131.

Hamilton, D.P., Burns, J.A., 1992. Orbital stability zones about asteroids. II - The destabilizing effects of eccentric orbits and of solar radiation. Icarus 96, 43–64.

Hamilton, D.P., Burns, J.A., 1994. Origin of Saturn's E Ring: Self-sustained, naturally. Science 264, 550–553.

Hamilton, D.P., Krivov, A.V., 1996. Circumplanetary dust dynamics: Effects of solar gravity, radiation pressure, planetary oblateness, and electromagnetism. Icarus 123, 503–523.

Hamilton, D.P., Krüger, H., 2008. The sculpting of Jupiter's gossamer rings by its shadow. Nature 453, 72–75.

Hamilton, D.P., Verbiscer, A.J., Skrutskie, M.F., 2012. Particle Properties in Saturn's Phoebe Ring, in: AAS/Division for Planetary Sciences Meeting Abstracts, p. 501.09.

Hartmann, W.K., Ryder, G., Dones, L., Grinspoon, D., 2000. The Time-Dependent Intense Bombardment of the Primordial Earth/Moon System, in: Canup, R.M., Righter, K., et al. (Eds.), Origin of the Earth and Moon, Univ. Arizona Press. pp. 493–512.

Henyey, L.G., Greenstein, J.L., 1941. Diffuse radiation in the galaxy. The Astrophysical Journal 93, 70–83.

Hodyss, R., Johnson, P.V., Stern, J.V., Goguen, J.D., Kanik, I., 2009. Photochemistry of methane–water ices. Icarus 200, 338–342.

Innanen, K.A., Zheng, J.Q., Mikkola, S., Valtonen, M.J., 1997. The Kozai mechanism and the stability of planetary orbits in binary star systems. AJ 113, 1915–1919.

Janson, M., Carson, J.C., Lafrenière, D., Spiegel, D.S., Bent, J.R., Wong, P., 2012. Infrared Non-detection of Fomalhaut b: Implications for the Planet Interpretation. ApJ 747, 116. 1201.4388.

Jewitt, D., Haghighipour, N., 2007. Irregular satellites of the planets: Products of capture in the early Solar System. ARA&A 45, 261–295.

Jewitt, D., Sheppard, S., Kleyna, J., Marsden, B.G., 2005. New satellites of Saturn. IAU Circ. 8523.

Johnson, R.E., 1990. Energetic charged-particle interactions with atmospheres and surfaces. volume 19. Springer-Verlag New York.

Jontof-Hutter, D., Hamilton, D.P., 2012a. The fate of sub-micron circumplanetary dust grains I: Aligned dipolar magnetic fields. Icarus 218, 420–432. 1201.3578.

Jontof-Hutter, D., Hamilton, D.P., 2012b. The fate of sub-micron circumplanetary dust grains II: Multipolar fields. Icarus 220, 487–502. 1206.0906.

Juhasz, A., Horanyi, M., 1995. Dust torus around Mars. J. Geophys. Res. 100, 3277–3284.

Kalas, P., Graham, J.R., Chiang, E., Fitzgerald, M.P., Clampin, M., Kite, E.S., Stapelfeldt, K., Marois, C., Krist, J., 2008. Optical Images of an Exosolar Planet 25 Light-Years from Earth. Science 322, 1345–. 0811.1994.

Kalas, P., Graham, J.R., Clampin, M., 2005. A planetary system as the origin of structure in Fomalhaut's dust belt. Nature 435, 1067–1070. arXiv:astro-ph/0506574.

Kalas, P., Graham, J.R., Fitzgerald, M.P., Clampin, M., 2013. STIS Coronagraphic Imaging of Fomalhaut: Main Belt Structure and the Orbit of Fomalhaut b. ArXiv e-prints 1305.2222.

Katz, B., Dong, S., Malhotra, R., 2011. Long-Term Cycling of Kozai-Lidov Cycles: Extreme Eccentricities and Inclinations Excited by a Distant Eccentric Perturber. Physical Review Letters 107, 181101. 1106.3340.

Kennedy, G.M., Wyatt, M.C., 2011. Collisional evolution of irregular satellite swarms: detectable dust around Solar system and extrasolar planets. MNRAS 412, 2137–2153. 1011.4858.

Kozai, Y., 1962. Secular perturbations of asteroids with high inclination and eccentricity. AJ 67, 591–598.

Kozai, Y., 1963. Motion of a Lunar Orbiter. PASJ 15, 301–312.

Kudielka, V., 1994. Balanced Earth satellite orbits. Celestial Mechanics and Dynamical Astronomy 60, 455–470.

Landgraf, M., 2000. Modeling the motion and distribution of interstellar dust inside the heliosphere. J. Geophys. Res. 105, 10303–10316. arXiv:astro-ph/9906300.

Laplace, P., 1805. Traité de mécanique céleste. volume 4. de l'Imprimerie de Crapelet.

Larwood, J.D., Kalas, P.G., 2001. Close stellar encounters with planetesimal discs: The dynamics of asymmetry in the β Pictoris system. MNRAS 323, 402–416. arXiv:astro-ph/0011279.

Lavvas, P., Yelle, R.V., Vuitton, V., 2009. The detached haze layer in Titan's mesosphere. Icarus 201, 626–633.

Levison, H.F., Duncan, M.J., 1994. The long-term dynamical behavior of short-period comets. Icarus 108, 18–36.

Levison, H.F., Duncan, M.J., 2000. Symplectically Integrating Close Encounters with the Sun. AJ 120, 2117–2123.

Li, G., Naoz, S., Kocsis, B., Loeb, A., 2013. Counter-orbiting Planets Were Flipped Over by a Coplanar Outer Object. ArXiv e-prints 1310.6044.

Liang, M., Yung, Y.L., Shemansky, D.E., 2007. Photolytically generated aerosols in the mesosphere and thermosphere of Titan. ApJ 661, L199–L202.

Lidov, M.L., 1962. The evolution of orbits of artificial satellites of planets under the action of gravitational perturbations of external bodies. Planet. Space Sci. 9, 719–759.

Lidov, M.L., Yarskaya, M.V., 1974. Integrable Cases in the Problem of the Evolution of a Satellite Orbit under the Joint Effect of an Outside Body and of the Noncentrality of the Planetary Field. Cosmic Research 12, 139.

Liseau, R., 1999. Molecular line observations of southern main-sequence stars with dust disks: alpha PS A, beta Pic, epsilon ERI and HR 4796 A. Does the low gas content of the beta PIC and varepsilon ERI disks hint of planets? A&A 348, 133–138.

Lithwick, Y., Naoz, S., 2011. The Eccentric Kozai Mechanism for a Test Particle. ApJ 742, 94. 1106.3329.

Lyra, W., Kuchner, M., 2013. Formation of sharp eccentric rings in debris disks with gas but without planets. Nature 499, 184–187. 1307.5916.

Mamajek, E.E., 2012. On the Age and Binarity of Fomalhaut. ApJ 754, L20. 1206.6353.

Mamajek, E.E., Bartlett, J.L., Seifahrt, A., Henry, T.J., Dieterich, S.B., Lurie, J.C., Kenworthy, M.A., Jao, W.C., Riedel, A.R., Subasavage, J.P., Winters, J.G., Finch, C.T., Ianna, P.A., Bean, J., 2013. The Solar Neighborhood. XXX. Fomalhaut C. AJ 146, 154. 1310.0764.

Marengo, M., Stapelfeldt, K., Werner, M.W., Hora, J.L., Fazio, G.G., Schuster, M.T., Carson, J.C., Megeath, S.T., 2009. Spitzer/Infrared Array Camera Limits to Planetary Companions of Fomalhaut and epsilon Eridani. ApJ 700, 1647–1657. 0906.0364.

Matthews, R.A., 1992. The Darkening of Iapetus and the Origin of Hyperion. Quarterly Journal of the Royal Astronomical Society 33, 253.

McCord, T.B., Johnson, T.V., Elias, J.H., 1971. Saturn and its satellites: Narrow band spectrophotometry (0.3-1.1 μm). ApJ 165, 413–424.

Mignard, F., Henon, M., 1984. About an unsuspected integrable problem. Cel Mech 33, 239–250.

Miller, C., Verbiscer, A.J., Chanover, N.J., Holtzman, J.A., Helfenstein, P., 2011. Comparing Phoebe's 2005 opposition surge in four visible light filters. Icarus 212, 819–834.

Mosqueira, I., Estrada, P.R., 2003. Formation of the regular satellites of giant planets in an extended gaseous nebula I: subnebula model and accretion of satellites. Icarus 163, 198–231.

Murray, C.D., Dermott, S.F., 1999. Solar System Dynamics. Cambridge U. Press, Cambridge.

Naoz, S., Farr, W.M., Lithwick, Y., Rasio, F.A., Teyssandier, J., 2011. Secular Dynamics in Three-Body Systems. ArXiv e-prints 1107.2414.

Nesvorný, D., Alvarellos, J.L.A., Dones, L., Levison, H.F., 2003. Orbital and collisional evolution of the irregular satellites. AJ 126, 398–429.

Nesvorný, D., Vokrouhlický, D., Morbidelli, A., 2007. Capture of irregular satellites during planetary encounters. AJ 133, 1962–1976.

Nicholson, P.D., Cuk, M., Sheppard, S.S., Nesvorny, D., Johnson, T.V., 2008. Irregular satellites of the giant planets, in: Barucci, M. A., Boehnhardt, H.,

Cruikshank, D. P., & Morbidelli, A. (Ed.), The Solar System Beyond Neptune, University of Arizona Press. Tucson. pp. 411–424.

Öpik, E.J., 1951. Collision probability with the planets and the distribution of planetary matter. Proc. R. Irish Acad. Sect. A 54, 165–199.

Ostro, S.J., West, R.D., Janssen, M.A., Lorenz, R.D., Zebker, H.A., Black, G.J., Lunine, J.I., Wye, L.C., Lopes, R.M., Wall, S.D., Elachi, C., Roth, L., Hensley, S., Kelleher, K., Hamilton, G.A., Gim, Y., Anderson, Y.Z., Boehmer, R.A., Johnson, W.T.K., the Cassini RADAR Team, 2006. Cassini RADAR observations of Enceladus, Tethys, Dione, Rhea, Iapetus, Hyperion, and Phoebe. Icarus 183, 479–490.

Pollack, J.B., Burns, J.A., Tauber, M.E., 1979. Gas drag in primordial circumplanetary envelopes - A mechanism for satellite capture. Icarus 37, 587–611.

Pollack, J.B., Cuzzi, J.N., 1980. Scattering by nonspherical particles of size comparable to wavelength - A new semi-empirical theory and its application to tropospheric aerosols. Journal of Atmospheric Sciences 37, 868–881.

Porco, C.C., Baker, E., Barbara, J., Beurle, K., Brahic, A., Burns, J.A., Charnoz, S., Cooper, N., Dawson, D.D., Del Genio, A.D., Denk, T., Dones, L., Dyudina, U., Evans, M.W., Giese, B., Grazier, K., Helfenstein, P., Ingersoll, A.P., Jacobson, R.A., Johnson, T.V., McEwen, A., Murray, C.D., Neukum, G., Owen, W.M., Perry, J., Roatsch, T., Spitale, J., Squyres, S., Thomas, P.C., Tiscareno, M., Turtle, E., Vasavada, A.R., Veverka, J., Wagner, R., West, R., 2005. Cassini Imaging Science: Initial Results on Phoebe and Iapetus. Science 307, 1237–1242.

Porco, C.C., West, R.A., Squyres, S., McEwen, A., Thomas, P., Murray, C.D., Del Genio, A., Ingersoll, A.P., Johnson, T.V., Neukum, G., Veverka, J., Dones, L.,

Brahic, A., Burns, J.A., Haemmerle, V., Knowles, B., Dawson, D., Roatsch, T., Beurle, K., Owen, W., 2004. Cassini imaging science: Instrument characteristics and anticipated scientific investigations at Saturn. Space Sci. Rev. 115, 363–497.

Quillen, A.C., 2006. Predictions for a planet just inside Fomalhaut's eccentric ring. MNRAS 372, L14–L18. arXiv:astro-ph/0605372.

Roatsch, T., Jaumann, R., Stephan, K., Thomas, P.C., 2009. Cartographic mapping of the icy satellites using ISS and VIMS data, in: Dougherty, M. K., Esposito, L. W., & Krimigis, S. M. (Ed.), Saturn from Cassini-Huygens, Springer. Dordrecht; New York. pp. 763–781.

Rosengren, A.J., Scheeres, D.J., 2014. Laplace Plane Modifications Arising from Solar Radiation Pressure. ApJ 786, 45.

Salmon, J., Canup, R.M., 2012. Lunar Accretion from a Roche-interior Fluid Disk. ApJ 760, 83. 1210.0932.

Schenk, P., Hamilton, D.P., Johnson, R.E., McKinnon, W.B., Paranicas, C., Schmidt, J., Showalter, M.R., 2011. Plasma, plumes and rings: Saturn system dynamics as recorded in global color patterns on its midsize icy satellites. Icarus 211, 740–757.

Shepard, M.K., Helfenstein, P., 2007. A test of the Hapke photometric model. Journal of Geophysical Research (Planets) 112, 3001.

Sheppard, S.S., Gladman, B., Marsden, B.G., 2003. Satellites of Jupiter and Saturn. IAU Circ. 8116.

Sheppard, S.S., Jewitt, D.C., Kleyna, J., Marsden, B.G., 2006. Satellites of Saturn. IAU Circ. 8727.

Simonelli, D.P., Kay, J., Adinolfi, D., Veverka, J., Thomas, P.C., Helfenstein, P., 1999. Phoebe: Albedo map and photometric properties. Icarus 138, 249–258.

Skrutskie, M.F., Masci, F., Fowler, J., Cutri, R.M., Verbiscer, A., Wright, E.L., 2011. Searching for outer planet debris disks/rings with WISE, in: EPSC-DPS Joint Meeting 2011, p. 1665.

Smith, B.A., Soderblom, L., Batson, R., Bridges, P., Inge, J., Masursky, H., Shoemaker, E., Beebe, R., Boyce, J., Briggs, G., et al., 1982. A new look at the saturn system: The voyager 2 images. Science 215, 504–537.

Soter, S., 1974. IAU Colloquium 28. Cornell University .

Spencer, J.R., Denk, T., 2010. Formation of Iapetus' extreme albedo dichotomy by exogenically triggered thermal ice migration. Science 327, 432–435.

Squyres, S.W., Sagan, C., 1983. Albedo asymmetry of iapetus. Nature 303, 782–785.

Tamayo, D., 2014. Consequences of an eccentric orbit for Fomalhaut b. MNRAS 438, 3577–3586. 1312.7020.

Tamayo, D., Burns, J.A., 2013. Consequences of an Eccentric Fomalhaut b, in: AAS/Division of Dynamical Astronomy Meeting, p. 300.03.

Tamayo, D., Burns, J.A., Hamilton, D.P., 2013a. Chaotic dust dynamics and implications for the hemispherical color asymmetries of the Uranian satellites. Icarus 226, 655–662. 1306.3973.

Tamayo, D., Burns, J.A., Hamilton, D.P., Hedman, M.M., 2011. Finding the trigger to Iapetus' odd global albedo pattern: Dynamics of dust from Saturn's irregular satellites. Icarus 215, 260–278.

Tamayo, D., Burns, J.A., Hamilton, D.P., Nicholson, P.D., 2013b. Dynamical instabilities in high-obliquity systems. AJ 145, 54. 1212.0028.

Tamayo, D., Burns, J.A., Nicholson, P.D., Hamilton, D.P., 2012a. Chaos at Uranus spreads dust across the regular satellites, in: AAS/Division of Dynamical Astronomy Meeting, p. 04.03.

Tamayo, D., Hedman, M.M., Burns, J.A., 2014. First observations of the Phoebe ring in optical light. Icarus 233, 1–8. 1401.6166.

Tamayo, D., Hedman, M.M., Burns, J.A., Kavelaars, J.J., 2012b. Observations of the Phoebe Ring with Cassini and Herschel: How Seeing Nothing Can Yield a Signal Half the Time, in: AAS/Division for Planetary Sciences Meeting Abstracts, p. 101.09.

Tholen, D., Zellner, B., 1983. Eight-color photometry of Hyperion, Iapetus, and Phoebe. Icarus 53, 341–347.

Thomas, P.C., Armstrong, J.W., Asmar, S.W., Burns, J.A., Denk, T., Giese, B., Helfenstein, P., Iess, L., Johnson, T.V., McEwen, A., Nicolaisen, L., Porco, C., Rappaport, N., Richardson, J., Somenzi, L., Tortora, P., Turtle, E.P., Veverka, J., 2007. Hyperion's sponge-like appearance. Nature 448, 50–56.

Tisserand, F., 1896. Traité de mécanique céleste. volume 4. Gauthier-Villars et fils.

Tomasko, M.G., West, R.A., 2009. Aerosol's in Titan's Atmosphere, in: Brown, R. H., Lebreton, J.-P., & Waite, J. H. (Ed.), Titan from Cassini-Huygens, Springer. Dordrecht; New York. pp. 297–321.

Tosi, F., Turrini, D., Coradini, A., Filacchione, G., 2010. Probing the origin of the dark material on Iapetus. MNRAS 403, 1113–1130.

Touma, J.R., Tremaine, S., Kazandjian, M.V., 2009. Gauss's method for secular dynamics, softened. MNRAS 394, 1085–1108. 0811.2812.

Tremaine, S., Touma, J., Namouni, F., 2009. Satellite dynamics on the Laplace surface. AJ 137, 3706–3717.

Turrini, D., Marzari, F., Beust, H., 2008. A new perspective on the irregular satellites of Saturn - I. Dynamical and collisional history. MNRAS 391, 1029–1051.

Turrini, D., Marzari, F., Tosi, F., 2009. A new perspective on the irregular satellites of Saturn - II. Dynamical and physical origin. MNRAS 392, 455–474.

Vashkov'yak, M.A., 1996. Periodically evolving satellite orbits in the double-averaged Hill problem with noncoplanar planes of motion of a perturbing point and the equator of an oblate planet. Astronomy Letters 22, 851–860.

Verbiscer, A.J., Skrutskie, M.F., Hamilton, D.P., 2009. Saturn's largest ring. Nature 461, 1098–1100.

Vokrouhlickỳ, D., Pokornỳ, P., Nesvornỳ, D., 2012. Öpik-type collision probability for high-inclination orbits. Icarus 219, 150–160.

Vyazovkin, S., Wight, C.A., 1997. Kinetics in solids. Annual Review of Physical Chemistry 48, 125–149.

Ward, W.R., 1981. Orbital inclination of Iapetus and the rotation of the Laplacian plane. Icarus 46, 97–107.

West, R., Knowles, B., Birath, E., Charnoz, S., di Nino, D., Hedman, M., Helfenstein, P., McEwen, A., Perry, J., Porco, C., Salmon, J., Throop, H., Wilson, D.,

2010. In-flight calibration of the Cassini imaging science sub-system cameras. Planet. Space Sci. 58, 1475–1488.

Wetherill, G.W., 1967. Collisions in the Asteroid Belt. J. Geophys. Res. 72, 2429–2444.

Wyatt, M.C., Dent, W.R.F., 2002. Collisional processes in extrasolar planetesimal discs - dust clumps in Fomalhaut's debris disc. MNRAS 334, 589–607. arXiv:astro-ph/0204034.